UNIVERSITÀ DEGLI STUDI DI UDINE

DIPARTIMENTO POLITECNICO DI INGEGNERIA E ARCHITETTURA

PHD IN INDUSTRIAL AND INFORMATION ENGINEERING

XXXI CYCLE

VIBRATION ENERGY HARVESTING WITH ELECTROMAGNETIC AND PIEZOELECTRIC TRANSDUCERS

AUTHOR:
Loris Dal Bo

SUPERVISOR:
Prof. Paolo Gardonio

UDINE 2018

ABSTRACT

This thesis presents theoretical and experimental work on time-harmonic vibration energy harvesting with electromagnetic and piezoelectric seismic and reactive transducers. The study is focussed on macroscale transducers built assembling multiple components fabricated with traditional processes and materials using classical industrial processes (milling, soldering, printing, etc.). The electromagnetic transducer is composed by a magnet component connected to a moving ferromagnetic ring and coil assembly via soft springs. The piezoelectric transducer is made by a thin cantilever beam with two piezoelectric patches bonded at the top and bottom sides and two tip masses fixed at the base end and at free end. The two prototypes are designed and built in such a way as they have similar weights and volumes for the base and suspended components and same fundamental natural frequencies. Both purely resistive and resistive-reactive harvesting impedance loads are considered. Expressions for the optimal impedances are derived in the frequency domain with reference to time harmonic base vibrations.

The study is based on simple lumped parameters models, which, however, take into account all physical effects that characterise the response of the two harvesters, including the effects of eddy currents losses and dielectric losses. Also, a unified energy formulation based on the frequency response functions of the electro-mechanical transduction coefficients and mechanical and electrical impedances of the two transducers is derived and validated experimentally.

The thesis is structured in three parts. The first part is focussed on the response and energy harvesting with the seismic transducers. The study shows that the maximum power harvested is obtained close to the fundamental natural frequency of the two devices and is significantly influenced by eddy current losses in the electromagnetic transducer and by the dielectric losses in the piezoelectric transducer. Comparing the two prototypes, the electromagnetic harvester is characterised by higher damping effect that reduces the stroke amplitude at the fundamental resonance frequency and thus the maximum power harvested per unit of acceleration. Alternatively, the piezoelectric device is affected by lower mechanical damping and so the power harvested is larger. If instead the harvested power per unit of stroke is examined, the result is opposite.

In the second part of the thesis the power harvesting with reactive electromagnetic and piezoelectric transducers, is investigated. The same transducers than those of the first part of the study are considered, with the seismic masses clamped to a solid block acting as an inertial reference system. Thus, the same models and analytical formulations developed for the seismic harvesters are used, assuming the proof masses are blocked. The study shows that the transducers become effective only for large vibrations of the base mass and furthermore the power harvested is not magnified in correspondence of their fundamental resonant frequency. Also, the electromagnetic harvester outperforms the piezoelectric harvester in the whole frequency range of work, both when the optimal complex impedance and the optimal resistive impedance loads are implemented.

The last part of the thesis is dedicated to the scaling laws for the physical properties and energy harvesting of the seismic and reactive transducers studied respectively in parts 1 and 2. The scaling analysis is limited to the case of tonal ambient vibrations and is carried out considering that the devices are operated at their fundamental natural frequency. An isotropic downscaling is assumed for both harvesters, therefore it is considered that the shapes of the components and of the whole devices do not change with the dimension. Both the optimal purely resistive and resistive-reactive loads are considered. The scaling of the transduction coefficients and electrical and mechanical parameters, which characterise the lumped parameter models of the electromagnetic and piezoelectric seismic and reactive transducers, is first provided. Volume power density normalized to the input squared acceleration and power efficiency are then examined with respect to the scaling length of the seismic harvesters. In addition, a comparative scaling stroke analysis is carried out for either seismic devices. Finally, the scaling laws of the power density and efficiency of the reactive electromagnetic and piezoelectric energy harvesters are investigated.

The thesis is enriched with 6 appendices that provide a detailed account of the modelling and scaling laws derived for and used in the study.

ACKNOWLEDGMENTS

First of all, I would like to thank my supervisor, Prof. Paolo Gardonio, for his support and guidance during my PhD.

I would also like to thank my colleagues and friends, Nicola Battistella, Roberto Del Sal, Daniel Casagrande, Aleksander Kras, Emanuele Turco and Michal Zientek for their suggestions and help.

I am extremely thankful to my parents who, through their support and encouragement, have helped me to get here. Also, I would like to express a great thank you to my grandfather for his sound advice and his willingness to listen to me.

Many thanks go to my friends with whom I shared the best moments during these three years.

On a personal level, my deepest gratitude goes to Alessia, for her patience and the support she gave me throughout course of PhD studies.

CONTENTS

LIST OF FIGURES

LIST OF TABLES

NOMENCLATURE

LIST OF ACRONYMS

AC	Alternating Current
CM	Coil Magnet
DC	Direct Current
FES	Flywheel Energy Storage
FRF	Frequency Response Function
GPS	Global Positioning System
KV	Kelvin Voigt Model
KL	Kimball and Lovell model
MEMS	Micro Electro Mechanical System
MFC	Macro Fiber Composite
PZT	Lead Zirconate Titanate
PVDF	Polyvinylidene Flouoride
RF	Radio Frequency
SMES	Superconducting Magnetic Energy Storage
WINS	Wireless Sensor Network
Z	Zener Model

LIST OF SYMBOLS

Latin letters

Parameter	**Description**	**Unit**
B	Magnetic field	[T]
B	Bending stiffness	[Nm]
c	Damping	[Ns/m]
C	Capacitance	[F]
D	Electric flux density	[q/m^2]
d	Strain/charge constant	[C/N]-[m/V]
E	Young's modulus	[N/m^2]
E	Electric field	[V/m]

e	Voltage	[V]
H	Heaviside function	[-]
h	Thickness	[m]
I	Second moment of area	[m^4]
i	Current	[A]
j	Imaginary number	[-]
k	Stiffness	[N/m]
l	Linear dimension	[m]
L	Coil inductance	[H]
L	Scaling law notation	[-]
m	Mass	[kg]
M	Bending moment	[Nm]
R	Resistance	[Ω]
S	Mechanical strain	[-]
T	Mechanical stress	[N/m^2]
t	Time	[s]
w	Displacement	[m]
ẇ	Velocity	[m/s]
x	Position in x coordinate	[m]
y	Position in y coordinate	[m]
z	Position in z coordinate	[m]

Greek letters

Parameter	**Description**	**Unit**
δ	Kronecker delta operator	[-]
δ	Delta Dirac function	[-]
ξ	Damping ratio	[-]
η	Loss factor	[-]
Π	Coupling modal term	[As]-[kg/Vs^2]
ε	Permittivity coefficient	[F/m]
τ	Time constant	[s]
π	Mathematical constant	[-]
ρ	Material density	[kg/m^3]
ρ	Electrical resistivity	[Ωm]
ϕ	Modal amplitude	[-]

ψ	Transduction coefficient	[N/A]-[N/V]
ω	Frequency	[rad/s]

Impedances

Parameter	Description	Unit
Z_m	Base impedance	[Ns/m]
Z_s	Suspension impedance	[Ns/m]
Z_e	Electrical impedance	[V/A]
Ψ	Transduction coefficient	[N/A]-[N/V]
Z_h	Electrical impedance of the load	[Ω/Hz]
C	Coupling coefficient	[-]

Frequency response functions

Parameter	Description	Unit
T_{ew}	Transducer electrical impedance	[Vs/m]
T_{fe}	Blocked force per unit of current	[N/V]
T_{fi}	Blocked force per unit of current	[N/A]
T_{iw}	Transducer electrical impedance	[As/m]
Y_{ei}	Electrical admittance	[A/V]
Z_{ei}	Electrical impedance	[V/A]
Z_{me}	Transducer base impedance	[Ns/m]
Z_{mi}	Transducer base impedance	[Ns/m]

Subscripts

Parameter	Description
a	Air
b	Base
CM	Coil magnet
e	Electrical element/voltage
ec	Eddy currents
E	Constant electric field
f	Force
h	Harvested
i	Current
m	Mechanical element/move

n	Natural frequency
PZT	Piezoelectric
R	Real
T	Constant temperature
Δw	Stroke
$\dot{w}$	Velocity

1

INTRODUCTION

This thesis is focussed on vibration energy harvesting with macro scale electro-magnetic and piezoelectric transducers, that are, transducers built assembling components fabricated with traditional methods. More specifically, this study considers either electromagnetic harvesters composed by a magnet and wire wound coil connected via soft metal springs or piezoelectric harvesters formed by a cantilever beam substrate with, bounded on either side, flexible piezoelectric MFC patches and a tip block mass. The size of the harvesters is assumed in the range of few cubic centimetres, such that, they can generate from milliwatts to tens of watts. Therefore, this study does not consider microscale electromagnetic and piezoelectric transducers, which are normally fabricated with micro electro mechanical systems (MEMS) technologies and, thus, normally have total dimensions of few cubic millimetres and generate micro and milliwatts.

This introductory section presents an overview of the primary driver behind this technology, that are wireless electronic devices and discusses the characteristics and limitations of the principal energy storage technologies, which are normally used to power wireless electronic devices. It then revises the principal features of local energy sources and respective energy harvesting systems. At this point, vibration energy harvesting is introduced in detail. The physics and modelling of electro-magnetic, piezoelectric, electrostatic harvesters is first revised in detail. Also, the scaling properties of seismic and reactive harvesters is discussed. The section is then concluded with an overview of the scope, contributes and structure of the thesis.

1.1 WIRELESS ELECTRONIC DEVICES

The past few decades have seen a continuous development of implanted/wearable electronic devices and wireless sensors, which are becoming progressively more pervasive in several fields of application. According to Mitcheson *et al*.[1] these

systems can be divided in two principal groups, which are defined with respect to applications. The first group is the so called *body sensor network* [2], [3], [4] for automated health care systems and medical remote sensing using wearable and implanted electronic devices [5] (e.g. blood pressure monitoring, electrocardiograph real-time processing, control devices, cochlear implants, etc. [5], [6], [7]). The objective of Body Sensor is to provide an integrated interface platform to ensure and facilitate the development of diffused monitoring systems. As schematically shown in Figure 1.1, several promising prototypes are starting to emerge in practical applications. For example, the blood glucose level of patients with diabetes can be monitored continuously checking the insulin delivery from an implanted reservoir. Also, there are already commercially implantable, multiprogrammable brain stimulators for the treatment of epilepsy or other debilitating neurological disorders, which can help patients that had important surgical operations. In cardiology, the role of implantable cardioverter-defibrillators has increasingly been recognized for their ability to prevent sudden cardiac attacks. The second group is the so called *wireless sensor network (*WINS*)* [7], [8], [9], [10], [11], [12], that includes several self-contained nodes, often called *motes* [1], which are used for industrial and machinery condition monitoring [13], [14], ambient intelligence and personal tracking [9], [14], structural monitoring of buildings and transportation infrastructures [15], [16], [17], [18], domestic condition monitoring and surveillance [19], condition monitoring and sensing for transportation vehicles [19], [20], [21], environment [22], [23], agriculture and food industry monitoring [24], [25], oil and gas pipelines, health monitoring [26] etc.

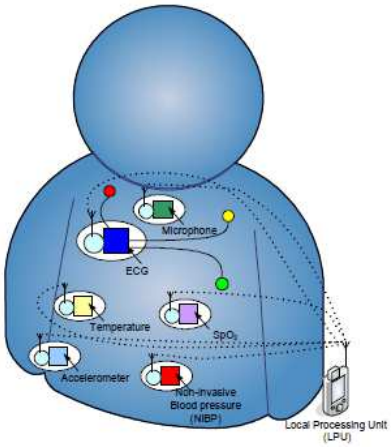

Figure 1.1: Basic design of the body sensor network [4].

As shown in Figure 1.2, WINS consist of a large number of small sensing nodes that: a) monitor the environment, b) process data (through the use of microprocessors) and c) send or receive processed information to or from other sensor motes. These individual sensing nodes are normally distributed in the space and propagate the measured signals to a centralised network, which collects data and provides to the end user. This system allows a base station to service a much larger network than would be possible with classical communication systems.

Portable and wireless electronic systems offer a number of advantages, such as for example: extended range of applications, flexibility, ease of installation (also in previously inaccessible locations), reduced material costs (e.g. wiring and connectors), reduced installation costs, reduced risks of failure in wiring and connectors, possibility of retrofitting existing machinery, replacement of the large transmission distances with multiple low power and low cost sensors, etc. [1], [23], [27].

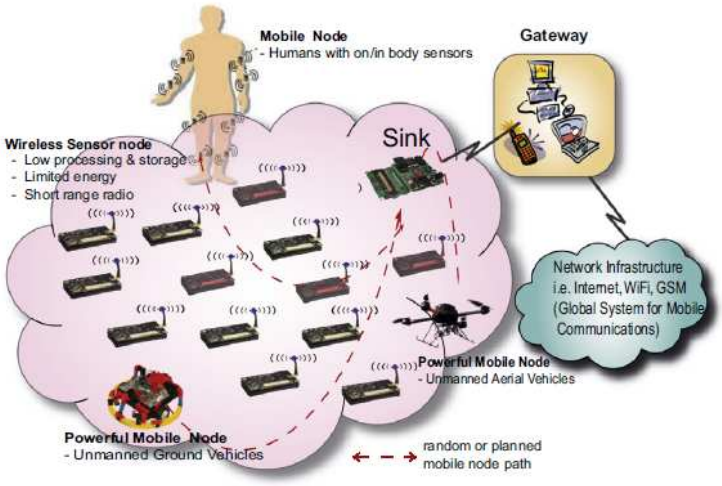

Figure 1.2: Example of a typical connection between body sensors and wireless sensor networks [28].

1.2 ENERGY STORAGE DEVICES

The recent advances in wireless sensors and communication devices, combined with their increased computing power, has brought to the development of fully automated

prognostic and monitoring systems for a large number of complex physical and biological systems. In this framework of constantly evolving technologies, sensing and communication devices are becoming progressively smarter and more powerful. As a result, they all need more energy to operate. Thus to ensure portable and wireless operation conditions, these systems require a local energy store [1], [11], [29], [30], [31]. The term energy store/ storage describes technology to convert energy from a form that is difficult to accumulate (i.e. electrical) to a storable form (mechanical, electrostatic, chemical, electrochemical, etc.). The stored energy can then be converted back into a directly usable form. There are various types of energy storage systems, which are characterised by different properties, such as energy or power capacity and time of charge/discharge. The choice of a particular storage technology depends on the application requirements. In the context of sensors and monitoring systems, energy storage units must satisfy a specific set of requirements related to their small size, cost, and low environmental impact.

In the majority of cases, because of their practicability and simplicity, electrochemical batteries offer the most practical and convenient solution [11], [32], [33]. Indeed, although hydrocarbon fuels can deliver one order of magnitude higher energy densities, compared to electrochemical batteries, they require rather complex energy converters such as miniature turbine engines, micro Stirling-engines, micro fuel cells. Also, the speed of intervention that is required and the different duration of the power supply make the electrochemical batteries more suitable for wireless systems.

It is important to recall that several other storage elements exist in practice, including, for example, flywheel energy storage (FES) [34] and superconducting magnetic energy storage (SMES) [35]. These systems are characterised by higher power densities and higher cycle lifetime, but have energy densities comparatively lower than those of electrochemical batteries. Also, the costs and the technological complexity make them less attractive. Another important device, typically used to storage energy is the capacitor or super-capacitor, constructed as an electrochemical double layer capacitor and characterised by high power density, high charge – discharge efficiency (up to 98 %) and wide operating temperatures compared to batteries. However, this technology is affected by a serious self – discharge which can reach 11% per day [36].

Finally, radioactive material miniature sources are characterised by long life but lower power densities than those of electrochemical batteries.

Hence, despite being characterised by a comparatively slower technological development, the combined functionality and low cost make the electrochemical batteries still the most common local energy storage devices for powering electronic systems and wireless sensors [37]. However, they often determine the size of the system and, in most cases, also its life and cost, since they require additional maintenance for replacement or recharging [1], [27], [32].

1.3 LOCAL ENERGY SOURCES

The constant evolution of solid-state electronics, circuit designs and Micro Electro-Mechanical Systems (MEMS) has brought to a significant miniaturisation and decrease in power consumption of implanted/wearable electronic devices and wireless sensors [1], [29], [38]. With the proliferation of these technologies, the power generation for small and micro devices is becoming an interesting and important research subject. Nowadays the batteries, which are the most common local energy sources, can be divided into two fundamental types: primary or secondary [32]. Primary batteries are non-rechargeable batteries and are characterised by high capacity and temperature stability; their main disadvantage is the need of periodic maintenance and replacement at the end of life. Secondary batteries, which can be divided in alkaline and acidic, are rechargeable but their number of charge/recharge cycles is still limited by cycling capacity. In general the lifetime of most electrochemical batteries is on the order of hundreds to thousands of charging/discharging cycles and their storage efficiency is comprised in a range from 60% to 80%, depending on the operational cycle and on the electrochemistry type [39], [40]. Compared to the electronics technology, battery technology have had a comparatively lower technological progress during the past few decades. In particular, they are unable to cope with the shrinking geometrical constraints and power density requirements necessary to run modern wireless systems. During the past few years new materials and designs have been proposed, which, however, are characterised by problems related to costs, reliability and safety. Therefore the replacement of batteries with other energy systems such as indeed energy harvesting devices has been the focus of a vast research activity carried out by many research groups in the world. The environment offers many sources of energy, indeed there is now a growing interest for energy harvesting from local inexhaustible energy sources,

such as for example: T thermal gradients, S light, W wind, RF electromagnetic radiation, M kinetic (e.g. solid/fluid motion) [1], [40], [41], naturally present in the environment or results from human activities. These sources can be used to run low power consumption electronic devices via an interface electronic circuit [42], [43], [44] which, in some cases, may incorporate micro-battery or super capacitor energy storage elements [1], [11], [29], [45], [46], [47]. As discussed in [1], [11], [29], [30], [48], [49], [50], each of these energy sources are characterised by specific features that bring in advantages and disadvantages for energy harvesting.

1.4 ENERGY HARVESTING

In general, "energy harvesting" refers to the nonchemical generation of a small amount of electrical energy on local scale using one of the energy conversion principles introduced above.

For example, the use of solar energy with solar cells, also under low light levels, is widely used in many consumer products to power calculators, watches and in general, any application where solar illumination is available and the power requirements can be withstood. In general, a photovoltaic harvester is able to produce a level of power from μW to MW depending on its surface area. A typical value of power density considered for the energy harvesting purposes is 15 $\mathrm{mW}/{c_m}^2$ [22]. Nevertheless, it is important to underline that in many applications the use of solar energy cannot be withstood, as for example in enclosed spaces where natural light is not available.

Compared to the solar radiation energy, the exploitation of the thermal energy is of particular interest because, in general, is always available and present in every natural and handmade environments and has a high power density. Thermal energy can be harvested from spatial gradients (thermoelectric effect), time domain variations (pyroelectric effect) or by means of ferroelectric phase transitions [51]. These methods of conversion are well suited in common applications such as automotive, human activities and data processing. For example, thermoelectric energy can be harvested from asphalt pavement roadways. The prototype described in Ref. [39] accumulates heat energy from the pavement surface and transfers it to the thermoelectric generators placed at the edge of the pavement. For example, a 64×64 mm prototype device was developed, which generates about 10 mW of

electrical power over a period of 8 h. Nevertheless, practical problems, such as the low efficiency (only about 5 – 6 %) and relatively high material costs poses practical limitation in the use of this form of energy.

Ambient radio waves are commonly present in a very large range of frequencies (3 kHz – 300 GHz) and power levels [51], especially in the areas where the density population is very high. Communication devices such as wireless radio networks, mobile base stations, mobile telephones and TV signals generally propagate RF electromagnetic fields in the environment. The ability to capture RF energy enables wireless charging of low power devices such as GPS autonomous sensors nodes and consumer electronics in comparison with solar and thermal energy harvesting [28]. The main advantage of RF-based energy harvesting is its availability in indoor locations [52]. However, the energy transmitted from the RF sources is very low unless the receiver is large and adjacent to the source. In addition, the nature of the source makes the use of the harvesters impractical inside conductive enclosures [53]. The analysis presented above brings to the conclusions that in many applications, energy harvesting based on the conversion of kinetic and potential mechanical energy to electrical becomes the only and most convenient option. For example the kinetic energy air flow can be extracted from air wind and converted into electricity by rotors or small wind turbines [22], [54]. Mendonca [55] reports the performances of a 6.9 cm radius turbine equipped with 6 blades and able to produce 439 mW of power with an efficiency of 14.3% at 7 m/s wind speeds. Other prototypes are described in Ref. [56] that use a wind flutter generator based on the aeroelastic flutter effect. Baranov [57] has used a hybrid power supply combining wind and solar radiation to power wireless nodes used to monitor carbon monoxide levels in civil areas and outdoor industrial structures. Hobeck and Inman [58] developed a new design of piezoelectric grass employed for fluid flow environment. Wireless power transmission based on acoustic energy has also recently been investigated, in particular for applications related to power implantable sensors and devices used for therapeutic functions. Furthermore, the possibility that acoustic waves have to penetrate into the liquids has enabled the powering of under-water sensors and communication networks [59]. An ultrasonic transcutaneous energy transfer system (UTET) designed to convert electrical energy from pressure waves, operating at frequency about 670 Hz and able to achieve 70 mW with an efficiency of 27 % has been reported in [60]. Other experiments have shown that implantable oscillators can achieved a vibration amplitude of 71 μm at a distance of 5 mm . Nevertheless the problems related to the human safety due to the interaction of the pressure waves with the human body and

the low efficiency related with the small power density of the acoustic waves makes this technology to be still immature for practical applications.

In general, kinetic energy related to body movements is a clean, stable, ubiquitous and abundant energy source [1], [37]. Indeed, significant levels of motion, normally occurring as vibrations, regular and impulsive displacements and driving forces/moments [29], [37], characterise most biological organisms (e.g. plants, animals, human beings), domestic and industrial appliances (e.g. washing machines, fridges, etc.), industrial plant equipment and machinery, transportation vehicles (e.g. cars, aircraft, etc.), transport infrastructures (e.g. bridges, railway, etc.), buildings [1], [11], [29], [48], [61].

Among the various forms of kinetic energy, vibration energy has received particular attention for its ubiquity and because it requires small size and lightweight transducers for conversion into electrical energy [19], [49]. In general, kinetic energy harvesters relies on simple electro-mechanical reactive or seismic (inertial) systems, which are excited either by imposed forces or imposed displacements which are exerted by the hosting body or structure [1].

1.5 VIBRATION ENERGY HARVESTING

In general, vibration energy is typically present in the form of displacements or forces and is commonly converted into electrical energy by using electro-mechanical transducers. The quantity of electrical energy that can be harvested from vibrations depends on several factors: first, type of excitation and its amplitude (deterministic, stochastic, pure tone, periodic, impulsive, white and coloured noise, etc.); second, the amount of kinetic energy available in the environment; third the transduction mechanisms used to convert the energy of the vibrations.

In general, vibration energy harvesting is based either on seismic or reactive harvesters, which can be respectively attached or embedded on the vibrating source [46]. Three types of transducers are normally employed [1], [11], [29], [27], [33], [37], [62], [63], [64], [65], [66] first electromagnetic, second piezoelectric and third electrostatic. Magnetostrictive transducers could also be employed in some cases, but comparatively fewer practical applications have been investigated up to present [1], [67].

In general, these transduction mechanisms generate electricity through mechanical strain of the transducer element or relative displacement/velocity of the transducer components produced by the vibrating source. Strain transduction exploits the deformation of a material which is typically a piezoelectric material [64]. Relative velocity transduction is instead implemented with coil-magnet linear transducers. Finally, the displacement transduction is associated to electrostatic transducers. Each transduction mechanism is characterised by specific physical phenomena that can vary with the complexity and architecture of the transducers [41]. Electromagnetic harvesting systems are based on the electromagnetic induction principle, i.e. a varying magnetic field induces a voltage across the wire of the coil. The most common coupling architecture is a cylindrical magnet, which oscillates inside a coil [68]. Piezoelectric harvesting systems are instead built with piezoelectric patches that produce a charge separation and thus a current flow, when strained. The most common architecture of piezoelectric harvesters is the cantilever beam substrate with piezoelectric layers bounded on either side. There are several types of piezoelectric transducers. Piezoceramic materials are characterised by high electro-mechanical coupling and efficiency conversion but low fracture toughness (see for example the Zirconate Titanate PZT). For this reason recently NASA has developed a new material, the Macro Fiber Composite (MFC) composed by piezo ceramic rods sandwiched between layers of adhesive, electrodes, and polyimide film [69], widely used in the piezoelectric energy harvesting field. Alternatively, there is a second class of piezoelectric materials made with PVDF, which guarantee high flexibility but comparatively lower electromechanical coupling and energy conversion efficiency. Electrostatic harvesters are formed by dielectric material that generates voltage based on the variation of its capacitance. More specifically, a current flow is produced when the charged electrodes are set into axial or shear relative motion by the external vibrations. The resulting change of electric charge causes the variation of the electrostatic field and thus an electric motion. A literature review of these transducers can be found in [70]. Finally, magnetostrictive harvesters are based on the Villari effect. Under the effect of strain, a magnetostrictive material induces a magnetic field, which can be set to interact with a coil wiring to produce electrical current [71]. No well-defined architectures can still be found in literature for such magnetostrictive devices. Comparing the electromagnetic and piezoelectric transducers, the second covers a larger range of volume power densities ($W/{c_m}^3$) [33]. In addition, the voltage output in the electromagnetic energy harvesters is very low and thus an increment of the voltage level is usually required to charge a storage component [72].

On the other hand, electromagnetic harvesters cover a larger range of surface power densities ($W/c_m{}^2$) and are characterised by lower mechanical quality factor, thus are more suitable for high amplitude vibrations.

During the past two decades a large number of vibration energy harvesting prototypes have been designed, built and tested, which are characterised by a wide range of dimensions, geometries, materials and construction techniques, [1], [27], [29], [33], [37], [38], [67], [71], [73], [74], [75], [76], [77], [78], [79], [80] (in particular see Tables A1, A2 in Ref. [50] and Table 2, 3 in Ref.[81]). Moreover, quite a few commercial products have been put in the market [82]. A comprehensive state of the art on vibration energy harvesting can be found in Ref. [71] and [83].

1.6 VIBRATION ENERGY HARVESTING: MODELS AND THEORIES

The research work on vibration energy harvesting systems covers several disciplines of engineering and various mathematical models have been proposed in literature to study such devices [72]. Initially, researchers tried to characterise the harvesting systems with lumped models formed by a single mechanical degree of freedom coupled to an electrical mesh. The fundamental principles of vibration energy harvesting were first set in Refs. [48], [84], [85], [86] starting from simple second order models formed by mass-spring-damper lumped elements connected in parallel, where the damper element accounts for both the system parasitic energy loss effects and the energy harvesting effect. Williams and Yates [84], first derived an expression for the "generated power" assuming time-harmonic vibrations and calculated the maximum power that can be harvested at the fundamental resonance frequency of a seismic harvester. Stephen [86] further examined this simple model and highlighted a number of shortfalls in the interpretation of the power expressions that often lead to wrong conclusions. In particular, he highlighted that the parasitic damping effect in the seismic harvester plays a role in both the vibration power input to the harvester and the electric power output from the harvester. Moreover, he noted that in principle the equation for maximum power harvested seems to indicate that, to reach a maximum, the harvester should be undamped. However this condition will lead to a overgrowing unstable response. Thus a certain amount of damping is needed in the harvester to have a stable response and finite amount of energy harvested. Also, he underlined that indeed the maximum power transfer to the load requires matching

between the harvester electromechanical load and the electrical load. Finally, he also noticed that the power extraction strongly depends on the maximum allowed stroke of the transducer. For example, Mehdi' Hendijanizade [87] has shown that, for limited range of motion of the moving mass, the optimal energy harvesting load differs from that of unconstrained seismic devices.

As pointed by some authors (for example see Ref. [72]), for the piezoelectric vibration energy devices, the simplified lumped parameter model neglects some key aspects of the coupled physical system, such as the higher order mechanical and electrical effects. In particular, the contribution of the distributed stiffness and inertia effects is usually not taken into account [72]. Many of these aspects and oversimplifications are discussed and summarized in [88]. A modal model, called as Rayleigh Ritz type model [89], was proposed in [90], [91]. This model was derived starting from Hamilton's Principle and modal expansion formulation for the beam vibration to obtain a discrete formulation in terms of modal amplitudes. Analytical solutions for the electromechanical piezoelectric model based on the modal expansion were given by [92], [93], along with experimental validation. Modal solutions are discussed also in [72], [94], [95], [96].

To increase the power output and amplify the working bandwidth, researchers have explored different devices and configurations and have proposed a variety of theoretical models and solutions. Considering that the linear resonant harvesters are not good to harvest energy from broadband or frequency varying excitations, some authors focused their efforts on the non-linearities in vibration based energy harvesting and the common second order linear equations employed to descript the dynamic characteristics were modified to take into account nonlinear dynamic responses [97], [98], [99], [100], [101], [102], [103], [104], [105], [106]. Under the hypothesis of harmonic excitation, Boisseau *et al.* [99] showed the possibility to increase the frequency bandwidth in which the energy can be harvested by means of nonlinear springs. The study indicates that the output power can be increased up to 48 % respect to the linear device. Maryam and Elliot [107] tried to extend the operational range of frequency excitation of an electromagnetic device introducing a cubic non-linear term for the viscous damper. Mann [108], [109] investigated a non-linear inertial energy harvester composed by a series of magnets which interacting make the system by-stable, reducing the constitutive equations in form of a Duffing oscillator (see also Ref. [110]). Ibrahim *et al.* [111] studied the nonlinear response of a cantilever beam with piezoelectric patches in which is exposed to a magnetic force generated by two magnets placed on either side of the tip of the beam with opposite

poles. A generic approach to introduce a mathematical model for mechanical non-linearities in systems of one or more degrees of freedom is discussed in detail in Ref.[100]. Also, non-linear Hysteresis phenomena for the piezoelectric devices is also taken into account in Ref. [112]. In addition to tonal excitations, these non-linear models have been further improved to consider as stochastic the ambient excitation [113], [114], [115], [116], [117], [118], [119], [120], [121], [122] (in particular see Chapter 2 of [123] and Langley's paper on mass law for nonlinear energy harvesters [114]). In this respect several studies were focused on widening the frequency bandwidth of the harvesters. Several configurations were proposed, such as for example mechanical stoppers, multimodal arrays, linear and non linear mechanical-electrical elements or bi-stable structures are shown in [124], [125], [126]. A self tuning piezoelectric energy harvester was also proposed in [127]. Tuning using switching methods were proposed in [128].

Normally, the response of energy harvesters is investigated considering simplified second order mechanical models that encompass the electric circuit as a resistive impedance load. From the electrical point of view, the alternating voltage output generated from the inertial harvesters requires to be rectified by using a rectified bridge (AC-DC converter) and then a regulator (DC-DC converter) connected to a storage component. These electrical power aspects require detailed model as shown in Refs. [43], [44], [97], [129], [130]. These articles provide detailed models and studies on the practical implementation of the interface electronic devices and regulator circuits. The non-linear electric effects derived from the introduction of AC-DC converter and DC–DC pulsewidth modulation and other optimization techniques were also considered in Refs. [131], [132], [133], [134], [135], [136], [137], [138].

1.7 VIBRATION ENERGY HARVESTING: SCALING SIZE

Since the first studies on energy harvesting were presented in the late 1990s, researchers have considered a wide range of technologies, architectures, strategies, dimensions, materials and operation modes. It is therefore difficult to identify a unique figure of merit for such devices. In general the harvested power varies with the characteristic surface and/or volume ([28], [139]). Therefore despite the vast assortment of systems that have been investigated, vibration energy harvesters can be classified in two broad categories: micro-scale harvesters (normally with size

$< 1\,\mathrm{cm}^2$) fabricated with micro-electro-mechanical System (MEMS) technology starting from batch silicon wafers and macro-scale harvesters (normally with size $> 1\,\mathrm{cm}^2$) assembled from discrete electro-mechanical components (springs, beams, block masses, magnets, coils, piezoelectric patches, etc.) [140]. In general, electromagnetic transducers are best suited for macro-scale seismic vibration energy harvesters [141], [142], which normally are composed by a coil-magnet cylindrical assembly (either with coil or magnet moving element) connected to each other either via helical springs or flexible cantilever beams (for example see Refs.[112], [143]). In fact as pointed in [67], [144], there is a practical dimension limit of the cross section and coil turns of the wire that can be used in the harvesting devices. An example of large size electromagnetic harvester used for civil scale structure and capable to produce 100 W with a 1kN of force at below 1Hz of frequency is proposed in [141]. Shen *et al.* [145] studied a macroscale pendulum-type electromagnetic harvester from low frequency structural vibration under earthquakes. Also, Simeone *et al.* [146] shown and demonstrated the effectiveness of an energy harvesting pendulum type with a level-dependent load. Another macroscale linear electromagnetic harvester installed in the structural cables of a bridge to scavenge the wind-induced vibration mechanical energy and able to produce a peak power of 233.49 mW is investigated in [147]. Nevertheless, a few micro-scale oscillatory electromagnetic harvester prototypes were also designed and fabricated using plane coils and tiny block magnets mounted on flexible links [74], [148], [149]. A silicon micromachined realization of such architecture with discrete magnet was published in 2007 by Serre [150]. The prototype proposed therein was able to reach a maximum power output of 55 μW for an excitation with 5.1 μm amplitude at about 300 Hz (18 m/s²). In addition to classical architectures, many other micro-prototypes have also been investigated [76]. Two promising types of microscale magnetic generators have emerged from the literature: rotational and hybrid devices. Rotational generators operate under constant driving torque while hybrid devices convert linear to rotational motion by means of eccentric rotors. Powers from μW to ten's of mW can be achived for inertial electromechanical harvesters of size 0.01 - 0.1 ${c_m}^3$ under tonal source acceleration of amplitude 10 $\mathrm{m/s}^2$ and for a range of frequency comprised between 1-100 Hz [149]. A comprehensive summary of many micro prototypes from literature is well summarized in Tables I, II, II in [74].

Moving to the piezoelectric transducers, these types of devices are better suited for macro-scale seismic vibration energy harvesting [65], [80], [151], [152], [153], [154] which are normally composed by a small cantilever beam with a tip block mass and

piezoelectric patch thin transducers on either faces [152]. For example Xie *et al*. [155] has identified a set-up and derived a mathematical model for a piezoelectric harvester which collects electrical energy from the wave motion of the sea. Such prototype is composed by a host cantilever beam of 3 m length equipped with ten MFC piezo-patches. It is able to collect up to 55 W for a sea wave of 3 m depth, 2 m height and 15 m length respectively. Hobeck and Inman [154] proposed the use of a set of 112 flexible piezoelectric arrays of 30 cm length in a wind tunnel to harvest the induced vibration energy flow of the air fluid. Gardonio and Zilletti [156] analysed the generation of power from an array of flexible stalks (300 x 25 x 0.25 mm) exposed to airflow. A smaller scale (5 c_m^3) piezoelectric harvester with cantilever beam configurations have been also investigated [157]. Indeed, piezoelectric microgenerators have been studied in Refs. [94], [158], [159], [160], [161], [162], [163]. These micro-electromechanical systems are relatively simple to fabricate [81], [164]. In the last ten years the development of miniature piezoelectric devices fabricated with the MEMS technique has been greatly improved, particularly with respect of new materials and new structure design and optimization. The harvesting performances, expressed in terms of mW/c_m^3 of MEMS prototypes proposed in the literature between the years 2009 - 2017 are summarised in Table 2 of [81]. Power levels from 1 μW [165] to ten's of mW are usually reached by such MEMS devices.

Electrostatic transducers are instead ideal only for micro-scale MEMS seismic vibration energy harvesters [149], [166], [167], [168], [169]. Normally these devices are composed by outer frame and inner block structures connected via folded springs and equipped with large arrays of comb fingers forming electrostatic transducers that work either in transverse or shear modes [27]. Examples of electrostatic micro-machined power generators are shown in [168] or [169], which can harvest 24 μW at 10 Hz and 1 μW with about 0.03 g^2/Hz of PSD vibration acceleration.

1.8 SCOPE AND OBJECTIVE OF THE THESIS

The scope of this thesis is to provide a comprehensive comparative study of vibration energy harvesting using electromagnetic and piezoelectric transducers. The study is focussed on macroscale transducers built assembling multiple components, which are fabricated from traditional materials using classical industrial processes (milling, bonding, soldering, printing, etc.). Recently, Mitcheson *at al*. [1] have presented a

comprehensive review on "*Energy Harvesting From Human and Machine Motion for Wireless Electronic Devices*".

In particular they provided a detailed overview of all technologies and studies carried out on kinetic energy harvesting and annotated towards the end of the article the following interesting, and to some extent surprising, observations on modelling and testing of prototype vibration energy harvesters:

- "***There has been significantly more work presented on electromagnetic generators than on the other two types***".

- "*The typical size of electromagnetic generators has been shrinking over the last decade*".

- "***Around half of the reported work contains information regarding models of microgenerators, the other half giving measured results of prototypes. There are six cases where results of a model and a prototype are presented; of these, the piezoelectric generator by Roundy et al. achieves the closest match between the model and measurements***".

- "*The designed operating frequency of most devices, independent of transducer type, is 50–200 Hz. Only three groups-Tashiro et al., Kulah et al., and our own-have attempted to design inertial micro- generators to operate at frequencies below 5 Hz*".

- "*There is a large variation in the amplitudes of the motion used to drive the generators, ranging from less than 1 nm to several millimeters. Generally, generators designed to work at higher frequencies are driven by lower displacement amplitude sources*".

In response to these observations, particularly the parts highlighted in bold, the objective of this thesis is thus to develop and validate experimentally a consistent modelling framework and unified energy formulation that take into account all physical features of electromagnetic and piezoelectric transducers and can be effectively used to contrast the vibration energy harvesting efficiency, particularly with respect to the scale of the transducers.

1.9 CONTRIBUTIONS OF THE THESIS

The main contributions of this thesis are:

- Realization and testing of two prototype vibration energy harvesters having similar weights, volumes and fundamental natural frequencies.
- Development of consistent lumped parameter models for electromagnetic and piezoelectric seismic and reactive vibration energy harvesters, which include the effects of eddy current damping and induction losses in the electromagnetic transducer and the effect of dielectric losses in the piezoelectric transducer.
- Development of a unified formulation for the transducer constitutive equations and input/harvested power and efficiency parameters.
- Accurate identification and validation of the mathematical models with measured mechanical impedance, electrical impedance and electrical to mechanical and mechanical to electrical transduction functions.
- Consistent energy analysis for the input/harvested power and efficiency with electromagnetic and piezoelectric seismic and reactive harvesters.
- Derivation of the scaling laws for electromagnetic and piezoelectric energy harvesters.
- Identification of general guidelines regarding the potential applications of both technologies based on the power/efficiency performances and transducer dimensions.

1.10 STRUCTURE OF THE THESIS

The thesis is organised in five chapters as detailed below.

CHAPTER TWO and THREE present the models, analytical formulations and simulations results respectively for the seismic and reactive electromagnetic and piezoelectric harvesters. The two chapters initially describe the electromagnetic and piezoelectric harvester prototypes considered in the study, summarizing their geometrical and physical properties. Consistent electromechanical lumped parameter models, which include eddy currents and dielectric losses are then derived and used to study and analyse the two vibration energy harvesters. A unified impedance formulation based on the constitutive electromechanical equations and energy analysis for the input harvested power and efficiency is then presented and validated experimentally. The

electric load conditions to maximise the vibration energy absorption from tonal vibrations of the base structure are also derived. Finally, the last section of chapter two also presents a comparative study based on the power harvested per unit stroke. The most important results are then summarised and commented.

CHAPTER FOUR introduces the scaling study of the electromagnetic and piezoelectric seismic and reactive energy harvesters. The principal scaling laws of the mechanical and electrical components for both harvesters are first revisited. The scaling laws are obtained with reference to a single variable L, which identifies the typical linear dimension of the entire device. Starting from the lumped parameter model and impedance analysis introduced in Chapter 2, a power input – output and efficiency formulation in terms of non-dimensional coupling coefficients is obtained and specified under the hypothesis of tonal base vibrations tuned to the fundamental natural frequency of the two seismic harvesters. The effects of scaling on the efficiency and harvested power normalized to the volume of the devices are then investigated. A comparative section, which includes the scaling stroke analysis and summarises the scaling power-efficiency results is then presented.

CHAPTER FIVE presents a summary of the presented studies and suggests ideas for future work.

2

SEISMIC VIBRATION HARVESTERS

This chapter compares with simulations and experiments the principal characteristics of time-harmonic vibration energy harvesting with electromagnetic and piezoelectric seismic transducers. The two seismic transducers are designed and built in such a way as they have a) similar weights and similar volumes of the base components b) similar weights and similar volumes of the moving components c) the same fundamental natural frequency, that is about 20 Hz. The electromagnetic prototype is a commercially available linear electromagnetic harvester composed by discrete components (NCM02-17-035-2F). Instead, the piezoelectric device was assembled in laboratory using off the shelve components (block masses, beam, MFC piezoelectric patches). The study is focused on equivalent lumped parameter models and a consistent formulation of the constitutive electromechanical equations for the two transducers so that a unified energy formulation is obtained for the two harvesters. Both transducers are connected to either a resistive-reactive or a purely resistive harvesting impedance load. The content of this chapter is based on Ref. [93].

2.1 SEISMIC TRANSDUCERS

Figure 2.1 shows: a) the pictures, b) the schematics and c) the lumped parameter models of (I) the coil-magnet and (II) the piezoelectric patch seismic transducers for vibration energy harvesting considered in this thesis. As shown in picture (a) and (b) the first prototype is formed by a magnetic cylindrical element, which is characterised by an inner cylindrical cut where it is housed a coil rigidly connected to the case of the transducer. The magnetic element is also connected to the case via soft axial springs, which allow relative motion between the coil and the magnet. The magnetic element is connected to the vibrating source [170]. The relative motion between the magnet and coil produces a back electromotive force, i.e. a voltage, at the terminals of the coil; *vice versa*, a current flow in the coil generates reactive forces on the

magnetic and on the coil-armature elements [104], [171], [172], [173]. As shown in figure (d) and picture (e) the second prototype harvester, is composed by a thin beam with one end fixed to the case and the other end connected to a tip block mass. The beam is equipped on the top and bottom side with two rectangular piezoelectric patches connected in parallel. The two piezoelectric layers are polarised in the same transverse upward direction and are electrically coupled in counter–phase parallel architecture. In this case the bending strain of the cantilever beam produces an electric displacement in the electrodes of the piezoelectric patches, and thus a current flow through the terminals when the patches are connected to the harvesting electrical circuit. Alternatively, the voltage generated at the terminals of the transducer produces a back bending strain effect on the cantilever beam.

As summarised in Table 2-1 and Table 2-2 the two prototypes shown in pictures (a) and (d) of Figure 2.1 were designed in such a way as they have similar volume and similar mass of the base elements and similar volume and similar mass of the seismic elements. Also, the axial stiffness of the spiral springs in the electromagnetic harvester and the bending stiffness of the composite beam in the piezoelectric harvester are such that the two harvesters are characterised by similar fundamental natural frequencies, i.e. 20 Hz. As can be noticed in Figure 2.1 (a, d) and summarized in Table 2-1 and Table 2-2, the slender beam piezoelectric seismic transducer occupies about five times the footprint area of the electromagnetic seismic transducer which has a compact cylindrical shape. Finally, the volume of the core magnet in the electromagnetic seismic transducer is about ten times than that of the two piezoelectric patches bonded on the beam substrate of the piezoelectric seismic transducer.

The other list of data reported in Table 2-1 and Table 2-2 were obtained from examination of the components of the two harvesters (geometry, weights), from mechanical and electrical static measurements (mechanical stiffness and electrical resistive, inductive/ capacitive properties) and from the information given in datasheets of the electromagnetic (H2W NCM02-17-035-2F) and piezoelectric patch (MFC Type M8514-P1) transduction elements. In addition, missing data were identified from the measured mechanical and electrical impedances FRFs and two electromechanical transduction functions FRFs, which, have been obtained both as modulus-phase and real-imaginary FRF graph as will be shown in Sec. 2.5.

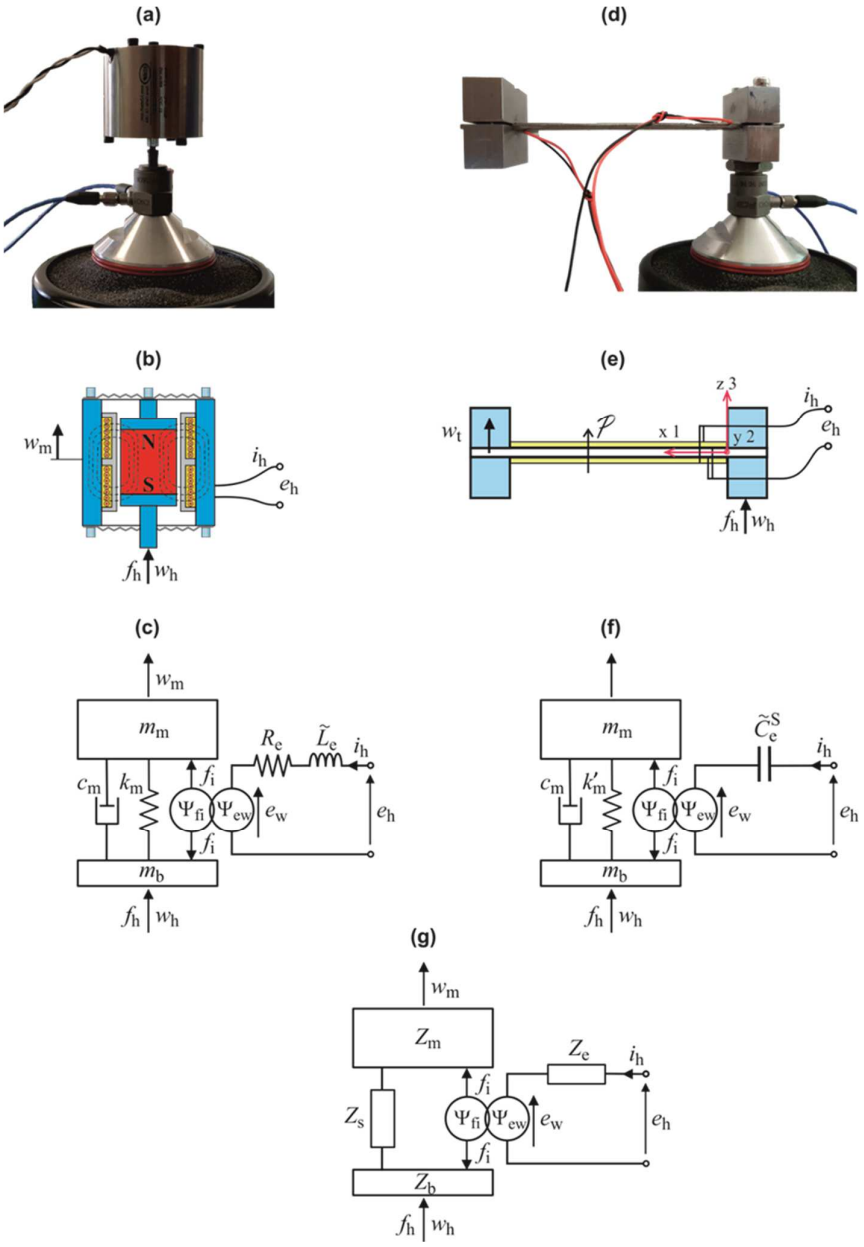

Figure 2.1: Pictures (a,d), functional drawings (b,e) and lumped parameter schematics (c,f), for the electromagnetic (left hand side) and piezoelectric (right hand side) seismic transducers. Common equivalent lumped parameter schematic for the two seismic transducers (g).

Table 2-1: Parameters of the coil magnet harvester.

Parameters	Value
Base mass and volume (inner magnet)	$m_b = 115 \times 10^{-3}$ kg $V_b = 1.206 \times 10^{-5}\ m^3$
Proof mass and volume (outer ring and coil)	$m_m = 185 \times 10^{-3}$ kg $V_m = 3.240 \times 10^{-5}\ m^3$
Transducer total mass and total volume	$m_{cm} = 300 \times 10^{-3}$ kg $V_{cm} = 4.446 \times 10^{-5}\ m^3$
Transducer footprint area	$A_{cm} = 1.5 \cdot 10^{-3}\ m^2$
Magnet radius and length	$R_m = 0.0153\ m$ $h_m = 0.0165\ m$
Outer ring volume	$V_y = 2.926 \times 10^{-5}\ m^3$
Outer ring electrical conductivity	$\sigma_y = 1.2 \times 10^7\ S/m$
Magnet magnetization per unit length	$M_0 = 10^6\ A/m$
Spiral springs equivalent stiffness	$k_m = 2777$ N/m
Fundamental natural frequency	$f_n = 19.5$ Hz
Viscous damping coefficient/ratio	$c_a = 2.15$ Ns/m $\xi_a = 0.05$
Eddy current damping coefficient/ratio	$c_{ec} = 7.37$ Ns/m $\xi_{ec} = 0.16$
Equivalent damping coefficient/ratio	$c_m = 9.52$ Ns/m $\xi_m = 0.21$
Electromagnetic transduction factor	$\psi_{CM} = 22.5$ N/A
Coil resistance	$R_e = 22\ \Omega$
Coil lossy inductance constant and exponent	$K_e = 0.034$ $n = 0.78$
Coil lossy inductance loss factor	$\eta_L = 0.36$

Table 2-2: Parameters of the piezoelectric harvester.

	Parameters	Value
Steel substrate	Width and thickness	$b = 20\ \text{mm}\quad h_s = 2\ \text{mm}$
	Length	$L = 140\ \text{mm}$
	Density	$\rho_s = 7800\ \text{kg/m}^3$
	Young's modulus	$Y_s = 20 \times 10^{10}\ \text{N/m}^2$
	Mass and volume	$m_s = 44 \times 10^{-3}\ \text{kg} \quad V_s = 0.56 \times 10^{-5}\ m^3$
Piezoelectric layers	Width and thickness	$b = 20\ \text{mm}\quad h_{pe} = 0.15\ \text{mm}$
	length	$L_p = 100\ \text{mm}$
	Density	$\rho_{pe} = 5440\ \text{kg/m}^3$
	Young's modulus	$Y_{pe}^E = 3 \times 10^{10}\ \text{N/m}^2$
	Strain/charge constant	$d_{31} = -170 \times 10^{-12}\ \text{m/V}$
	Permittivity under constant stress	$\bar{\varepsilon}_{33}^T = 6.3 \times 10^{-9}\ \text{F/m}$
	Electrical conductivity	$\sigma_{pe} = 4.5 \times 10^{-8}\ S/m$
	Electromechanical coupling factor	$k_{31}^2 = 0.14$
	Mass and volume	$m_{2l} = 3.9 \times 10^{-3}\ \text{kg} \quad V_{2l} = 0.06 \cdot 10^{-5}\ m^3$
Lumped elements	Base (block) mass and volume	$m_b = 126 \times 10^{-3}\ \text{kg} \quad V_b = 1.76 \times 10^{-5}\ m^3$
	Proof (block) mass and volume	$m_m = 189 \times 10^{-3}\ \text{kg} \quad V_m = 2.64 \times 10^{-5}\ m^3$
	Transducer total mass and total volume	$m_{PZT} = 363 \times 10^{-3}\ \text{kg}$ $V_{PZT} = 5.03 \times 10^{-5}\ m^3$
	Transducer footprint area	$A_{pzt} = 3.4 \cdot 10^{-3}\ m^2$
	Equivalent proof mass	$m_m = 215 \times 10^{-3}\ \text{kg}$
	Equivalent stiffness with the piezo-electrodes in short circuit	$k_m = 3369\ \text{N/m}$
	Additional equivalent stiffness with piezo-electrodes in open circuit	$\Delta k = 47\ \text{N/m}$
	Fundamental natural frequency (short circuit)	$f_n = 20\ \text{Hz}$
	Equivalent viscoelastic damping coefficient and ratio	$c_m = 0.7\ \text{Ns/m} \qquad \xi_m = 0.013$
	Equivalent piezoelectric transduction factor	$\psi_{PZT} = -0.0026\ \text{N/V}$
	Capacitance of the two piezoelectric layers	$C_e^T = 1.68 \times 10^{-7}\ \text{F}$

2.2 LUMPED PARAMETER MODEL

The dynamic response of the two inertial transducers is briefly revised here considering the two equivalent lumped parameter models shown in the schematics (c) and (f) of Figure 2.1, which, for simplicity, are detailed respectively in Appendix A and Appendix B. These models are characterised by equivalent mechanical and equivalent electrical parts. These two parts are joined via a *current-controlled force generator* and a *relative velocity-controlled voltage generator* that identify the electromechanical transduction effects.

Considering first the electromagnetic transducer, as shown in Figure 2.1 (c), the mechanical part is composed by a base mass (inner magnet) and a proof mass (outer ferromagnetic ring and coil assembly), which are connected to each other via a spring (spiral springs) and a damper (air and eddy currents damping), with in parallel an idealised *current-controlled reactive force generator*, whose strength is linked to the current flowing in the coil via a complex FRF. The damper accounts for the air damping that develops in the tiny gap between the coil and magnet and for the damping effect produced by eddy currents that develop in the ferromagnetic ring component of the transducer [174], [175], [176]. The sky-hook air damping produced on the outer surface of the moving ferromagnetic ring was found comparatively smaller than the air damping effect produced in the gap between the coil and the magnet and thus was assumed negligible in the model. Also, as synthesized in Table 2-1, the electromagnetic seismic transducer at hand is characterised by a rather large eddy currents damping effect, which is about 3.4 times larger than the air damping. The electrical part is composed by an idealised *relative velocity-controlled voltage generator*, that produces a voltage per unit relative velocity between the coil and the magnet proportionally to a voltage-velocity transduction transfer function. This voltage source is connected in series to a resistor and a lossy inductor (inductive effect influenced by eddy currents that develops in the wiring of the coil ([177], [178], [179]).

Similarly, for the piezoelectric transducer, as shown in Figure 2.1 (f), the mechanical part consists of a base mass (base block) and a moving mass (beam and tip block equivalent mass) connected to each other via a spring (beam modal bending stiffness) and a damper (beam Kelvin-Voight viscoelastic equivalent damping [72]) with in parallel a *current-controlled reactive force generator*, whose magnitude depends on the current input to the transducer via a transduction FRF. As discussed in Ref. [72], the air loading on the beam laminate produces a distributed sky-hook viscous damping effect, which, however, was found comparatively smaller than the

viscoelastic bending damping and, thus, was neglected in the model. The electrical part is composed by a *relative velocity-controlled voltage generator*, whose strength is proportional to the relative velocity between the moving and base blocks via a transduction FRF. This voltage generator is connected in series to a lossy capacitor component (piezoelectric layers characterised by dielectric losses [180], [181], [182], [183]).

The mechanical and electrical parameters in the lumped element model for the coil–magnet inertial transducer are derived straightforwardly from inspection of the system shown in in Figure 2.1. Instead, the mechanical and electrical parameters in the lumped element model for the piezoelectric transducer require a more complex analysis of the electro-mechanical flexural response of the cantilever beam with the piezoelectric patches and the tip mass shown in Figure 2.1 (d). In brief, the flexural response of the beam was derived considering only the first flexural mode that characterise the flexural response of the beam-piezoelectric patches laminate and tip block mass. Thus, the lumped parameter model shown in the schematic of Figure 2.1 (f) considers the physical mass and the modal mass, modal stiffness and modal damping of the first flexural mode of the clamped smart beam. These modal parameters are specifically normalised to allow the construction of the lumped parameter model shown in Figure 2.1 (f), which considers the physical base mass and the modal proof mass connected via the modal stiffness and modal damping. This requires the introduction of a virtual displacement w_m for the equivalent proof mass, which does not correspond to the effective physical displacement of the tip mass w_t but it refers to a particular coordinate $\bar{x}$ respect the clamped end of the beam.

As one can readily notice, the two schematics in Figure 2.1 (c) and (f) present identical topologies of the mechanical and of the electrical parts. Therefore, the constitutive equations that govern the response of the two transducers and the energy formulation for the power harvested by the two transducers are derived in the following sections with reference to the common schematic shown in Figure 2.1 (g).

2.3 CONSTITUTIVE EQUATIONS

The constitutive equations are derived considering time-harmonic vibrations described with phasors given in the complex form $f(\mathrm{t}) = \mathrm{Re}\{f(\omega)\exp(\mathrm{j}\omega t)\}$, where $f(\omega)$ is the complex amplitude of the function, ω is the circular frequency and

$j = \sqrt{-1}$. As normally done in vibration studies, the formulation will thus refer to the complex amplitudes $f(\omega)$ of the time-harmonic functions $f(t)$ and, for simplicity, the frequency dependence will be omitted. Considering the common equivalent lumped parameter model shown in Figure 2.1 (g), the electromechanical response of the two lumped parameter models can be expressed in the frequency domain with the following matrix expression:

$$\begin{bmatrix} f_h \\ e_h \end{bmatrix} = \begin{bmatrix} Z_{mi} & T_{fi} \\ T_{ew} & Z_{ei} \end{bmatrix} \begin{bmatrix} \dot{w}_h \\ i_h \end{bmatrix}, \tag{2.1}$$

where, f_h, $\dot{w}_h$ are respectively the complex amplitudes of the force and velocity at the base of the seismic transducers and e_h, i_h are the complex amplitudes of the voltage and current across the terminals of the transducer. As can be deduced from the formulations presented in Appendices A and B, the mechanical and electrical impedance FRFs and the two electromechanical transduction FRFs are given by the following expressions

$$Z_{mi} = \left.\frac{f_h}{\dot{w}_h}\right|_{i_h=0} = Z_b + \frac{Z_s Z_m}{Z_t}, \tag{2.2}$$

$$T_{fi} = \left.\frac{f_h}{i_h}\right|_{\dot{w}_h=0} = \Psi_{fi}\frac{Z_m}{Z_t}, \tag{2.3}$$

$$T_{ew} = \left.\frac{e_h}{\dot{w}_h}\right|_{i_h=0} = \Psi_{ew}\frac{Z_m}{Z_t}, \tag{2.4}$$

$$Z_{ei} = \left.\frac{e_h}{i_h}\right|_{\dot{w}_h=0} = Z_e - \frac{\Psi_{fi}\Psi_{ew}}{Z_t}, \tag{2.5}$$

where

$$Z_m = j\omega m_m, \tag{2.6}$$

$$Z_b = j\omega m_b. \tag{2.7}$$

Also, for the coil-magnet transducer

$$Z_e = R_e + j\omega \tilde{L}_e, \tag{2.8}$$

$$Z_s = \frac{k_m}{j\omega} + c_m, \tag{2.9}$$

$$Z_t = Z_s + Z_m = \frac{k_m}{\mathrm{j}\omega} + c_m + \mathrm{j}\omega m_m, \tag{2.10}$$

while for the piezoelectric transducer

$$Z_e = \frac{1}{\mathrm{j}\omega \tilde{C}_e^S}, \tag{2.11}$$

$$Z_s = \frac{\tilde{k}_m'}{\mathrm{j}\omega} + c_m, \tag{2.12}$$

$$Z_t = Z_s + Z_m = \frac{\tilde{k}_m'}{\mathrm{j}\omega} + c_m + \mathrm{j}\omega m_m. \tag{2.13}$$

Considering first the electromagnetic seismic transducer, as discussed in Appendix A, m_b, m_m are the base and proof masses, k_m, is the suspension stiffness and $c_m = c_a + c_{ec}$ is the equivalent damping coefficent, which is composed by two terms for the air damping c_a and the eddy curent damping c_{ec} [174], [175], [176]. Also, R_e is the coil resistance while $\tilde{L}_e$ is the coil lossy inductance [177], [178], [179], which is given by $\tilde{L}_e = K_e'(1 - \mathrm{j}\eta_L)$, where η_L is the inductive loss factor. As shown in Appendix A, $K_e' = \sin(n\pi/2)K_e\omega^{n-1}$ and $\eta_L = \cos(n\pi/2)/\sin(n\pi/2)$, where the constants K_e and n are reported in Table 2-1: Parameters of the coil magnet harvester. Parameters of the coil magnet harvester were identified from the electric impedance of the electromagnetic seismic transducer. Moving next to the piezoelectric seismic transducer, as discussed in Appendix B, m_b is the base mass, m_m is the equivalent proof mass of the beam laminate and tip mass assembly and c_m is the equivalent viscoelastic damping coefficient. Also the stiffness is composed by two terms: $\tilde{k}_m' = k_m + \Delta\tilde{k}$, where k_m and $\Delta\tilde{k}$ are the beam laminate and tip mass assembly equivalent stiffnesses when the electrodes are respectively in short and in open circuit. The additional stiffness $\Delta\tilde{k}$ is actually a complex term that includes also the effects of dielectric losses in the piezoelectric material. More specifically $\Delta\tilde{k} = K_{pe}\frac{\tilde{k}_{31}^2}{1-\tilde{k}_{31}^2}$ where K_{pe} is a stiffness term and $\tilde{k}_{31}^2 = k_{31}^2/(1 - \mathrm{j}\eta_C)$. Here k_{31}^2 is the electromechanical coupling factor of the piezoelectric material [184] and $\eta_c(\omega) \cong \sigma_{pe}/(\bar{\varepsilon}_{33}^T\omega)$ is the frequency dependent dielectric loss factor of the material, which, as shown in Appendix B, depends on the permittivity of the piezoelectric material in transverse direction under constant stress $\bar{\varepsilon}_{33}^T$ and the electrical conductivity of the piezoelectric material σ_{pe} [180], [181], [182], [183]. Also, $\tilde{C}_e^S = \tilde{C}_e^T\left(1 - \tilde{k}_{31}^2\right)$ and $\tilde{C}_e^T = 2\bar{\varepsilon}_{33}^T\frac{bL}{h_{pe}}(1-\mathrm{j}\eta_C)$ are the lossy capacitances of the two piezoelectric layers respectively under constant strain, i.e. $S_1 = 0$, and under

constant stress, i.e. $T_1 = 0$ [184]. To conclude, the transduction coefficients for the electromagnetic seismic transducer are given by:

$$\Psi_{fi} = \frac{f_i}{i_h} = \psi_{CM}, \tag{2.14}$$

$$\Psi_{ew} = \frac{e_w}{\dot{w}_r} = -\psi_{CM}, \tag{2.15}$$

where f_i is the reactive force produced on the coil and on the magnet components and $\dot{w}_r = \dot{w}_m - \dot{w}_h$ is the relative velocity between the coil and the magent. Also,

$$\psi_{CM} = Bl, \tag{2.16}$$

is the electromagnetic transduction factor, where B is the magnetic flux density in the air gap between the coil and the magnet and l is the length of the winding [185], [186], [187], [188] . Alternatively, the transduction coefficients for the piezoelectric seismic harvester are given by:

$$\Psi_{fi} = \frac{f_i}{i_h} = \frac{\psi_{PZT}}{\mathrm{j}\omega \tilde{C}_e^S}, \tag{2.17}$$

$$\Psi_{ew} = \frac{e_w}{\dot{w}_r} = \frac{\psi_{PZT}}{\mathrm{j}\omega \tilde{C}_e^S}, \tag{2.18}$$

where, as discussed in Appendix B, ψ_{PZT} is the equivalent piezoelectric transduction factor for the bending strain produced by the first natural mode of the clamped beam laminated:

$$\psi_{PZT} = \bar{e}_{31} b\left(h_s + h_{pe}\right) \frac{\phi_1'(L)}{\phi_1(\bar{x})}. \tag{2.19}$$

Here, $\phi_1(x)$ and $\phi_1'(x) = \frac{\mathrm{d}\phi_1(x)}{\mathrm{d}x}$ are the amplitude and slope of the first flexural mode of the composite beam and tip mass assembly with the base mass clamped. Also, $\bar{x}$ identifies a specific point along the beam, which can be derived by solving the implicit Eq. (B.73) given in Appendix B. Finally, as discussed in Appendix B.1.1, $\bar{e}_{31}$ is the stress/charge constant for the piezoelectric material derived with reference to Euler–Bernoulli beam model [72]. Also, b is the width of the metallic substrate and piezoelectric layers and h_s, h_{pe} are respectively the thickness of the metallic substrate

and piezoelectric layers. According to Hunt's notation [185], the transduction coefficients in Eqs. (2.14)-(2.15) and Eqs. (2.17)-(2.18) should read: Ψ_{fi} force per current and Ψ_{ew} electromotive force per relative velocity. Thus the Ψ_{fi} coefficient gives the reactive force exerted between the base and moving masses per unit current flowing in the transducer while the Ψ_{ew} coefficient gives the electromotive force, i.e. voltage, generated at the terminals of the transducer per unit relative velocity between the base and moving masses. The transduction coefficients for the electromagnetic seismic harvester assembly are given by real values with opposite signs: $\Psi_{fi} = \psi_{CM}$ and $\Psi_{ew} = -\psi_{CM}$. Instead, neglecting the effects produced by dielectric losses, the transduction coefficients for the piezoelectric layers are given by equal imaginary, frequency dependent, values: $\Psi_{fi} = \Psi_{ew} = \frac{\psi_{PZT}}{\mathrm{j}\omega\bar{C}_e^S}$. Piezoelectric transduction occurs via strain rather than strain rate,[184], [186], [188]. Thus, since the formulation introduced above refers to strain rate, i.e. relative velocity between the base and moving masses in the lumped parameter model, the piezoelectric transduction coefficients are characterised by a $1/(\mathrm{j}\omega)$ factor as highlighted in Ref. [188].

The T_{fi} and T_{ew} FRFs in Eq. (2.1) represent the electromechanical transduction FRFs for both seismic transducers, which give the base force effect produced by the transducer per unit current flowing in the blocked seismic transducer, i.e. $T_{fi} = f_h/i_h|_{\dot{w}_h=0}$, and the electromotive force generated at the terminals of the transducer per unit velocity at the base of the open circuit seismic transducer, i.e. $T_{ew} = e_h/\dot{w}_h|_{i_h=0}$. Also, $Z_{ei} = e_h/i_h|_{\dot{w}_h=0}$ is the output electrical impedance of the blocked seismic transducer while $Z_{mi} = f_b/\dot{w}_h|_{i_h=0}$ is the input mechanical impedance of the open circuit seismic transducer.

2.4 PRINCIPAL PROPERTIES OF THE TWO TRANSDUCERS

Before moving on to the analysis of the mechanical impedance, electrical impedance and electromechanical transduction FRFs, the constitutive Eqs.(2.1) are examined here to highlight two important intrinsic features that characterise the electromagnetic and piezoelectric seismic transducers considered in this study. The first is related to reciprocity[184], [185], [186] ,[188], which occurs when the so called *electro-mechanical* and *mechano-electrical* impedances defined here,

$$Z_{em} = \frac{e_h}{\dot{w}_h}\bigg|_{f_h=0} = T_{ew} - \frac{Z_{ei}Z_{mi}}{T_{fi}}, \tag{2.20}$$

$$Z_{me} = \frac{f_h}{i_h}\bigg|_{e_h=0} = T_{fi} - \frac{Z_{ei}Z_{mi}}{T_{ew}}, \tag{2.21}$$

are equal, that is

$$Z_{em} = Z_{me}. \tag{2.22}$$

Considering first the electromagnetic seismic transducer, according to Eqs.(2.3), (2.4) and (2.14), (2.15), (2.16), the electromechanical transduction FRFs have same magnitude but opposite sign, i.e. $T_{fi} = -T_{ew}$ such that the impedance Eqs.(2.20) and (2.21) are equal in magnitude but reversed in algebraic sign, i.e. $Z_{em} = -Z_{me}$. Thus, the electromagnetic seismic transducer is "antireciprocal". In contrast, considering the piezoelectric seismic transducer, according to Eqs.(2.3), (2.4) and (2.17), (2.18), (2.19) the electromechanical transduction FRFs have same magnitude and same sign, i.e. $T_{fi} = T_{ew}$, which indicates that $Z_{em} = Z_{me}$ and thus the piezoelectric seismic transducer is "reciprocal". These properties are often referred to the *skew–symmetry* or *symmetry* of the constitutive equations. Indeed, for the two transducers at hand, the constitutive equations given in Eq.(2.1) can be expanded in the following matrix expressions,

$$\begin{bmatrix} f_h \\ e_h \end{bmatrix} = \begin{bmatrix} Z_b + \dfrac{Z_s Z_m}{Z_t} & \psi_{CM}\dfrac{Z_m}{Z_t} \\ -\psi_{CM}\dfrac{Z_m}{Z_t} & Z_e + \dfrac{\psi_{CM}^2}{Z_t} \end{bmatrix} \begin{bmatrix} \dot{w}_h \\ i_h \end{bmatrix}, \tag{2.23}$$

$$\begin{bmatrix} f_h \\ e_h \end{bmatrix} = \begin{bmatrix} Z_b + \dfrac{Z_s Z_m}{Z_t} & \dfrac{\psi_{PZT}}{\mathrm{j}\omega\tilde{C}_e^S}\dfrac{Z_m}{Z_t} \\ \dfrac{\psi_{PZT}}{\mathrm{j}\omega\tilde{C}_e^S}\dfrac{Z_m}{Z_t} & Z_e + \dfrac{\psi_{PZT}^2}{\omega^2\tilde{C}_e^{S^2}Z_t} \end{bmatrix} \begin{bmatrix} \dot{w}_h \\ i_h \end{bmatrix}, \tag{2.24}$$

which highlight that the electromagnetic seismic transducer is *skew–symmetric*, i.e. the off diagonal electromechanical transduction FRFs in the matrix of Eq.(2.23) have equal magnitude and opposite sign, while the piezoelectric seismic transducer is *symmetric*, i.e. the off diagonal electromechanical transduction FRFs in the matrix of Eq.(2.24) have equal magnitude and equal sign. In other words, the electromagnetic seismic transducer has *irreversible* electromechanical transduction FRFs whereas the

piezoelectric seismic transducer has *reversible* electromechanical transduction FRFs and thus the former is an *antireciprocal* transducer while the latter is a *reciprocal* transducer. However, it should be highlighted that, as discussed by Hunt [185] and other authors, the sign reversal in the electromechanical transduction FRFs of the electromagnetic seismic transducer arises from a shortcoming of the *right-hand screw* sign convention used to define the positive directions of the physical variables that describe the electromagnetic transduction phenomenon and from the choice of the independent variables in Eqs.(2.23) and (2.24) [189].

The second aspect worth considering is the fact that the expressions of all four FRFs in the constitutive equations for the two transducers include the $1/Z_t$ second order term, which magnifies the amplitudes of the four FRFs in correspondence of the fundamental resonance frequency of the seismic transducers. Therefore, it is expected that the *mechanical-to-electrical* and *electrical-to-mechanical* energy conversions are particularly effective at the fundamental resonance frequency of the transducers. Likewise, the mechanical and electrical impedance FRFs are likely to be largely affected by the mechanical resonant response of the seismic transducers in correspondence of the fundamental resonance frequency of the seismic transducers.

2.5 IMPEDANCE AND TRANSDUCTION FRF

The simulated and measured 10 Hz – 1 kHz spectra of the mechanical and electrical impedances and the two electromechanical transduction FRFs that form the constitutive Eq.(2.1) for the electromagnetic and piezoelectric seismic transducers shown in Figure 2.1 are now analysed. To highlight in detail all the features that characterise the four FRFs of the two transducers, both modulus-phase and real-imaginary graphs are presented and examined. The simulated FRFs given in Eqs. (2.2)-(2.5) have been derived using the physical parameters summarised in Table 2-1 and Table 2-2 that were identified from the two transducers depicted in Figure 2.1 (a, b). At frequencies below 10 Hz the base mass and moving mass move approximately in phase and no power can be harvested. Also, for frequencies greater than 1 kHz, the dynamic response of the two harvesters is greatly reduced and so the energy harvesting. Therefore, throughout this thesis, the simulations and experimental results will be shown in frequency ranges comprised between 10 Hz and 1 kHz.

At first, the simulated FRFs for the electromagnetic seismic transducer depicted by the solid blue lines in Figure 2.2 and Figure 2.3 are examined. As can be deduced from Eq. (2.2), the mechanical impedance Z_{mi} is defined considering the coil in open circuit, i.e. $i_h = 0$, in which case there is no electromechanical coupling between the coil and magnet and therefore the impedance function entirely depends on the mechanical response of the transducer. As can be noticed from the solid blue line in Plot (a) of Figure 2.2 and Figure 2.3, the mechanical impedance FRF is characterised by low- and high-frequency asymptotic mass behaviours, which are proportional respectively to the total mass of the transducer $m_m + m_b$ and to the base mass of the transducer m_b. These two asymptotic behaviours converge to a peak at the fundamental resonance frequency of the transducer, at about 19.5 Hz, and close to a smooth antiresonance trough, at about 36 Hz. The transition between the two mass effects is effectively smoothened by the significant eddy currents damping effect that characterises the transducer. The phase starts at +90° and, due to the relatively high damping effect and to the vicinity of the resonance and antiresonance frequencies, undergoes only a −90° phase lag and then a +90° phase lead, respectively at the resonance and antiresonance frequencies, such that at higher frequencies, it levels at +90°. As discussed in Refs. [190], [191], at low frequencies below the fundamental resonance frequency at 19.5 Hz, the base and seismic masses of the transducer oscillate in phase as if they were a solid body and thus produce a reactive inertial impedance effect proportional to the total mass of the transducer. At high frequencies, above the antiresonance at 36 Hz, the seismic mass is characterised by rather little oscillations compared to those of the base mass such that it acts as a seismic reference point for the transducer. Therefore, also at higher frequencies, the mechanical base impedance is characterised by a reactive mass impedance effect, in this case proportional to the base mass of the transducer, i.e. mass of the inner magnetic element. At frequencies close to the resonance frequency at 19.5 Hz, the base and seismic masses undergo counter-phase oscillations [190], [191], whose amplitude is however limited by the large eddy currents damping effect. According to Eq.(2.5), the electrical impedance Z_{ei} is characterised by the superimposition of two components: the coil resistive-inductive impedance Z_e and the electromechanical impedance ψ_{CM}^2/Z_t. The electrical impedance of the coil Z_e is characterised by a resistance R_e in series with a lossy inductance $\tilde{L}_e$ that takes into account the effect of eddy currents that develops in the coil wire of the transducer [177], [178] , [179].

As can be noticed in Plot (d) of Figure 2.2 and Figure 2.3, at low frequencies below the cut off frequency $f_{RL} = R_e/(2\pi L_e) = 805$ Hz, the electric impedance Z_e is

characterised by a real part, which is controlled by the resistive effect R_e of the coil only. At higher frequencies above 805 Hz, the lossy inductive component $\tilde{L}_e$ becomes relevant such that the electric impedance Z_e is characterised by both real and imaginary parts that, as discussed in Appendix A, rise proportionally to $\omega^{0.78}$. As can be noted in Plot (d) of Figure 2.2 and Figure 2.3, the second term due to the electromechanical impedance ψ_{CM}^2/Z_t becomes relevant in correspondence of the transducer fundamental resonance frequency and produces a resonance peak at about 19.5 Hz, which confirms one of the characteristic properties for seismic transducers discussed in Section 2.4. As found for the mechanical impedance Z_{mi}, the resonance peak is smoothened by the large eddy currents damping effect that characterises this electromagnetic seismic transducer.

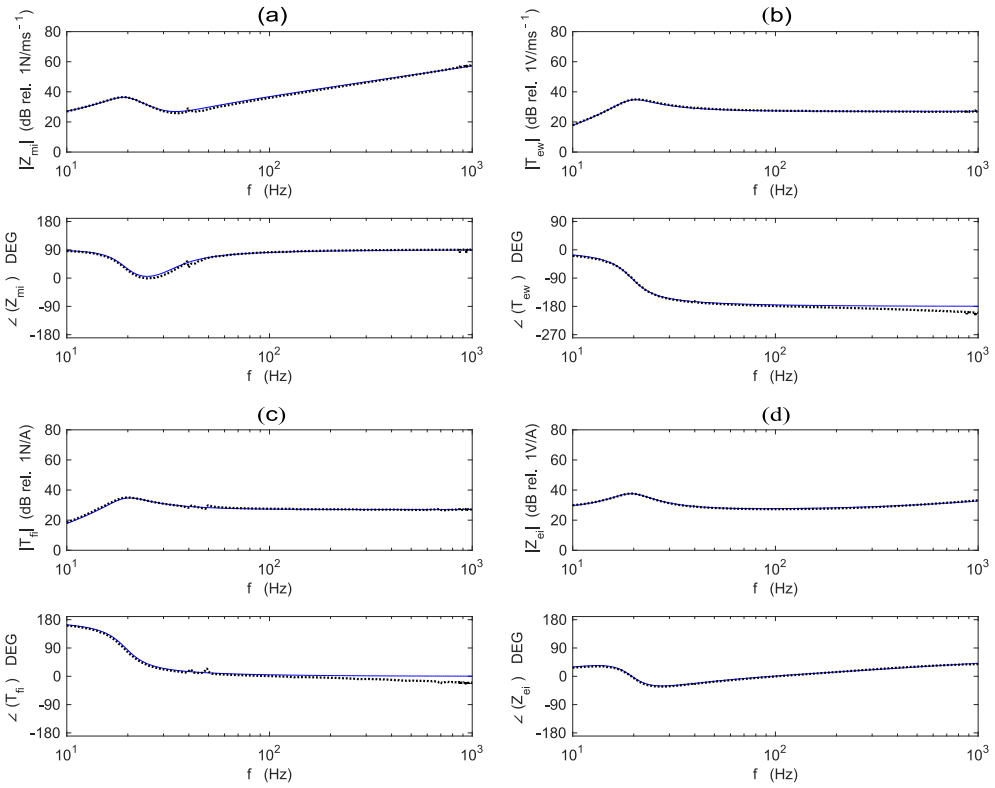

Figure 2.2: Modulus-phase diagrams of the four characteristic FRFs for the electromagnetic seismic transducer. Simulated (solid blue line) and measured (dotted black line) FRFs.

As discussed in Section 2.4, the electromagnetic transducer is *skew-symmetric*, i.e. *antireciprocal*; thus, the electromechanical transduction functions T_{fi} and T_{ew}, given respectively by Eqs.(2.3), (2.4) have the same modulus and opposite phase or, alternatively, inverted real parts and inverted imaginary parts. Indeed, as can be noticed in Plots (b) and (c) of Figure 2.2 and Figure 2.3, at low frequencies the moduli of T_{fi} and T_{ew} rise proportionally to ω^2 towards a peak at the fundamental resonance frequency of the seismic transducer, i.e. 19.5 Hz. Also in this case, the resonance peak is smoothened by the significant eddy currents damping effect. At frequencies above 50 Hz, the modulus levels to a constant value such that the seismic transducer both generates a constant force per unit current and produces a constant voltage source per unit relative velocity of the proof mass with respect to the case.

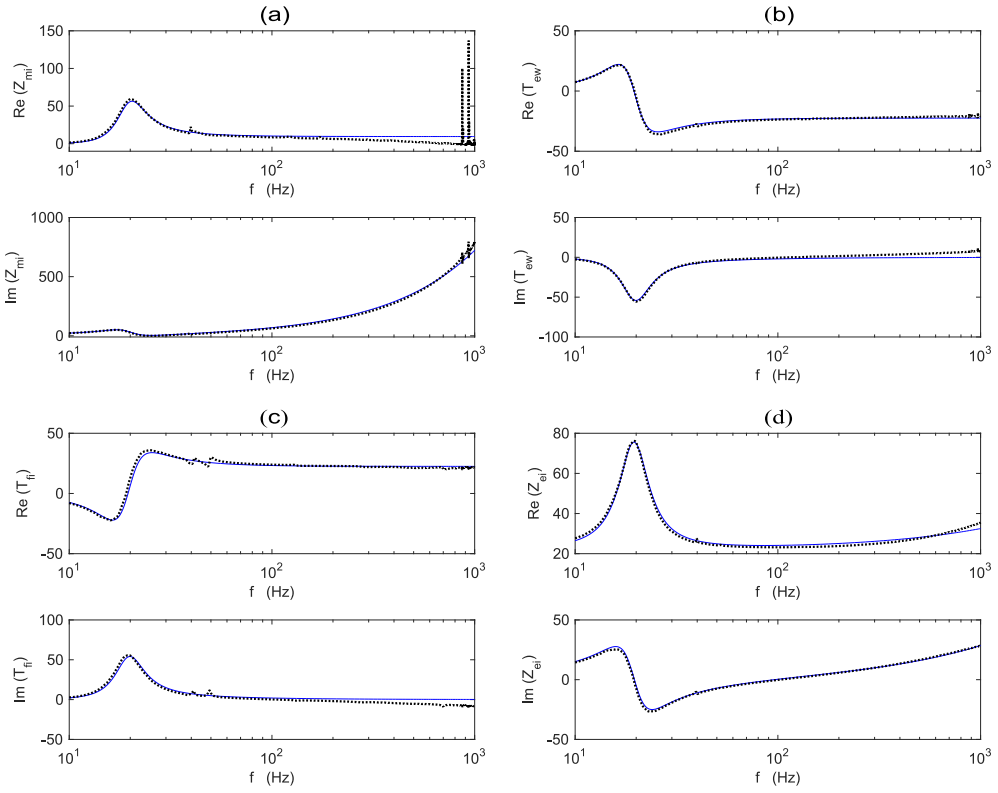

Figure 2.3: Real-imaginary diagrams of the four characteristic FRFs for the electromagnetic seismic transducer. Simulated (solid blue line) and measured (dotted black line) FRFs.

The phase spectra of T_{fi} and T_{ew} start respectively at $+180°$ and $0°$, and in correspondence of the resonance frequency undergo a $-180°$ phase lag. Thus, for this transducer, the constant force-current or voltage-stroke velocity transduction effects are characterised by active power transfer properties. In particular, at frequencies higher than the fundamental resonance frequency of the seismic transducer, the constant force-current or voltage-stroke velocity transduction effects are characterised by a negative sign with respect to the notation indicated in the lumped parameter model, which indicates an opposite flow of power with respect to the notation indicated in the lumped parameter model (c) of Figure (2.1. It is important to emphasise that, as discussed in Section (2.4), this apparent mismatch of power flow is merely due to the right-hand screw sign convention used to define the positive directions of the physical variables that describe the electromagnetic transduction phenomenon [185].

The validity of these simulation results was verified against measured FRFs taken on the prototype transducer shown in Figure 2.1 (a). Appendix F lists the equipment and shows the experimental set-up used to measure the characteristic FRFs of the two transducers. The FRFs of the mechanical and electrical impedances, Z_{mi} and Z_{ei}, and of the two electromechanical transduction functions, T_{fi} and T_{ew}, were measured in the frequency range between 10 Hz and 1 kHz. As can be noticed by contrasting the dotted black lines (measurements) and the solid blue lines (simulations) in Figure 2.2 and Figure 2.3, the experimental FRFs overlap rather well with the simulated FRFs. There are just a couple of small glitches in the four measured FRFs between 35 and 45 Hz, probably caused by the presence of small rocking vibration modes of the suspended ferromagnetic ring and coil assembly, which are not taken into account in the model. Also, Plot (a) in Figure 2.3 shows two additional sharp resonance peaks in the frequency range comprised between 800 and 1000 Hz. These are probably due to local flexural modes of the two spiral springs that hold together the outer ferromagnetic ring and coil assembly with the inner magnetic element of the transducer, which were also not taken into account in the model. Finally, Plots (b) and (c) in Figure 2.2 and Figure 2.3 show that, with respect to the simulated results, the measured electromechanical transduction FRFs T_{fi} and T_{ew} are characterised by a small phase divergence at higher frequencies, which is related to a mismatch between the measured and simulated imaginary parts. This is due to higher order dynamic effects of the transducer occurring at frequencies just above the 1 kHz upper limit of the plots in Figure 2.2 and Figure 2.3, which are not considered in the model used to simulate the characteristic FRFs of the electromagnetic seismic transducer.

The simulated FRFs for the piezoelectric seismic transducer depicted by the solid blue lines in Figure 2.4 and Figure 2.5, are now examined. The spectrum of the mechanical base impedance Z_{mi}, given by Eq.(2.2), is very similar to that derived for the electromagnetic transducer. Indeed, as shown by the solid line in Plot (a) of Figure 2.4 and Figure 2.5, it is characterised by mass behaviours at low and high frequencies, proportional respectively to the total mass $m_m + m_b$ and to the base mass m_b of the cantilever beam with piezoelectric transducers and tip mass, which are linked by a sharp resonance peak at about 20 Hz and a narrow antiresonance trough at about 33 Hz. In this case, the phase starts at $+90°$ and undergoes a full $-180°$ phase lag at the fundamental resonance frequency at about 20 Hz and a full $+180°$ phase recovery at the antiresonance frequency at about 33 Hz, such that, at higher frequencies, it levels at $+90°$. In this case the fact that the impedance Z_{mi} is defined for open circuit condition, i.e. $i_h = 0$, implies that, the stiffness term $\tilde{k}'_m = k_m + \Delta\tilde{k}$ in the expressions (2.12), (2.13) of the impedances Z_s, Z_t, is characterised by two components.

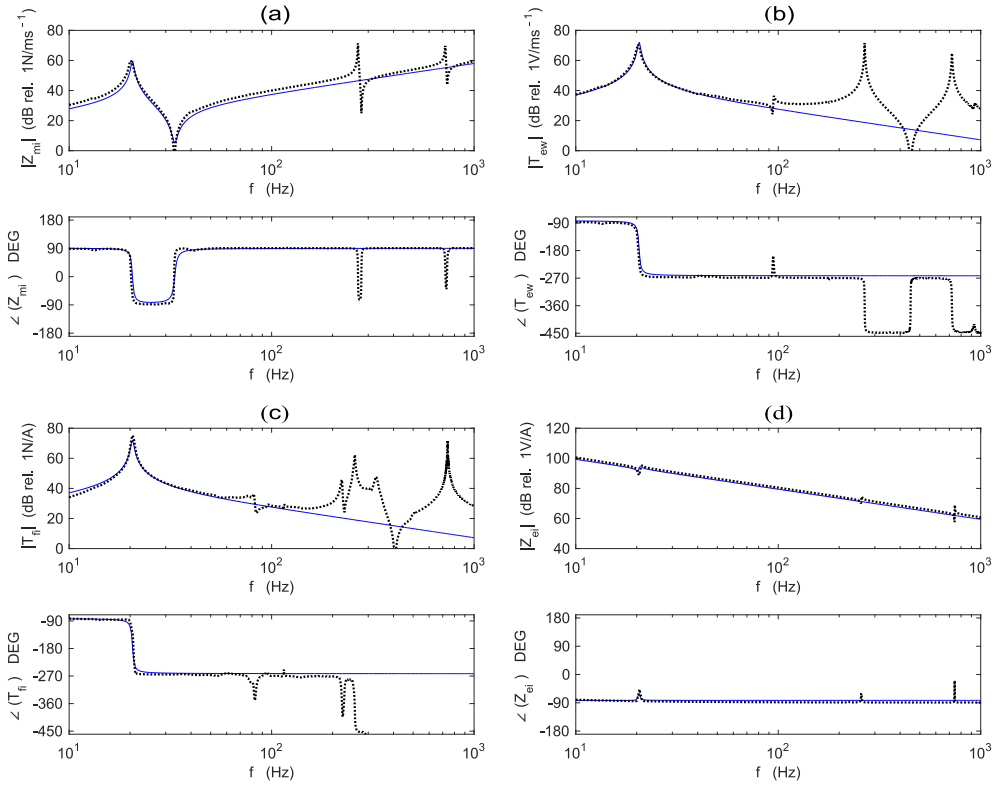

Figure 2.4: Modulus-phase diagrams of the four characteristic FRFs for the piezoelectric seismic transducer. Simulated (solid blue line) and measured (dotted black line) FRFs.

The first, k_m is due solely to the mechanical bending stiffness of the beam laminate and tip mass assembly produced when the electrodes are in short circuit, whereas the second $\Delta\tilde{k}$ encompass the additional back electromechanical stiffness effect that is produced when the electrodes are in open circuit. Thus, the second term tends to slightly enhance the bending stiffness of the composite beam with the electrodes in short circuit, such that, as shown in Ref. [192], the fundamental resonance frequency of the seismic transducer is only slightly higher than that measured with the piezoelectric layers in short circuit. Also, as shown in Appendix B, the equivalent stiffness $\Delta\tilde{k}$ is actually a complex term, which encompass the energy dissipation effect produced by the lossy dielectric property of the piezoelectric material.

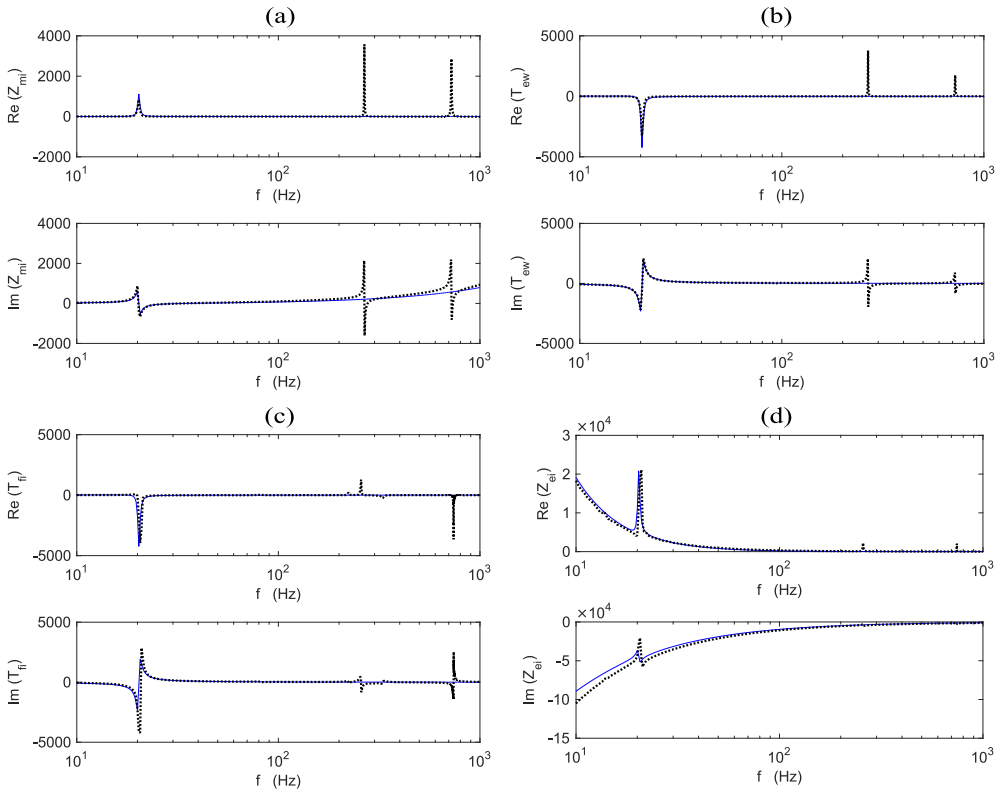

Figure 2.5: Real-imaginary diagrams of the four characteristic FRFs for the piezoelectric seismic transducer. Simulated (solid blue line) and measured (dotted black line) FRFs.

As discussed in Ref. [170] and shown in Appendix B.2, the resistive effect produced by dielectric losses is relatively small and confined to low frequencies. Thus, the

principal energy dissipation effect in this seismic transducer is due to the viscoelastic loss in the composite beam. This effect is however, much weaker than the air and eddy currents damping effects present in the electromagnetic seismic transducer. Therefore, as can be noticed by contrasting Figure 2.2 (a) and Figure 2.4 (a), compared to that for the electromagnetic seismic transducer, the mechanical impedance function for the piezoelectric seismic transducer is characterised by a sharper resonance peak followed by a narrower antiresonance trough. According to Eq. (2.5), as found for the electromagnetic seismic transducer, the electrical impedance Z_{ei} is given by the superposition of two terms, that is the piezoelectric layers capacitive impedance Z_e and electromechanical impedance $\frac{\psi_{PZT}^2}{\omega^2 \tilde{C}_e^{S^2} Z_t}$. In this case, as described in Appendix B and shown in Figure 2.1 (f), the electrical impedance $Z_e = \frac{1}{\mathrm{j}\omega \tilde{C}_e^S}$ is characterised by a lossy capacitor $\tilde{C}_e^S = \tilde{C}_e^T\left(1 - \tilde{k}_{31}^2\right)$. Plot (d) of Figure 2.4 shows a typical capacitive impedance function, with a modulus that drops proportionally to ω^{-1} and a phase equal to $-90°$. However, Plot (d) of Figure 2.5 highlights that, at low frequencies, around and below the fundamental resonance frequency of the seismic transducer at about 20 Hz, the resistive effect due to the dielectric losses becomes relevant. Also in this case, as discussed in Section 2.4, Plots (d) in Figure 2.4 and Figure 2.5 show that the second term due to the electromechanical impedance $\frac{\psi_{PZT}^2}{\omega^2 \tilde{C}_e^{S^2} Z_t}$ produces a small resonance peak at the fundamental resonance frequency, at about 20 Hz.

As anticipated in Section 2.4, the piezoelectric seismic transducer is symmetric, i.e. reciprocal, thus the electromechanical transduction coefficients T_{fi} and T_{ew}, given respectively by Eq.(2.3) and Eq.(2.4), have equal modulus and equal phase. The spectra of the electromechanical transduction coefficients T_{fi} and T_{ew} for the piezoelectric seismic transducer greatly differ from those found for the electromagnetic transducer. In fact, at low frequencies, the modulus rises proportionally to ω^1 towards a sharp resonance peak at the fundamental resonance frequency of the transducer at about 20 Hz, whose amplitude is controlled by the relatively small viscoelastic damping effect in the beam laminate. At higher frequencies, the modulus decreases proportionally to ω^{-1}. The phase spectra of both T_{fi} and T_{ew} start at $-90°$ and undergo a $-180°$ phase lag in correspondence to the 20 Hz fundamental resonance frequency. Thus, with this transducer, the constant force-current or voltage-stroke velocity transduction effects are characterised by reactive power transfer effects. This characteristic is due to the mechanical-to-electrical and electrical-to-mechanical transduction effects of piezoelectric materials,

which are respectively proportional to strain and charge rather than strain rate and current.

As done for the coil-magnet transducer, the validity of these simulation results was checked against measured FRFs taken on the prototype transducer shown in Figure 2.1 (d). The experimental setup and equipment used to produce these measurements are shown in Appendix F. The FRFs of the mechanical and electrical impedances, Z_{mi} and Z_{ei}, and of the two electromechanical transduction functions, T_{fi} and T_{ew}, were measured in the frequency range between 10 Hz and 1 kHz. In this case, contrasting the dotted black lines (measurements) and the solid blue lines (simulations) shown in Figure 2.4 and Figure 2.5, it is noted that the simulated FRFs reproduce quite closely the measured FRFs up to about 90 Hz. At higher frequencies the measured FRFs follow the asymptotic behaviours of the simulated FRFs, although they are characterised by additional resonance peaks and antiresonance troughs, particularly in the Z_{mi}, T_{fi}, T_{ew} FRFs. These new features are due to the dynamics of higher order flexural modes of the composite beam with the tip block, which are not taken into account in the model used to derive the four FRFs given in Eqs.(2.2) - (2.5). With respect to the *symmetry* (i.e. *reciprocity*) feature that characterises this seismic transducer, the measured T_{fi}, T_{ew} FRFs overlap quite well. There is just a very little mismatch in correspondence of the resonance peak at about 80 Hz and a somewhat more marked mismatch between 100 and 250 Hz, where the T_{fi} FRF is characterised by two additional resonance peaks with respect to the T_{ew} FRF. These two additional resonance peaks are related to torsional modes of the composite beam, which, due to the non-perfect alignment of the piezoelectric layers with the longitudinal axis of the beam substrate, are excited when the T_{fi} FRF is measured. Nevertheless, the comparison between simulated and measured FRFs indicate that the model proposed in this study accurately reproduce the mechanical and electrical impedance functions, Z_{ei} and Z_{mi}, and the two electromechanical transduction functions, T_{fi} and T_{ew}, of the piezoelectric transducer up to about 70 Hz. Thus, the model can be suitably used to predict the power absorbed by the piezoelectric seismic transducer in correspondence to its fundamental resonance frequency where, as will be shown in Section 2.6, the maximum energy harvesting occurs.

2.6 ENERGY ANALYSIS

Since the constitutive equations for the two seismic transducers were derived in the same form, a unified energy formulation is introduced in this section to study three key parameters necessary to characterise the energy harvesting properties with the electromagnetic and the piezoelectric seismic transducers, that is: first, the power harvested; second, the power input and third, the efficiency. These functions are derived for the cases where the electromagnetic and piezoelectric seismic transducers are connected to electrical harvesting loads characterised either by complex or real optimal impedance functions. To this end, the two seismic electromechanical transducers are conveniently represented with the equivalent schematic shown in Figure 2.6 [185]. The scheme is formed by a two port (four terminal) network comprising a mechanical mesh with input variables $\dot{w}_h$ and f_h and mechanical impedance Z_{mi}, which is coupled to an electrical mesh with input electrical variables e_h and i_h and electrical impedance Z_{ei} through a black box called transducer having electromechanical transduction coefficients T_{ew} and T_{fi}. The energy harvesting configuration is then completed by connecting to the electrical terminals the impedance of the harvesting load Z_h and considering an ideal mechanical velocity source $\dot{w}_b$ acting at the base of the two seismic transducers. To fully characterise the two seismic harvesters, the power harvested, power input and efficiency is also analysed with respect to the stroke of the two transducers. Indeed, as anticipated in the introduction and described in Refs. [86], [107], [193], [194] for example, non-linear effects are often employed to operate the harvesters at their maximum allowed strokes so as to make the most of power harvesting for a wide range of amplitudes of the ambient vibrations.

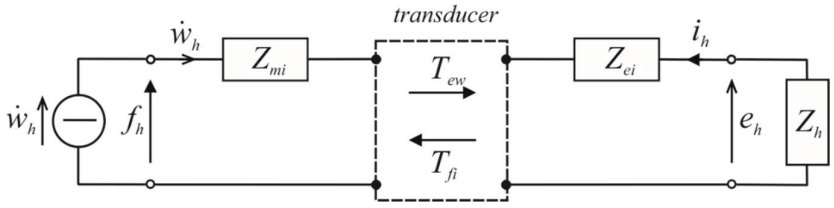

Figure 2.6: Equivalent schematic representation of the two seismic electromechanical transducers connected to the harvesting electrical load.

The results presented in the following section are based on the spectra of the optimal impedance harvesting loads and the spectra of the power harvested, of the power

input and of the efficiency. Before moving on to the analysis of these graphs, it is important to recall that this study is focussed on time-harmonic energy harvesting. Therefore, the spectra of the optimal impedance of the harvesting load Z_h should not be interpreted as the Power Spectral Densities (PSD) of the harvesting loads. On the contrary, they give the values of the complex impedance that should be implemented to guarantee the maximum energy harvesting with the two seismic harvesters for a given excitation frequency. Also, it is important to anticipate that the graphs presented and analysed in the following three sections are all characterised by two spectra, both of which were derived from simulations using either the analytical expressions (solid blue lines) or the measurements (dotted black lines) of the four constitutive FRFs, Z_{mi}, T_{fi}, T_{ew}, Z_{ei}, that characterise the two transducers as depicted in Figure 2.2 - Figure 2.3 and in Figure 2.4 - Figure 2.5. The latter results are quite important since, although obtained from "off line experiments", they give detailed indications on the effective power harvested and effective power input of the two prototype seismic harvesters shown in Figure 2.1 (a) and Figure 2.1 (d) that have been considered in this study.

2.7 HARVESTED POWER

For time-harmonic vibrations, the time averaged harvested power is given by

$$\bar{P}_h = \lim_{T\to\infty} \frac{1}{T} \int_0^T P_h(t)\mathrm{d}t\,, \tag{2.25}$$

where the instantaneous harvested power is given by

$$P_h(t) = e_h(t) i_h(t), \tag{2.26}$$

and $e_h(t)$, $i_h(t)$ are the voltage across and current through the harvesting load. Assuming time-harmonic functions, the following impedance relation holds for the harvesting element:

$$e_h = -Z_h i_h, \tag{2.27}$$

where Z_h is the electrical impedance of the harvesting circuit. Also, considering the electric mesh of the harvesters shown in Figure. 2.6 and recalling that the transducers yield a voltage

$$e_h = T_{ew}\dot{w}_h, \tag{2.28}$$

the harvesting current can be derived straightforwardly by analysing the mesh with Kirchhoff's voltage law, which gives:

$$i_h = -\frac{T_{ew}}{Z_{ei} + Z_h}\dot{w}_h. \tag{2.29}$$

Thus, for harmonic vibrations, the time average harvested power is derived from Eqs. (2.25) to (2.29) as follows:

$$\bar{P}_h = \frac{1}{2}\mathrm{Re}\{Z_h\}|i_h|^2 = \frac{1}{2}\mathrm{Re}\{Z_h\}\left|-\frac{T_{ew}}{Z_{ei} + Z_h}\right|^2 |\dot{w}_h|^2. \tag{2.30}$$

Eq.(2.30) suggests that the harvested power depends on the impedance of the harvesting circuit. The complex impedance that maximizes the harvested power at each frequency can be derived using Fermat's theorem on the stationary points for n-dimensional functions [195], which, in this case, sets the following two conditions:

$$\frac{\partial \bar{P}_h}{\partial \mathrm{Re}\{Z_h\}} = 0 \text{ and } \frac{\partial \bar{P}_h}{\partial \mathrm{Im}\{Z_h\}} = 0\,. \tag{2.31a,b}$$

Solving Eq.(2.31) leads to the following condition for the optimal impedance of the harvesting circuit:

$$Z_h = Z_{ei}^*, \tag{2.32}$$

where * is the complex conjugate operator. The maximum for the harvested power $\bar{P}_h$ is thus obtained when the electric impedance of the harvesting circuit Z_h is the complex conjugate of the electrical impedance of the freely suspended seismic transducer Z_{ei} given in Eq.(2.5). This result is in line with the maximum power transfer theorem [195], which, assuming time-harmonic functions, states that a load

collects the maximum amount of power from a source when its resistance is equal to the internal resistance of the source and when the imaginary part of the impedance of the load has opposite sign than the imaginary part of the impedance of the source. Such optimal complex impedance can be produced in practice with a resistance and inductance in series. When the reactive part of the optimal impedance is very large such that it cannot be generated in practice with passive electrical components, active circuits involving operational amplifiers could be used, although this may greatly limit the net harvested power and thus turn out also impractical.

Substituting the optimal condition for Z_h given in Eq.(2.32) into Eq.(2.30), the maximum harvested power results:

$$\bar{P}_h = \frac{1}{8}\frac{|T_{ew}|^2}{\mathrm{Re}\{Z_{ei}\}}|\dot{w}_h|^2, \tag{2.33}$$

which, using the formulation presented in Section 2.3, can be specified respectively for the electromagnetic and for the piezoelectric seismic harvesters. It should be highlighted that Eq.(2.33) is obtained under the assumption that the seismic devices can withstand any stroke. Thus, no restrictions on their range of the base vibration are assumed. As discussed in Refs. [87], [146] in practical devices the maximum relative displacement is limited, thus the formula in Eq.(2.33) cannot be used and Eq.(2.32) should be modified in order to consider this constrain.

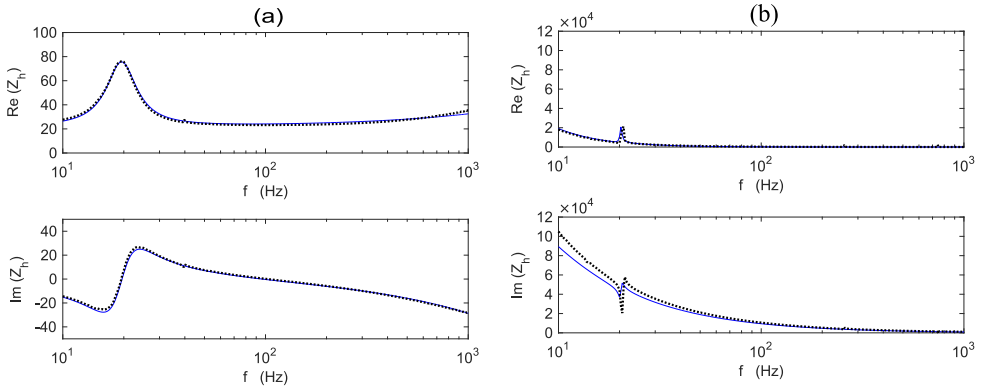

Figure 2.7: Comparison between the simulated (solid blue line) and measured (dotted black line) spectra of the Real and Imaginary parts of the optimal impedance $Z_h = Z_{ei}^*$ of the harvesting circuits for (a) the electromagnetic and (b) the piezoelectric seismic harvesters.

Figure 2.7 shows the real and imaginary parts of the simulated (solid blue lines) and measured (dotted black lines) impedances of the harvesting load $Z_h = Z_{ei}^*$ that would maximise the harvested power at each frequency with the electromagnetic seismic transducer (Plot a) and with the piezoelectric seismic transducer (Plot b). As already observed in Section 2.5, the simulated spectra corresponds fairly well with those derived from the measured FRFs of the electrical impedance Z_{ei}. Plot (a) indicates that, when the electromagnetic seismic transducer is used, the impedance of the harvesting load should be characterised by a real positive part whose amplitude peaks in correspondence of the transducer fundamental resonance frequency and by an imaginary part with amplitude that moves from negative to positive values, and thus becomes zero, in correspondence of the fundamental resonance frequency of the transducer. At higher frequencies, above the cut off frequency at 805 Hz where the lossy inductive effect of the coil winding becomes relevant, the real positive part gradually rises while the imaginary part turns again to progressively larger negative values. As discussed in Section 2.5, the amplitude of the real part peak is controlled by the large eddy currents damping that characterises this electromagnetic seismic transducer. As will be discussed below and in Section 2.10, this is a very important feature, since it sets the maximum energy that can be harvested with the electromagnetic seismic transducer at the fundamental resonance frequency. Alternatively, Plot (b) shows that, when the piezoelectric seismic transducer is used, the impedance of the harvesting load should be characterised by both real and imaginary positive parts that uniformly decrease as the frequency rises, apart from a small peak discontinuity in correspondence of the fundamental resonance frequency of the transducer. Here, the dielectric losses in the piezoelectric layers play a key role in the energy harvesting. In fact, as discussed below and detailed in Appendix B.2.1, if they were not taken into account, apart from frequencies close to the fundamental resonance frequency of the transducer, the real part of the optimal impedance of the harvesting load would rapidly tend to zero. This would lead to the idealised case where the same level of maximum power harvesting would be possible for any excitation frequency [92], [93], [196]. Thus, it is rather important the model for the piezoelectric seismic harvester includes a complex capacitance that accounts for the dielectric losses in the piezoelectric layers. To conclude this analysis, contrasting the two Plots in Figure 2.7, it jumps out that the real/imaginary components of the optimal harvesting impedance for the piezoelectric seismic transducer are three to four orders of magnitude greater than the real/imaginary components of the optimal harvesting impedance for the electromagnetic seismic transducer. Also, the spectra of

the optimal resistive impedance of the harvesting load, Z_h simulated from the analytical expressions for the constitutive FRFs correspond fairly well with those derived from the measured FRFs of the electrical impedance Z_{ei}.

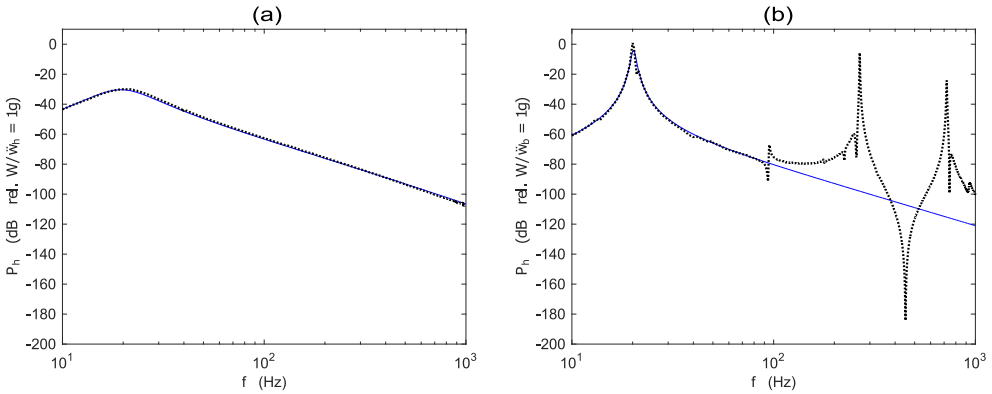

Figure 2.8: Spectra of the power harvested with reference to a $1g$ base acceleration for (a) the electromagnetic and (b) the piezoelectric seismic harvesters with optimal harvesting impedances $Z_h = Z_{ei}^*$ simulated using either the analytical expressions (solid blue lines) or the measurements (dotted black lines) of the four constitutive FRFs, Z_{mi}, T_{fi}, T_{ew}, Z_{ei}.

Figure 2.8 shows the simulated spectra of the 10 Hz to 1 kHz power harvested per 1g base acceleration with the electromagnetic seismic harvester (Plot a) and with the piezoelectric seismic harvester (Plot b) when the harvesting circuits are characterised by the optimal complex impedance $Z_h = Z_{ei}^*$ (the symbol 1g is hereafter used as standard acceleration due to gravity, i.e. 1g = 9.80665 m/s^2). Plot (a) shows that when the harvesting circuit implements at each frequency the optimal impedance derived in Eq.(2.32) and shown in Plot (a) of Figure 2.7, the spectrum of the harvested power is characterised by a smooth peak centred at the fundamental resonance frequency of the seismic transducer, with a maximum level of the harvested power equal to 33 mW/1g. According to Plot (a) in Figure 2.7, the maximum energy harvesting is thus obtained with a purely resistive load of about 75.5 Ω. The spectra of the harvested power simulated from analytical FRFs expressions (solid blue lines) and measured FRFs (dotted black lines) perfectly overlap in the whole frequency range, which confirms the validity of the analytical expressions derived for the constitutive FRFs of the electromagnetic harvester in Section 2.3 and Appendix A. According to Eq.(2.33), the time average harvested power depends on the electrical impedance Z_{ei} and the electromechanical transduction function T_{ew}, which, as

discussed in Sections 2.4 and 2.5, at the fundamental resonance frequency of the transducer, are controlled by damping, in particular the eddy currents damping effect. Thus, the maximum level of power that can be harvested with the electromagnetic seismic transducer is controlled by the eddy currents damping.

Moving to the piezoelectric harvester, Plot (b) of Figure 2.8 shows that when the harvesting circuit implements at each frequency the optimal impedance derived in Eq.(2.32) and depicted in Plot (b) of Figure 2.7, the spectrum of the harvested power is characterised by a sharp peak at the fundamental resonance frequency of the seismic transducer, with a maximum level of the harvested power equal to 700 mW/1g. In this case, according to Plot (b) of Figure 2.7, the maximum energy harvesting is obtained with a resistive and reactive load of $2.3 \times 10^4\ \Omega$ and $4.5 \times 10^4\ \Omega$ respectively. Contrasting the spectra of the harvested power simulated from analytical expressions (solid blue lines) and measurements (dotted black lines) of the four constitutive FRFs Z_{mi}, T_{fi}, T_{ew}, Z_{ei}, it can be easily noted that they overlap only up to about 80 Hz. Indeed, as observed in the analysis of the constitutive FRFs presented in Figure 2.4 and Figure 2.5, the analytical expressions for the constitutive FRFs of the piezoelectric transducer derived in Section 2.2 and Appendix B do not reproduce higher frequencies dynamic effects due to higher order natural modes of the composite beam and tip block, which are instead encompassed in the measured FRFs. Thus, as shown by the dotted black line in Plot (b) of Figure 2.8, the spectrum of the harvested power is characterised by two additional sharp peaks at 267 Hz and 720 Hz where the harvested power is about 300 mW/1g and 60 mW/1g respectively. According to Plot (b) in Figure 2.7, the impedance of the harvesting load at these two frequencies is much smaller than that in correspondence of the fundamental resonance frequency. For instance, at 267 Hz, it should be characterised by a resistive load of $2.2 \times 10^3\ \Omega$ and a reactive load of $5 \times 10^3\ \Omega$. Thus, given that the level of harvested power at the first and second resonance frequencies is not far away, it may result more practical setting the harvester to work in correspondence of its second resonance frequency. This would be particularly the case, if the piezoelectric layers were dimensioned and shaped in such a way as to efficiently detect the second natural mode of the composite beam and tip mass [197]. To conclude the analysis of Plot (b) in Figure 2.8, it is worth noting how the spectrum of the harvested power simulated from measured FRFs (dotted black line) is characterised by some anomalies such has narrow drops or small crests that are not related to antiresonance and resonance effects. This problem arises from the fact that the spectrum has been simulated from measured FRFs, which, although the spectra shown in Figure 2.4 and Figure 2.5 looks

impeccable, still are characterised by small imperfections that, as discussed in Ref. [198], produce the glitches observed in the power harvested spectrum depicted by the dotted black line in Plot (b) of Figure 2.8. Nevertheless, the simulation results accurately reproduce the spectrum of the energy harvested at low frequencies in correspondence to the fundamental resonance frequency of the transducer. As anticipated above, this result is not trivial since it requires an appropriate modelling of the dielectric losses in the piezoelectric patch transducers. In fact, if they were not taken into consideration, as shown in Appendix B.2.1, the optimal impedance of the harvesting load could be chosen in such a way as the same level of maximum power could be harvested for any excitation frequency [92], [93], [196].

Comparing the spectra in Plots (a) and (b) of Figure 2.8, it is noted that, although the piezoelectric harvester outperforms the electromagnetic harvester in correspondence of the fundamental and higher order resonance frequencies, the electromagnetic harvester performs better at low frequencies below the fundamental resonance at 19.5 Hz and also at frequencies comprised between about 30 Hz and about 100 Hz.

Often, practical harvesters are equipped with purely resistive electric loads in which case the harvesting electrical impedance is bound to be purely real. In this case, the purely real impedance that maximizes the harvested power at each frequency is obtained by setting only the condition (a) of Eq.(2.31), which gives:

$$Z_{h,R} = |Z_{ei}|. \tag{2.34}$$

Thus, in this case the maximum for the harvested power $\bar{P}_h$ is produced when the electric impedance of the harvesting circuit $Z_{h,R}$ equals the modulus of the electrical impedance of the freely suspended seismic transducer Z_{ei} given in Eq.(2.5). Substituting the optimal condition for $Z_{h,R}$ given in Eq.(2.34) into Eq.(2.30), leads to the following expression for the maximum harvested power:

$$\bar{P}_h = \frac{1}{4}\frac{|T_{ew}|^2}{|Z_{ei}| + \mathrm{Re}\{Z_{ei}\}}|\dot{w}_h|^2, \tag{2.35}$$

which, recalling Eqs.(2.4), (2.5) in conjunction with the formulation presented in Section 2.3, can be specified respectively for the electromagnetic and for the piezoelectric seismic harvesters.

The two Plots in Figure 2.9 show the simulated (solid blue lines) and measured (dotted black lines) real impedances of the harvesting load $Z_{h,R}$ that would maximise the harvested power at each frequency with the electromagnetic seismic transducer (Plot a) and with the piezoelectric seismic transducer (Plot b).

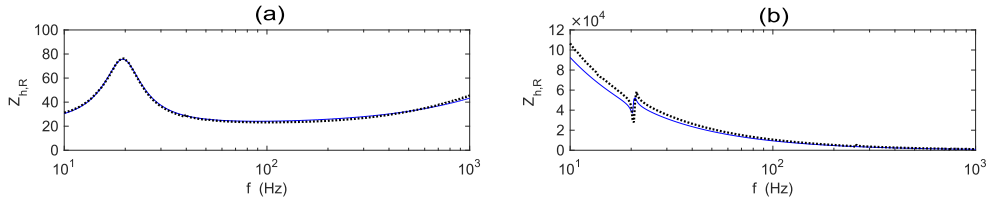

Figure 2.9: Comparison between the simulated (solid blue line) and measured (dotted black line) spectra of the real optimal impedance $Z_{h,R} = |Z_{ei}|$ of the harvesting circuits for (a) the electromagnetic and (b) the piezoelectric seismic harvesters.

Considering first the harvester with the electromagnetic seismic transducer, Plot (a) shows that the spectrum of the real harvesting load $Z_{h,R}$ is quite similar to the real part of the spectrum of the complex load, i.e. Re$\{Z_h\}$. More specifically, compared to the spectrum of Re$\{Z_h\}$, the spectrum of $Z_{h,R}$ is characterised by a peak, which has same amplitude but covers a slightly wider frequency band than that in the spectrum of Re$\{Z_h\}$. As discussed above, the amplitude of this peak is controlled by the eddy currents damping effect that characterises this electromagnetic seismic transducer. Also, at frequencies above the cut off frequency at 805 Hz, where the lossy inductive effect of the coil winding becomes relevant, the spectrum of $Z_{h,R}$ rises monotonically at a slightly higher rate than that of the spectrum of Re$\{Z_h\}$.

Plot (b) in Figure 2.9 shows that for the harvester with the piezoelectric seismic transducer, the spectrum of the real harvesting load $Z_{h,R}$ is instead similar to that of the imaginary part of the spectrum of the complex load, i.e. Im$\{Z_h\}$. Thus, the amplitude of the resistive load uniformly decreases as the frequency rises from values of about 10×10^4 Ω at about 10 Hz, except for a small trough and peak discontinuity in the vicinity of the fundamental resonance frequency of the transducer.

Comparing the two Plots in Figure 2.9, it is noted that the optimal resistive impedance for the piezoelectric seismic transducer is three to four orders of magnitude greater than the real part of the optimal harvesting impedance for the electromagnetic seismic transducer. Also, the spectra of the optimal resistive impedance of the harvesting load, $Z_{h,R}$ simulated from the analytical expressions for

the constitutive FRFs correspond fairly well with those derived from the measured FRFs of the electrical impedance Z_{ei}.

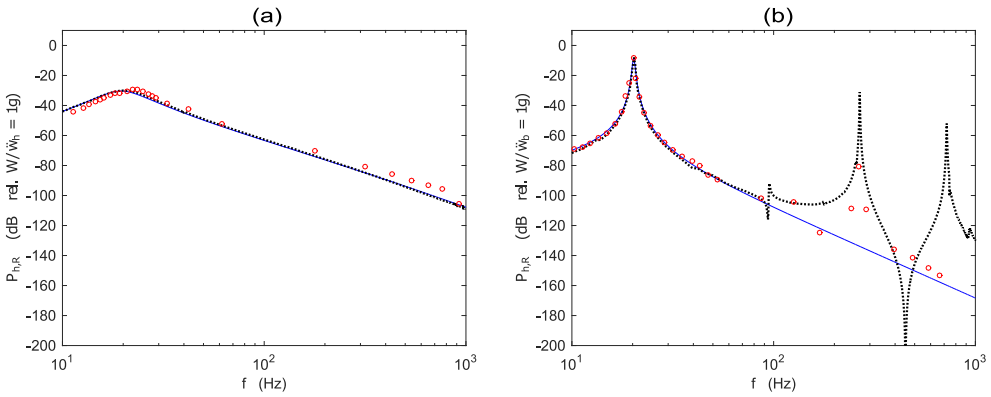

Figure 2.10: Spectra of the power harvested with reference to a $1g$ base acceleration for (a) the electromagnetic and (b) the piezoelectric seismic harvesters with optimal harvesting impedances $Z_{h,R} = |Z_{ei}|$ simulated using either the analytical expressions (solid blue lines) or the measurements (dotted black lines) of the four constitutive FRFs, Z_{mi}, T_{fi}, T_{ew}, Z_{ei} and measured experimentally (red circles).

Figure 2.10 shows the simulated spectra of the 10 Hz to 1 kHz power harvested per 1g base acceleration with the electromagnetic seismic harvester (Plot a) and with the piezoelectric seismic harvester (Plot b) when the harvesting circuits are characterised by the optimal real impedance $Z_{h,R} = |Z_{ei}|$. Considering first the electromagnetic harvester, Plot (a) shows that when the harvesting circuit implements at each frequency the optimal real impedance load given in Eq.(2.34) and depicted in Plot (a) of Figure 2.9, the spectrum of the harvested power is very similar to that found when the optimal complex impedance load given in Eq.(2.32), and shown in Plot (a) of Figure 2.7, is implemented. Thus, it is characterised by a smooth peak centred in correspondence of the fundamental resonance frequency of the seismic transducer and the maximum level of the harvested power is equal to 33 mW/1g. As was noticed above for the complex harvesting load, also with the purely resistive harvesting load, the maximum harvested power is controlled by damping produced by the eddy currents that develops in the ferromagnetic outer ring of this seismic harvester. For instance, if, as shown in Appendix B.2.1, this effect was annihilated, the maximum level of the harvested power would rise to 173 mW/1g. This is a rather important feature of energy harvesting with electromagnetic seismic transducers, which should be carefully considered for the design of an effective harvester. According to Plot (a)

in Figure 2.9, the maximum energy harvesting is obtained with a purely resistive load of about 76 Ω. This is the same value found for the complex optimal impedance load. Thus it can be concluded that, with the electromagnetic seismic harvester, the maximum harvested power is obtained when the harvester is operated at its fundamental resonance frequency with a purely resistive load whose magnitude can be equally derived as either $Z_{ei}^{*}(\omega_n)$ or $|Z_{ei}(\omega_n)|$. Also in this case, the spectra of the harvested power simulated from analytical FRFs expressions (solid blue lines) and measured FRFs (dotted black lines) perfectly overlap in the whole frequency range.

To reinforce the value of the results presented in this study, on line experiments were implemented at specific frequencies for the harvested power when optimal resistors with resistances taken from Plot (a) of Figure 2.9 are connected to the seismic electromagnetic harvester shown in Figure 2.1 (a). As one can readily see from the red circles in Plot (a) of Figure 2.10, these measured power levels further confirm the validity of the proposed model for the constitutive FRFs of the transducer presented in Section 2.3 and Appendix A and the validity of the formulation for the energy harvested proposed in this study. The small discrepancies between measured and predicted levels of the energy harvested at higher frequencies above 300 Hz are probably due to the difficulty of measuring with accuracy low levels of power.

Considering now the piezoelectric harvester, Plot (b) of Figure 2.10 shows that also in the case where the harvesting circuit implements at each frequency the optimal real impedance derived in Eq.(2.34) and depicted in Plot (b) of Figure 2.9, the spectrum of the harvested power is very similar to that found when the optimal complex impedance load given in Eq.(2.32) and shown in Plot (b) of Figure 2.7 is implemented. Indeed, the spectrum of the harvested power is characterised by a sharp peak at the fundamental resonance frequency of the seismic transducer, with a peak level of the harvested power equal to 350 mW/1g. In this case, according to Plot (b) of Figure 2.9, the maximum energy harvesting is obtained with a resistive load of 5.05×10^4 Ω. Also in this case, comparing the spectra of the harvested power simulated from analytical FRFs expressions (solid blue lines) and measured FRFs (dotted black lines), it is noted that they overlap only up to about 70 Hz. As discussed above, this is due to the fact that the analytical expressions for the constitutive FRFs of the piezoelectric transducer derived in Section 2.3 and Appendix B do not reproduce higher frequencies dynamic effects due to higher order natural modes of the composite beam and tip block, which are instead encompassed in the measured FRFs as can be noticed in Figure 2.4 and Figure 2.5. As shown by the dotted black line in Plot (b) of Figure 2.10, the spectrum of the harvested power is characterised by two additional sharp peaks at 267 Hz and

721 Hz where the harvested power is about 25 mW/1g and 3 mW/1g respectively, which, according to Plot (b) of Figure 2.9, are produced with resistive loads of $5.3 \times 10^3\ \Omega$ and $2.8 \times 10^3\ \Omega$ respectively. In this case the harvested power at the second resonance frequency is considerably lower than that harvested at the first resonance frequency. Thus, when a resistive real optimal load is implemented, it seems more practical setting the harvester to work in correspondence of its first resonance frequency only. In this case, the spectrum of the harvested power simulated from measured FRFs (dotted black line) is not characterised by the anomalies noticed in Plot (b) of Figure 2.8. Also in this case, on line experiments were implemented at specific frequencies for the harvested power when optimal resistors with resistances taken from Plot (b) of Figure 2.9 are connected to the seismic piezoelectric harvester shown in Figure 2.1 (d). As one can readily see from the red circles in Plot (b) of Figure 2.10, these measured power levels further confirm the validity of the proposed model for the constitutive FRFs of the transducer presented in Section 2.3 and Appendix B below 70 Hz while they indicate that the simulated result from measured FRFs provides a more accurate estimate of the harvested power at higher frequencies above 70 Hz. However, it should be noticed that there are some discrepancies at higher frequencies, which as discussed above, are probably due to the difficulty of measuring low levels of power, particularly in correspondence of the sharp antiresonance through at about 460 Hz. As already argued, this is merely due to the fact that the model considers only the fundamental flexural natural mode of the composite beam and tip mass, and thus it fails to reproduce the resonant contributions of higher order modes.

Plots (a) and (b) of Figure 2.10 show that also in this case the piezoelectric harvester outperforms the electromagnetic harvester in correspondence of the fundamental and higher order resonance frequencies although the electromagnetic harvester performs better at low frequencies below the fundamental resonance at about 20 Hz and at frequencies comprised between about 30 Hz and about 100 Hz.

2.8 INPUT POWER

The time averaged input power to the electromagnetic and piezoelectric harvesters is given by:

$$\bar{P}_i = \lim_{T\to\infty} \frac{1}{T}\int_0^T P_i(t)\mathrm{d}t\,, \tag{2.36}$$

where the instantaneous input power is given by:

$$P_i(t) = f_h(t)\dot{w}_h(t), \tag{2.37}$$

and, as specified in Figure 2.1 (c) and Figure 2.1 (f), $f_h(t)$, $\dot{w}_h(t)$ are the force and velocity at the base of the two seismic transducers. In this case, assuming time harmonic functions, the force at the base of the transducers can be derived from the first equation of the matrix expression in Eq.(2.1) assuming the current is given by Eq. (2.29) so that:

$$f_h = Z_{mh}\dot{w}_h, \tag{2.38}$$

where Z_{mh} is the base impedance of the seismic harvesters when the transducers are connected to the harvesting circuit characterised by the electrical impedance Z_h:

$$Z_{mh} = Z_{mi} - \frac{T_{ew}T_{fi}}{Z_{ei}+Z_h}. \tag{2.39}$$

Thus, for harmonic vibrations, the time average input power is derived from Eqs. (2.36) to (2.39) as follows:

$$\bar{P}_i = \frac{1}{2}\mathrm{Re}\{Z_{mh}\}|\dot{w}_h|^2 = \frac{1}{2}\mathrm{Re}\left\{Z_{mi} - \frac{T_{ew}T_{fi}}{Z_{ei}+Z_h}\right\}|\dot{w}_h|^2. \tag{2.40}$$

When the harvesting load implements the optimal complex impedance of Eq.(2.32), i.e. $Z_h = Z_{ei}^*$, the input power expression given above becomes:

$$\bar{P}_i = \frac{1}{2}\mathrm{Re}\left\{Z_{mi} - \frac{T_{ew}T_{fi}}{2\mathrm{Re}\{Z_{ei}\}}\right\}|\dot{w}_h|^2, \tag{2.41}$$

which, using the constitutive FRFs given in Eqs.(2.1)-(2.4) and the formulation presented in Section 2.3, can be specified respectively for the electromagnetic and piezoelectric seismic harvesters. Figure 2.11 shows the simulated spectra of the 10 Hz to 1 kHz power input per 1g base acceleration with the electromagnetic seismic

harvester i.e. Plot (a) and with the piezoelectric seismic harvester i.e. Plot (b) when the harvesting loads are characterised by the optimal complex impedance derived in Eq.(2.32), that is $Z_h = Z_{ei}^*$. Starting with the electromagnetic seismic harvester, when the harvesting circuit implements at each frequency the optimal complex impedance $Z_h = Z_{ei}^*$ depicted in Plot (a) of Figure 2.7, the power input to the transducer peaks in correspondence of its fundamental resonance frequency, i.e. 19.5 Hz, where it reaches a value of about 120 mW/1g, and then monotonically falls down with frequency. As found for the harvested power, the peak value at 19.5 Hz is controlled by the strong eddy currents damping effect that characterises the electromagnetic seismic transducer. The simulated spectra based on analytical expressions (solid blue line) and measurements (dotted black line) of the four constitutive FRFs, Z_{mi}, T_{fi}, T_{ew}, Z_{ei}, perfectly overlap up to about 250 Hz. At higher frequencies, there is an increasingly larger mismatch, which, as highlighted in Section 2.5, is due to higher order dynamic effects of the transducer occurring just above 1 kHz, which are not accounted in the model used to simulate the characteristic FRFs of the transducer.

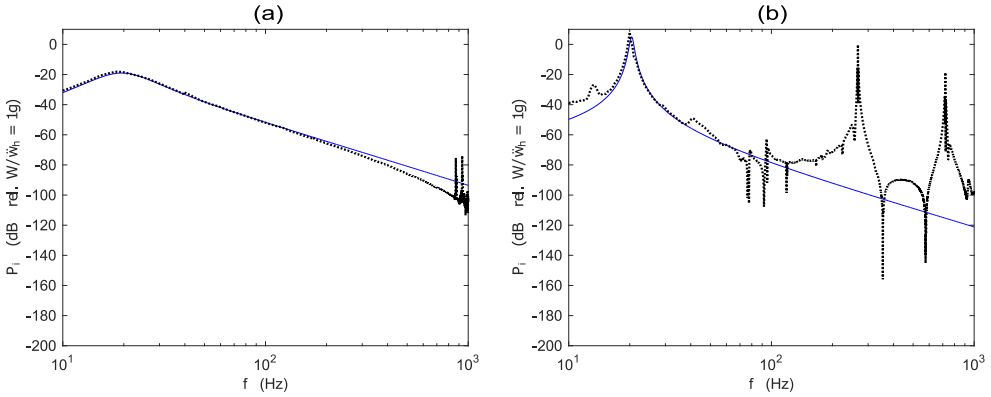

Figure 2.11: Spectra of the power input with reference to a 1g base acceleration for (a) the electromagnetic and (b) the piezoelectric seismic harvesters with optimal harvesting impedances $Z_h = Z_{ei}^*$ simulated using either the analytical expressions (solid blue lines) or the measurements (dotted black lines) of the four constitutive FRFs, Z_{mi}, T_{fi}, T_{ew}, Z_{ei}.

Moreover, the spectrum simulated using the measured constitutive FRFs (dotted black line) shows two sharp resonance peaks in the frequency band comprised between 800 and 1000 Hz, which, as discussed in Section 2.5, are probably due to local flexural natural modes of the two spiral springs that connect the outer ferromagnetic ring and coil assembly to the inner magnetic element of the transducer.

Moving to the piezoelectric seismic harvester, when the harvesting circuit implements at each frequency the optimal complex impedance $Z_h = Z_{ei}^*$ depicted in Plot (b) of Figure 2.7, the input power to the transducer peaks in correspondence of its fundamental resonance frequency, i.e. 20 Hz, where it reaches a value of about 1900 mW/1g. As found for the harvested power, the simulation result based on the analytical expressions of the four constitutive FRFs (solid blue line), monotonically falls down at higher frequencies. In contrast, the simulation result based on the measured constitutive FRFs (dotted black line), is characterised by two additional sharp resonance peaks at about 267 Hz and 721 Hz, where the input power reaches peak values of 700 mW/1g and 100 mW/1g. As discussed in the previous section, this mismatch is due to the fact that the analytical expressions for the constitutive FRFs Z_{mi}, T_{fi}, T_{ew}, Z_{ei} of the piezoelectric transducer derived in Section 2.3 and Appendix B do not take into account the effects of higher order flexural modes of the composite beam and tip block, which are instead part of the measured FRFs. As noted for the harvested power, the spectrum simulated from measured constitutive FRFs (dotted black line) is characterised by narrow drops or small crests anomalies, which are not related to antiresonance or resonance effects. On the contrary they arise from the calculus of power based on measured FRFs, which are affected by small errors in the real and imaginary parts, that is in the modulus and phase, which, as discussed in Ref. [196], produce the glitches observed in the dotted black spectrum.

To conclude this analysis, it is noted that the spectra of the input and harvested power by the electromagnetic seismic harvester shown in Plots (a) of Figure 2.11 and Figure 2.8 are quite similar to each other, except that, on average, the spectrum of the input power is relatively higher by about 11.2 dB. Likewise the spectra of the input and harvested power by the piezoelectric seismic harvester shown in Plots (b) of Figure 2.11 and Figure 2.8 also show similar features, with the spectrum of the input power being shifted up by about 8.7 dB. For both harvesters, the surplus of power input with respect to the power harvested is lost by the dissipative effects in the two seismic transducers.

When the harvesting electrical component is characterised by a purely resistive impedance such that according to Eq.(2.34) $Z_{h,R} = |Z_{ei}|$, the power input to the harvesters given by Eq.(2.40) becomes:

$$\bar{P}_i = \frac{1}{2}\mathrm{Re}\left\{Z_{mi} - \frac{T_{ew}T_{fi}}{Z_{ei} + |Z_{ei}|}\right\}|\dot{w}_h|^2. \tag{2.42}$$

As seen above, this expression can be specified for the electromagnetic and piezoelectric seismic harvesters by substituting in it the expressions for the constitutive FRFs given in Eqs.(2.2) - (2.5) derived from the expressions given in the formulation of Section 2.3.

Figure 2.12 shows the simulated spectra of the 10 Hz to 1 kHz power input per 1g base acceleration with the electromagnetic seismic harvester i.e. Plot (a) and with the piezoelectric seismic harvester i.e. Plot (b) when the harvesting circuits are characterised by the optimal real impedance given in Eq.(2.34), i.e. $Z_{h,R} = |Z_{ei}|$. Considering first the electromagnetic seismic harvester with the harvesting circuit implementing at each frequency the optimal real impedance $Z_{h,R} = |Z_{ei}|$ depicted in Plot (a) of Figure 2.9, the power input to the transducer reaches the maximum level of 120 mW/1g at its fundamental resonance frequency, i.e. 19.5 Hz, and then falls down monotonically with frequency. Again, this value is controlled by the high eddy currents damping effect that characterises this seismic transducer. Also in this case, the spectra simulated using the analytical expressions (solid blue line) and the measured (dotted black line) constitutive FRFs, Z_{mi}, T_{fi}, T_{ew}, Z_{ei}, closely overlap up to about 250 Hz. At higher frequencies, there is an increasingly larger mismatch, which, as highlighted above and in Section 2.5, are probably due to higher order dynamic effects of the transducer occurring just above 1 kHz, which are not accounted in the model for the constitutive FRFs.

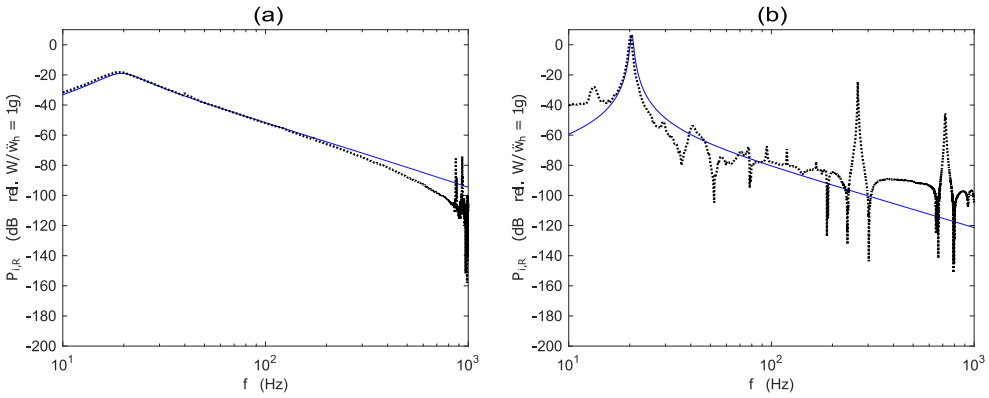

Figure 2.12: Spectra of the input power with reference to a 1g base acceleration for (a) the electromagnetic and (b) the piezoelectric seismic harvesters with optimal harvesting impedances $Z_{h,R} = |Z_{ei}|$ simulated using either the analytical expressions (solid blue lines) or the measurements (dotted black lines) of the four constitutive FRFs, Z_{mi}, T_{fi}, T_{ew}, Z_{ei}.

Also, between 800 and 1000 Hz, the spectrum simulated using the measured constitutive FRFs (dotted black line) shows the two sharp resonance peaks, which should be due to local flexural natural modes of the two spiral springs that connect the outer and inner components of the transducer.

Considering next the piezoelectric seismic harvester with the harvesting circuit implementing at each frequency the optimal real impedance $Z_{h,R} = |Z_{ei}|$ depicted in Plot (b) of Figure 2.9, the input power to the transducer reaches the maximum level of 2100 mW/1g in correspondence of the sharp resonance peak at 20 Hz. As noticed above and in the previous Section, at higher frequencies, the simulation result derived from the analytical expressions of the four constitutive FRFs (solid blue line), monotonically falls down. In contrast, the simulation result based on the measured constitutive FRFs (dotted black line) is characterised by two additional sharp resonance peaks at about 267 Hz and 721 Hz, where the input power reaches peak values of 58 mW/1g and 5 mW/1g. As seen above and in the previous section, this mismatch is due to the fact that the analytical expressions for the constitutive FRFs Z_{mi}, T_{fi}, T_{ew}, Z_{ei} derived in Section 2.3 and Appendix B neglects the effects of higher order flexural modes of the composite beam and tip block assembly. Finally, the spectrum simulated from measured constitutive FRFs (dotted black line) is rather irregular with many narrow drops and small crests, which, as noticed above and in the previous section, is due to fact that the FRFs used to simulate the power expression are characterised by small measurement errors [198].

In conclusion, as noticed above, the spectra of the input and harvested power by either the electromagnetic or the piezoelectric harvesters, shown respectively in Plots (a) and in Plots (b) of Figure 2.10 and Figure 2.12, are quite similar to each other, except that, the level of the spectrum of the input power is shifted up 11.2 dB for the piezo and 15.6 dB for the coil magnet. Again, the surplus of power input with respect to the power harvested is lost by the mechanical and electrical dissipative effects in the two seismic transducers.

2.9 EFFICIENCY

To fully characterise how well the electromagnetic and the piezoelectric seismic harvesters convert the input power to harvested power the following efficiency ratio is considered in this section:

$$E = \frac{\bar{P}_h}{\bar{P}_i}, \tag{2.43}$$

where $\bar{P}_h$ and $\bar{P}_i$ are given in Eqs. (2.30) and (2.40) respectively such that:

$$E = \frac{\mathrm{Re}\{Z_h\}\left|-\frac{T_{ew}}{Z_{ei}+Z_h}\right|^2}{\mathrm{Re}\left\{Z_{mi}-\frac{T_{ew}T_{fi}}{Z_{ei}+Z_h}\right\}}. \tag{2.44}$$

When the two harvesters are set to implement the harvesting load with either the optimal complex impedance, $Z_{h,} = Z_{ei}^*$, or the optimal real impedance, $Z_{h,R} = |Z_{ei}|$, the above expression for the efficiency becomes respectively:

$$E = \frac{1}{4}\frac{|T_{ew}|^2}{\mathrm{Re}\{Z_{ei}\}\mathrm{Re}\left\{Z_{mi}-\frac{T_{ew}T_{fi}}{2\mathrm{Re}\{Z_{ei}\}}\right\}}, \tag{2.45}$$

$$E_R = \frac{1}{2}\frac{\frac{|T_{ew}|^2}{|Z_{ei}|+Re\{Z_{ei}\}}}{Re\left\{Z_{mi}-\frac{T_{ew}T_{fi}}{Z_{ei}+|Z_{ei}|}\right\}}. \tag{2.46}$$

Figure 2.13 and Figure 2.14 show the simulated spectra of the 10 Hz to 1 kHz efficiency when the electromagnetic seismic harvester i.e. Plot (a) and piezoelectric seismic harvester i.e. Plot (b) are connected to harvesting loads that implement respectively the optimal complex impedance $Z_h = Z_{ei}^*$ and the optimal real impedance $Z_{h,R} = |Z_{ei}|$. Plots (a) in Figure 2.13 and Figure 2.14 show that the spectra of the efficiency for the electromagnetic seismic harvester simulated from analytical FRFs expressions (solid blue lines) and measured FRFs (dotted black lines) satisfactorily overlap up to about 171 Hz. At higher frequencies the efficiency simulated from measured FRFs (dotted black lines) becomes inaccurate because of the bias errors in the calculation of the harvested and input power with the measured FRFs, which are then magnified in the calculus of the efficiency power ratio. This problem is even more relevant in the spectra of the efficiency for the piezoelectric seismic harvester shown in Plots (b) of Figure 2.13 and Figure 2.14. Indeed, the spectra simulated from analytical FRFs expressions (solid blue lines) are characterised by a smooth continuous lines. In contrast, the spectra simulated from measured FRFs (dotted black lines) are characterised by segmented lines, which, actually, do not accurately overlap with the solid blue lines. As can be noticed in the four Plots of

Figure 2.4 and Figure 2.5, the measured FRFs (dotted black lines) used to calculate the harvested and input power are characterised by additional resonance peaks and antiresonance troughs. Although these FRFs graphically looks well defined, after a careful analysis, it was noticed that they are characterised by bias errors in most of the 8 Hz to 1 kHz frequency range, which affect the calculus of the harvested and input power and thus leads to significant errors in the calculus of the efficiency power ratios.

Considering now the configuration with the optimal complex impedance load shown in Figure 2.13, as depicted in Plot (a), the electromagnetic seismic harvester is characterised by a somewhat constant efficiency of about 28% over the whole frequency range up to 1 kHz. In contrast, according to Plot (b), the efficiency of the piezoelectric seismic harvester is independent to the frequency and equal at about 33%. Moving to the configuration with the optimal real impedance load shown in Figure 2.14, Plot (a) indicates that the efficiency of the electromagnetic seismic harvester is still equal to 28% at low frequencies up to about 19.5 Hz and then gradually falls down such that, at 1 kHz, it is about 22%.

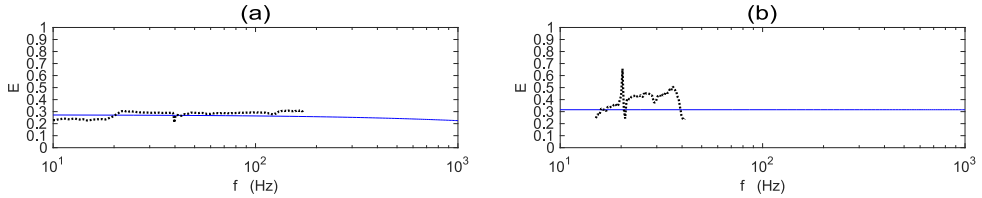

Figure 2.13: Spectra of the efficiency for (a) the electromagnetic and (b) the piezoelectric seismic harvesters with the optimal harvesting impedances $Z_h = Z_{ei}^*$ simulated using either analytical expressions (solid blue line) or the measurements (dotted black line).

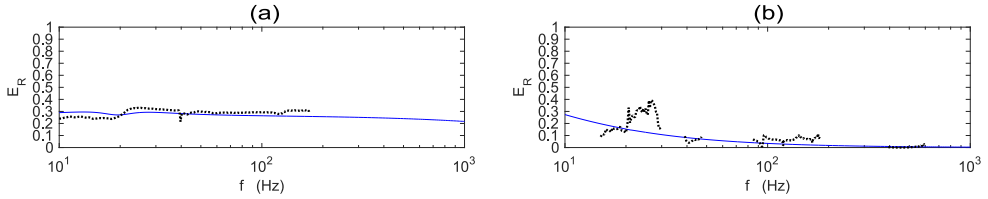

Figure 2.14: Spectra of the efficiency for (a) the electromagnetic and (b) the piezoelectric seismic harvesters with an optimal harvesting impedances $Z_{h,R} = |Z_{ei}|$ simulated using either analytical expressions (solid blue line) or the measurements (dotted black line).

Plot (b) shows instead that the efficiency of the piezoelectric seismic harvester drops proportionally to frequency and, at the fundamental resonance frequency of the transducer, is equal to about 17%. In particular, the efficiencies of the electromagnetic and piezoelectric seismic harvesters at the transducers fundamental resonance frequency result respectively 28% and 33%, for the optimal complex loads, and respectively 28% and 17%, for the optimal real (resistive) loads. These results indicate that, when the optimal complex impedance harvesting load is implemented, the piezoelectric harvester is more efficient than the electromagnetic harvester to convert the input power into the harvested power. Instead, when the optimal real impedance harvesting load is implemented, the electromagnetic harvester results more efficient that the piezoelectric harvester. These results are however specific to the transducers considered in this study. For instance, if the high eddy currents loss that affects the electromagnetic harvester was annihilated, considering the results presented in Appendix A, the efficiency for the real harvesting load would rise to 42%, thus well above the 28% found for the electromagnetic harvester considered in this study. This suggests that the inherent damping effects in the two seismic transducers play a key role in the conversion of the input mechanical power into harvested electrical power. In particular, the efficiency and thus the energy harvesting of the electromagnetic harvester can be greatly improved if the seismic transducer is carefully designed in such a way as to minimise the effects of eddy currents.

2.10 STROKE

As discussed by Stephen [86], the energy harvesting property of a seismic harvester should also be analysed with reference to the maximum stroke allowed by the transducer, that is the maximum relative displacement between the seismic mass and the base mass. The results derived above assume the harvester can withstand any stroke. In practice, this is not the case, since, for large displacements of the base mass, the relative motion of the seismic mass may reach saturation points. For the electromagnetic seismic harvester, this effect is due to non-linear stiffening of the spiral springs or to the presence of end stops that limit large oscillations of the suspended ferromagnetic ring and coil assembly. Alternatively, for the piezoelectric seismic harvester, this effect is due to the non-linear increase in bending stiffens of the beam laminated for large oscillations of the tip mass. Thus, to fully characterise

the energy harvesting with the two systems considered in this paper, the strokes of the electromagnetic and piezoelectric seismic transducers are now considered. Inspection of the lumped parameter element scheme in Figure 2.1 (g) leads to the following equation of motion for the seismic mass and Kirchhoff equation for the electric mesh of the transducers:

$$Z_t(\dot{w}_m - \dot{w}_h) = -Z_m\dot{w}_h + \Psi_{fi}i_h, \tag{2.47}$$

$$e_h = Z_e i_h - \Psi_{ew}(\dot{w}_m - \dot{w}_h). \tag{2.48}$$

Also, according to the notation shown in the scheme in Figure 2.6, the following relation holds for the impedance of the harvesting load:

$$e_h = -Z_h i_h. \tag{2.49}$$

After some mathematical manipulations the three Eqs.(2.47), (2.48) and (2.49) give the following relation for the transducer stroke per unit base displacement

$$\frac{w_m - w_h}{w_h} = -\frac{Z_m}{Z_t - \dfrac{\Psi_{fi}\Psi_{ew}}{Z_e + Z_h}}. \tag{2.50}$$

Figure 2.15 and Figure 2.16 show the simulated (solid blue lines) and simulated from measured FRFs (dotted black lines) strokes per unit base displacement of the two transducers, respectively when they are connected to the optimal complex impedance load given in Eq.(2.32) (Figure 2.7) and when they are connected to the optimal real impedance load given in Eq.(2.34) (Figure 2.9). The graphs based on measured FRFs were obtained considering the reciprocal of Eq.(2.50), which is given by the following expression: $\frac{w_h}{w_m - w_h} = -\frac{Z_t}{Z_m} + \frac{\Psi_{fi}\Psi_{ew}}{Z_m(Z_e + Z_h)}$. The first term in this expression was derived from direct measurement of the stroke per unit base displacement when the transducers are in open circuit, which corresponds to $Z_h = \infty$, such that $H_{\mathrm{oc}} = \frac{w_m - w_h}{w_h}|_{Z_h=\infty} = -\frac{Z_m}{Z_t}$. The second term was derived from direct measurement of the electric impedance Z_e, assuming the relative motion of the transducer seismic and base masses is blocked, i.e. $w_m - w_h = 0$. Also, the impedances of the optimal harvesting loads were obtained from Eq.(2.32) and Eq.(2.34) using the measured electrical impedance Z_{ei}. The impedance of the seismic mass Z_m and the product of the transduction coefficients $\Psi_{fi}\Psi_{ew}$ were instead derived from Eqs. (2.6) and (2.14),

(2.15), (2.17), (2.18) using measured constants. In summary, the stroke per unit base displacement from measured FRFs was simulated using the following relation:

$$\frac{w_m - w_h}{w_h} = \frac{1}{\frac{1}{H_{\mathrm{oc}}} + \frac{\Psi_{fi}\Psi_{ew}}{Z_m(Z_e + Z_{h)}}}, \tag{2.51}$$

where H_{oc}, Z_e, Z_h resulted from measured FRFs and Z_m Ψ_{fi}, Ψ_{ew} where calculated from Eqs.(2.6) and (2.14), (2.15), (2.17), (2.18) using parameters identified experimentally.

Figure 2.15 and Figure 2.16 show similar graphs for the spectra of the strokes per unit base displacement of the electromagnetic and piezoelectric seismic harvesters. As anticipated in the discussion of the base impedance FRFs presented in Section 2.5, at very low frequencies the base and seismic masses move together such that the stroke is small. However, as the frequency rises towards the fundamental resonance frequency of the transducers, the two masses increasingly move out of phase such that the stroke progressively rise to a peak value. At higher frequencies the amplitude of the seismic mass displacement progressively drops toward zero so that the stroke tends to be equal to the imposed base displacement. The spectra simulated from analytical FRFs expressions (solid blue lines) and measured FRFs (dotted black lines) perfectly overlap in the whole frequency range. The spectra simulated from measured FRFs for the piezoelectric seismic harvester show additional resonance peaks and antiresonance troughs due to the higher order bending modes of the composite beam and tip mass assembly, which are not modelled in the analytical FRFs. The amplitude of these peaks is however much smaller than that of the peak at the fundamental resonance frequency of the transducer and thus do not influence the operation of the harvester. Contrasting Plots (a) with Plots (b) in Figs. 2.15 and 2.16, it can be noticed that the peak stroke per unit base displacement of the piezoelectric seismic transducer is respectively 15 and 20 times greater than that of the electromagnetic transducer. As discussed in Section 2.5, this is due to the higher damping effect produced by the air in the gap between the magnet and the coil and by the eddy currents that develop in the cylindrical ferromagnetic ring element.

As pointed out by Stephen [86], the peak amplitude of the stroke plays an important role in the functioning of seismic harvesters. Indeed, the results presented in the previous section are valid only for limited ranges of base vibrations such that the resulting strokes do not reach the saturation limits. For instance, assuming the

electromagnetic and piezoelectric seismic harvesters considered in this study are operated at their fundamental resonance frequency where the stroke is maximum, the electromagnetic harvester can be effectively used for relatively higher amplitude base vibrations, whereas the piezoelectric harvester is more suitable for low amplitude base vibrations. If instead the harvesters are operated at frequencies above their fundamental resonance frequency there is no substantial difference in using the two harvesters, which actually can withstand base vibrations with amplitude close to their maximum allowed stroke before saturation.

These aspects suggest that the results produced in Section 2.7 for the harvested power should be analysed also with respect to the stroke of the transducers. For instance, if the peak value of the energy harvested is normalised with respect to the stroke of the transducer at the fundamental resonance frequency of the two transducers, the following conclusions would be drawn. First, when the harvesters implement the complex impedance load, the electromagnetic harvester would produce $30\,\frac{\mathrm{m}W}{\mathrm{mm}}$ whereas the piezoelectric seismic harvester would generate $5\,\frac{\mathrm{m}W}{\mathrm{mm}}$. Alternatively, when the harvesters implement the real (resistive) impedance load, the electromagnetic harvester would still produce $30\,\frac{\mathrm{m}W}{\mathrm{mm}}$ whereas the piezoelectric seismic harvester would generate $1.3\,\frac{\mathrm{m}W}{\mathrm{mm}}$. If the outer ferromagnetic ring of the electromagnetic seismic transducer was not affected by eddy currents, as discussed in Appendix B.2.1, the transducer would be less damped and the stroke per unit base displacement would rise by 3.8 times. As a result the electromagnetic harvester would produce $12\,\frac{\mathrm{m}W}{\mathrm{mm}}$. Therefore, the peak value of the harvested power with respect to stroke results greater for the electromagnetic seismic transducer both with the complex and real impedance harvesting loads.

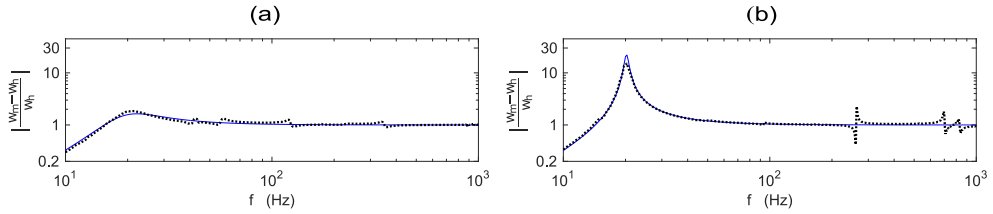

Figure 2.15: Stroke per unit base displacement of the (a) electromagnetic and (b) piezoelectric seismic harvesters with the optimal complex harvesting impedances $Z_h = Z_{ei}^*$. Simulated (solid blue line) and simulated using measured impedances (dotted black line).

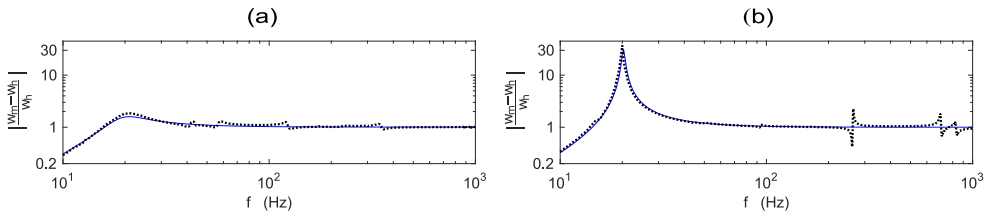

Figure 2.16: Stroke per unit base displacement of the (a) electromagnetic and (b) piezoelectric seismic harvesters with the optimal real (resistive) harvesting impedances $Z_{h,R} = |Z_{ei}|$. Simulated (solid blue line) and simulated using measured impedances (dotted black line).

Similar considerations can be made also for the input power per unit strokes of the transducers. The efficiency can then be calculated with reference to the maximum stroke of the transducers. For instance, when the harvesters implement the complex impedance load, the electromagnetic and piezoelectric harvesters would absorb respectively 110 $\frac{\mathrm{m}W}{\mathrm{mm}}$ and 14 $\frac{\mathrm{m}W}{\mathrm{mm}}$. Alternatively, when the harvesters implement the real (resistive) impedance load, the two harvesters would absorb respectively 110 $\frac{\mathrm{m}W}{\mathrm{mm}}$ and 8 $\frac{\mathrm{m}W}{\mathrm{mm}}$. If the outer ferromagnetic ring of the electromagnetic seismic transducer was not affected by eddy currents, the electromagnetic harvester would absorb 30 $\frac{\mathrm{m}W}{\mathrm{mm}}$. Therefore, the efficiency at the resonance frequency of the electromagnetic and piezoelectric seismic transducers calculated with respect to the stroke of the two harvesters would result respectively equal to 27% and 36% for complex impedance loads and to 27% and 15% for the real impedance loads. Actually, if the electromagnetic seismic transducer was not affected by eddy currents, the efficiency would rise to 40%. These results indicate that, with reference to stroke, the piezoelectric harvester is more efficient to convert the mechanical power into electrical harvested power when the complex impedance harvesting load is implemented whereas the electromagnetic harvester is more efficient when the real impedance harvesting load is implemented, particularly if the eddy currents losses were annihilated.

3

REACTIVE VIBRATION HARVESTERS

Seismic harvesters can be effectively used in applications where there is no body or system the transducer can be reacted off. However, as highlighted in the previous Chapter, these harvesters effectively work in narrow frequency bands centred at their fundamental natural frequencies. Therefore, whenever there is access to a relative motion or a strain deformation in the ambient, it is preferable to use reactive harvesters, where indeed the transducer is reacted off the components of the vibrating body or system. As discussed in Refs. [1], [199] and documented below, reactive harvesters are particularly effective at low frequencies. Therefore they effectively complement seismic harvesters, which instead tend to work at higher frequencies in correspondence to their fundamental resonance frequencies. Practical applications of reactive harvesters include machine tools, railway tracks, buildings, power generating floors, human activities (foot motion), etc. [199].

The aim of this chapter is thus to present a theoretical and experimental study contrasting the constitutive equations and the energy harvesting properties of two reactive vibration energy harvesting devices. The study considers coil-magnet and piezoelectric cantilever beam reactive harvesters, which as shown in Figure 3.1 (a, d) were obtained from the seismic harvesters considered in Chapter 2 by clamping the inertial moving parts, i.e. the housing Yoke and coil assembly and the tip block mass respectively.

3.1 REACTIVE TRANSDUCERS

When the Yoke - coil assembly and the tip mass respectively of the electromagnetic and piezoelectric prototypes shown respectively in Figure 2.1 (a) and Figure 2.1 (b) are clamped on a rigid frame structure, the resulting reactive transducers can be idealised as shown in the pictures (b, e) and schematics (c, f) of Figure 3.1.

As indicated in picture 3.1 (b), the electromagnetic reactive transducer is composed by a coil–magnet, with the magnet mounted via soft spiral springs and the coil rigidly fixed to the case, which is clamped to a rigid host structure. The relative motion between the magnet and the fixed coil produces a back electromotive force, i.e. a voltage, at the terminals of the coil; vice versa, a current flow in the coil generates reactive forces on the magnetic and on the coil-armature elements.

Table 3-1: Parameters of the coil magnet harvester.

Parameters	Value
Base mass and volume (inner magnet)	$m_b = 115 \times 10^{-3}$ kg $V_b = 1.206 \times 10^{-5}\ m^3$
Spiral springs equivalent stiffness	$k_m = 2777$ N/m
Fundamental natural frequency	$f_n = 25.4$ Hz
Viscous damping coefficient/ratio	$c_a = 2.15$ Ns/m $\xi_a = 0.05$
Eddy current damping coefficient/ratio	$c_{ec} = 7.37$ Ns/m $\xi_{ec} = 0.16$
Equivalent damping coefficient/ratio	$c_m = 9.52$ Ns/m $\xi_m = 0.21$
Electromagnetic transduction factor	$\psi_{CM} = 22.5$ N/A
Coil resistance	$R_e = 22\ \Omega$
Coil lossy inductance constant - exponent	$K_e = 0.034$ $n = 0.78$
Coil lossy inductance loss factor	$\eta_L = 0.36$

Table 3-2: Parameters of the piezoelectric harvester.

Parameters	Value
Base mass and volume	$m_{bl} = 126 \times 10^{-3}$ kg $V_b = 1.76 \times 10^{-5}\ m^3$
Transducer total mass and total volume	$m_{PZT} = 174 \times 10^{-3}$ kg $V_{PZT} = 2.39 \times 10^{-5}\ m^3$
Equivalent proof mass	$m_b = 134.5 \times 10^{-3}$ kg
Equivalent stiffness with the piezo-electrodes in short circuit	$k_m = 10360$ N/m
Additional equivalent stiffness with piezo-electrodes in open circuit	$\Delta k = 48.7$ N/m
Fundamental natural frequency (short circuit)	$f_n = 44.2$ Hz
Equivalent viscoelastic damping coefficient and ratio	$c_m = 0.59$ Ns/m $\xi_m = 0.008$
Equivalent piezoelectric transduction factor	$\psi_{PZT} = -0.0029$ N/V
Capacitance of the two piezoelectric layers	$C_e^T = 1.68 \times 10^{-7}$ F

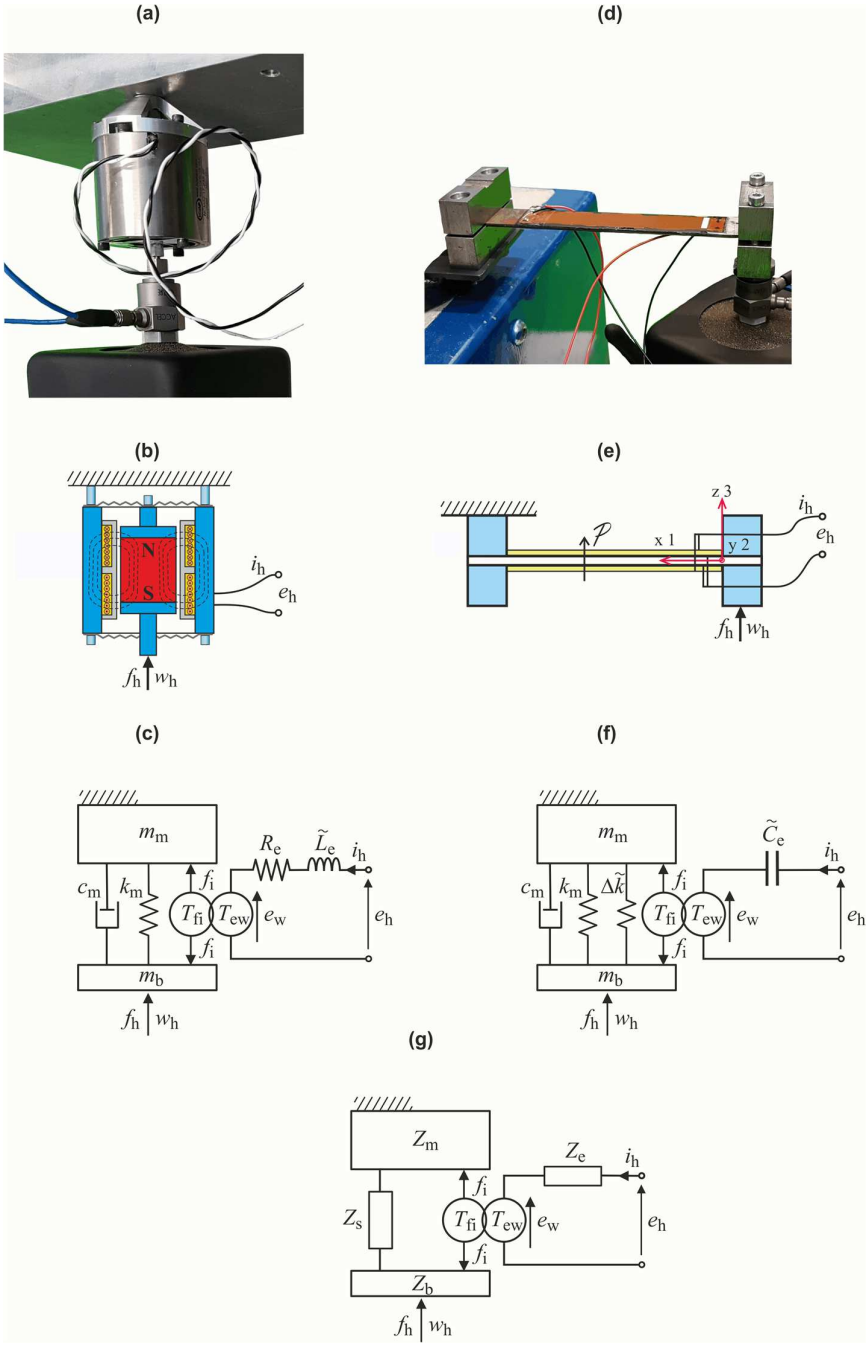

Figure 3.1: Pictures (a,d), functional drawings (b,e) and lumped parameter schematics (c,f), for the electromagnetic (left hand side) and piezoelectric (right hand side) reactive transducers. Common equivalent lumped parameter schematic for the two reactive transducers (g).

As shown in picture 3.1 (e), the piezoelectric reactive harvester is composed by a thin beam with one end clamped to a fixed housing structure and the other moving end is equipped with a tip block mass. The beam is equipped on the top and bottom side with two rectangular piezoelectric patches connected in parallel. In this case, the relative motion between the housing structure and the tip mass produces a bending strain of the cantilever beam, which, in turn, produces a separation of electric charge in the electrodes of the piezoelectric patches. Alternatively, a bending strain effect is produced on the cantilever beam when a voltage is applied at the terminals of the piezoelectric patches. The two models in Figure 3.1 (c, f) are characterised by a lumped parameter mechanical schematic and an electrical mesh with lumped electric components. These two parts are joined via a *current-controlled force generator* and an *absolute velocity-controlled voltage generator* that exemplify the electromechanical transduction effects. Assuming the mechanical parts move as a single degree of freedom system, the dynamic responses of the electromagnetic and piezoelectric reactive transducers can be derived straightforwardly from the equivalent lumped parameter models of the reactive transducers, as shown in Plot (g) of Figure 3.1 and as described respectively in Appendix C.1 and Appendix C.2. The list of the electro-mechanical components (weights, stiffness, resistance, inductance, capacitance, transduction coefficient) for the two reactive harvesters are summarized in Table 3-1 and Table 3-2. The missed data can be found in Table 2-1 and Table 2-2.

3.2 LUMPED PARAMETER MODELS

Considering first the electromagnetic transducer, as shown in Figure 3.1 (c) the mechanical part is modelled with a base moving mass (inner magnet) connected to the host structure via soft (spiral) springs and a damper with in parallel a *current reactive force generator*. As discussed in Chapter 2 and Appendix A, the damper takes into account the effects of both air and eddy current losses. *A velocity-controlled voltage generator*, whose strength is proportional to the absolute velocity between the moving base and the fixed case composes the electrical part. This voltage generator is connected in series to a resistor and a (lossy) inductor.

As shown in Figure 3.1 (f), the piezoelectric reactive transducer is modelled with a base moving mass connected to a rigid host structure via a spring (beam modal bending stiffness) and damper with in parallel a *current-controlled reactive force*

generator. As discussed in Chapter 2 and Appendix B, the damper takes into account the effects air and material losses with a Kelvin-Voight viscoelastic damping model. *A velocity-controlled voltage generator*, whose strength is proportional to the absolute velocity between the moving base and the fixed host structure composes the electrical part. A lossy capacitor is connected in series to the voltage generator ([180], [181], [182], [183]).

Similarly to the electromagnetic seismic transducer, the mechanical and electrical scheme for the coil–magnet reactive harvester were derived straightforwardly from inspection of the system shown in Figure 3.1 (a). Instead, moving to the reactive piezoelectric transducer, the mechanical scheme and electrical mesh required the derivation of the flexural response of the beam considering only the contribution of the first flexural natural mode of the assembly beam laminate. Contrary to the seismic harvester model shown in Figure 2.1 (d) and derived in Appendix B, the lumped parameter model shown in the schematic of Figure 3.1 (f) does not require the introduction of a virtual displacement $\bar{x}$ for the equivalent proof mass because in this case the cantilever beam is not excited by its inertia. Thus the reference point of the moving base mass corresponds to the free end of the beam.

The mechanical and the electrical parts of the two schematics in Figs. 3.1 (c) and 3.1 (f) present identical topologies. Therefore, the constitutive equations, which identify the dynamic response of the two transducers and the energy formulation for the power harvested can be derived in the following sections with reference to the schematic shown in Fig. 3.1 (g).

3.3 CONSTITUTIVE EQUATIONS

The constitutive equations for the two reactive transducers are here recalled using the unified formulation derived in Chapter 2 for the two seismic transducers. Thus considering time-harmonic vibrations described in complex form as $f(\mathrm{t}) = \mathrm{Re}\{f(\omega)\exp(\mathrm{j}\omega t)\}$, where $f(\omega)$ is the complex amplitude of the function, ω is the circular frequency and $\mathrm{j} = \sqrt{-1}$, the constitutive equations for the electromechanical response of the two reactive transducers have been derived with the following matrix formulation:

$$\begin{bmatrix} f_h \\ e_h \end{bmatrix} = \begin{bmatrix} Z_{mi} & T_{fi} \\ T_{ew} & Z_{ei} \end{bmatrix} \begin{bmatrix} \dot{w}_h \\ i_h \end{bmatrix}, \tag{3.1}$$

where, f_h, $\dot{w}_h$ are the complex amplitudes of the force and velocity at the base of the reactive transducers and e_h, i_h are the complex amplitudes of the voltage and current across the terminals of the reactive transducers. The mechanical and electrical impedance FRFs and the two-electromechanical transduction FRFs are in this case given by:

$$Z_{mi} = \left.\frac{f_h}{\dot{w}_h}\right|_{i_h=0} = Z_b + Z_s, \tag{3.2}$$

$$T_{fi} = \left.\frac{f_h}{i_h}\right|_{\dot{w}_h=0} = \Psi_{fi}, \tag{3.3}$$

$$T_{ew} = \left.\frac{e_h}{\dot{w}_h}\right|_{i_h=0} = \Psi_{ew}, \tag{3.4}$$

$$Z_{ei} = \left.\frac{e_h}{i_h}\right|_{\dot{w}_h=0} = Z_e, \tag{3.5}$$

where

$$Z_b = \mathrm{j}\omega m_b. \tag{3.6}$$

Also, for the coil-magnet transducer

$$Z_e = R_e + \mathrm{j}\omega \tilde{L}_e, \tag{3.7}$$

$$Z_s = \frac{k_m}{\mathrm{j}\omega} + c_m, \tag{3.8}$$

while for the piezoelectric transducer

$$Z_e = \frac{1}{\mathrm{j}\omega \tilde{C}_e^S}, \tag{3.9}$$

$$Z_s = \frac{\tilde{k}_m'}{\mathrm{j}\omega} + c_m. \tag{3.10}$$

In analogy to the seismic transducers, the term m_b is the base mass, k_m is the suspension stiffness and $c_m = c_a + c_{ec}$ is the equivalent damping coefficient composed by two terms 1) air damping c_a and 2) eddy current damping c_{ec} [174],

[175], [176]. Also, R_e is the coil resistance and $\tilde{L}_e$ is the coil lossy inductance [177]–[179], identified by $\tilde{L}_e = K'_e(1 - \mathrm{j}\eta_L)$, where η_L is the inductive loss factor. Also, $K'_e = \sin(n\pi/2)K_e\omega^{n-1}$ and $\eta_L = \cos(n\pi/2)/\sin(n\pi/2)$, where the constants K_e and n reported in Table 3-1 were identified from the measured spectra of the electric impedance Z_{ei} of the electromagnetic device. Moving to the piezoelectric reactive transducer, m_b is the equivalent proof mass of the beam laminate and tip mass assembly and c_m is the equivalent viscoelastic damping coefficient. Also the stiffness is composed by two terms $\tilde{k}'_m = k_m + \Delta\tilde{k}$, where k_m and $\Delta\tilde{k}$ are the beam laminate and tip mass assembly equivalent stiffness when the electrodes are respectively in short and in open circuit. The additional stiffness $\Delta\tilde{k} = K_{pe}\frac{\tilde{k}_{31}^2}{1-\tilde{k}_{31}^2}$ is a complex term that includes also the effects of dielectric losses in the piezoelectric material. Here K_{pe} is a stiffness term equal to $K_{pe} = \frac{\psi_{pzt}^2}{\tilde{C}_e^T\tilde{k}_{31}^2}$ and $\tilde{k}_{31}^2 = k_{31}^2/(1 - \mathrm{j}\eta_C)$, with k_{31}^2 the electromechanical coupling factor of the piezoelectric material [184] and $\eta_c(\omega) \cong \sigma_{pe}/(\bar{\varepsilon}_{33}^T\omega)$ the frequency dependent dielectric loss factor of the material, identified by the permittivity of the piezoelectric material in transverse direction under constant stress $\bar{\varepsilon}_{33}^T$ and on the electrical conductivity of the piezoelectric material σ_{pe} [180]–[183]. Also, $\tilde{C}_e^S = \tilde{C}_e^T\left(1 - \tilde{k}_{31}^2\right)$ and $\tilde{C}_e^T = 2\bar{\varepsilon}_{33}^T\frac{bL}{h_{pe}}(1-\mathrm{j}\eta_C)$ are the lossy capacitances of the two piezoelectric layers respectively under constant strain, i.e. $S_1 = 0$, and under constant stress, i.e. $T_1 = 0$ [58]. Finally, the electromechanical coupling coefficients for the electromagnetic reactive transducer are given by:

$$\Psi_{fi} = \frac{f_i}{i_h} = \psi_{CM}, \tag{3.11}$$

$$\Psi_{ew} = \frac{e_w}{\dot{w}_h} = -\psi_{CM}, \tag{3.12}$$

where f_i is the reactive force produced on the coil and on the magnet components, i_h is the current which flows trough the coil wire and $\dot{w}_h$ is the absolute velocity of the magnet. Also:

$$\psi_{CM} = Bl, \tag{3.13}$$

is the electromagnetic transduction factor, where B is the magnetic flux density in the air gap between the coil and the magnet and l is the length of the winding [184]–[186], [188]. Besides, for the piezoelectric reactive harvester:

$$\Psi_{fi} = \frac{f_i}{i_h} = -\frac{\psi_{PZT}}{\mathrm{j}\omega \tilde{C}_e^S}, \tag{3.14}$$

$$\Psi_{ew} = \frac{e_w}{\dot{w}_r} = -\frac{\psi_{PZT}}{\mathrm{j}\omega \tilde{C}_e^S}, \tag{3.15}$$

where as discussed in Appendix C, ψ_{PZT} is the equivalent piezoelectric transduction factor for the bending strain produced by the first natural mode of the clamped beam laminated:

$$\psi_{PZT} = \bar{e}_{31} b\left(h_s + h_{pe}\right) \frac{\phi_1'(L)}{\phi_1(L)}. \tag{3.16}$$

Here, $\phi_1(L)$ and $\phi_1'(L) = \left.\frac{\mathrm{d}\phi_1(x)}{\mathrm{d}x}\right|_{x=L}$ are the amplitude and slope of the first flexural mode of the clamped composite beam calculated at tip mass assembly. Furthermore, $\bar{e}_{31}$ is the stress/charge constant for the piezoelectric material derived with reference to Euler–Bernoulli beam model (Appendix B), b is the width of the metallic substrate and piezoelectric layers and h_s, h_{pe} are the thickness of the metallic substrate and piezoelectric layers respectively. According to Hunt's notation [185], the transduction coefficients in Eqs.(3.11), (3.12) and (3.14), (3.15) should read: Ψ_{fi} force per current and Ψ_{ew} electromotive force per base velocity. Thus, the Ψ_{fi} coefficient gives the reactive force exerted to the base moving mass per unit current flowing in the transducer while the Ψ_{ew} coefficient gives the electric voltage generated at the terminals of the transducer per unit velocity of the moving base mass. The transduction coefficients for the electromagnetic reactive harvester assembly are given by real values with opposite signs: $\Psi_{fi} = \psi_{CM}$ and $\Psi_{ew} = -\psi_{CM}$. Instead, the transduction coefficients without piezoelectric losses for the piezoelectric layers are given by two equal positive imaginary frequency dependent values $\Psi_{fi} = \Psi_{ew} = -\frac{\psi_{PZT}}{\mathrm{j}\omega C_e^S}$. As already mentioned for the seismic harvesters, also the piezoelectric transduction for the reactive transducer occurs via strain rather than strain rate [184]–[186], [188]. Thus, since the formulation introduced above refers to strain rate i.e. absolute velocity of the base mass in the lumped parameter model, the piezoelectric transduction coefficients are characterised by a $1/(\mathrm{j}\omega)$ factor.

The T_{fi} and T_{ew} FRFs in Eq.(3.1) are the electromechanical transduction frequency response functions for both reactive transducers, which give the force effect produced by the transducer per unit current flowing in the blocked reactive devices, i.e. $T_{fi} =$

$f_h/i_h|_{\dot{w}_h=0}$ and the electric voltage generated at the terminals of the transducer per unit velocity of the open circuit reactive device i.e. $T_{ew} = e_h/\dot{w}_h|_{i_h=0}$. Finally, $Z_{ei} = e_h/i_h|_{\dot{w}_h=0}$ is the output electrical impedance of the blocked reactive transducer while $Z_{mi} = f_h/\dot{w}_h|_{i_h=0}$ is the input mechanical impedance of the open circuit reactive transducer.

3.4 PRINCIPAL PROPERTIES OF THE TWO TRANSDUCERS

For both transducers, the constitutive equations given in Eq. (3.1) can be rearranged in the matrix expressions of Eqs.(3.17), (3.18), where $Z_t = Z_b + Z_s$. As seen for the inertial transducers, these two equations specify that the electromagnetic reactive transducer is *skew–symmetric*, while the piezoelectric reactive transducer is *symmetric*, where the *skew-symmetry* or *symmetry* depends on the algebraic sign of the transduction coefficients, which are respectively opposite for the first and equal for the second:

$$\begin{bmatrix} f_h \\ e_h \end{bmatrix} = \begin{bmatrix} Z_t & \psi_{CM} \\ -\psi_{CM} & Z_e \end{bmatrix} \begin{bmatrix} \dot{w}_h \\ i_h \end{bmatrix}, \tag{3.17}$$

$$\begin{bmatrix} f_h \\ e_h \end{bmatrix} = \begin{bmatrix} Z_t & -\dfrac{\psi_{PZT}}{\mathrm{j}\omega \tilde{C}_e^S} \\ -\dfrac{\psi_{PZT}}{\mathrm{j}\omega \tilde{C}_e^S} & Z_e \end{bmatrix} \begin{bmatrix} \dot{w}_h \\ i_h \end{bmatrix}. \tag{3.18}$$

As highlighted for the seismic transducers, the sign reversal in the electromechanical transduction FRFs of the electromagnetic reactive device arises from the sign convention used to define the positive directions of the physical variables and from the definition of the independent variables used in Eq.(3.17), [189].

In contrast to seismic harvesters, the Z_t second order term is not present in the two transduction FRFs for the reactive harvesters and thus no magnitude amplification is observable in the energy conversion. Moving to the mechanical and electrical FRFs, the electrical impedance is only characterised by the electrical lumped elements of the transducers and thus is not affected by electromechanical-coupling contributions. Also, for the coil magnet, the mechanical FRF is determined only by the mechanical resonant response of the reactive transducer. Instead, for the piezoelectric device, the mechanical FRF is characterised also by a back electromechanical stiffness effect $\Delta\tilde{k}$.

3.5 IMPEDANCE AND TRANSDUCTION FRFS

In Figs. 3.2 – 3.5 are compared the simulated and measured spectra of the four FRFs given in Eq.(3.1) for the electromagnetic and for the piezoelectric reactive transducers shown in the schematics (a, d) of Figure 3.1. The analysis is limited to the frequency range comprised between 10 Hz and 1 kHz. To properly highlight in detail all the features that characterise the four FRFs of the two transducers, both modulus-phase and real-imaginary graphs are presented and examined. For the simulated FRFs given in Eqs.(3.2)-(3.5) the physical parameters are derived using Table 3-1 and Table 3-2.

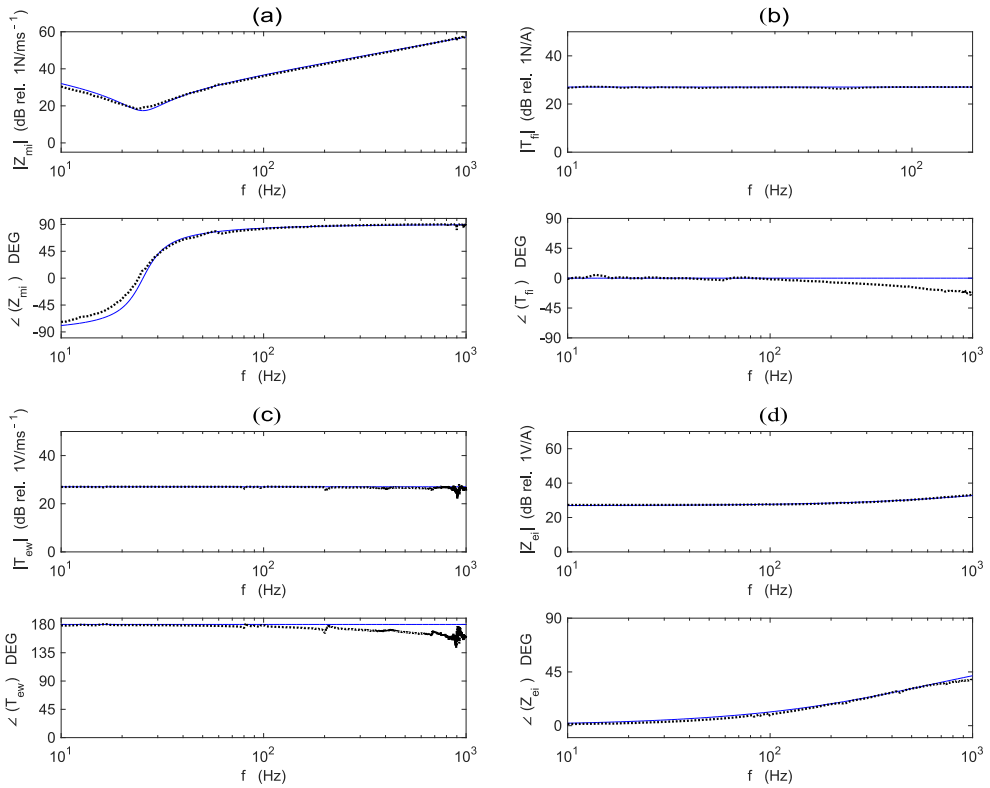

Figure 3.2: Modulus-phase diagrams of the four characteristic FRFs for the electromagnetic reactive transducer. Simulated (solid blue line) and measured (dotted black line) FRF.

Firstly, the simulated FRFs for the electromagnetic reactive harvester are considered. As can be noticed from Eq.(3.2), similarly to the seismic device, the mechanical impedance Z_{mi} is defined assuming the coil in open circuit, i.e. $i_h = 0$. Thus it is

characterised by the mechanical response of the transducer only. As can be deducted from the solid blue line in Plot (a) of Figs. (3.2 and (3.3, the mechanical impedance FRF is characterised by stiffness behaviour and mass behaviour at low and high frequencies respectively, which are proportional to the spring stiffness k_m and the moving base mass m_b of the transducer. These two asymptotic behaviours are linked via a smooth antiresonance trough, at about 25 Hz. The eddy currents damping effect contributes to reduce the amplitude of the fundamental anti-resonance peak. The phase starts at $-90°$, undergoes a $+90°$ phase lag at antiresonance frequency and then a $+90°$ phase lead at higher frequencies, reaching a $+90°$ value.

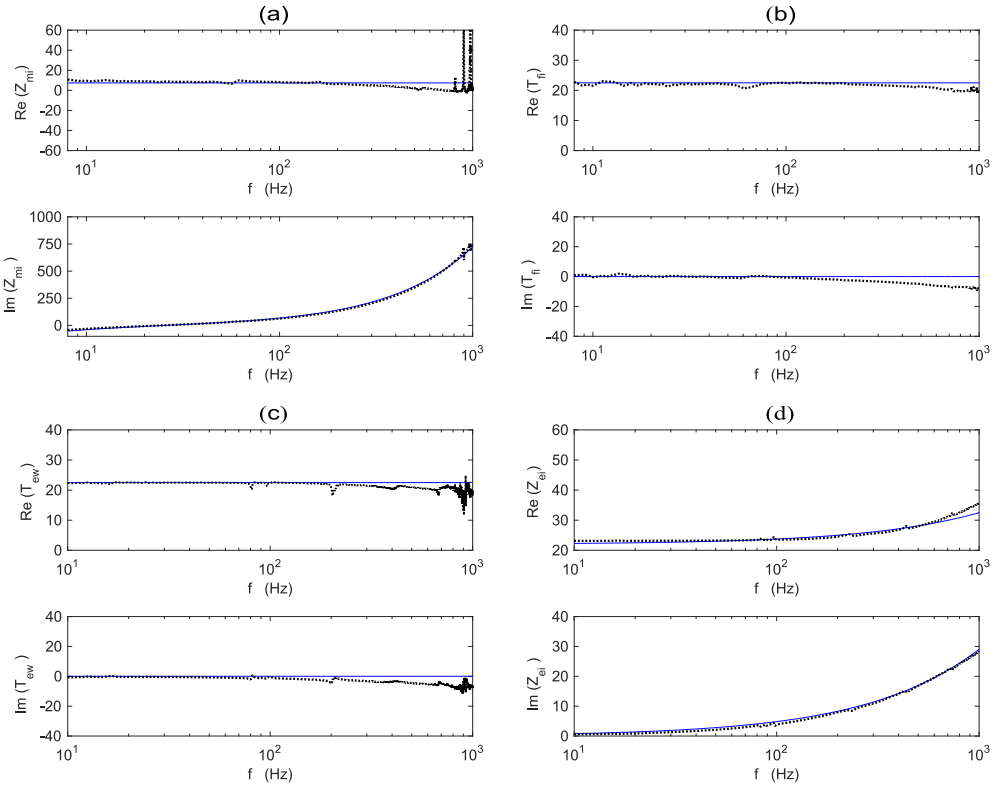

Figure 3.3: Real-imaginary diagrams of the four characteristic FRFs for the electromagnetic reactive transducer. Simulated (solid blue line) and measured (dotted black line) FRFs.

At frequencies lower than the anti-resonance frequency at 25 Hz, the seismic base mass of the transducer oscillates at 90° phase lead and thus produces a reactive spring impedance effect proportional to the stiffness of the transducer. At high frequencies,

above 25 Hz, the seismic base mass moves with little oscillations having 90° phase lead and thus the impedance is characterised by a reactive mass impedance effect, proportional to the base moving mass of the transducer. At frequencies close to the anti-resonance frequency at 25 Hz, the amplitude of the base mass oscillation is restricted by the air and eddy currents damping effect.

According to Eq. (3.5) the electrical impedance does not include an electromechanical contribution of the mechanical second order term and thus the electrical impedance Z_{ei} is simply equal to the coil resistive-inductive impedance Z_e. Similarly to the seismic transducer the electric impedance Z_e is composed by the resistance R_e in series with a lossy inductance $\tilde{L}_e$ that takes into account the effect of eddy currents developed in the coil wire [177]–[179].

As can be noticed in Plot (d) of Figure 3.2 and Figure 3.3, below the cut off frequency $f_{RL} = R_e/(2\pi L_e) = 805$ Hz, the electric impedance Z_{ei} is resistive, and thus is characterised by a constant real part .At higher frequencies above 805 Hz, the lossy inductive effect becomes dominant such that an imaginary and real rising part characterise the electric impedance .

As anticipated in Section 3.4, the electromagnetic transducer is *skew-symmetric* and thus *antireciprocal*. As a result, the electromechanical transduction functions T_{fi} and T_{ew}, given respectively by Eqs.(3.3), (3.4) are real and characterised respectively by positive and negative signs or, alternatively, have same modulus and opposite phase. Indeed, as can be noticed in Plots (b) and (c) of Figure 3.2 and Figure 3.3 , in the whole frequency range the transduction FRFs are characterised by a constant value equal to the transduction coefficient $\psi_{CM} = Bl$ given in Eq.(3.13). Therefore, the reactive transducer acts respectively as a constant force source per unit current flowing into the coil wire and as a constant electromotive source per unit stroke velocity. The phase of T_{fi} and T_{ew} are respectively equal to 0° and 180° in the whole frequency range. Thus, the constant force-current or voltage-stroke velocity transduction effects are characterised by active power transfer properties. As mentioned for the electromechanical seismic transducer, the opposite algebraic sign in the transduction coefficients indicates a power which flows in opposite direction with respect to the notation indicated in the lumped parameter model (c) of Figure 3.1. This mismatch is again due to the right-hand screw sign convention used to define the positive directions of the physical variables that describe the electromagnetic transduction phenomenon [185] rather than an effective mismatch of power flow.

These four simulated FRFs are compared with the measured FRFs obtained from the prototype of Figure 3.1 (a) and shown in Figure 3.2 and Figure 3.3 in a range of

frequencies comprised between 10 Hz and 1 kHz. First of all, taking into consideration the mechanical and electrical FRFs Z_{mi} and Z_{ei} shown in Figures 3.2 and 3.3, the measured FRFs (dotted black lines) match quite well the simulated FRFs (solid blue line), with the exception of a small mismatch at frequencies comprised between 800 and 1000 Hz. Moving now to the electromechanical transduction FRFs T_{fi} and T_{ew} shown in Plots (b, c) of Figure 3.2 and Figure 3.3, both measured FRFs agree quite closely with the simulated FRFs. There is just a small divergence in the phase Plots, especially at upper frequencies. This mismatch is probably caused by dynamic effects of the housing Yoke clamping, which is not taken into account in the model.

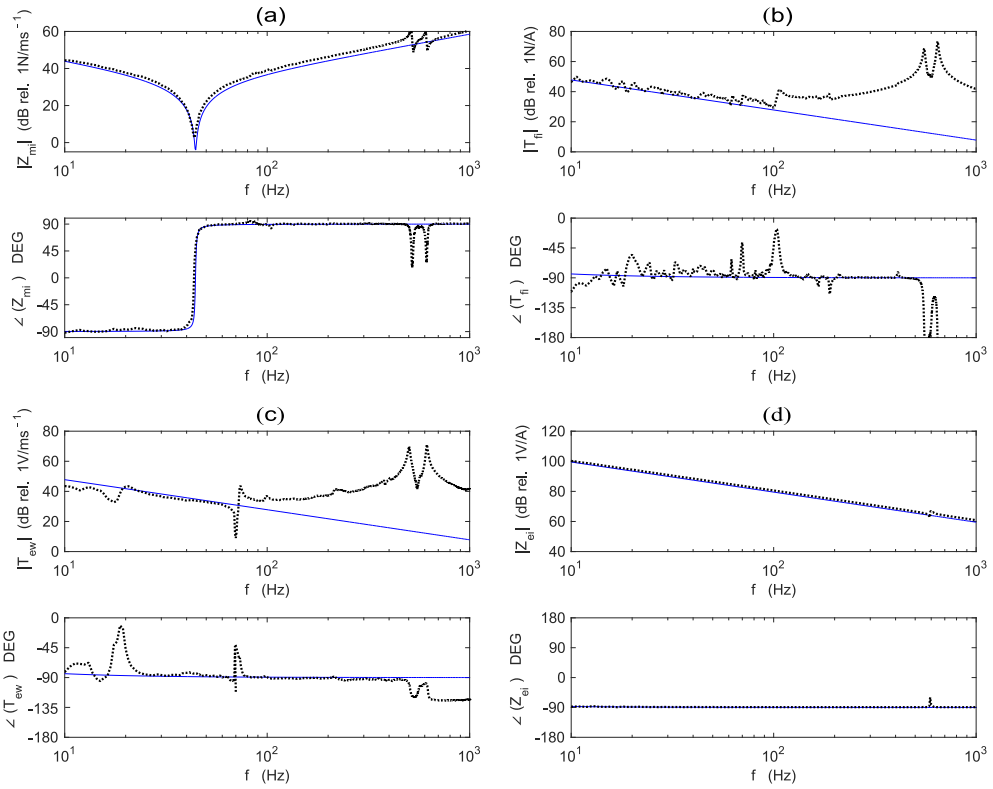

Figure 3.4: Modulus-phase diagrams of the four characteristic FRFs for the piezoelectric reactive transducer. Simulated (solid blue line) and measured (dotted black line) FRFs.

Moving to the simulated FRFs for the piezoelectric reactive transducer shown in Figure 3.4 and Figure 3.5, the spectrum of the mechanical impedance Z_{mi} results comparable to that depicted for the electromagnetic transducer. In fact, considering

the solid blue line in Plot (a) of Figure 3.4, the amplitude inversely decreases with the frequency and reaches a minimum in correspondence of the fundamental anti-resonance frequency of the transducer. It then monotonically increases linearly with the frequency. The phase starts at $-90°$ and undergoes through a $+180°$ phase lag at the fundamental resonance frequency at about 40 Hz, reaching a $+90°$ phase value. Similar to the piezoelectric seismic harvester, the mechanical impedance Z_{mi} for the piezoelectric reactive transducer is defined in open circuit boundary condition i.e. $i_h = 0$ and thus a supplementary term $\Delta\tilde{k}$ due to the back electromechanical stiffness caused by the capacitive piezoelectric effect is added to the mechanical bending stiffness k_m of the sandwich beam laminate. This equivalent stiffness $\Delta\tilde{k}$ is actually a complex term, which includes the energy losses produced by non-ideal piezoelectric material insulator, which, as discussed in Appendix B, are confined in the low frequency range.

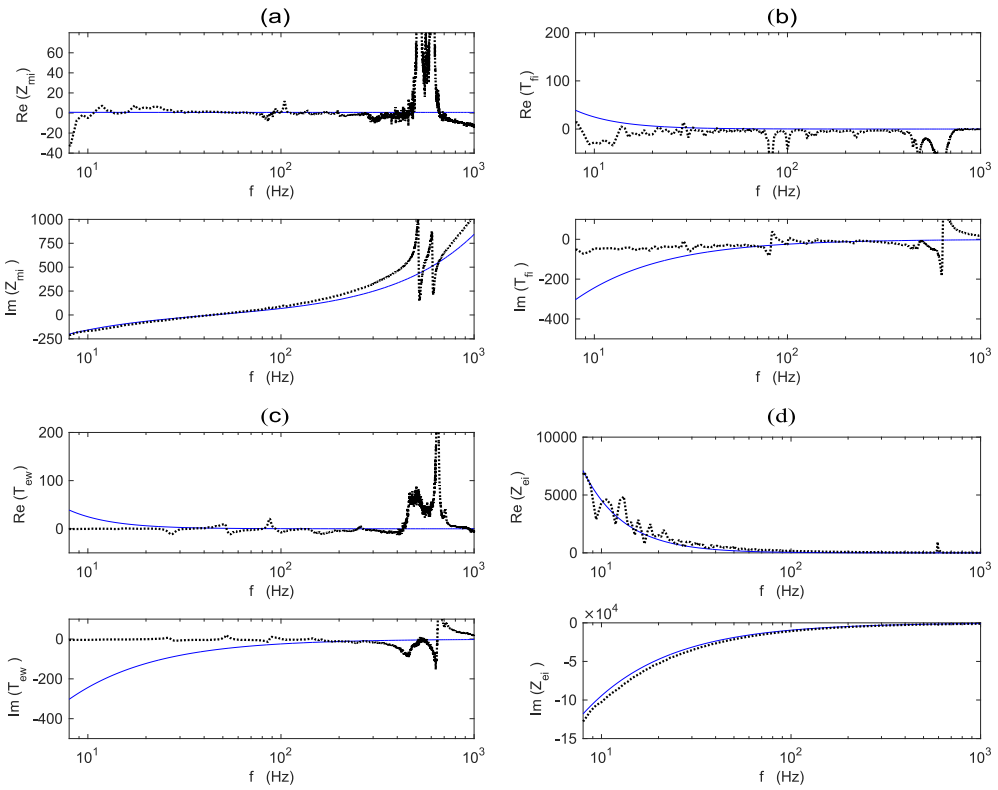

Figure 3.5: Real-imaginary diagrams of the four characteristic FRFs for the piezoelectric reactive transducer. Simulated (solid blue line) and measured (dotted black line) FRFs.

Indeed, neglecting the effect of air damping, the principal energy dissipation effect in the reactive piezoelectric transducer is due to the mechanical losses in the composite beam. This implies that, compared to the coil magnet transducer, a narrower anti-resonance peak characterises the mechanical impedance Z_{mi} of the piezoelectric reactive device. Moving to Eq.(3.5), the electrical impedance Z_{ei} is only given by the capacitive effect of the piezoelectric layers $Z_e = 1/\mathrm{j}\omega\tilde{C}_e^S$, where $\tilde{C}_e^S = \tilde{C}_e^T\left(1 - \tilde{k}_{31}^2\right)$ is the loss capacitor under constant strain. Plot (d) of Figure 3.4 shows a capacitive impedance FRF function, with a modulus inversely proportional to the frequency and constant phase equal to $-90°$. The real and imaginary Plots shown in Figure 3.4 (d) emphasises the resistive effect below the anti-resonance frequency.

Moving to the piezoelectric transduction FRFs, the coefficients T_{ew}, T_{fi} given respectively by Eq.(3.3) and Eq.(3.4), have equal modulus and equal phase and thus the transducer is symmetric, i.e. reciprocal. In contrast to the electromechanical transducer, the spectra of the electromechanical transduction coefficients T_{fi} and T_{ew} for the piezoelectric reactive transducer have a capacitive behaviour and thus the amplitude decreases inversely proportional to the frequency. The phase spectra of both T_{fi} and T_{ew} has a $-90°$ shift in the whole frequency range and thus both the force-current and electromotive stroke-velocity transduction effects are characterised by reactive power transfer effects due to the strain and charge transduction phenomena of piezoelectric materials.

As done for the coil-magnet transducer, the validity of these simulations was checked against measured FRFs taken on the prototype transducer shown in Figure 3.1 (d). The two mechanical and electrical impedances Z_{mi} and Z_{ei} and the two electromechanical transduction FRFs T_{fi} and T_{ew} were measured across the frequency range comprised between 10 Hz and 1 kHz. In this case, contrasting the dotted black lines (measurements) and the solid blue lines (simulations) shown in Figure 3.4 and Figure 3.5 , it is noted that the simulated FRFs reproduce quite closely the measured FRFs up to about 90 Hz. At higher frequencies the measured FRFs follow quite closely the asymptotic behaviours of the simulated FRFs, although they are characterised by additional resonance peaks and antiresonance troughs, particularly in the Z_{mi}, T_{fi}, T_{ew} FRFs. As already noticed for the inertial transducers, the lumped model of the piezoelectric harvester considers only the fundamental bending vibration mode of the beam laminate and thus the contribution of the higher flexural modes are neglected. This leads to differences between the analytical model and the experimental results for frequencies higher than the fundamental resonance frequency. With respect to the *symmetry* (i.e. *reciprocity*) feature that identifies this reactive transducer, the measured

FRFs T_{fi}, T_{ew} overlap quite well the simulations up to 100 Hz. There is a rather marked mismatch between 10 and 20 Hz for the T_{ew} FRF and a very little mismatch at frequencies lower than 100 Hz for the T_{fi} FRF. These issues are probably caused by the experiment setup which does not meet rigorously the assumptions made in the model. However, the comparison between simulated and measured FRFs suggests that the proposed piezoelectric model reproduce sufficiently well the mechanical and electrical impedance functions Z_{ei} and Z_{mi} and the two electromechanical transduction functions T_{fi} and T_{ew}. It follows that the proposed lumped models can be suitably used to predict the power harvested and absorbed with the electromagnetic and piezoelectric harvesters.

3.6 ENERGY ANALYSIS

A unified energy formulation for the power harvested, power input and efficiency for the two devices is derived in this section. As done for the seismic harvesters, these three functions are obtained assuming that the transducers are connected to a purely real or complex electric load. Figure 3.6 shows the scheme of the two-port network used to derive the energy analysis. The mechanical mesh has input variables $\dot{w}_h$ and f_h and mechanical impedance Z_{mi}. The electrical mesh has input variables e_h and i_h and both ports are connected via the transduction FRFs T_{ew} and T_{fi} by the transducer black box. Finally, an electric load is connected to the electric terminals of the transducer.

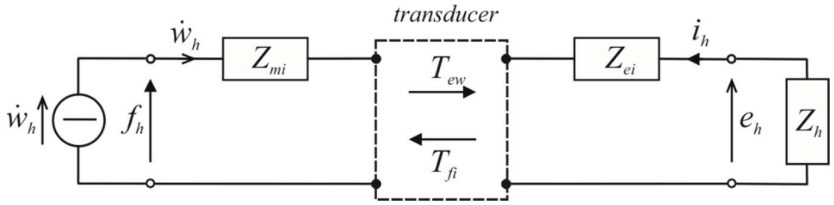

Figure 3.6: Equivalent schematic representation of the two reactive electromechanical transducers connected to the harvesting electrical load.

The results are obtained assuming time harmonic excitation and optimal harvesting loads. The spectra of the harvested power, input power and efficiency are presented.

The graphs are derived using analytical expressions (solid blue line) and measurements (dotted black line) of the four constitutive FRFs Z_{mi}, T_{fi}, T_{ew}, Z_{ei}.

3.7 HARVESTED POWER

For time-harmonic vibrations, the time averaged harvested power is given by

$$\bar{P}_h = \lim_{T\to\infty} \frac{1}{T}\int_0^T P_h(t)\mathrm{d}t, \tag{3.19}$$

so applying the same procedure derived for the seismic harvesters (Eqs. (2.26)-(2.29)) it results:

$$\bar{P}_h = \frac{1}{2}\mathrm{Re}\{Z_h\}|i_h|^2 = \frac{1}{2}\mathrm{Re}\{Z_h\}\left|-\frac{T_{ew}}{Z_{ei}+Z_h}\right|^2 |\dot{w}_h|^2. \tag{3.20}$$

In order to find the optimal complex load, which maximize the power harvested, Eq.(3.20) is derived with respect to the real and imaginary part of the complex electric load and set to zero:

$$\frac{\partial \bar{P}_h}{\partial \mathrm{Re}\{Z_h\}} = 0 \text{ and } \frac{\partial \bar{P}_h}{\partial \mathrm{Im}\{Z_h\}} = 0\,. \tag{3.21a,b}$$

Solving Eq.(3.21) the two conditions lead to the following optimal impedance condition for the harvesting circuit:

$$Z_h = Z_{ei}^*, \tag{3.22}$$

where * is the complex conjugate operator. Applying the optimal impedance condition in Eq.(3.20), the maximum harvested power results:

$$\bar{P}_h = \frac{1}{8}\frac{|T_{ew}|^2}{\mathrm{Re}\{Z_{ei}\}}|\dot{w}_h|^2, \tag{3.23}$$

which using the formulation presented in Section 3.3 can be specified respectively for the electromagnetic and for the piezoelectric reactive harvesters.

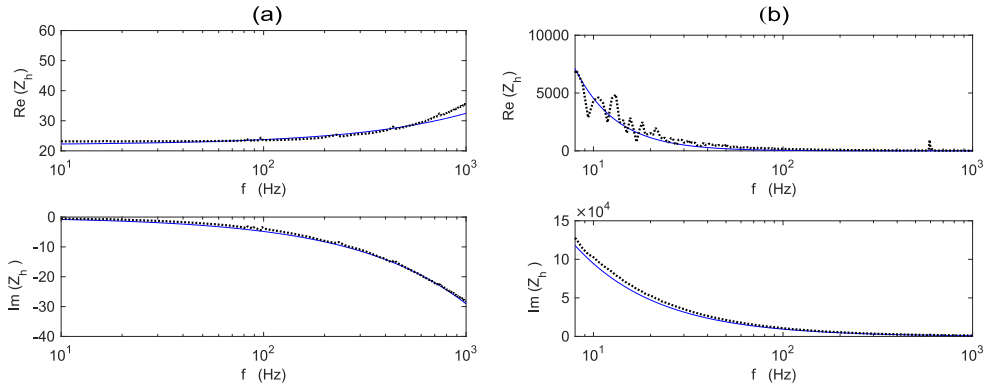

Figure 3.7: Comparison between the simulated (solid blue line) and measured (dotted black line) spectra of the Real and Imaginary parts of the optimal impedance $Z_h = Z_{ei}^*$ of the harvesting circuits for (a) the electromagnetic and (b) the piezoelectric reactive harvesters.

Figure 3.7 shows the real and imaginary parts of the simulated (solid blue line) and measured (dotted black lines) optimal complex electric loads, which maximize the power harvested for (a) the electromagnetic and (b) piezoelectric reactive harvesters. The observed results of the simulated spectra correspond fairly well with those derived from the measured FRFs of the electrical impedance Z_{ei}.

Plot (a) shows that when the electromagnetic reactive transducer is considered, the impedance of the harvesting load should have a constant real positive part for a range of frequencies comprised between 10 Hz and 800 Hz and then a rising real part above the cut off frequency (i.e. 805 Hz) because of the lossy inductive effect [177]. Moving to the imaginary part, the amplitude moves from zero to progressively larger negative values. If the piezoelectric reactive transducer is considered, the impedance of the harvesting load is characterised by both real and imaginary positive parts, represented by a decreasing trend converging to zero for very high frequencies. In particular at low frequencies the real part is due to the conductive dielectric loss effect of the piezoelectric transducer, which produces a flow of current into the piezoelectric patches. Thus, the dielectric losses in the piezoelectric layers play a fundamental role in the energy harvesting. As discussed in Appendix B, no explicit solution for the optimal energy harvesting load derived in Eq.(3.21a,b) can be found if the dielectric losses are not taken into account.

Comparing the two Plots in Figure 3.7 with the Plots of Figure 2.7 it is noted that the spectra of the optimal complex harvesting loads are not characterised by peaks at the fundamental resonance frequency of the reactive transducers. In addition, contrasting the two plots in Figure 3.7 it comes out that the real/imaginary components of the optimal harvesting impedance for the piezoelectric reactive transducer is four orders of magnitude greater than the real/imaginary components of the optimal harvesting impedance for the electromagnetic reactive transducer. Also, the complex conjugate of the FRF measured spectra of the electrical impedance for both transducers match quite well with the simulated FRFs.

Figure 3.8 shows the simulated spectra of the 10 Hz to 1 kHz power harvested per 1g base acceleration amplitude with the electromagnetic reactive harvester (Plot (a)) and with the piezoelectric reactive harvester (Plot(b)) when the harvesting circuits are characterised by the optimal complex impedance $Z_h = Z_{ei}^*$. Plot (a) shows that if the optimal electrical impedance derived from Eq.(3.22) and shown in Plot (a) of Figure 3.7 is implemented in the harvesting circuit, the spectrum of the harvested power is characterised by a decreasing amplitude. In fact, according to the harvesting power equation of Eq.(3.23) and with reference to Plots (a,d) of Figure 3.2 and Figure 3.3, the transduction FRF T_{ew} is constant in the whole frequency range while the real part of the electric impedance Z_{ei} grows in amplitude only at frequencies above 800 Hz. Thus since Figure 3.8 refers to base acceleration, the power harvested is characterised by a $1/\omega^2$ additional factor that generates this decreasing trend shown in Figure 3.8 (a) .

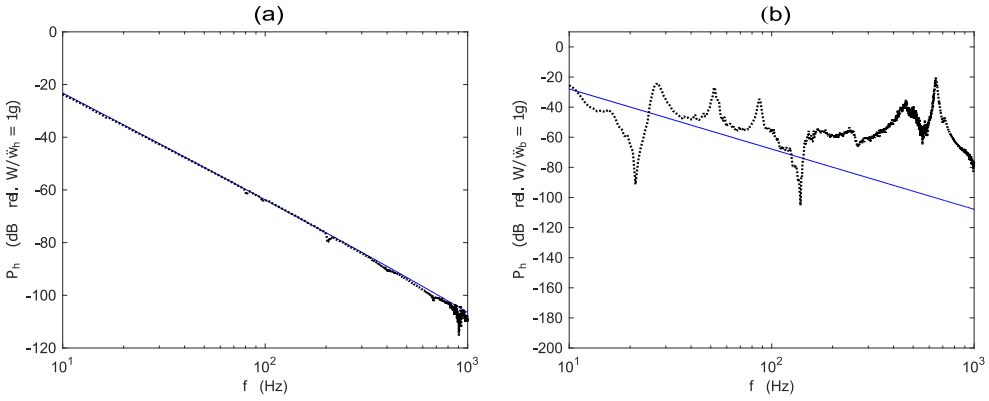

Figure 3.8: Spectra of the power harvested with reference to a 1 g base acceleration for (a) the electromagnetic and (b) the piezoelectric reactive harvesters with optimal harvesting impedances $Z_h = Z_{ei}^*$ simulated using either the analytical expressions (solid blue) or the measurements (dotted black lines) of the four constitutive FRFs, Z_{mi}, T_{fi}, T_{ew}, Z_{ei}.

It is interesting to note that, if the eddy current losses in the wire are not present the harvested power per unit of base velocity imposed would be constant and equal to $P_h = (\psi_{CM}^2/\mathrm{R}_e)\,|\dot{w}_m\,|^2$. If the lossy inductance $\tilde{L}_e$ is also considered, the power harvested becomes $P_h = \left(\psi_{CM}^2/(\,\mathrm{R}_e + \omega\,\mathrm{Im}\{\tilde{L}_e\}\right)|\dot{w}_m\,|^2$ and thus tends to decrease as the frequency is incremented.

According to Plot (a) of Figure 3.7 the maximum power harvested is thus obtained with a purely resistive load for a range of frequencies comprised between 10 and 800 Hz. An imaginary reactive load is also required if the frequency of excitation is above 800 Hz. The spectra of the harvested power simulated from analytical FRFs expressions (solid blue lines) and measured FRFs (dotted black lines) perfectly overlap in the whole frequency range, confirming the validity of the analytical expressions derived for the constitutive FRFs of the electromagnetic harvester in Section 3.3 and Appendix C. A mismatch is only present in the frequency range comprised between 800 and 1000 Hz, probably caused by the higher order dynamic flexural modes of the spiral springs.

Moving to the piezoelectric harvester, Plot (b) of Figure 3.8 shows that if the harvesting circuit implements at each frequency the optimal complex impedance calculated from Eq.(3.22) and shown in Plot (b) of Figure 3.7, the spectrum of the harvested power is characterised by a trend that uniformly decreases as the frequency rises. Similarly to the electromagnetic reactive transducer, the harvested power only depends on the electromechanical transduction coefficient ψ_{pzt} and the electrical elements of the piezoelectric device, composed in this case by a lossy inductance $\tilde{C}_e^S$. As anticipated above, the introduction of an appropriate modelling of the dielectric losses for the piezoelectric patch of the transducer is of great of importance because otherwise no real part for the optimal impedance of the harvesting load could be found and no power could be harvested for any frequency of excitation [92],[93],[196]. Contrasting the spectra of the harvested power simulated from analytical expressions (solid blue lines) and from measurements (dotted black lines) of the four constitutive FRFs Z_{mi}, T_{fi}, T_{ew}, Z_{ei}, relevant discrepancies are noticed in the whole frequency range. This problem arises from the fact that the spectrum has been simulated from measured FRFs, which, are still characterised by small imperfections that, as discussed in Ref. [198], produce the anomalies observed in the power harvested spectrum depicted by the dotted black line in Plot (b) of Figure 3.8. Comparing the spectra in Plots (a) and (b) of Figure 3.8, it is noted that the electromagnetic harvester outperforms the piezoelectric harvester in the whole frequency range.

If the harvesters are equipped with purely resistive electric loads, the harvesting electrical impedance must be purely real. In this specific case, the purely real impedance that allows to obtain the maximum power harvested at each frequency is found by imposing only the condition (a) of Eq. (3.21), which gives:

$$Z_{h,R} = |Z_{ei}|. \tag{3.24}$$

This expression suggests that maximum power $\bar{P}_h$ is achieved for each frequency when the electric impedance of the harvesting circuit $Z_{h,R}$ is equal to the module of the electric impedance of the reactive transducers Z_{ei} given in Eq.(3.5). Thus substituting the optimal real electric impedance $Z_{h,R}$ into Eq. (3.20) leads to the following harvested power expression:

$$\bar{P}_h = \frac{1}{4}\frac{|T_{ew}|^2}{|Z_{ei}| + \mathrm{Re}\{Z_{ei}\}}|\dot{w}_h|^2. \tag{3.25}$$

Using the formulation derived in Section 3.3, Eq.(3.25) can be specified respectively for the electromagnetic and for the piezoelectric reactive harvesters.

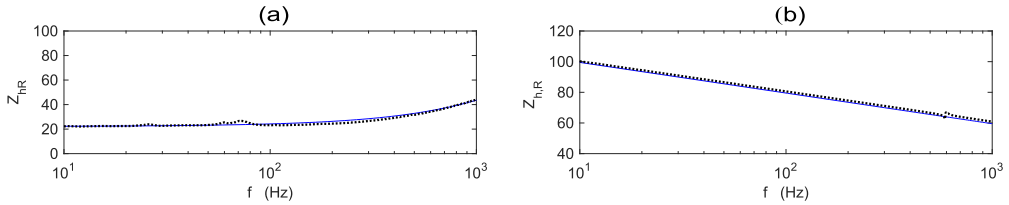

Figure 3.9: Comparison between the simulated (solid blue line) and measured (dotted black line) spectra of the real optimal impedance $Z_{h,R} = |Z_{ei}|$ of the harvesting circuits for (a) the electromagnetic and (b) the piezoelectric reactive harvesters.

The two Plots in Figure 3.9 show the simulated (solid blue lines) and measured (dotted black lines) optimal real harvesting impedances $Z_{h,R}$, which maximizes the harvested power at each frequency using the electromagnetic reactive transducer (Plot (a)) and with the piezoelectric reactive transducer (Plot (b)). Considering first the optimal electric load of the electromagnetic reactive transducer shown in Plot (a), the spectrum of the real harvesting load $Z_{h,R}$ is very similar to the real part of the spectrum of the complex load, i.e. $\mathrm{Re}\{Z_h\}$. In detail, compared to the spectrum of

Re $\{Z_h\}$, the spectrum of real harvested load $Z_{h,R}$ is characterised by a similar constant resistive trend appreciable up to the cut off frequency at 805 Hz .Then, the inductive effects of the winding coil becomes predominant and thus the spectrum of $Z_{h,R}$ rises monotonically at a slightly higher values than those of the spectrum of Re$\{Z_h\}$.

Moving to the piezoelectric reactive harvester, Plot (b) in Figure 3.9 shows that the spectrum of the real harvesting load $Z_{h,R}$ is not similar to the real part of Z_h but is instead comparable to that of the imaginary part of the spectrum of the complex load, i.e. Im $\{Z_h\}$. Thus, the amplitude of the resistive load starts from a value of 9×10^4 Ω at about 10 Hz and then uniformly drops down as the frequency rise, reaching 900 Ω at 1000 Hz. The measured spectrum in Plot (a) denotes a similar behaviour with respect to the simulated spectrum and confirms the congruences denoted for the real part in Figure 3.7 (a). Instead, the experimental result (dotted black line) in Figure 3.9 (b) shows a very good matching with the theoretical prediction unlike the real part result shown in Figure 3.7 (b). This can be explained by the fact that the capacitive effect has a very large magnitude and dominates the real part, which can't be appreciated.

Considering the two Plots in Figure 3.9, it can be noted that the optimal resistive impedance for the electromagnetic reactive transducer is three to four orders of magnitude smaller than the real part of the optimal harvesting impedance for the piezoelectric seismic transducer. In addition, no peaks due to the electromechanical transduction phenomena can be appreciated in the whole frequency range.

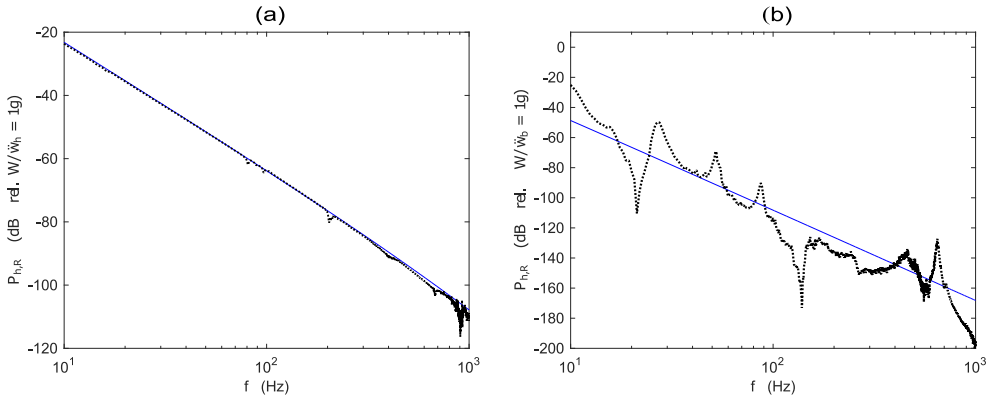

Figure 3.10: Spectra of the power harvested with reference to a 1 g base acceleration for (a) the electromagnetic and (b) the piezoelectric reactive harvesters with optimal harvesting impedance $Z_{h,R} = |Z_{ei}|$ simulated using either the analytical expressions (solid blue lines) or the measurements (dotted black lines) of the four constitutive FRFs, Z_{mi}, T_{fi}, T_{ew}, Z_{ei}.

Figure 3.10 shows the simulated spectra of the 10 Hz to 1 kHz power harvested per 1g base acceleration with the electromagnetic reactive harvester (Plot (a)) and with the piezoelectric reactive harvester (Plot (b)) when the optimal real harvesting circuit of impedance $Z_{h,R} = |Z_{ei}|$ is connected. Taking into account the electromagnetic harvester, Plot (a) shows that implementing at each frequency the optimal real impedance load given in Eq.(3.24) and depicted in Plot (a) of Figure 3.9, the resulting spectrum of the harvested power $P_{h,R}$ is very similar to that found when the optimal complex impedance load given in Eq.(3.23) and shown in Plot (a) of Figure 3.7 is implemented. Thus, it is characterised by a decreasing trend as the frequency rises. No resonance peaks are present. As was noted for the complex harvesting load, also with the purely resistive harvesting load the maximum harvested power is controlled by the transduction constant coefficient and by the electrical FRF, which characterises the reactive transducer. Thus the harvested power is not affected by the mechanical properties of the harvester, in particular it is not affected by the air damping produced between the magnet and ferromagnetic Yoke and by the eddy currents that develops in the ferromagnetic outer ring of this reactive harvester. As discussed in Chapter 2, the harvested power by the seismic harvesters is instead dominated by the mechanical damping. According to Plots (a) of Figure 3.8 and Figure 3.10, with the electromagnetic reactive harvester similar values of harvested power can be obtained when the device implements either a purely resistive load $Z_{h,R} = |Z_{ei}|$ or a complex electric load of magnitude $Z_h = Z_{ei}^*$. Similar to the complex impedance case, the spectra of the harvested power simulated from analytical FRFs expressions (solid blue lines) and measured FRFs (dotted black lines) match quite well in the whole frequency range, except at very high frequencies. Such discrepancies above 900 Hz are probably due to higher order dynamic effects of the transducer, which are not considered in the model used to simulate the FRFs of the transducer.

Moving to the piezoelectric harvester, Plot (b) of Figure 3.10 shows that when the harvesting circuit implements at each frequency the optimal real impedance derived in Eq. (3.24) and depicted in Plot (b) of Figure 3.9, the spectrum of the harvested power has a very similar trend to that found when the optimal complex impedance load given in Eq.(3.22) and shown in Plot (b) of Figure 3.7 is implemented. Indeed, the spectrum of the harvested power is characterised by a decreasing trend in the whole frequency range. The only difference is due to the amplitude, which for the real optimal impedance case is comparatively smaller by about 20 dB.

According to Plot (b) of Figure 3.9, the maximum power harvested is obtained at low frequency with a resistive load of $9 \times 10^4\ \Omega$. Comparing the spectra of the

harvested power simulated from analytical FRFs expressions (solid blue line) and measured FRFs (dotted black line), a consistent mismatch is found in the whole frequency range. As discussed above, this is due to the fact that the measured expressions of the constitutive FRFs of the piezoelectric transducer shown in Figure 3.4 and Figure 3.5 contain small errors, which, however, are greatly magnified when the power is calculated. Plots (a) and (b) of Figure 3.10 show that also in this case the electromagnetic harvester outperforms the piezoelectric harvester in whole frequency range.

3.8 INPUT POWER

Similarly to the seismic harvesters, the time averaged input power for the electromagnetic and the piezoelectric reactive devices is given by:

$$\bar{P}_i = \lim_{T\to\infty} \frac{1}{T} \int_0^T P_i(t) \mathrm{d}t, \tag{3.26}$$

where the instantaneous input power is given by:

$$P_i(t) = f_h(t)\dot{w}_h(t), \tag{3.27}$$

and $f_h(t)$, $\dot{w}_h(t)$ are the force and velocity of the base masses of the two reactive transducers. Assuming time harmonic functions, the force at the base mass of the transducers can be derived from the first equation of the matrix expression in Eq. (3.1). Assuming the current is given by Eq.(2.29) follows:

$$f_h = Z_{mh}\dot{w}_h, \tag{3.28}$$

where Z_{mh} is the base impedance of the reactive harvesters when the transducers are connected to the optimal harvesting circuit characterised by the electrical impedance Z_h:

$$Z_{mh} = Z_{mi} - \frac{T_{ew}T_{fi}}{Z_{ei} + Z_h}. \tag{3.29}$$

Thus, substituting Eqs.(3.28) and (3.29) into Eq.(3.27) the time average input power is derived as follows:

$$\bar{P}_i = \frac{1}{2}\mathrm{Re}\{Z_{mh}\}|\dot{w}_h|^2 = \frac{1}{2}\mathrm{Re}\left\{Z_{mi} - \frac{T_{ew}T_{fi}}{Z_{ei}+Z_h}\right\}|\dot{w}_h|^2. \tag{3.30}$$

Considering the optimal complex impedance $Z_h = Z_{ei}^*$, the input power expression becomes:

$$\bar{P}_i = \frac{1}{2}\mathrm{Re}\left\{Z_{mi} - \frac{T_{ew}T_{fi}}{2\mathrm{Re}\{Z_{ei}\}}\right\}|\dot{w}_h|^2. \tag{3.31}$$

Eq.(3.31) can be specified respectively for the electromagnetic and piezoelectric reactive harvesters.

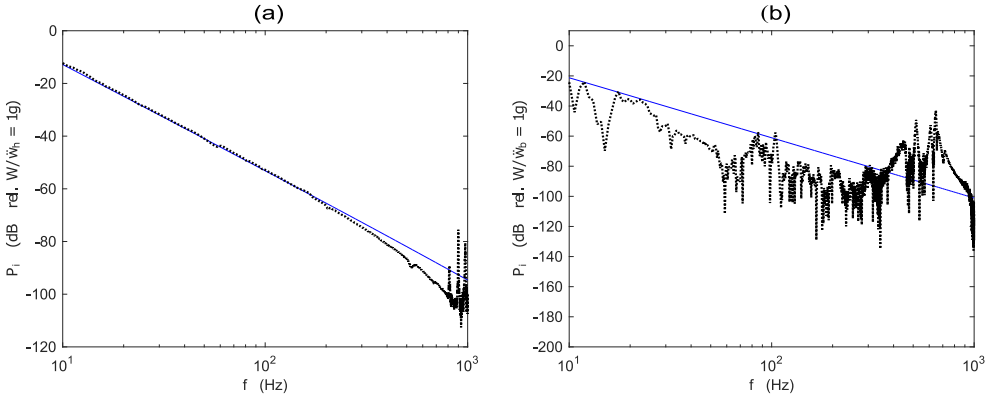

Figure 3.11: Spectra of the power input with reference to a 1 g base acceleration for (a) the electromagnetic and (b) the piezoelectric reactive harvesters with optimal harvesting impedances $Z_h = Z_{ei}^*$ simulated using either the analytical expressions (solid blue lines) or the measurements (dotted black lines) of the four constitutive FRFs, Z_{mi}, T_{fi}, T_{ew}, Z_{ei}.

Figure 3.11 shows the simulated spectra of the 10 Hz to 1 kHz power input per 1g base acceleration with the electromagnetic (Plot (a)) and piezoelectric (Plot (b)) reactive harvesters when the harvesting loads characterised by the optimal complex impedance $Z_h = Z_{ei}^*$ derived in Eq.(3.22) are implemented. Considering at first the electromagnetic reactive device, implementing at each frequency the complex harvesting impedance $Z_h = Z_{ei}^*$ depicted in Plot (a) of Figure 3.7, the power input

starts at a value of 228 mW/1g and then monotonically falls down with frequency. No peaks can be appreciated in the whole spectrum and in comparison with the power harvested shown in Figure 3.8 , the spectra of the input power of Figure 3.11 is quite similar except that the input power is relatively higher by about 11,37 dB . The simulated spectra based on analytical expressions (solid blue line) and measurements (dotted black line) of the four constitutive FRFs, Z_{mi}, T_{fi}, T_{ew}, Z_{ei}, perfectly overlap up to about 800 Hz.

As previously discussed in Section (3.7) for the power harvested, the increasingly larger mismatch between simulation and measured spectra, particularly visible at higher frequencies, is due to higher order dynamic effects of the transducer, which are not taken into account in the model used to simulate the characteristic FRFs of the electromagnetic harvester.

Considering now the piezoelectric reactive harvester, when the harvesting circuit implements at each frequency the optimal complex impedance $Z_h = Z_{ei}^*$ depicted in Plot (b) of Figure 3.7, the input power to the transducer using the simulated FRFs monotonically falls down as the frequency increases. Instead, the simulation based on the measured constitutive FRFs (dotted black line), is characterised by drops and crests anomalies. This result is not related to antiresonance or resonance effects but arise from the calculus of the power based on measured FRFs, which are affected by small errors in the real and imaginary parts, or in the modulus and phase, and, as discussed in Ref.[198], produce the glitches observed in the dotted black spectrum.
In conclusion, as for the electromagnetic reactive transducer, the spectra of the harvested and input power by the piezoelectric reactive harvester shown in Plots (b) of Figure 3.8 and Figure 3.11 also shows similar features, with the spectrum of the input power being shifted up by about 6.68 dB with respect to the harvested power. For both transducers, the surplus of power input with respect to the power harvested is dissipated by the electrical and mechanical losses in the two reactive harvesters.

Moving now to the case when the harvesting electrical component is characterised by a purely resistive impedance $Z_{h,R} = |Z_{ei}|$ found in Eq.(3.24) and depicted in Figure 3.9, the power input given by Eq. (3.30) becomes:

$$\bar{P}_i = \frac{1}{2}\mathrm{Re}\left\{Z_{mi} - \frac{T_{ew}T_{fi}}{Z_{ei} + |Z_{ei}|}\right\}|\dot{w}_h|^2. \tag{3.32}$$

This expression can be specified for the electromagnetic and piezoelectric reactive

harvesters by substituting it in the expressions for the constitutive FRFs given in Eqs. (3.2)- (3.5).

Figure 3.12 shows the simulated spectra of the 10 Hz to 1 kHz power input per 1g base acceleration with the electromagnetic (Plot (a)) and piezoelectric (Plot (b)) reactive transducers when the harvesting circuit implements the optimal real impedance given in Eq.(3.24), i.e. $Z_{h,R} = |Z_{ei}|$. Starting from the electromagnetic reactive device, implementing at each frequency the harvesting circuit characterised by the optimal real impedance $Z_{h,R} = |Z_{ei}|$, the power input starts at a maximum value at about 10 Hz and then falls down monotonically with frequency. Also, in this case the spectra of the power input simulated using the analytical expressions (solid blue line) and the measured (dotted black line) constitutive FRFs, Z_{mi}, T_{fi}, T_{ew}, Z_{ei}, closely overlap up to about 800 Hz. At higher frequencies, there is an increasingly larger mismatch, which, as discussed above, and also in Section 2, is probably due to higher order dynamic effects of the transducer occurring just above 1 kHz, which are not accounted in the model for the constitutive FRFs.

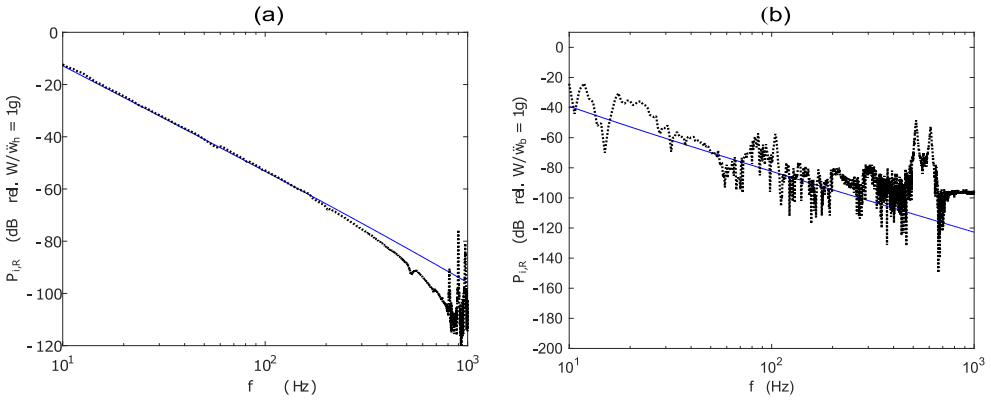

Figure 3.12: Spectra of the input power with reference to a 1 g base acceleration for (a) the electromagnetic and (b) the piezoelectric reactive harvesters with optimal harvesting impedances $Z_{h,R} = |Z_{ei}|$ simulated using either the analytical expressions (solid blue lines) or the measurements (dotted black lines) of the four constitutive FRFs, Z_{mi}, T_{fi}, T_{ew}, Z_{ei}.

Moving now to the piezoelectric reactive device, implementing at each frequency the harvesting circuit with the optimal real impedance $Z_{h,R} = |Z_{ei}|$ depicted in Plot (b) of Figure 3.9, the input power to the transducer starts with a maximum level of power of 11 mW/1g at 10 Hz and monotonically drops down as the frequency increases. As can be noticed, the spectrum simulated from measured constitutive FRFs (dotted

black line) is rather irregular with many narrow drops and small crests, which, as already mentioned, is due to fact that the FRFs used to simulate the power expression are characterised by small errors generated during the measurements [198], which are greatly amplified in the calculus of the power harvested.

In conclusion, as shown above, the spectra of the input and harvested power for both the electromagnetic and the piezoelectric harvesters, shown respectively in Plot (a) and in Plot (b) of Figure 3.12 and Figure 3.10 , are quite similar to each other, except for the level of the spectrum of the input power which is shifted up 11.4 dB and 9.5 dB for the coil magnet and piezoelectric harvester respectively. Also, as for the optimal complex electric load case, the surplus of power input with respect to the power harvested is dissipated and thus lost by the inherent mechanical damper and electrical resistance.

3.9 EFFICIENCY

In analogy to the seismic harvesters, in order to characterise the capacity to convert the input power to the harvested power, the efficiency ratio is defined as:

$$E = \frac{\bar{P}_h}{\bar{P}_i}, \tag{3.33}$$

where $\bar{P}_h$ and $\bar{P}_i$ are given in Eqs.(3.20) and (3.30) respectively such that:

$$E = \frac{\mathrm{Re}\{Z_h\}\left|-\frac{T_{ew}}{Z_{ei}+Z_h}\right|^2}{\mathrm{Re}\left\{Z_{mi}-\frac{T_{ew}T_{fi}}{Z_{ei}+Z_h}\right\}}. \tag{3.34}$$

Implementing the harvesting loads with either the optimal complex impedance, $Z_h = Z_{ei}^*$, or the optimal real impedance, $Z_{h,R} = |Z_{ei}|$, Eq.(3.34) can be specified as follows:

$$E = \frac{1}{4}\frac{|T_{ew}|^2}{\mathrm{Re}\{Z_{ei}\}\mathrm{Re}\left\{Z_{mi}-\frac{T_{ew}T_{fi}}{2\mathrm{Re}\{Z_{ei}\}}\right\}}, \tag{3.35}$$

$$E_R = \frac{1}{2} \frac{\frac{|T_{ew}|^2}{|Z_{ei}| + Re\{Z_{ei}\}}}{Re\left\{Z_{mi} - \frac{T_{ew}T_{fi}}{Z_{ei} + |Z_{ei}|}\right\}}. \tag{3.36}$$

Figure 3.13 and Figure 3.14 show the simulated spectra of the 10 Hz to 1 kHz efficiency when the electromagnetic (Plot (a)) and piezoelectric (Plot (b)) reactive harvesters are connected to harvesting loads that implement the optimal complex impedance $Z_h = Z_{ei}^*$ and the optimal real impedance $Z_{h,R} = |Z_{ei}|$ respectively. Considering at first the electromagnetic harvester, Plots (a) of Figure 3.13 and Figure 3.14 show that the simulated spectra of the efficiency obtained from the analytical FRFs expressions (solid blue lines) have a somewhat constant efficiency at about 30 % in a whole frequency range. A slight decrease of the efficiency can be appreciated only for high frequencies at about 1000 Hz. Compared to the simulated spectra from the measured FRFs, the efficiency (dotted black lines) satisfactorily overlap up to about 215 Hz and then grows up monotonically with frequency. At higher frequencies the efficiency simulated from measured FRFs (dotted black lines) becomes inaccurate because of the bias errors in the calculation of the harvested and input power with the measured FRFs, which are then magnified in the calculus of the efficiency power ratio. Such problem becomes relevant in the spectra of the efficiency for the piezoelectric reactive harvester shown in Plots (b) of Figure 3.13 and Figure 3.14, where the simulations from analytical FRFs expressions (solid blue lines) are only shown. This is because the spectra simulated from measured FRFs (dotted black lines) do not accurately overlap with the solid blue lines. Plot (b) in Figure 3.13 shows that when the optimal reactive impedance $Z_h = Z_{ei}^*$ is implemented, the efficiency of the piezoelectric reactive harvester is characterised by a somewhat constant efficiency at about 45% in the entire frequency range. Moving to Plot (b) of Figure 3.14 ,the configuration with the optimal real impedance $Z_{h,R} = |Z_{ei}|$ indicates that the efficiency, which at 10 Hz is about to 37%, gradually falls down such that, at 1 kHz, is close to 0% . These results show that, when the optimal complex harvesting load is implemented, the efficiency of the piezoelectric transducer is higher at about 15 % than the electromagnetic harvester to convert the input power into the harvested power. Instead, when the optimal real impedance load is implemented, the electromagnetic harvester results more efficient than the piezoelectric harvester, in particular for frequencies up to 50 Hz.

As already indicated in Section 2.9 for the seismic harvesters, these results are however specific to the transducers considered in this study. For instance, if the

transduction coefficient of the devices is increased by 20% by increasing the magnetic field B of the coil magnet or the piezoelectric strain charge constant d_{31} of the piezoelectric harvester, the efficiency implementing the real-reactive harvesting load would rise respectively to 4 % and 3%. This suggests that the design of the two reactive transducers plays a key role in the conversion of the input mechanical power into harvested electrical power.

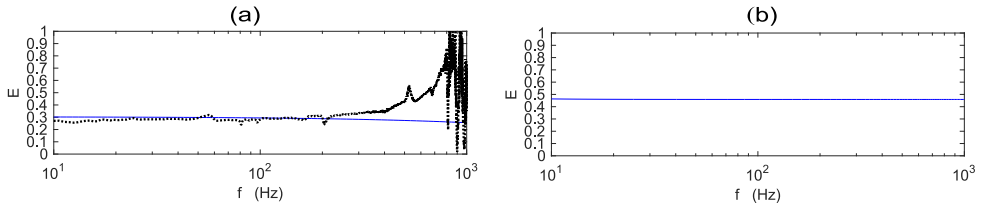

Figure 3.13: Spectra of the efficiency for (a) the electromagnetic and (b) the piezoelectric reactive harvesters with the optimal harvesting impedances $Z_h = Z_{ei}^*$ simulated using either analytical expressions (solid blue line) or the measurements (dotted black line).

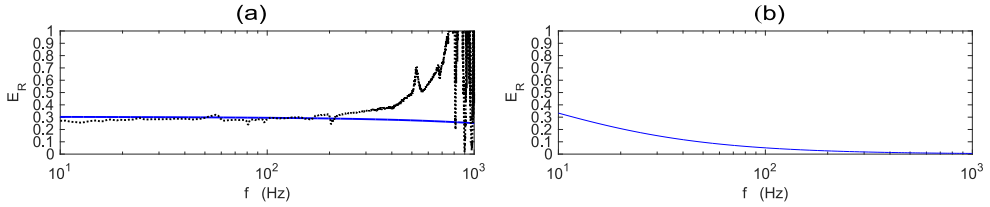

Figure 3.14: Spectra of the efficiency for (a) the electromagnetic and (b) the piezoelectric reactive harvesters with an optimal harvesting impedances $Z_{h,R} = |Z_{ei}|$ simulated using either analytical expressions (solid blue line) or the measurements (dotted black line).

4

VIBRATION ENERGY HARVESTING: SCALING STUDY

This chapter presents a comparative study on the scaling laws of vibration energy harvesters using either seismic or reactive electromagnetic and piezoelectric transducers. The aim of this chapter is to give a detailed account of how the efficiency and harvested power density vary with the dimension so that, the potential (large- or small-scale) applications of these transducers can be assessed. The study is primarily focussed on seismic harvesters, which present a general case. The scaling laws of reactive harvesters is briefly revised at the end of the chapter since it recalls most of the results and conclusions drawn for the seismic harvesters. Starting from the models presented in Chapter 2 and Appendix A and B, a new energy and then scaling formulation is derived under the assumption of steady state oscillation at the fundamental mechanical frequency of the transducers, assuming they are driven by a base acceleration of 1 g amplitude. An isotropic downscaling is assumed for both harvesters and therefore no change of shape takes place as the transducers are scaled up or down. Using the notation described by Madou and Trimmer [200], [201] the scaling laws are obtained with reference to a single variable L, which represents the linear proportional scale of the entire device. In addition, it is assumed that the scale $L = 1$ refers to the size of the two harvester prototypes built for this study (See Figure 4.1). Also, the upper and lower scaling limits were chosen considering the dimensions of typical prototypes reported in literature [50], [81], [82].

This chapter is structured in eight sections. At first, the derivation of a two port network formulation that can be suitably used to implement the scaling study of the two seismic harvesters is reformulated starting from that presented in the previous chapters. In sections 4.2 - 4.6 the scaling properties of the harvested power and efficiency are derived and specified in terms of non-dimensional electromechanical coupling coefficients and loss factors of the two seismic transducers. In particular, as proposed by Beeby *et al*. [140], the power scaling analysis has been performed by normalizing the power to the total volume of the device and to the amplitude of the input acceleration squared. This normalized power density with respect to the

fundamental resonance frequency provides an ideal figure of merit to compare the energy performances of the two harvesters considered in this study. To this end, the downscaling of the fundamental mechanical and electrical properties that characterise the components of the models (b) and (d) in Figure 4.2 is briefly revisited.

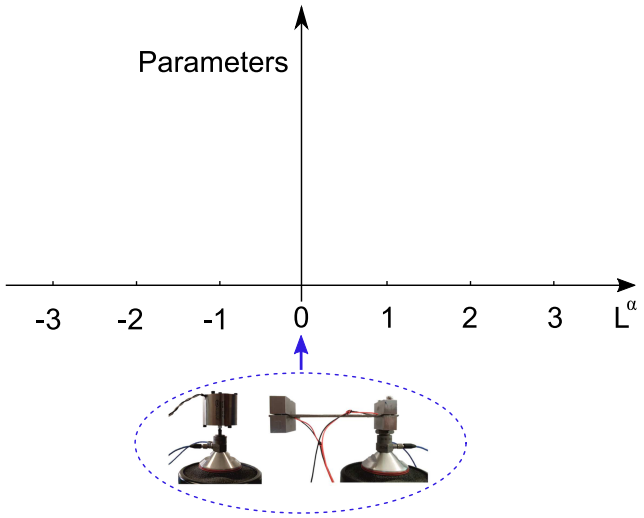

Figure 4.1: Scaling laws of the harvesters for different values of α.

A comparative analysis of the two harvesters is then proposed in section 4.7. The section closes with a comprehensive analysis of the stroke scaling of the two seismic transducers. The scaling of the reactive harvesters is finally presented in section 4.8.

4.1 LUMPED MODEL

Considering the schematics of the prototype electromagnetic and piezoelectric seismic harvesters shown in Figure 4.2 (a,c), the lumped parameter models vibrating-based energy harvesting transducers shown in Figure 4.2 (b,d) are taken into account for such study. Starting from the picture (a) of Figure 4.2, the electromagnetic harvester is formed by a permanent magnet free to move inside a voice coil housed in the external cylindrical case of the transducer. The magnet and external case are connected via soft spiral springs. Moving to Figure 4.2 (c), the piezoelectric harvester is formed by a cantilever beam blocked at the moving base and with a tip mass clamped at the other end. Two piezoelectric patches are bounded on the top and the

bottom of the beam laminate. As shown in Figure 4.2 (b,d), the two systems are modelled with consistent electromechanical parameter models; in particular are characterised by an electrical mesh and mechanical part joined together with *current-controlled force generator* and *relative velocity-controlled voltage generator* and with *voltage-controlled force generator* and *relative velocity-controlled current generator* respectively for the electromagnetic and piezoelectric harvester.

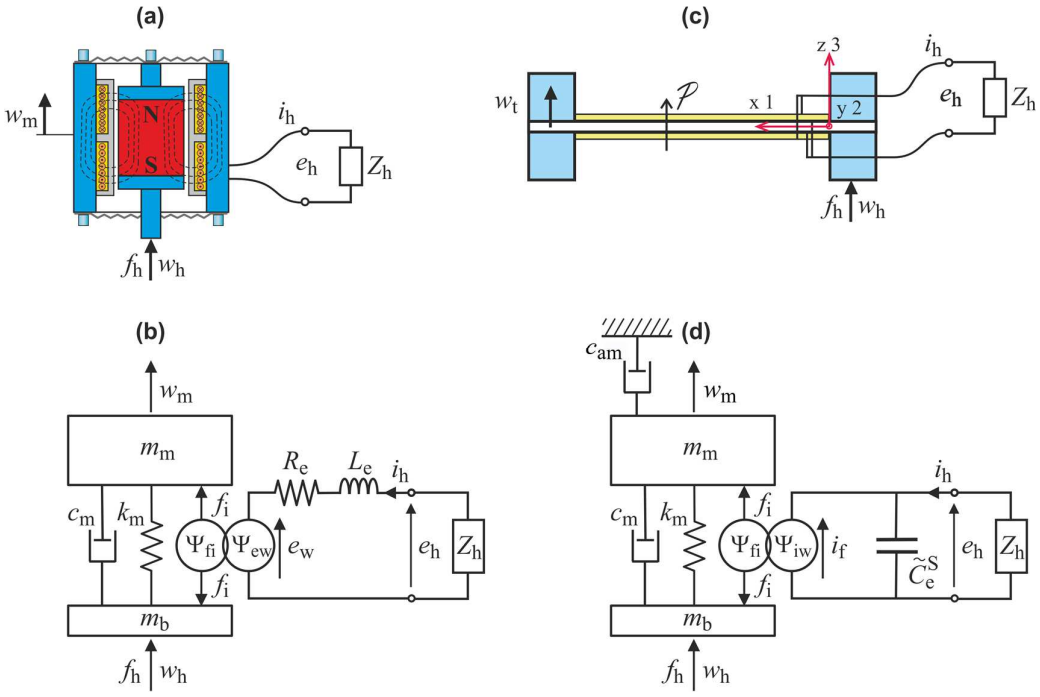

Figure 4.2: Functional drawings (a, c) and lumped parameter schematics (b, d), for the electromagnetic (left hand side) and piezoelectric (right hand side) seismic transducers.

For the scaling study it is assumed that the two transducers are connected either to optimal resistive and reactive or purely resistive harvesting loads. The analysis is restricted to steady state base excitation at the fundamental resonance frequency of the devices. In fact as shown in Appendix D, for tonal base excitation, the maximum power harvested by either electric loads occurs at a frequency close to the transducers fundamental natural frequency. This assumption gives the opportunity to simplify the model of the electromagnetic seismic harvester neglecting the lossy inductance effect that is particular effective only at frequencies above 1 KHz. Compared to Chapter 2, the air loading on the beam laminate, which produces a distributed sky-

hook viscous damping effect, is not neglected, since compared to the viscoelastic material losses, air damping widely varies with the scaling size. The constitutive equations and the energy and efficiency formulation of the electromagnetic and piezoelectric seismic transducers are derived with respect to the equivalent lumped parameter models shown in the schematics (b) and (d) of Figure 4.2.

4.2 CONSTITUTIVE EQUATIONS

In analogy to Ref.[185], the two harvesters are characterised in this study by the following two port network equations for the electromagnetic (4.1) and piezoelectric (4.2) harvester respectively:

$$\begin{bmatrix} f_h \\ e_h \end{bmatrix} = \begin{bmatrix} Z_{mi} & T_{fi} \\ T_{ew} & Z_{ei} \end{bmatrix} \begin{bmatrix} \dot{w}_h \\ i_h \end{bmatrix}, \tag{4.1}$$

$$\begin{bmatrix} f_h \\ i_h \end{bmatrix} = \begin{bmatrix} Z_{me} & T_{fe} \\ T_{iw} & Y_{ei} \end{bmatrix} \begin{bmatrix} \dot{w}_h \\ e_h \end{bmatrix}. \tag{4.2}$$

Here f_h, $\dot{w}_h$, e_h, i_h are the complex amplitudes of the force and velocity at the base and the voltage and current through the terminals of the seismic transducers. Based on the constitutive Eqs.(A.32)-(A.34) and (B.76), (B.77), (B.79), the mechanical impedance, electrical impedance and the two electromechanical transduction FRFs are given by the following expressions:

$$Z_{mi} = \left.\frac{f_h}{\dot{w}_h}\right|_{i_h=0} \\ Z_{me} = \left.\frac{f_h}{\dot{w}_h}\right|_{e_h=0} = Z_b + \frac{Z_s Z_m}{Z_t}, \tag{4.3a,b}$$

$$T_{fi} = \left.\frac{f_h}{i_h}\right|_{\dot{w}_h=0} \\ T_{fe} = \left.\frac{f_h}{e_h}\right|_{\dot{w}_h=0} = \Psi_{em}\frac{Z_m}{Z_t}, \tag{4.4a,b}$$

$$T_{ew} = \left.\frac{e_h}{\dot{w}_h}\right|_{i_h=0} \\ T_{iw} = \left.\frac{i_h}{\dot{w}_h}\right|_{e_h=0} = -\Psi_{me}\frac{Z_m}{Z_t}, \tag{4.5a,b}$$

$$Z_{ei} = \frac{e_h}{i_h}\Big|_{\dot{w}_h=0} = Z_e + \frac{\Psi_{em}\Psi_{me}}{Z_t}, \tag{4.6}$$

$$Y_{ei} = \frac{i_h}{e_h}\Big|_{\dot{w}_h=0} = \frac{1}{Z_e} + \frac{\Psi_{em}\Psi_{me}}{Z_t}, \tag{4.7}$$

where

$$Z_m = \mathrm{j}\omega m_m + c_{am}, \tag{4.8}$$

$$Z_b = \mathrm{j}\omega m_b, \tag{4.9}$$

$$Z_s = \frac{k_m}{\mathrm{j}\omega} + c_m, \tag{4.10}$$

$$Z_t = Z_s + Z_m = \frac{k_m}{\mathrm{j}\omega} + c_m + c_{am} + \mathrm{j}\omega m_m. \tag{4.11}$$

For the electromagnetic harvester c_m can be specified as follows:

$$c_m = c_a + c_{ec}. \tag{4.12}$$

Also, for the coil-magnet transducer:

$$Z_e = R_e + \mathrm{j}\omega L_e, \tag{4.13}$$

while for the piezoelectric transducer:

$$Z_e = \frac{1}{\mathrm{j}\omega \tilde{C}_e} = \frac{1}{\mathrm{j}\omega C_e^s(1 - j\eta_c)}. \tag{4.14}$$

Finally, the transduction terms Ψ_{em} and Ψ_{me} for the electromagnetic and the piezoelectric harvesters are given respectively by:

$$\Psi_{em} = \Psi_{me} = \psi_{CM} = Bl, \tag{4.15}$$

$$\Psi_{em} = \Psi_{me} = \psi_{PZT} = \bar{e}_{31} b\big(h_s + h_{pe}\big)\frac{\phi_1'(L)}{\phi_1(\bar{x})}. \tag{4.16}$$

For both devices m_b, m_m, k_m are the base mass, proof mass and the suspension stiffness. The terms c_m and c_{am} represent the total internal and external damping coefficients due respectively to the relative and absolute motion of the harvester components. In particular, for the coil magnet, the damping coefficient c_m is composed by two contributes c_{ec} and c_a ,which represent the effect of the repulsive force generated by the eddy currents into the Yoke and the viscous Couette air damping acting between the inner gap of the moving magnet and the internal cylindrical surface of the housing case [202]. Moving to the piezoelectric device, the damping coefficient c_m represents the structural internal damping while c_{am} identifies the contribution of air damping, which acts on the absolute velocity of the moving mass. For the electromagnetic harvester, compared to the other loss effects, the effect of the squeeze air damping that develops on the cylindrical housing Yoke can be neglected and thus c_{am} is considered negligible. Furthermore, R_e and L_e are the electrical resistance and inductance of the electromagnetic coil while $C_e^S = C_e^T(1 - k_{31}^2)$ is the capacitance of the piezoelectric layers under constant strain, where k_{31}^2 is the electromechanical coupling factor of the piezoelectric material [184]. Also, $\eta_C(\omega) = \sigma_{pe}/\bar{\varepsilon}_{33}^S\omega$ is the dielectric loss factor of the piezoelectric material [180]–[183] introduced to identify the lossy capacitance under constant strain $\tilde{C}_e^S = C_e^s(1 - j\eta_C)$.

Moving to the transduction factors, for the electromagnetic harvester, B is the magnetic flux density of the permanent magnet and l is the length of the winding coil [184]–[186], [188]. Also, for the piezoelectric harvester $\phi_1(x)$ and $\phi_1'(x) = \frac{\mathrm{d}\phi_1(x)}{\mathrm{d}x}$ are the amplitude and slope of the first flexural mode of the composite clamped beam with the tip mass attached at the end, b is the width of the metallic substrate and piezoelectric layers, h_s, h_{pe} are respectively the thickness of the beam and the single piezoelectric layer and $\bar{e}_{31}$ is the stress/charge constant for the piezoelectric material [72]. Finally, as discussed in Chapter 2 and in Appendix B, $\bar{x}$ identifies a specific point along the beam, which allows the derivation of the lumped equivalent model shown in Figure 4.2 (d).

The FRFs T_{fi} and T_{ew} derived in Eq.(4.1) represent the electromechanical transduction FRFs for the electromagnetic seismic device, which gives the base force effect produced by the transducer per unit current flowing in the blocked seismic harvester, i.e. $T_{fi} = f_h/i_h|_{\dot{w}_h=0}$, and the electromotive force generated at the terminals of the transducer per unit velocity at the base of the open circuit seismic transducer, i.e. $T_{ew} = e_h/\dot{w}_h|_{i_h=0}$. Analogously the FRFs T_{fe}, T_{iw} derived in Eq.(4.2) represent the electromechanical transduction FRFs for the piezoelectric seismic device, which

provide the base force generated by the transducer per unit of voltage imposed across the electric circuit in the blocked seismic transducer, i.e. $T_{fe} = f_h/e_h|_{\dot{w}_h=0}$ and the current generated per unit velocity at the base of the short circuited seismic transducer, i.e. $T_{iw} = i_h/\dot{w}_h|_{e_h=0}$. Finally, $Z_{ei} = e_h/i_h|_{\dot{w}_h=0}$, $Y_{ei} = i_h/e_h|_{\dot{w}_h=0}$ and $Z_{mi} = f_b/\dot{w}_h|_{i_h=0}$, $Z_{me} = f_b/\dot{w}_h|_{e_h=0}$ are the output electrical impedance and admittance of the blocked seismic transducer and the input mechanical impedance in the open and short circuited electrical configuration for the electromagnetic and piezoelectric harvesters respectively.

4.3 ENERGY AND EFFICIENCY FORMULATION FOR THE SCALING STUDY OF THE ELECTROMAGNETIC HARVESTER

As derived in Appendix D.1, when the optimal complex electric load $Z_h = Z_{ei}^*$ given in Eq.(2.32) and depicted in Plot (a) of Figure 2.7 is implemented, for both transducers the harvested power is maximized in correspondence of their fundamental mechanical natural frequency. Also, based on Plots (a, b) of Figure 2.10, if the harvesting circuit implements at each frequency the optimal real impedance $Z_s = |Z_{ei}|$ derived in Eq.(2.34) and depicted in Plot (a) of Figure 2.9, the spectrum of the harvested power is characterised by a sharp peak at the fundamental resonance frequency. Thus, based on these results it is reasonable to focus the scaling study of the electromagnetic and piezoelectric harvesters with reference to a tonal excitation whose frequency is close to their fundamental mechanical frequency; that is a frequency where the power harvested is maximum and thus the seismic harvester should operate.

4.3.1 Harvested power

When the electromagnetic transducer is used for energy harvesting purposes, an electric load of impedance Z_h is connected at the terminals of the electrical circuit. Assuming time harmonic constant excitation $\dot{w}_h$ at the base, the relation between the voltage at the terminals e_h and the current i_h, which flows through the circuit, is:

$$e_h = -Z_h i_h, \tag{4.17}$$

where Z_h is the electrical load impedance of the harvesting circuit.
Substituting Eq.(4.17) into Eq.(4.1), it follows:

$$i_h = -\frac{T_{ew}}{Z_{ei} + Z_h}\dot{w}_h. \tag{4.18}$$

The power harvested to the load results:

$$\bar{P}_h = \frac{1}{2}\mathrm{Re}\{Z_h\}|i_h|^2 = \frac{1}{2}\mathrm{Re}\{Z_h\}\left|-\frac{T_{ew}}{Z_{ei} + Z_h}\right|^2 |\dot{w}_h|^2. \tag{4.19}$$

As seen in Chapter 2, according to the Fermat's theorem [195], the complex electric load Z_h, which maximizes the harvested power at each frequency is given by:

$$Z_h = Z_{ei}^*, \tag{4.20}$$

where * denotes the complex conjugate.
Instead, if Z_h is assumed to be purely real, the optimal electric load becomes:

$$Z_{h,R} = |Z_{ei}|. \tag{4.21}$$

Substituting in Eq.(4.19) the two optimal electrical impedances given in Eqs.(4.20) and (4.21) the following expressions for the maximum power harvested are derived:

$$\bar{P}_h = \frac{1}{8}\frac{|T_{ew}|^2}{\mathrm{Re}\{Z_{ei}\}}|\dot{w}_h|^2, \tag{4.22}$$

$$\bar{P}_h = \frac{1}{4}\frac{|T_{ew}|^2}{|Z_{ei}| + \mathrm{Re}\{Z_{ei}\}}|\dot{w}_h|^2, \tag{4.23}$$

for the complex and purely real electric loads respectively.
Specifying Eqs.(4.22), (4.23) for a time harmonic excitation $\dot{w}_h$ tuned to the fundamental natural frequency i.e. $\omega = \omega_n = \sqrt{k_m/m_m}$ of the electromechanical transducer gives:

$$\bar{P}_h = \frac{1}{8}\frac{k_m m_m}{c_m}\frac{\mathrm{C}_{eml}}{1 + \mathrm{C}_{eml}}|\dot{w}_h|^2, \tag{4.24}$$

$$\bar{P}_{h,R} = \frac{1}{4}\frac{k_m m_m}{c_m}\frac{1}{\rho_c}|\dot{w}_h|^2, \tag{4.25}$$

where ρ_c was defined as $\rho_c \triangleq \frac{1+\mathrm{C}_{eml}}{\mathrm{C}_{eml}} + \sqrt{\left(\frac{1+\mathrm{C}_{eml}}{\mathrm{C}_{eml}}\right)^2 + \left(\frac{1}{\mathrm{C}_{emh}}\right)^2}$ and, in analogy to Ref. [203], C_{eml} is identified as the non-dimensional electromagnetic coupling coefficient at low frequencies:

$$\mathrm{C}_{eml} = \frac{(Bl)^2}{c_m R_e}. \tag{4.26}$$

This coefficient is defined as the ratio between the mechanical impedances of the base driven electromechanical transducer excited in correspondence of its mechanical natural frequency ω_n, respectively when the electrical circuit of the device is opened and short-circuited and the value of the mechanical natural frequency ω_n is lower than the cut-off frequency $\omega_c = R_e/L_e$.

In addition, a high frequencies non-dimensional electromagnetic coupling coefficient C_{emh} can be derived:

$$\mathrm{C}_{emh} = \frac{(Bl)^2}{\omega_n c_m L_e}, \tag{4.27}$$

which is defined as the ratio between the transducer mechanical impedances calculated in correspondence of its mechanical natural frequency ω_n respectively when the circuit of the harvester is opened and short-circuited and the mechanical natural frequency ω_n is higher compared to the cut-off frequency ω_c. (For more details see Appendix D.2).

4.3.2 Input power

Substituting in Eq.(4.1) the expression of the current i_h derived in Eq. (4.18), the mechanical response of the electromagnetic harvester can be interpreted in terms of its base impedance:

$$Z_{mh} = \frac{f_h}{\dot{w}_h} = Z_{mi} - \frac{T_{ew}T_{fi}}{Z_{ei} + Z_h}, \tag{4.28}$$

where f_h and $\dot{w}_h$ are the time harmonic force and velocity at the base of the transducer and Z_{mh} is the mechanical base impedance.
For harmonic vibrations, the time average mechanical input power is given by:

$$\bar{P}_i = \frac{1}{2}\mathrm{Re}\{Z_{mh}\}|\dot{w}_h|^2 = \frac{1}{2}\mathrm{Re}\left\{Z_{mi} - \frac{T_{ew}T_{fi}}{Z_{ei}+Z_h}\right\}|\dot{w}_h|^2. \tag{4.29}$$

The above expression can then be straightforwardly specified for the two optimal electrical impedances derived in Eq.(4.20) and (4.21):

$$\bar{P}_i = \frac{1}{2}\mathrm{Re}\left\{Z_{mi} - \frac{T_{ew}T_{fi}}{2\mathrm{Re}\{Z_{ei}\}}\right\}|\dot{w}_h|^2, \tag{4.30}$$

$$\bar{P}_{i,R} = \frac{1}{2}\mathrm{Re}\left\{Z_{mi} - \frac{T_{ew}T_{fi}}{Z_{ei}+|Z_{ei}|}\right\}|\dot{w}_h|^2. \tag{4.31}$$

Considering $\omega = \omega_n = \sqrt{k_m/m_m}$, the two equations above reduces to the following expressions respectively for the optimal complex and purely real harvester loads:

$$\bar{P}_i = \frac{1}{4}\frac{k_m m_m}{c_m}\frac{2+\mathrm{C}_{eml}}{1+\mathrm{C}_{eml}}|\dot{w}_h|^2 \tag{4.32}$$

$$\bar{P}_{i,R} = \frac{1}{2}\frac{k_m m_m}{c_m}\left[1 - \frac{\rho_c}{{\rho_c}^2 + \left(\frac{1}{\mathrm{C}_{emh}}\right)^2}\right]|\dot{w}_h|^2. \tag{4.33}$$

4.3.3 Efficiency

From Eq.(2.43) the power harvesting efficiency E is defined as:

$$E = \frac{\bar{P}_h}{\bar{P}_i}, \tag{4.34}$$

where $\bar{P}_h$ and $\bar{P}_i$ are the time average harvested and input power. Thus, substituting Eq.(4.19) and Eq.(4.29) into Eq.(4.34) gives:

$$E = \frac{\mathrm{Re}\{Z_h\}\left|-\frac{T_{ew}}{Z_{ei}+Z_h}\right|^2}{\mathrm{Re}\left\{Z_{mi}-\frac{T_{ew}T_{fi}}{Z_{ei}+Z_h}\right\}}. \tag{4.35}$$

Implementing the optimal complex impedance $Z_h = Z_{ei}^*$, or the optimal real impedance, $Z_{h,R} = |Z_{ei}|$, the above expression becomes respectively:

$$E = \frac{1}{4}\frac{|T_{ew}|^2}{\mathrm{Re}\{Z_{ei}\}\mathrm{Re}\left\{Z_{mi}-\frac{T_{ew}T_{fi}}{2\mathrm{Re}\{Z_{ei}\}}\right\}}, \tag{4.36}$$

$$E_R = \frac{1}{2}\frac{\frac{|T_{ew}|^2}{|Z_{ei}|+\mathrm{Re}\{Z_{ei}\}}}{\mathrm{Re}\left\{Z_{mi}-\frac{T_{ew}T_{fi}}{Z_{ei}+|Z_{ei}|}\right\}}. \tag{4.37}$$

Assuming $\omega = \omega_n = \sqrt{k_m/m_m}$, the two equations above become:

$$E = \frac{\mathrm{C}_{eml}}{4+2\mathrm{C}_{eml}}, \tag{4.38}$$

$$E_R = \frac{1}{2}\frac{1}{\rho_c}\frac{\rho_c^2+\left(\frac{1}{\mathrm{C}_{emh}}\right)^2}{\rho_c^2+\left(\frac{1}{\mathrm{C}_{emh}}\right)^2-\rho_c}, \tag{4.39}$$

respectively for optimal resistive-reactive and purely real harvesting load.

4.4 ELECTROMAGNETIC HARVESTER: SCALING LAWS

In the following subsection, the scaling laws for the principal physical properties of the electromagnetic transducer depicted in Plot (a) of Figure 4.2 are first revised. The downscaling of the normalized power density and efficiency is then considered.

4.4.1 Physical parameters

The derivation of the scaling laws for the power harvested and efficiency is characterised by the scaling of the coupling coefficients C_{eml} and C_{emh}. These two

terms are identified by the principal mechanical and electrical elements that compose the lumped model of the seismic transducer shown in Figure 4.2 (b). The scaling laws of such parameters are depicted below.

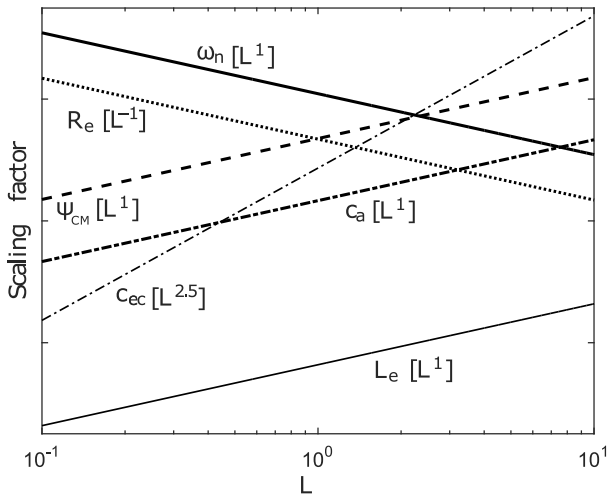

Figure 4.3: Scaling laws of the Couette air film damping coefficient c_a (dash-dotted line) and eddy current damping c_{ec} (thin dash-dotted line), mechanical natural frequency ω_n (solid line), electrical resistance R_e (dotted line), transduction coefficient ψ_{CM} (dashed line), inductance L_e (thin solid line).

Figure 4.3 shows that, as the size of the transducer is scaled up, the fundamental natural frequency ω_n and the electric resistance R_e tend to decrease inversely to the dimension i.e. $[L^{-1}]$, while the air damping coefficient c_a , the electric inductance L_e and the transduction coefficient ψ_{CM} rise up proportionally to dimension i.e. $[L]$. Finally the eddy current damping c_{ec} scales as the power of $[L^{2.5}]$. As discussed by Gardonio and Gonzalez [204], the proof mass of the electromagnetic device can be calculated as $m_m = \rho\pi\emptyset^2 h/4$, where $\emptyset$, h and ρ are the outer diameter , height and average density respectively and thus scales as the cube of the dimension i.e. $[L^3]$. Also, the suspension stiffness can be calculated as [205] $k_m = 3EA/h$,where E, A and h are respectively the Young's modulus of elasticity of the material and the base area and height of the spiral springs of the transducer. So, the stiffness scales linear to the dimension i.e. $[L]$. As a result, the mechanical natural frequency $\omega_n = \sqrt{k_m/m_m}$ scales with the inverse of the first power of dimension i.e. $[L^{-1}]$. The transduction coefficient is defined as $\Psi_{em} = \Psi_{me} = \Psi_{CM} = Bl$, where B is the magnetic flux density, which as shown in Refs. [206], [207] remains unchanged with scaling, i.e.$[L^0]$, and l is the

length of the winding coil. It follows that the transduction coefficient scales down with the first power of dimension, i.e.$[L]$. The electrical resistance of the coil wire is given by [203] $R_e = \rho_e l/A$, where ρ_e is the resistivity of the wire material (independent with scaling i.e.$[L^0]$), l is the length of the wire and A is the cross sectional area of the wire too. Thus R_e clearly scales with the inverse of the first power of dimension i.e. $[L^{-1}]$.
The detailed derivation of the scaling laws for the viscous air damping coefficient c_a, the eddy current damping c_{ec} and the inductance L_e are reported in Appendix D.4.

4.4.2 Power and efficiency

Recalling Eqs.(4.24), (4.25) and considering the results shown in Figure 4.3, the scaling laws of the harvested power density and efficiency for the electromechanical transducer have been derived numerically considering the physical parameters of the prototype depicted in Plot (a) of Figure 2.1 and listed in Table 2-1.
Figure 4.4 shows the scaling laws of the harvested power normalized to the total volume of the device per unit of 1g base acceleration for $\omega = \omega_n = \sqrt{k_m/m_m}$ and for the optimal complex (Plot (a)) and purely real (Plot (b)) electric loads. The source acceleration $1g$ at the base of the electromechanical transducer is assumed regardless of the harvester dimension.

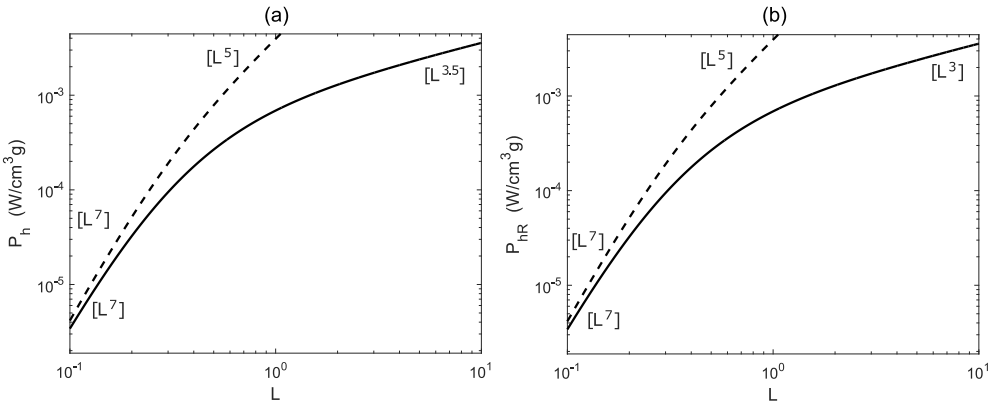

Figure 4.4: Scaling law of the power harvested density P_h implementing (a) the optimal complex electric load and (b) the optimal purely real electric load when the effect of the eddy currents c_{ec} is present (solid line) and is neglected (dashed line).

Analysis of Plots (a, b) in Figure 4.4 shows that for both optimal electric loads implemented the electromagnetic harvester is characterised by higher power density at largescale, in particular if the effect of the eddy currents that develops in the ferromagnetic outer ring is annihilated. In fact, the upper bound of the normalized power density in both plots suggests that a much higher upper limit can be reached if the eddy current losses are removed from the transducer.

On the contrary, reducing the dimension of the device, the power density decreases to a point it converges to the same scaling law i.e.$[L^7]$ for either types of losses and for both optimal harvesting load configurations. This effect, can be explained by the fact that the Couette air damping losses completely dominate over the eddy current losses, which, therefore, become negligible at small scales.

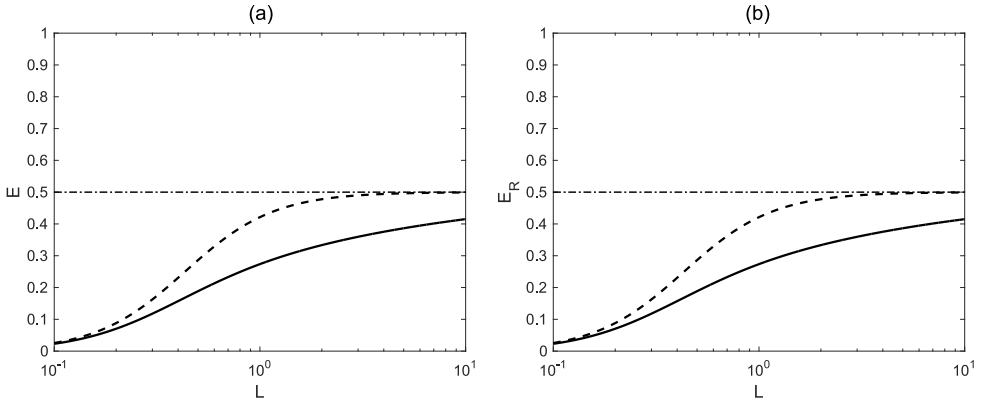

Figure 4.5: Scaling laws of the efficiency implementing (a) the optimal complex and (b) optimal purely real electrical loads when the effect of the eddy currents c_{ec} is present (solid line) and is neglected (dashed line).

Moving to the analysis of the efficiency, Figure 4.5 shows the variation of the power efficiency with the scale dimension of the electromagnetic harvester when the optimal complex (Plot (a)) and the purely real (Plot (b)) electric loads are implemented. Taking into account Figure 4.5 (a) and considering Eq.(4.38), it results that the efficiency is only dependent on the electromechanical coupling coefficient C_{eml} whose scaling law can be derived from inspection of Eq.(4.26) and Figure 4.3 . It follows that the harvesting performances of the electromagnetic seismic harvester increases with the size and reaches the maximum value of 0.5, for which very low power is absorbed from the mechanical damper of the transducer and equal power is dissipated from its internal resistance and harvested to the electric load. The same conclusions can be

drawn for the real harvesting load. Considering Figure 4.5 (b) and Eq.(4.39), the inductance scaling effect is also present via the contribution of the non-dimensional electromagnetic coupling factor C_{emh}, defined in Eq.(4.27) and derived in Appendix D.2.

It is interesting to note that assuming for the electromagnetic harvester a damping coefficient c_m that, as proposed in Ref. [203], scales as the square of the power i.e. $[L^2]$, the coefficient C_{emh} remains unchanged with scaling i.e. $[L^0]$ and Eq.(4.25) can be approximated to Eq.(4.24), implying that no distinction can be made between the two scaling efficiency configurations shown in graphs (a) and (b) of Figure 4.5.

4.5 ENERGY AND EFFICIENCY FORMULATION FOR THE SCALING STUDY OF THE PIEZOELECTRIC HARVESTER

This section presents and discusses the scaling behaviour of the power density and efficiency for the piezoelectric seismic harvester. In the following subsection the energy and efficiency formulation is derived for either the optimal complex and purely real electric loads and then specified at the fundamental natural frequency of the transducer, where the maximum power absorption occurs for tonal vibrations.

4.5.1 Energy harvesting

The scaling study for the harvested power density and efficiency of the piezoelectric seismic harvester was implemented using a similar formulation to that presented above for the electromagnetic harvester. In this case, assuming a time harmonic constant excitation $\dot{w}_h$ at the base, the current i_h that flows through the terminals of the electrical impedance was assumed:

$$i_h = -e_h Y_h, \tag{4.40}$$

where e_h is the voltage across the terminals of the electrical load and Y_h is its admittance, defined as the inverse of the electric impedance of the harvesting load connected across the terminals of the transducer.

Substituting Eq.(4.40) into Eq.(4.2), the relation between the voltage e_h and the base velocity $\dot{w}_h$ can be written as:

$$e_h = \frac{-T_{iw}}{Y_{ei} + Y_h} \dot{w}_h. \tag{4.41}$$

Thus the time averaged power harvested to the generic load results:

$$\bar{P}_h = \frac{1}{2}\mathrm{Re}\{Y_h\}|e_h|^2 = \frac{1}{2}\mathrm{Re}\{Y_h\}\left|\frac{-T_{iw}}{Y_{ei} + Y_h}\right|^2 |\dot{w}_h|^2. \tag{4.42}$$

It is now straightforward finding that Eq.(4.42) is maximized with respect to the electric admittance if

$$Y_h = Y_{ei}^*, \tag{4.43}$$

$$Y_{h,R} = |Y_{ei}|, \tag{4.44}$$

where Eqs.(4.43), (4.44) refer to an optimal resistive-reactive or purely resistive load respectively. These results match with what found for the coil magnet in Eqs.(4.20), (4.21) and for both transducers in Eqs.(3.22), (3.24) of Chapter 2.
Substituting in Eq.(4.42) Eqs.(4.43) and (4.44), the following expressions are derived for the maximum power harvested for the resistive-reactive (Eq.(4.45)) and purely resistive (Eq.(4.46)) electric load respectively:

$$\bar{P}_h = \frac{1}{8}\frac{|T_{iw}|^2}{\mathrm{Re}\{Y_{ei}\}}|\dot{w}_h|^2, \tag{4.45}$$

$$\bar{P}_{h,R} = \frac{1}{4}\frac{|T_{iw}|^2}{|Y_{ei}| + \mathrm{Re}\{Y_{ei}\}}|\dot{w}_h|^2. \tag{4.46}$$

Specifying Eqs.(4.45), (4.46) at the fundamental natural frequency of the piezoelectric transducer i.e. $\omega = \omega_n = \sqrt{k_m/m_m}$, it follows that:

$$\bar{P}_h = \frac{1}{8}\frac{k_m m_m}{c_m}\frac{\mathrm{C}_{PZ}}{\eta_C + \mathrm{C}_{PZ}}|\dot{w}_h|^2, \tag{4.47}$$

$$\bar{P}_{h,R} = \frac{1}{2}\frac{k_m m_m}{c_m}\frac{\mathrm{C}_{PZ}\,\rho_d}{1 + (\mathrm{C}_{PZ} + \eta_C + \rho_d)^2}|\dot{w}_h|^2, \tag{4.48}$$

where ρ_d was defined as $\rho_d \triangleq \sqrt{1+(\mathrm{C}_{PZ}+\eta_C)^2}$ and, in analogy to the electromechanical harvester, C_{pz} identifies the non-dimensional piezoelectric coupling coefficient:

$$\mathrm{C}_{pz} = \frac{\psi_{PZT}^2}{\omega_n C_e^s (c_m + c_{am})}, \tag{4.49}$$

defined as the ratio between the mechanical impedances of the base driven piezoelectric transducer respectively in short circuit and open circuit condition (for more details see Appendix D.2).
Also, inspection of the formulas in Eqs.(4.47) and (4.48) show that the frequency dependent dielectric loss factor of the material $\eta_C(\omega)$ introduced in Chapter 2 and derived in Appendix B.2 is now defined in correspondence of the fundamental natural frequency of the piezoelectric transducer:

$$\eta_C = \frac{\sigma_{pe}}{\omega_n \bar{\varepsilon}_{33}^s}, \tag{4.50}$$

where σ_{pe} and $\bar{\varepsilon}_{33}^s$ are respectively the conductivity and the electrical permittivity of the piezoelectric material under constant strain [181].

4.5.2 Input power

Substituting Eq.(4.41) in Eq.(4.1), the mechanical response of the piezoelectric harvester can be written in terms of its base impedance:

$$Z_{mh} = \frac{f_h}{\dot{w}_h} = Z_{me} - \frac{T_{fe}T_{iw}}{Y_{ei}+Y_h}, \tag{4.51}$$

where f_h and $\dot{w}_h$ are the time harmonic force and velocity at the base and Z_{mh} is the mechanical impedance.
So, for harmonic vibrations, the time average mechanical input power is given by:

$$\bar{P}_i = \frac{1}{2}\mathrm{Re}\{Z_{mh}\}|\dot{w}_h|^2 = \frac{1}{2}\mathrm{Re}\left\{Z_{me} - \frac{T_{fe}T_{iw}}{Y_{ei}+Y_h}\right\}|\dot{w}_h|^2. \tag{4.52}$$

This expression can now be specified for the two optimal electrical admittances derived in Eqs.(4.43) and (4.44):

$$\bar{P}_i = \frac{1}{2}\mathrm{Re}\left\{Z_{me} - \frac{T_{fe}T_{iw}}{2\mathrm{Re}\{Y_{ei}\}}\right\}|\dot{w}_h|^2, \tag{4.53}$$

$$\bar{P}_{i,R} = \frac{1}{2}\mathrm{Re}\left\{Z_{me} - \frac{T_{fe}T_{iw}}{Y_{ei} + |Y_h|}\right\}|\dot{w}_h|^2, \tag{4.54}$$

which in correspondence of the mechanical natural frequency of the harvester i.e. $\omega = \omega_n = \sqrt{k_m/m_m}$ can be written as:

$$\bar{P}_i = \frac{1}{4}\frac{k_m m_m}{c_m}\frac{2\eta_C + \mathrm{C}_{PZ}}{\eta_C + \mathrm{C}_{PZ}}|\dot{w}_h|^2, \tag{4.55}$$

$$\bar{P}_{i,R} = \frac{1}{2}\frac{k_m m_m}{c_m}\left[1 - \mathrm{C}_{PZ}\frac{\mathrm{C}_{PZ} + \eta_C + \rho_d}{1 + \left(\mathrm{C}_{PZ} + \eta_C + \rho_d\right)^2}\right]|\dot{w}_h|^2. \tag{4.56}$$

4.5.3 Efficiency

The power efficiency $E = \bar{P}_h/\bar{P}_i$ can now be specified for the piezoelectric energy harvester using Eq.(4.42) and Eq.(4.52):

$$E = \frac{\mathrm{Re}\{Y_h\}\left|\frac{T_{iw}}{Y_{ei} + Y_h}\right|^2}{\mathrm{Re}\left\{Z_{me} - \frac{T_{fe}T_{iw}}{Y_{ei} + Y_h}\right\}}. \tag{4.57}$$

Thus, considering the optimal complex load of admittance $Y_h = Y_{ei}^*$, or the optimal purely real load of admittance $Y_{h,R} = |Y_{ei}|$ derived respectively in Eqs.(4.43) and (4.44), the above expression becomes:

$$E = \frac{1}{4}\frac{|T_{iw}|^2}{\mathrm{Re}\{Y_{ei}\}\,\mathrm{Re}\left\{Z_{me} - \frac{T_{fe}T_{iw}}{2\mathrm{Re}\{Y_{ei}\}}\right\}}, \tag{4.58}$$

$$E_R = \frac{1}{2}\frac{|T_{iw}|^2}{(|Y_{ei}| + Re\{Y_{ei}\})\,Re\left\{Z_{me} - \frac{T_{fe}T_{iw}}{Y_{ei} + |Y_{ei}|}\right\}}, \tag{4.59}$$

which, assuming $\omega = \omega_n = \sqrt{k_m/m_m}$ become:

$$E = \frac{\mathrm{C}_{PZ}}{4\,\eta_C + 2\mathrm{C}_{PZ}} \tag{4.60}$$

$$E_R = \frac{\mathrm{C}_{PZ}\,\rho_d}{[(\mathrm{C}_{PZ} + \eta_C + \rho_d)^2 + 1] - \mathrm{C}_{PZ}[\mathrm{C}_{PZ} + \eta_C + \rho_d\,]}, \tag{4.61}$$

respectively for the optimal complex and purely real electric loads.

4.6 PIEZOELECTRIC HARVESTER: SCALING LAWS

In this subsection the scaling laws of the fundamental electrical and mechanical physical parameters of the piezoelectric transducer depicted in schematic (c) of Figure 4.2 are first revised. The downscaling of the normalized harvested power density and efficiency are then considered.

4.6.1 Physical parameters

As for the electromagnetic harvester, the scaling of the power density and efficiency of the piezoelectric transducer can be derived analysing how the fundamental mechanical and electrical coefficients in Eqs.(4.47), (4.48), (4.60), (4.61) vary with the scaling of dimension. With reference to the data of the prototype shown in Plot (d) of Figure 2.1 and listed in Table 2-2, the following numerical simulations of the scaling parameters are derived.

Figure 4.6 shows that, increasing the size of the piezoelectric harvester, the fundamental natural frequency ω_n decreases inversely as $[L^{-1}]$, since the equivalent moving mass m_m and the stiffness k_m of the lumped parameter model scale respectively as $[L^3]$ and $[L^1]$. The scaling law of the material damping c_m, as well as the piezoelectric transduction coefficient ψ_{PZT}, the dielectric loss factor η_c and the electric capacitance C_e^S varies as the first power of the dimension, i.e. $[L^1]$. Finally the viscous air damping coefficient c_{am} acting on the surface of the cantilever beam scales with the power of 1.7 i.e. $[L^{1.7}]$ [208]. The derivation of the scaling laws for each mechanical and electrical coefficient shown in Figure 4.6 requires a somewhat more elaborate analysis of the electromagnetic parameters and are reported in Appendix D.5.

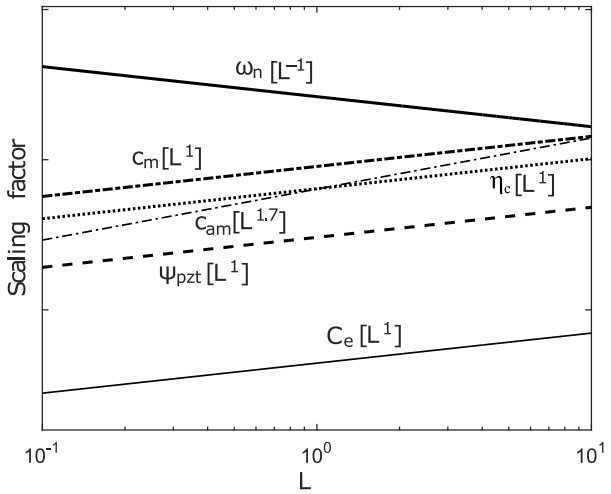

Figure 4.6: Scaling laws of air damping coefficient c_{am} (thin dash-dotted line) and material damping c_m (dash dotted line), mechanical natural frequency ω_n (solid line), dielectric loss factor η_c (dotted line), transduction coefficient Ψ_{PZT} (dashed line), capacitance C_e (thin solid line).

4.6.2 Power and Efficiency

The simulated scaling laws of the power density and efficiency for the piezoelectric energy harvester is now analysed. Figure 4.7 shows the scaling laws of the harvested power density normalized to harmonic acceleration of amplitude 1g for both optimal electric loads considered in this study (complex and purely real) when the contribution of the air damping is neglected (dashed line) and when is taken into account (solid line). Plots (a, b) indicate that for both optimal harvesting loads the normalized power density increases as the size of the device is larger. Also, as can be noticed in both graphs, the additional contribution of the air damping (solid line) compared to material damping only (dashed line) reduces the normalized power density of very large harvesters. This effect, particularly visible at the higher scaling end, can be explained by the fact that at large dimensions the air damping becomes predominant and reduces the stroke of the seismic mass, thus reducing the amount of power that could be harvested (see Plots (b) of Figure 4.12 and Figure 4.13).

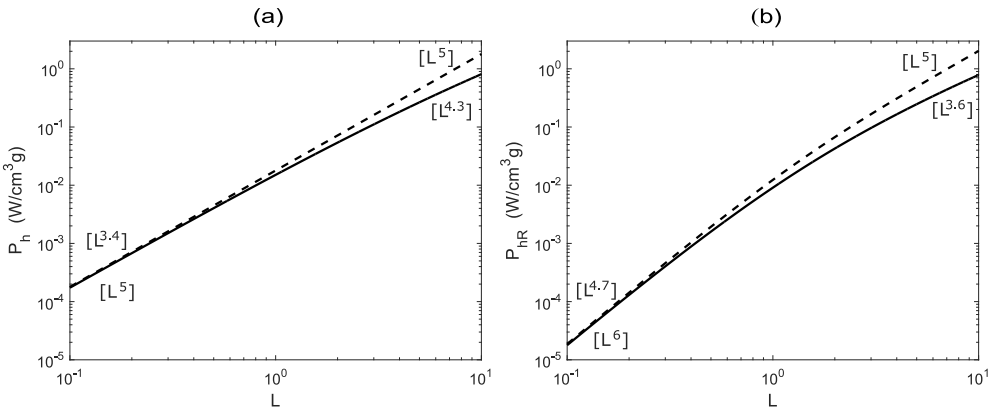

Figure 4.7: Scaling laws of the harvested power density P_h implementing (a) the optimal complex electric load and (b) the optimal purely real electrical load when the effect of the air damping c_{am} is present (solid line) and neglected (dashed line).

Moving to power efficiency, Plot (a) in Figure 4.8 shows that when the optimal complex impedance load given in Eq.(4.43) is implemented, the piezoelectric seismic harvester is characterised by a somewhat constant efficiency, which decreases proportionally to $[L^{-0.7}]$ as the size of the device increases. If the air damping effect is neglected the efficiency becomes constant.

Moving to Plot (b) of Figure 4.8, when the configuration with the optimal purely real electric load derived in Eq. (4.44) is considered, the efficiency of the device increases with dimension and, in case of solely material damping contribution (dashed line), converges to the same constant value obtained in Figure 4.8(a) for the complex impedance load when the effect of the air damping is not taken into account. If the contribution of the squeeze air damping is also considered (solid line), the efficiency has a maximum value for a particular size and then falls down at larger scale.

Dielectric losses in the piezoelectric layers of the seismic harvester strongly influence the scaling laws for the harvesting power and harvesting efficiency. Figure 4.9 shows an important scaling effect related to these losses, that originates in the piezoelectric patches of the harvester and are modelled as a loss factor $\eta_c(\omega_n) = \sigma_{pe}/\varepsilon_{33}^S\omega_n$ in the lumped parameter model.

Plot (a) of Figure 4.9 shows that, incrementing the performances of the piezoelectric layers of the transducer and thus reducing the dielectric losses of the material (i.e. $\sigma_{pe} \to 0$) the power efficiency of the harvester increases reaching the maximum theoretical value of 0.5. This result demonstrates that if the air damping can be

neglected (for example if the device works in vacuum) a constant efficiency of 0.5 can be obtained independently from the scaling size if the optimal resistive reactive electric load is implemented. In this particular condition, equal power is dissipated by the inherent mechanical damping effect in the transducer and harvested in the external optimal electrical load.

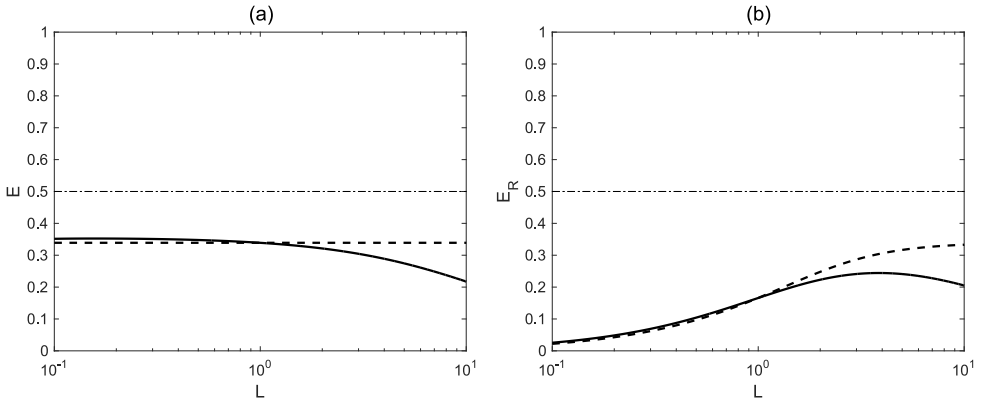

Figure 4.8: Variation of the power efficiency of the piezoelectric transducer implementing (a) the optimal complex electric load and (b) the optimal purely real electric load when the effect of the air damping c_{am} is present (solid line) and is neglected (dashed line).

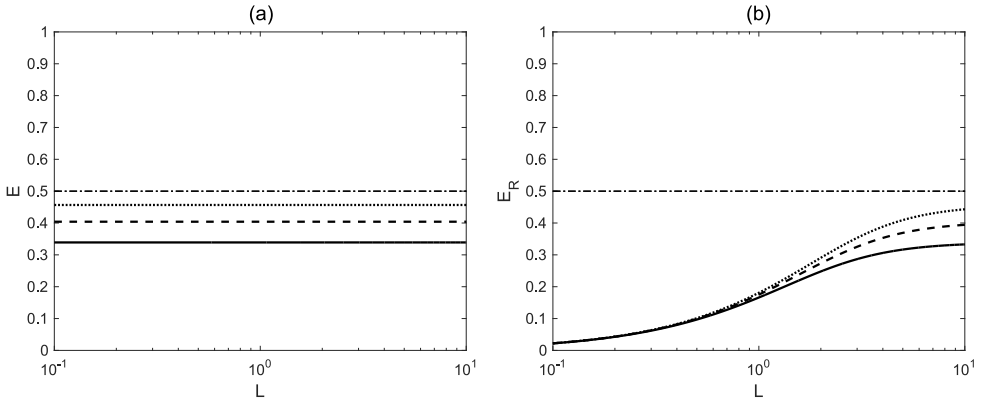

Figure 4.9: Variation of the power efficiency of the piezoelectric transducer implementing (a) the optimal complex electric load and (b) the optimal purely real electrical load when the air damping c_a is neglected and for different values of the piezoelectric conductivity σ_{pe}: 0.7 σ_{pe} (solid line), 0.5 σ_{pe} (dashed line), 0.3 σ_{pe} (dash dotted line).

According to Plot (b), a maximum theoretical efficiency of 0.5 can also be reached for large-scale size if the optimal purely resistive electrical load is implemented. In this case for small dimensions the coefficient C_{pz} is not large and thus the coupling is not strong. Most of the power is dissipated from the mechanical damper of the device. Anyway this is an idealised case and as shown in Chapter 2 and Appendix B, for a proper analysis of the optimal load and consequent harvested power, it is mandatory to consider and model the dielectric losses of the piezoelectric material.

4.7 COMPARATIVE ANALYSIS

This section presents a comparative study for the scaling properties of the harvested power and harvesting efficiency with the electromagnetic and piezoelectric seismic transducers.

4.7.1 Harvested power

Assuming the electromagnetic and piezoelectric transducers have the same mass m_m and stiffness k_m and assuming optimal complex electrical loads are implemented, the quotient between the power harvested from the two transducers reduces to:

$$r_p = \left.\frac{\bar{P}_{hM}}{\bar{P}_{hp}}\right|_{opt} = \frac{c_{m,p}}{c_{m,M}} \frac{\mathrm{C}_{eml}}{\mathrm{C}_{PZ}} \frac{\eta_c + \mathrm{C}_{PZ}}{1 + \mathrm{C}_{eml}}, \tag{4.62}$$

where $\bar{P}_{hM}$ and $\bar{P}_{hp}$ are the harvested powers derived respectively in Eq. (4.24) and Eq.(4.47) for the coil magnet and piezoelectric transducer. Moving to the case when the optimal purely real electric load is implemented, the quotient becomes:

$$r_{pR} = \left.\frac{\bar{P}_{hRM}}{\bar{P}_{hRp}}\right|_{opt} = \frac{1}{4} \frac{c_{m,p}}{c_{m,M}} \frac{\mathrm{C}_{eml}}{1 + \mathrm{C}_{eml}} \frac{1 + (\mathrm{C}_{PZ} + \eta_C + \rho_d)^2}{\mathrm{C}_{PZ}\, \rho_d}, \tag{4.63}$$

where $\bar{P}_{hRM}$ and $\bar{P}_{hRp}$ are the harvested powers derived respectively in Eq. (4.25) and Eq.(4.48) for the electromagnetic and piezoelectric transducers. The results of the numerical simulations of Eqs.(4.62), (4.63) based on the data of Table 2-1 and Table 2-2 are shown in Figure 4.10.

Considering at first Figure 4.10 (a), for small dimensions the power harvested from the electromagnetic transducer scales down more rapidly compared to the piezoelectric device when either the reactive and purely real electric loads are implemented. For larger scales the eddy currents effect becomes relevant and, especially for the complex - real electric load configuration (Plot (a)), the power harvested by the electromagnet scales up more slowly with respect to that of the piezo harvester. If the coil magnet transducer is well designed (and thus the effect of the eddy currents is minimized), Plot (b) shows that also for large dimensions, the power harvested from the electromagnetic harvester scales up more rapidly compared to the piezoelectric harvester. In addition, without the eddy currents damping effect (dashed line) the somewhat linearly rising dashed lines in Plots (a, b) of Figure 4.10 suggests that, if the harvesters produce the same power at their original dimension (i.e. L^0) and their size becomes larger, more power can be absorbed with the electromagnetic harvester than with the piezoelectric harvester. Conversely, for small dimensions, the piezoelectric harvester is instead producing more power absorption.

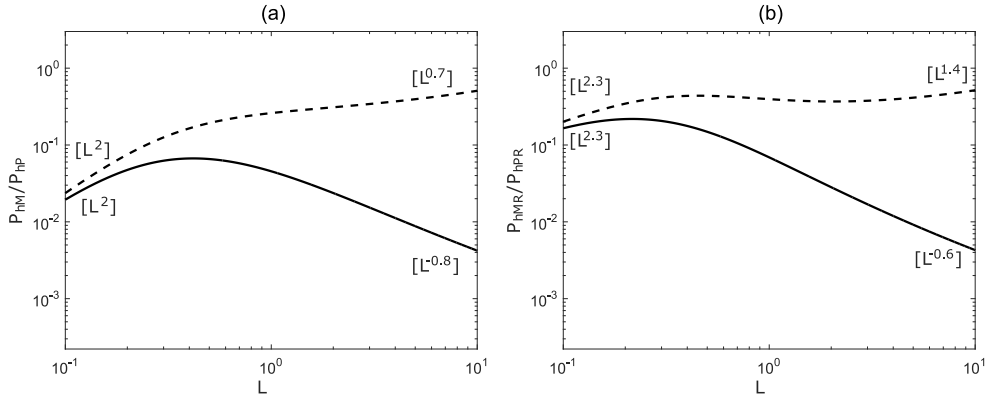

Figure 4.10: Electromagnetic and piezoelectric harvested power ratios implementing (a) the optimal complex and (b) the purely real electrical load, neglecting (dashed line) and considering (solid line) the eddy current losses.

Moving to Figure 4.11, Plots (a, b) compare the efficiencies of the electromagnetic and piezoelectric harvesters depicted respectively in Figure 4.5 and Figure 4.8 for the complex and purely real optimal electrical loads. Considering the dashed line in Figure 4.11 (a,b), as already mentioned in the previous sections, for both electric loads, the performance of the coil magnet (dashed line) monotonically increases with the dimension and reaches a maximum value of 0.5. The presence of the eddy currents

(dash dotted line) reduces the efficiency incremental rate but has no effect on the value of the horizontal asymptote (i.e. 0.5) reached by the curve. Moving to the piezoelectric harvester, the solid line in Plot (a) of Figure 4.11 shows that when the optimal complex electric load is implemented the efficiency tends to be constant for small size and gradually drops down when the scale is increased. A maximum efficiency equal to 0.5 is reached for small scales only if the dielectric losses of the material are not present. (As described in Section 2 and Appendix B, to properly study the energy harvesting with the piezoelectric seismic transducer it is necessary to model the dielectric losses).

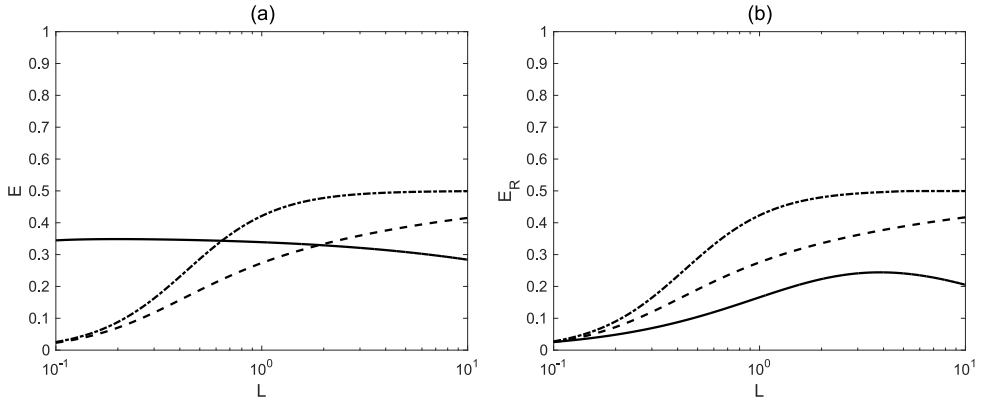

Figure 4.11: Efficiency of the electromagnetic (dashed lines) and piezoelectric (solid line) harvester implementing (a) the optimal complex and (b) the purely real electric load including (dashed line) and neglecting (dash-dotted line) the eddy current losses.

Moving to Plot (b), when the configuration with the optimal purely real electric load is considered (solid line), the efficiency of the piezoelectric transducer tends to rise up to a point where it reaches a maximum value and then monotonically falls down due to the air damping effect.

In conclusion, these results show that when the optimal complex harvesting load is implemented, the piezoelectric harvester is more efficient than the electromagnetic harvester for small dimensions, whereas when the size is very large the electromagnetic device exhibits a superior power efficiency with respect to the piezo transducer. When the optimal real electrical impedance load is implemented, the electromagnetic harvester results more efficient than the piezoelectric harvester in the entire scaling bandwidth.

4.7.2 *Stroke*

As discussed by Gardonio *et al.* [204] and other authors [190], [203], to properly characterise the seismic harvesters, the maximum stroke allowed by the transducers should be also taken into consideration. To fully characterise the energy harvesting with the two systems considered in this study, the scaling laws of the stroke for the electromagnetic and piezoelectric seismic transducers excited by a base displacement tuned to their fundamental resonance frequency are now considered. Here the simulations are performed assuming that the harvesters can withstand any displacement. It should be highlighted that this is a rather significant assumption, since in practice the stroke is always limited by geometrical constrains (e.g. end stops for the coil magnet relative displacement) or stiffening effects of the elastic component (e.g. non linear bending deformation of the beam harvester).
Inspection of the lumped parameter scheme shown in Figure 4.2 (b) leads to the following equation of motion for the seismic mass and Kirchhoff equation for the electric mesh of the electromagnetic device:

$$Z_m(\dot{w}_m - \dot{w}_h) = -Z_s(\dot{w}_m - \dot{w}_h) + \Psi_{em} i_h, \tag{4.64}$$

$$e_h = \Psi_{me}(\dot{w}_m - \dot{w}_h) + \mathrm{Z}_e i_h. \tag{4.65}$$

Similarly, inspection of the lumped parameter element scheme in Figure 4.2 (d) provides two similar equations for the piezoelectric harvester:

$$Z_m(\dot{w}_m - \dot{w}_h) = -Z_s(\dot{w}_m - \dot{w}_h) + \Psi_{em} e_h, \tag{4.66}$$

$$i_h = \Psi_{me}(\dot{w}_m - \dot{w}_h) + \mathrm{Y}_e e_h. \tag{4.67}$$

Also, according to the notation shown in Figure 4.2 (b) and Figure 4.2 (d), the following relations hold for the impedances – admittances of the harvesting loads:

$$e_h = -Z_h i_h, \tag{4.68}$$

$$i_h = -Y_h e_h. \tag{4.69}$$

After some mathematical manipulations Eqs.(4.64), (4.65) and (4.66), (4.67) combined with Eqs.(4.68) and (4.69) give the following relations for the stroke per unit base displacement for the electromagnetic and piezoelectric harvester respectively:

$$\frac{w_m - w_h}{w_h} = -\frac{Z_m}{Z_t + \frac{\Psi_{em}\Psi_{me}}{Z_e + Z_h}}, \tag{4.70}$$

$$\frac{w_m - w_h}{w_h} = -\frac{Z_m}{Z_t + \frac{\Psi_{em}\Psi_{me}}{Y_e + Y_h}}. \tag{4.71}$$

Figure 4.12 and Figure 4.13 show the simulated scaling laws for the stroke per unit base displacement of the two transducers, respectively when they are connected to the optimal complex electric load given in Eqs.(4.20), (4.43) and when they are connected to the optimal real electric load given in Eqs.(4.21), (4.44). The simulations are performed assuming that the transducers operate at their fundamental natural frequency i.e. $\omega = \omega_n = \sqrt{k_m/m_m}$.

The graphs for the electromagnetic seismic transducer depicted in Plots (a) of Figure 4.12 and Figure 4.13 show very similar scaling and the same laws when the optimal complex and purely real harvesting loads are implemented. Considering first the case where the eddy currents are present (solid line), the stroke amplitude grows proportionally to the first power of dimension i.e. $[L^1]$ and peaks at a particular dimension of the transducer. At larger sizes, the stroke progressively decreases and falls down with power -0.5 of L i.e $[L^{-0.5}]$.

In those cases where effects of eddy currents can be neglected (dotted line), the stroke is characterised by a rising trend proportional to $[L^1]$, which increases to $[L^2]$ for very large dimensions.

Moving to the piezoelectric seismic transducer, the simulated scaling laws of the stroke per unit of base displacement show a somewhat linear rising behaviour, i.e. $[L^1]$, in the entire scaling range. In particular, as can be noticed in both Plots (b) of Figure 4.12 and Figure 4.13, the contribution of the air damping (solid line), which becomes very dominant at large scales, tends to decrease the stroke.

Contrasting Plots (a) with Plots (b) in Figure 4.12 and Figure 4.13, it can be noticed that, at the bottom end of the scaling range, the stroke per unit base displacement of the piezoelectric seismic transducer is respectively 2 and 5 times greater than that of the electromagnetic harvester. This difference is also noticeable at the top end of the scaling range, where the stroke of the piezoelectric harvester is respectively greater than 2.4 and 4.5 times that of the electromagnetic transducer and becomes even greater (more than 100 times) if the eddy currents effects are considered in the electromagnetic transducer.

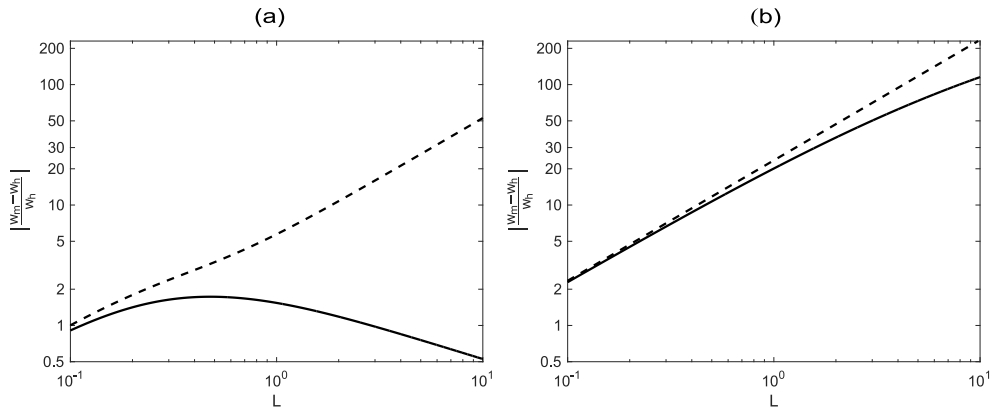

Figure 4.12: Scaling stroke per unit base displacement at the fundamental resonance frequency of (a) the electromagnetic seismic harvester when the effect of the eddy currents c_{ec} is present (solid line) and neglected (dashed line) and (b) the piezoelectric seismic harvester when the effect of the air damping c_{am} is present (solid line) and neglected (dashed line) implementing the optimal complex harvesting load.

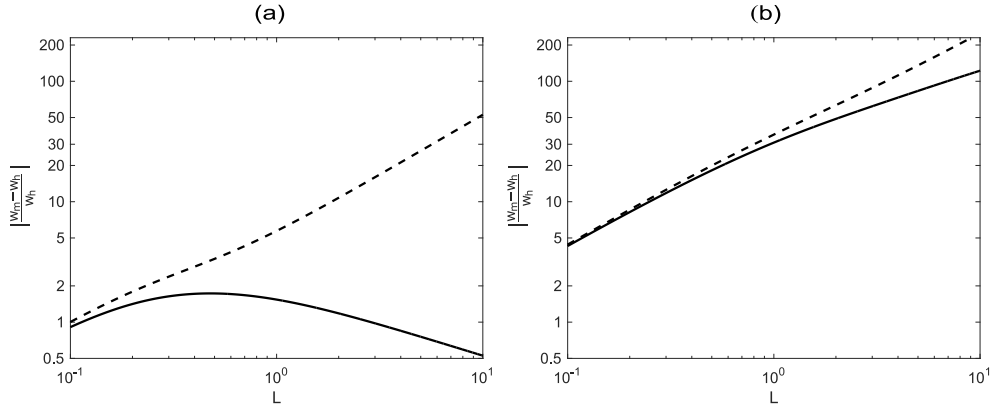

Figure 4.13: Scaling stroke per unit base displacement at the fundamental resonance frequency of (a) the electromagnetic seismic harvester when the effect of the eddy currents c_{ec} is present (solid line) and neglected (dashed line) and (b) the piezoelectric seismic harvester when the effect of the air damping c_{am} is present (solid line) and neglected (dashed line) implementing the optimal real harvesting load.

It is clear that these simulations are valid only for limited ranges of base vibrations such that the resulting strokes do not reach the saturation limits. In addition, the values of the stroke amplitude found above depend on the dimensions and physical properties used in simulations, which refer to the prototypes studied in Chapter 2. Nevertheless, as already discussed in Chapter 2.10, this study suggests that the piezoelectric energy harvester could be affected by operational problems related to

the bending deflection range of the beam transducer and thus can be effectively used for low amplitude base vibrations. On the contrary, the electromagnetic harvester seems to be more suitable for larger amplitudes base vibrations.

4.8 REACTIVE HARVESTERS

As mentioned in the introduction of this chapter, this final section discusses scaling laws for the electromagnetic and piezoelectric reactive harvesters. In general, reactive harvesters subjected to an imposed displacement at their base are particularly suited for every low frequency energy harvesting conditions. In fact, they do not show the amplified stroke, and thus energy harvesting magnification, at their fundamental natural frequency, which, in this case, is given by $\omega_n = \sqrt{k_m/m_b}$, where m_b is the mass of the moving base. Nevertheless, to offer a fair comparison, the scaling laws presented in this section assume the harvesters are operated at their fundamental natural frequency i.e. at $\omega = \omega_n = \sqrt{k_m/m_b}$.

4.8.1 Electromagnetic Harvester

Considering the results depicted in Figure 4.3 and considering the formulation presented in section 4.3, the power harvested, power input and efficiency given in Eqs. (4.19), (4.29), (4.34) can be straightforwardly specified for the optimal complex impedance $Z_h = Z_{ei}^*$ and frequency of excitation $\omega = \omega_n = \sqrt{k_m/m_b}$ of the electromagnetic reactive transducer:

$$\bar{P}_h = \frac{1}{8}\frac{(Bl)^2}{\mathrm{R}_e}|\dot{w}_h|^2, \tag{4.72}$$

$$\bar{P}_i = \frac{1}{2}c_m\left(1 + \frac{\mathrm{C}_{eml}}{2}\right)|\dot{w}_h|^2, \tag{4.73}$$

$$E = \frac{\mathrm{C}_{eml}}{4 + 2\mathrm{C}_{eml}}. \tag{4.74}$$

Similarly, specifying Eqs. (4.19), (4.29), (4.34) for the purely resistive electric load $Z_h = |Z_{ei}|$ at the fundamental resonance frequency of the reactive device i.e. $\omega = \omega_n = \sqrt{k_m/m_b}$, it follows:

$$\bar{P}_{h,R} = \frac{1}{4}\frac{(Bl)^2}{\mathrm{R}_e}\frac{1}{\rho_{rc}}|\dot{w}_h|^2, \tag{4.75}$$

$$\bar{P}_{i,R} = \frac{1}{2}c_m\left(1 + \mathrm{C}_{eml}\frac{\rho_{rc}}{\rho_{rc}^2 + \left(\frac{\omega_n}{\omega_c}\right)^2}\right)|\dot{w}_h|^2, \tag{4.76}$$

$$E_R = \frac{\mathrm{C}_{eml}}{2\rho_{rc}}\frac{\rho_{nc}^2 + \left(\frac{\omega_n}{\omega_c}\right)^2}{\rho_{rc}^2 + \left(\frac{\omega_n}{\omega_c}\right)^2 + \mathrm{C}_{eml}\,\rho_{rc}}. \tag{4.77}$$

Here $\rho_{rc} = 1 + \sqrt{1 + \left(\frac{\omega_n}{\omega_c}\right)^2}$ and $\omega_c = R_e/L_e$. Comparing Eqs.(4.72), (4.74), (4.75), (4.77) with those derived in Eqs.(4.24), (4.38), (4.25), (4.39), it is noted that the scaling of the power harvested from the reactive transducer is only influenced by the transduction coefficient Bl, inductance L_e and electric resistance R_e. Thus, in contrast to the seismic harvester, the mechanical losses, and in particular the eddy current losses, do not affect the power harvested by the electromagnetic reactive transducer. This result is of great of importance because, as depicted in Figure 4.4, at large scales, the eddy current losses play a key role in the reduction of the power harvested from the electromagnetic seismic harvester. The scaling laws of the normalised power harvested depicted in the graphs (a) and (b) of Figure 4.14 show that, for either optimal load configurations, the harvested power increases with the size.

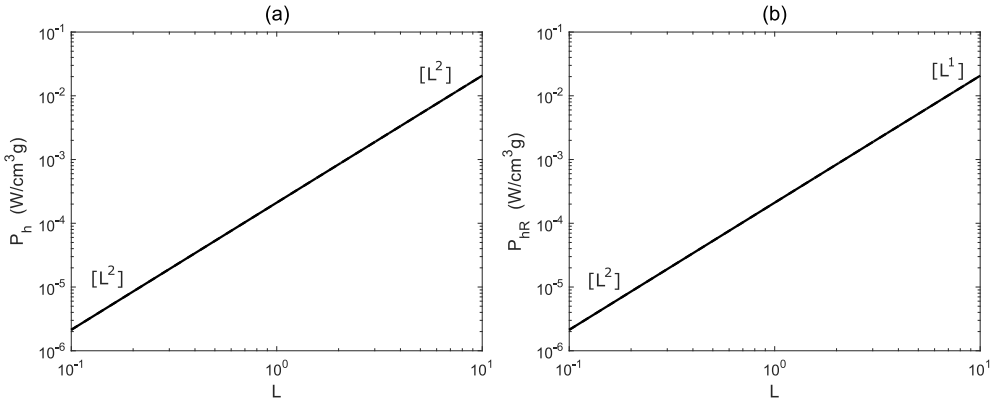

Figure 4.14: Scaling law of the power harvested density P_h implementing (a) the optimal complex electric load and (b) the optimal purely real electric load.

Moving to the analysis of the scaling efficiency, the formulas in Eqs.(4.74) and (4.38), obtained when the optimal complex electric load is implemented, are the same for either the reactive and seismic vibration energy harvesters. Thus identical scaling laws are derived. Instead, if the purely real electric load is considered, Eq.(4.77) compared to Eq. (4.39) shows a different scaling for the harvesting energy efficiency. Nevertheless, the numerical simulations confirms that also in this case, the efficiency of the seismic and reactive electromagnetic harvesters follows similar laws.

4.8.2 Piezoelectric Harvester

The scaling study of the piezoelectric reactive harvester is obtained from a formulation analogue to that presented in Section 4.5.
Substituting the optimal condition $Y_h = Y_{ei}^*$ into Eqs.(4.42), (4.52), (4.57) and specifying at $\omega = \omega_n = \sqrt{k_m/m_b}$, the power harvested, power input and efficiency are given by:

$$\bar{P}_h = \frac{1}{8} R_p (\psi_{PZT})^2 |\dot{w}_h|^2, \tag{4.78}$$

$$\bar{P}_i = \frac{1}{2}(c_m + c_{am}) \left(1 + \frac{\mathrm{C}_{PZ}}{2\eta_C}\right) |\dot{w}_h|^2, \tag{4.79}$$

$$E = \frac{\mathrm{C}_{PZ}}{4\eta_C + 2\mathrm{C}_{PZ}}. \tag{4.80}$$

Here R_p is identified as $R_p = 1/\omega_n C_e^S \eta_C$ and represents the real part of the complex impedance of the piezoelectric lossy capacitor i.e. $\tilde{C}_e^S = C_e^S(1 - j\eta_c)$ at the fundamental mechanical frequency of the piezoelectric transducer.
Moving to the purely real electric load case, implementing the optimal resistive load of admittance $Y_h = |Y_{ei}|$, Eqs.(4.42), (4.52), (4.57) can be specified as follows:

$$\bar{P}_h = \frac{1}{4} R_p \frac{(\psi_{PZT})^2}{\rho_{rd}} |\dot{w}_h|^2, \tag{4.81}$$

$$\bar{P}_i = \frac{1}{2}(c_m + c_{am}) \left(1 + \mathrm{C}_{PZ} \frac{\rho_{rd}}{{\rho_{rd}}^2 + \left(\frac{\omega_d}{\omega_n}\right)^2} \right) |\dot{w}_h|^2, \tag{4.82}$$

$$E_R = \frac{\mathrm{C}_{PZ}}{2\eta_C \rho_{rd}} \frac{{\rho_{rd}}^2 + \left(\frac{\omega_d}{\omega_n}\right)^2}{{\rho_{rd}}^2 + \left(\frac{\omega_d}{\omega_n}\right)^2 + \mathrm{C}_{PZ}\rho_{rd}}, \tag{4.83}$$

where ρ_{rd} is defined as $\rho_{rd} = 1 + \sqrt{1 + \left(\frac{\omega_d}{\omega_n}\right)^2}$ and $\omega_d = 1/R_p C_e^S$.

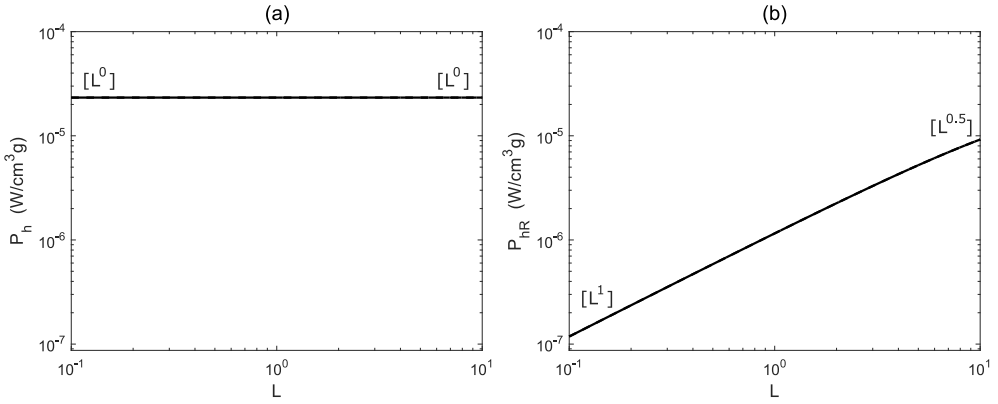

Figure 4.15: Scaling law of the power harvested density P_h implementing (a) the optimal complex electric load and (b) the optimal purely real electric load.

Compared to the electromagnetic reactive transducer, inspection of the formulas in Eqs.(4.78), (4.80), (4.81), (4.83) and (4.47), (4.60), (4.48), (4.61) shows that similar conclusions can be drawn. In particular, the same scaling power efficiency can be obtained for both the seismic and reactive piezoelectric energy harvesters if the optimal resistive reactive load is implemented. Different scaling efficiency seems instead to arise from inspection of Eqs.(4.83) and (4.61). Nevertheless, numerical simulations on the power efficiency of the reactive transducer have shown very similar trend to that depicted in Plot (b) of Figure 4.8.

Moving to the analysis of the power harvested, in Eqs. (4.78) and (4.81) there is no contribution of the mechanical losses and the transduction coefficient ψ_{PZT}, electric capacitance C_e^S and lossy factor η_C are the only parameters that characterise the power scaling of the piezoelectric reactive device.

Plot (a) of Figure 4.15 shows that, if the complex electric load is implemented, constant power density can be obtained independently from the size of the piezoelectric reactive harvester. Moving to Plot (b), when the configuration with the optimal purely real electric load is considered, the normalised power density is instead characterised by an increasingly monotone trend.

5

CONCLUSION AND FUTURE WORK

This thesis has presented theoretical and simulation/experimental comparative study on the energy harvesting using electromagnetic and piezoelectric seismic and reactive transducers. The study has been limited to energy harvesting from tonal ambient vibrations. In addition, scaling laws have been established for the harvested power density and efficiency for the two seismic and two reactive prototypes studied. Also, a stroke analysis has been performed for the seismic harvesters.

To provide a fair comparison study, the two seismic transducers were designed and built in such a way as to have similar weights and similar volumes of the respective base and moving components and comparable fundamental natural frequencies. The reactive harvesters were constructed by simply clamping the moving components of the seismic devices.

In Chapter 2 the seismic transducers were described and studied starting from equivalent lumped parameter models that allowed the derivation of a consistent formulation of the constitutive electromechanical equations for the two systems and a unified energy formulation for the two harvesters. In particular, compared to classical simplified models, the lumped parameter model for the piezoelectric seismic transducer was reworked in such a way as the electrical part is composed by a lossy capacitor connected in series. Furthermore, the proposed models, considered also the effects of electromagnetic (eddy currents) and dielectric losses, which have been found to play a fundamental role in the energy harvesting with the electromagnetic and piezoelectric seismic transducers respectively, although, usually, they are not taken into consideration in energy harvesting studies. The electromechanical response functions FRFs used to define the constitutive equations were first analysed in detail comparing simulations and experiments. The principal results of this analysis can be summarised as follows:

- The two harvesters are characterised by typical mechanical impedance of seismic systems, that is, mass behaviours at low and high frequencies linked

by a resonance peak at the fundamental resonance frequency and antiresonance closely follower.

- The electrical impedance of the electromagnetic transducer is dominated by the resistive component at low frequency, by the mechanical resonance at fundamental natural frequency where the mechanical to electrical impedance effect is relevant and by inductive effects which, due to eddy currents in the coil wire of the transducer, is characterised by frequency dependent resistive and inductive effects. For the piezoelectric transducer, the electrical impedance is instead characterised by the capacitive effect which, at low frequencies, is heavily affected by dielectric losses. The mechanical to electrical impedance effect is negligible, apart at the fundamental natural frequency where in any case it produces a very small effect.

- The electromechanical transduction functions for both seismic transducers becomes relevant at the fundamental natural frequency where a distinctive peak is present and where the energy conversion is therefore maximised. While for the electromagnetic the transduction functions remain constant at higher frequencies, for the piezoelectric reach a peak and then decreases. Indeed the piezoelectric transducer is characterised by a $1/(j\omega)$ factor, that is, they are in quadrature with respect to those for the electromagnetic transducer. This is because the electromagnetic transduction relates force to current and voltage to velocity whereas the piezoelectric transduction relates force to charge and voltage to strain.

The energy harvesting study has considered two configurations of the harvesting circuit, which are characterised by either a resistive-reactive or a purely real impedance set to maximise the harvested power. The complex impedance necessary to maximise the harvested power was found to be given by the complex conjugate of the electrical impedance of the seismic transducers, which is line with the maximum power transfer theorem. Alternatively, the purely real impedance necessary to maximise the harvested power was found equal to the modulus of the electrical impedance of the seismic transducers. The maxima of the harvested power and input power was found for both transducers to occur in correspondence of the fundamental resonance frequency of the transducers. The piezoelectric transducer is characterised by additional resonances produced by higher order flexural modes of the beam

laminate and tip mass, which however are characterised by smaller power harvesting peak values. In general, the piezoelectric harvester outperforms the electromagnetic harvester in correspondence of the fundamental and higher order resonance frequencies, even if the peaks of power is very tight and thus the vibration conversion is limited to a very narrow band operation. In fact the electromagnetic harvester performs better at low frequencies below the fundamental resonance and also at frequencies comprised between the fundamental resonance frequency and the resonance frequency due to the first higher order resonant mode of the piezoelectric harvester. The peak energy harvesting property of the two seismic harvesters was analysed also limiting the range of motion of the proof mass and thus with reference to the maximum allowed stroke of the transducers (i.e. linear motion).

Table 5-1: Energy harvesting properties with the two seismic transducers (* simulation results assuming no eddy current effects in the outer ring of the electromagnetic seismic transducer).

Transducer type	Base mass Proof mass Total mass (kg)	Base volume Proof volume Total volume (m^3)	Res. freq. (Hz)	Z_h	$\mathrm{Re}(Z_h)$ (Ω)	$\mathrm{Im}(Z_h)$ (Ω)	$\frac{\bar{P}_h}{\ddot{w}_h}$ $\left(\frac{\mathrm{mW}}{1\mathrm{g}}\right)$	$\frac{\bar{P}_i}{\ddot{w}_h}$ $\left(\frac{\mathrm{mW}}{1\mathrm{g}}\right)$	$\frac{\bar{P}_h}{\Delta w}$ $\left(\frac{\mathrm{mW}}{\mathrm{mm}}\right)$	$\frac{\bar{P}_i}{\Delta w}$ $\left(\frac{\mathrm{mW}}{\mathrm{mm}}\right)$	$E(\ddot{w}_h)$	$E(\Delta w)$
EM	0.115 0.185 0.300	1.21×10^{-5} 3.24×10^{-5} 4.45×10^{-5}	19.5	Complex	75.5	1	33	120	30	110	0.28	0.27
				Real	76	—	33	120	30	110	0.28	0.27
				Real*	256	—	173	412	12	30	0.42	0.4
PZT	0.126 0.189 0.363	1.76×10^{-5} 2.64×10^{-5} 5.03×10^{-5}	20	Complex	23000	45000	700	1900	5	14	0.33	0.36
				Real	50500	—	350	2100	1.3	8	0.17	0.15

The peak values of the energy harvested, energy input and efficiency to convert input to harvested power at the fundamental resonance frequency of the two harvesters with reference to $1g$ base acceleration are summarised in Table 5-1; in addition the values of the optimal harvesting impedances are also presented. These data show that when the optimal complex impedance harvesting load is implemented, the

piezoelectric harvester is more efficient than the electromagnetic harvester whereas, when the optimal real impedance harvesting load is implemented, the electromagnetic harvester results more efficient that the piezoelectric harvester. These results are largely dependent on the inherent electrical and mechanical damping in the two seismic transducers. For instance, in Appendix A is shown that if the high eddy current losses in the electromagnetic harvester was reduced (for example by separating the housing yoke disk into two part), the efficiency for the real harvesting load would rise from 28% to 42%. Therefore, the energy harvesting of the electromagnetic harvester can be greatly improved if the seismic transducer is carefully designed in such a way as to minimise the effects of eddy currents. Also, as shown in Appendix B.2.1, to properly study the energy harvesting with the piezoelectric seismic transducer, it is necessary to model the effect of dielectric losses, otherwise the formulation would lead to an unphysical result where the harvester could generate a constant level of power at any frequency.

Table 5-1 also summarises the power per unit of stroke at the fundamental natural frequency. In particular the electromagnetic harvester absorbs more power per unit stroke than the piezoelectric harvester for both the complex and real impedance harvesting loads are implemented. However, when the complex impedance-harvesting load is implemented, the piezoelectric harvester is more efficient to convert the mechanical power into electrical power whereas, when the real impedance harvesting load is implemented, the electromagnetic harvester results more efficient, and even more if the eddy currents losses were reduced.

Chapter 3 has presented a comparative study on the energy harvested by electromagnetic and piezoelectric reactive harvesters. Based on the study of Chapter 2, the two systems were modelled with consistent electro-mechanical lumped parameter models to allow the derivation of a unified formulation for the energy harvesting and thus a direct comparison of the electro-mechanical response and energy harvesting properties of the two devices. Analogously to the seismic devices, the study has been limited to energy harvesting from tonal ambient vibrations. It was shown that the two harvesters are characterised by typical mechanical impedances of mass driven mass-spring dashpot systems, where in this case the mass is actually the base mass subject to the ambient vibrations. The electrical impedance of the electromagnetic transducer is dominated by the resistive and lossy-inductive effects of the coil and no mechanical to electrical transduction contribution is present. For the piezoelectric transducer, the electrical impedance is instead only characterised by the lossy capacitive effect. The electromechanical FRFs of the electromagnetic

harvester are simply characterised by its transduction coefficient and thus remain constant in the whole frequency range. The transduction FRFs for the piezoelectric transducer are instead characterised by its transduction coefficient multiplied by a $1/(j\omega)$ factor and thus they are in quadrature with respect to those for the electromagnetic transducer. The experimental FRFs of the electromagnetic harvester denotes a good matching with the simulated FRFs in the whole frequency band, except for frequencies higher than 800 Hz, where the higher order dynamic effects of the transducer components become relevant. Instead, the experiments with the piezoelectric reactive harvester show, a discrepancy for frequencies higher than the fundamental natural frequency of the cantilever laminate beam with tip mass, in particular over 100 Hz. This is caused by the dynamic effects of higher order flexural modes of the beam laminate and tip mass and by the unwanted mechanical dynamics of the hosting structure used in the experiments.

Similar to Chapter 2 the study on the harvested power has considered two configurations of the harvesting circuit, which are characterised by either a complex or a purely real impedance, which are set to maximise the absorbed power. The study on the harvested power considered a base acceleration of the base mass equal to 1g. When the devices implement the optimal complex impedance, the electromagnetic reactive harvester generates a power of 70 $\frac{\mathrm{m}W}{\mathrm{g}}$ at about 10 Hz, while the piezoelectric reactive harvester generates a power of 44 $\frac{\mathrm{m}W}{\mathrm{g}}$ at about 10 Hz. Alternatively, when the devices implement the optimal real impedance, the electromagnetic and piezoelectric reactive harvesters generate respectively 70 $\frac{\mathrm{m}W}{\mathrm{g}}$ and 3.5 $\frac{\mathrm{m}W}{\mathrm{g}}$ at about 10 Hz. For both transducers the level of harvested power decreases with frequency. This depends on the electromechanical properties of the systems as well as on the amplitude of oscillation of the moving base mass, which decreases with frequency. In summary, the electromagnetic device is more effective than the piezoelectric device to harvest power for both cases where the real and complex optimal impedances are implemented. An important aspect worth considering concerns the fact that the input/harvested power is not magnified at a resonance frequency. Therefore, if the host structure imposes a motion to the moving mass no amplification of the energy conversions is expected. A further analysis on the power input to the harvesters has shown that the two devices can transfer the input power to the harvesting load with different efficiencies. In general, the electromagnetic reactive device implementing either the optimal complex or real impedance loads is characterised by similar efficiencies close to 30% over the whole frequency range up to 1 kHz. The

piezoelectric harvester is instead characterised by constant efficiency of about 45% when the optimal complex load is implemented and an increasingly lower efficiency, which is about 38% at 10 Hz, for the purely real harvesting load.

Chapter 4 investigated the scaling laws that characterise the electro-mechanical response and vibration energy harvesting of the seismic and reactive electromagnetic and piezoelectric transducers shown in Plots (a, d) of Figure 2.1 and Figure 3.1. The study primarily is focused on the seismic harvesters, which represent the most general case. Scaling laws for the reactive transducers were reviewed at the end of the section. The lumped parameter model presented in Chapter 2 for the piezoelectric seismic transducer was reworked in such a way as the mechanical part is composed by spring and damper elements in parallel and the electrical part is composed by a lossy capacitor and current-velocity transduction element in parallel. The air viscous effect was also introduced in the lumped piezoelectric model by means of a damper acting on the moving mass. The scaling laws were derived with reference to a single variable L, which identifies the linear dimension of the two devices. As derived in Appendix D.1 and depicted in Chapter 2, both seismic harvesters are particularly effective when they operate at frequencies close to their fundamental natural frequency; therefore the analyses were restricted to the hypothesis of tonal excitation tuned to the fundamental natural frequency of the two seismic harvesters. This has given the opportunity to simplify the model of the electromagnetic seismic device, neglecting the coil losses, which are particularly effective only at frequencies above 1 KHz. On the contrary, the dielectric losses of the piezoelectric seismic harvester were found being a key feature also in the power-scaling analysis. Specifying the energy formulation based on the FRFs of both transducers, power input – output formulas in terms of non-dimensional coupling coefficients were obtained. These expressions were then used to characterise the efficiency of the two transducers to convert vibration into electrical energy. The study has shown that the parameters, which characterise the scaling laws for the harvested power and the efficiency depend on the mechanical and electrical reactive (mass, spring, inductor, capacitor) and dissipative (damper, resistor) components as well as on the transduction coefficients in the two lumped parameter models shown in the schematics (b, d) of Figure 4.2 and (c, f) of Figure 3.1. In particular, incrementing the size (i.e. L) of both harvesters the fundamental natural frequency ω_n decreases proportionally to $[L^{-1}]$, since the mass and the stiffness of the two systems scale respectively as $[L^3]$ and $[L^1]$. Also, the transduction coefficients of both transducers scale as the first power of the dimension i.e. $[L^1]$. Moreover, for the electromagnetic harvester the scaling of the air viscous

damping coefficient c_a, that describes the air losses that develop in the tiny gap between the magnet and the coil-Yoke assembly, scales up with the first power of dimension, i.e. $[L^1]$, while the eddy currents damping coefficient c_{ec} that describes the losses caused by the interaction of the magnetic field and the eddy currents that develop in the conductive housing ring scales as $[L^{2.5}]$. Moving to the piezoelectric harvester the material damping coefficient c_m that describes the viscoelastic losses in the composite beam scales as the first power of the dimension i.e. $[L^1]$, while the air damping coefficient c_{am} that gives the losses produced by the interaction between the beam and the air scales with the power of 1.7 i.e. $[L^{1.7}]$.

In the last part of the chapter a comparison between the two seismic harvesters for both the optimal resistive reactive and purely real harvesting loads implemented is proposed, which however showed similar scaling laws than those found for the inertial harvesters. The principal outcomes of the scaling study can be summarised in the following points:

- Implementing both the optimal complex or purely real harvesting loads the efficiency of the electromagnetic harvester, starting from very low amplitude values for small dimension size, tends to rise and reaches the maximum of 50 % as the size increases. If the eddy current losses are neglected, this result is reached in a narrower dimension span.

- Implementing the optimal complex harvesting load, the efficiency of the piezoelectric harvester is constant and equal to 50% only if the material damping is present; alternatively, it is less than 50% and independent of the size if also the dielectric losses are taken into account. If the air damping is added, the efficiency decreases as the scale is increased. For the optimal purely real harvesting load configuration, similarly to the electromagnet device, the efficiency of the piezoelectric harvester affected only by material damping, tends to rise from very low values to a maximum of 50% as the dimension is scaled up. When the dielectric losses are also considered, this transition occurs in a same manner but reaches a less value equal to that of the optimal complex case. Finally, the efficiency in presence of material damping, dielectric losses and air damping tends to drop both at low and large dimensions. Thus there is an optimal scale where the efficiency is maximum.

- The scaling laws of the power density per unit of base acceleration ($W/c_m{}^3$ g) revealed that for both harvesters the power density achievable increases as the size is scaled up regardless the optimal complex or purely real electrical loads are implemented. In particular, for small dimensions, the power density harvested by the electromagnetic device scales up more rapidly with respect to that of the piezoelectric device. For large dimensions, this applies only if the eddy current losses in the electromagnetic harvester are annihilated and the purely real electric load is considered. Therefore, without eddy current losses in the electromagnetic device, the power harvested by the piezoelectric transducer is less affected by the dimensional changes at very large and small dimension sizes.

- The numerical simulations of the power ratios shown in Figure 4.10 suggest that, if the two devices with comparable dimensions produce the same harvested power at their original size (i.e. at L^0) and if the electromagnetic harvester is well designed (i.e. no eddy currents develop in the Yoke and coil elements), for increasingly smaller dimensions the piezoelectric harvester absorbs more power than the electromagnet device. Conversely, the electromagnetic system captures more energy for larger size.

- The study on the scaling of the stroke of the electromagnetic and piezoelectric seismic transducers at their fundamental resonance frequency has shown that the amplitude of oscillation of the moving mass per unit of base displacement rises if the harvesters are scaled up, regardless the resistive-reactive or purely resistive harvesting impedance loads are implemented. However, if the electromagnetic device is affected by eddy currents phenomena, the scaling of the stroke for both impedance loads is characterised by a peak centred in correspondence of a particular dimension, which depends on the mechanical and electrical properties of the harvester. In addition, the stroke amplitude of the piezoelectric harvester has proved to be greater from 2 to 5 times than that of the electromagnetic device or even 100 to 200 times if the electromagnetic harvester is characterised by eddy currents. This suggests that, in a way eddy currents may actually be beneficial to limit excessive stroke effects in large size harvesters.

The theoretical asymptotes of the power law efficiencies for large and small dimension sizes under different loss effects are summarised in Table 5-2.

Table 5-2: Asymptote of efficiency scaling laws.

Transducer	Damping	Complex load Z_h	Real load Z_{hR}
EM			
Small size	$c_a + c_{ec}$	0%	0%
	c_a	0%	0%
Large size	$c_a + c_{ec}$	50%	50%
	c_a	50%	50%
PZT			
Small size	$c_m + c_{am}$	< 50%	0%
	c_m	< 50%	0%
Large size	$c_m + c_{am}$	0 %	0%
	c_m	< 50%	< 50%

Finally, the scaling analysis of the reactive harvesters working at their fundamental natural frequencies have shown that the efficiency exhibits similar laws than those of the seismic harvesters, regardless the optimal complex or purely resistive harvesting impedance loads are implemented. In contrast, the scaling analysis of the normalized power density revealed that the harvested power by the reactive transducers is independent of their mechanical losses, which instead strongly influence the power scaling law of the seismic devices. In particular, the normalised power harvested with the electromagnetic transducer exhibits a rising trend, proportional to the square of the dimension, i.e. $[L^2]$, along the entire scaling bandwidth and for both load configurations. Moving to the piezoelectric harvester, a constant power density can be obtained if the optimal resistive-reactive load is implemented. A rising power trend with increasing size is instead achieved if the purely real electric load is considered.

5.1 FUTURE WORK

The study presented in this thesis has brought up a number of topic worth considering in the future studies, which are summarised in the four points reported below:

- Consider the possibility of replacing the resistive-reactive electric loads with an energy scavenging circuit and investigate a practical electrical interface circuit to obtain a more accurate result of the input-harvested power and efficiency.

- Develop a self-tuning system such that the resonance frequency of the second order seismic transducer automatically adapts to the frequency band or tone that characterises the ambient vibration.

- Consider other forms of seismic ambient vibration sources (for example broadband or random excitation) for the energy harvesting applications in order to compare such results with those obtained for tonal excitation.

- Study and investigate the possibility to introduce non-linearities in the mechanical domain model and in the AC-DC electrical conversion system of the harvesters in order to obtain a more accurate prediction of the electromechanical response at relatively high excitation levels.

LIST OF PUBLICATIONS

1. **L. Dal Bo**, P.Gardonio, D. Casagrande, S. Saggini, Smart panel with switching and sweeping piezoelectric patch vibration: Experimental results, *Journal of Mechanical Systems and Signal Processing* 120, (2019) 308-325.

2. **L. Dal Bo** and P. Gardonio, Energy harvesting with electromagnetic and piezoelectric transducers: unified theory and experimental validation, *Journal of Sound and Vibration* 433, (2018) 385-424.

3. P. Gardonio, **L. Dal Bo**, M. Zientek and S. Saggini, Experimental implementation of piezoelectric patch tuneable vibration absorbers. *XIIIth International Conference on Recent Advances in Structural Dynamics*, Lyon (FR), 15-17 April 2019.

4. P. Gardonio and **L. Dal Bo**, Scaling of electromagnetic and piezoelectric seismic harvesters. *XIIIth International Conference on Recent Advances in Structural Dynamics*, Lyon (FR), 15-17 April 2019.

5. M. Zientek, P. Gardonio, **Loris Dal Bo**, Piezoelectric patches with multi-resonant shunts for multiple frequency band vibration control. *The 29th International Conference on Noise and Vibration Engineering*, Leuven (BE), 17-19 September 2018.

6. **L. Dal Bo** and P. Gardonio, Experimental implementation of switching and sweeping piezoelectric patch vibration absorbers. *The 24th International Congress on Sound and Vibration*, London (UK), 23-27 July 2017.

7. **L. Dal Bo** and P. Gardonio, Smart panel with switching and sweeping piezoelectric patch vibration absorbers. *The 8th International Conference on Smart Structures and Materials and 6th International Conference on Smart Materials and Nanotechnology in Engineering*, Madrid (ES), 5-8 June 2017.

8. **L. Dal Bo** and P. Gardonio, Vibration energy harvesting with electromagnetic and piezoelectric seismic transducers: experimental results. *The 8th International*

Conference on Smart Structures and Materials and 6th International Conference on Smart Materials and Nanotechnology in Engineering, Madrid (ES), 5-8 June 2017.

9. **L. Dal Bo** and P. Gardonio, Comparison between electromagnetic and piezoelectric seismic vibration energy harvesters. *The 28th International Conference on Noise and Vibration Engineering*, Leuven (BE), 17-19 September 2016.

10. E. Turco, P. Gardonio and **L. Dal Bo**, Time-varying shunted electro-magnetic tuneable vibration absorber. *The 13th International Conference on Motion and Vibration Control* (MoViC) *and 12th International Conference on Recent Advances in Structural Dynamics* (RASD), Southampton (UK), 3-6 July 2016.

A

ELECTROMAGNETIC SEISMIC TRANSDUCER

A.1 CONSTITUTIVE EQUATIONS

The moving-coil transducer is an energy converter which transforms the electrical power into mechanical power and *vice versa*. This device is composed by a permanent cylindrical magnet, which is free to move axially within the cylindrical yoke where the coil is housed. The magnet generates a magnetic flux density **B** in the air gap and coil-yoke element. The electromechanical constitutive laws are defined by inspection of the constitutive fundamental equations, which govern the dynamics of the components that form the transducer. The transduction equations of the moving-coil transducer follow from Faraday law and Lorentz force law.

A.1.1 Electro-magnetic transduction Fundamental Equations

Faraday's law states that by varying in time the flux of the magnetic field ϕ concatenated with a closed loop wire of length l, an electromotive force (f.e.m.) e_w, which is given by the following law is produced:

$$e_w(t) = -\frac{d\phi(\mathrm{t})}{dt} = -\frac{d}{dt}\int_S \boldsymbol{B}\cdot\boldsymbol{n}\, ds. \tag{A.1}$$

Here S is the surface defined by the closed wire loop and **n** is the normal versor to the surface S. Considering the notation in Figure A.1, **n** is defined considering the right-turn screw rule with reference to the **t**-tangent unit vector. Also the positive and negative signs for e_w are defined with reference to the generator's convention.
After some mathematical manipulations of the integral term in Eq.(A.1), the temporal derivative of the flux ϕ can be expressed as follows:

$$\frac{d\phi(\mathrm{t})}{dt} = \int_S \left[\frac{\partial \mathbf{B}}{\partial t} + \dot{\boldsymbol{w}}\,\nabla\cdot\mathbf{B} \; - \nabla\times(\dot{\boldsymbol{w}} \times \boldsymbol{B})\right]\cdot \boldsymbol{n}\,\mathrm{dS}\,, \tag{A.2}$$

where $\dot{\boldsymbol{w}}$ is the velocity of the wire loop in direction $\boldsymbol{n}$.

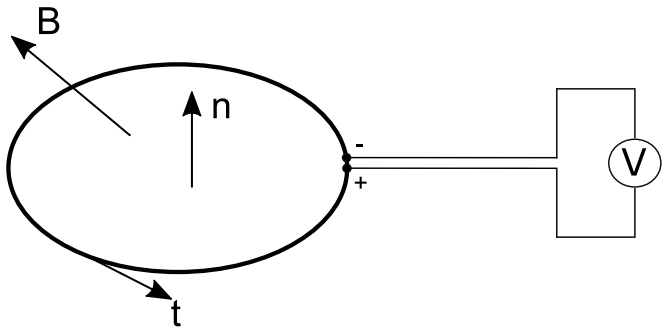

Figure A.1: Induced voltage in a wire.

Since the magnetic flux density **B** has zero divergence (i.e. $\cdot\,\mathbf{B} = \mathbf{0}$) and is generated by a permanent magnet (i.e. there is no temporal variation $\frac{\partial \mathbf{B}}{\partial t} = 0$) Eq.(A.2) becomes:

$$\frac{d\phi(\mathrm{t})}{dt} = -\int_S \nabla\times(\dot{\boldsymbol{w}} \times \boldsymbol{B})\cdot \boldsymbol{n}\,\mathrm{dS}\,. \tag{A.3}$$

Applying Stokes theorem to Eq.(A.3) follows:

$$\frac{d\phi(\mathrm{t})}{dt} = -\int_l \dot{\boldsymbol{w}} \times \boldsymbol{B}\cdot \boldsymbol{t}\,dl, \tag{A.4}$$

where l is the length of the wire loop and the versors **n** and **t** are related together according to the right handed screw rule. Recalling Eq.(A.1) and using Eq.(A.4) it follows:

$$e_w(t) = \int_l \dot{\boldsymbol{w}} \times \boldsymbol{B}\cdot \boldsymbol{t}\,dl. \tag{A.5}$$

Taking into account the definition of electrical voltage (i.e. $e_w = \int_l \boldsymbol{E}\cdot\boldsymbol{t}\,dl$) it can be verified that the f.e.m. generated by the motion of a loop wire with respect to the

magnetic flux density $\boldsymbol{B}$ gives the electrical work carried out by a specific electric force per unit of charge i.e. $\boldsymbol{E} = \boldsymbol{F}/q$ which is also called induced electromotive force. Respect to the notation shown in Figure A.1 , **E** has the same direction of **t**, therefore a wire loop in motion with velocity $\dot{\boldsymbol{w}}$ generates a positive voltage e_w.
In parallel, a charge particle q moving at velocity $\dot{\boldsymbol{w}}$ in a magnetic field $\boldsymbol{B}$ is subjected to the Lorentz force [209]:

$$\boldsymbol{f_L} = q\,\dot{\boldsymbol{w}} \times \boldsymbol{B}. \tag{A.6}$$

Considering a current-carrying conductor, the phenomenon is characterised by the motion of a large number of negative particles $q = -e$ (i.e. electrons). When the conductor is immersed in a magnetic field, each electron is subjected to the Lorentz Force. Therefore, the impacts that the moving electrons have with the ions of the crystalline lattice of the conducting material produce a net force on the conducting wire. Considering Eq.(A.6) and referring to a filiform conductor, the Lorentz force can be rewritten in a form known as the second elementary Laplace law [209]:

$$\boldsymbol{f_i} = \int_l i\,d\boldsymbol{l} \times \boldsymbol{B}. \tag{A.7}$$

Here i refers to the current that moves through the wire conductor while dl identifies the infinitesimal portion of conductor oriented according to the normal of the cross-section of the wire and whose direction is defined by the direction of the current i (Figure A.2). This law expresses the fact that the magnetic Lorentz force on an infinitesimal piece of wire (dl) run by current is orthogonal to the conductor and to the magnetic field (**B**) and is oriented with respect to dl and **B** according to the right-hand rule convention.

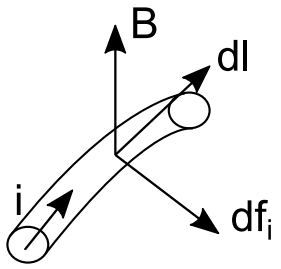

Figure A.2: Force on a current path conductor element immersed in a magnetic flux density **B.**

A.1.2 Ideal transducer

The coil-magnet components of the electromechanical transducer considered in this thesis, move along linear paths. Therefore vector relations that characterise the physical phenomena can be specified with scalar relationships. Furthermore, the mechanical and electrical variables that govern the transduction mechanisms are directly linked to each other. In order to obtain a rigorous analytical formulation it is therefore necessary to identify a reference system and thus a positive sign convention for the two electrical (i.e. current and voltage) and mechanical (i.e. force and velocity) variables. For this purpose a natural definition occurs from Lenz's law, which leads to the minus sign in Eq.(A. 1). In fact, considering the notation shown in Figure A.1, if the (undeformable) loop wire is short circuited and moves in a same direction of the versor **n**, a current flow is produced trough the wire, which is given by:

$$i_h = \frac{e_h}{R} = -\frac{1}{R}\frac{d\phi}{dt}. \tag{A.8}$$

Here R is the internal electrical resistance of the conductive material. The current i_h produces a field $\boldsymbol{B}_h$ whose direction is associated with the current i_h (i.e. with the versor **t**), considering the right-hand screw rule. The term $\boldsymbol{B}_h$ is oriented alongside with versor **n** (first elementary law of Laplace [209]), i.e at magnetic flux density **B**, and therefore tends to compensate for the decrease of the magnetic flow ϕ. If the electric resistance of the wire loop tends to zero, the compensation would be perfect and the chained flux would remain constant.

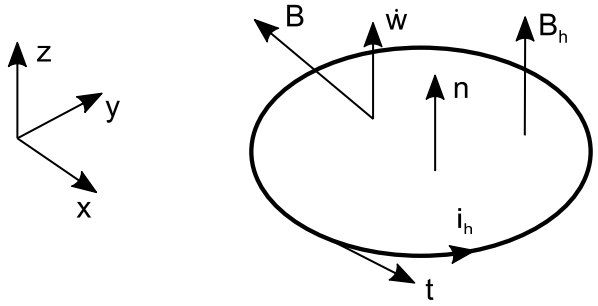

Figure A.3: Lentz law on the direction of the induced currents by temporal variation of the magnetic flux density **B**.

Thus if the force and velocity have the same orientation, the resulting voltage drop and current flow will have same orientation as that of the induced electric field. Moreover, combination of a positive voltage and current will generate a negative force. Therefore, considering the notation shown in Figure A.3, recalling Eqs.(A.5) and(A.7) and assuming that the wire loop moves only along **z** axis, the two transduction equations can be specified as follows:

$$\boldsymbol{f_i} = \int_{\boldsymbol{l}} i_h \, d\boldsymbol{l} \times \boldsymbol{B}, \tag{A.9}$$

$$e_w(t) = \int_{l} \boldsymbol{\dot{w}_z} \times \boldsymbol{B} \cdot \boldsymbol{t} \, dl. \tag{A.10}$$

These expressions can be rewritten as follows:

$$f_{ext} = -iBl, \tag{A.11}$$

$$e_h = \dot{w}Bl, \tag{A.12}$$

where f_{ext} is defined as the the external force (direct according to the positive axis z) necessary to balance the Lorentz force f_i. Notice that the transducer constant Bl appearing in Eqs.(A.11), (A.12) have the dimension of V s/m or N/A.
From the relations (A.11), (A.12) is possible to highlight the fundamental characteristic of the transducer, that is the electrical to mechanical and mechanical to electrical conversion of energy. In fact, adding the mechanical power $f_{ext}\dot{w}$ employed to move the wire and the generated electric power given by $e_h i_h$ results:

$$f_{ext}\dot{w} + e_h i_h = -i\dot{w}Bl + \dot{w}Bli = 0. \tag{A.13}$$

In other words, in each element of the wire moving in a magnetic field **B** and subjected to a current flow i_h, the supplied/generated mechanical power is equal to the generated/supplied electrical power. So the moving-coil transducer cannot store energy, and operates as an ideal electromechanical converter.

1.1.1 Inertial transducer

As shown in Figure 2.1 (a), the transducer considered in this study is characterised by a core magnetic element and a coil assembly. Assuming n turns for the coil wire conductor, Eqs.(A.11), (A.12) can be rewritten for this sytem as follow:

$$f_{ext} = -i_h Bl, \tag{A.14}$$

$$e_h = \dot{w}_r Bl, \tag{A.15}$$

where l is the total length of the coil winding and $\dot{w}_r = \dot{w}_m - \dot{w}_h$ is the relative velocity between the magnet and the coil , assumed positive in elongation.
Considering the damping and elastic effects in the transducer, Eq.(A.14) becomes:

$$f_{ext} = -i_h Bl + k_m w_r + c_m \dot{w}_r. \tag{A.16}$$

Here, k_m is the equivalent axial stiffness of the top and bottom spiral springs that connect the outer ferromagnetic ring and coil assembly to the inner magnetic element. Also, c_m is the viscoelastic damping coefficient for: a) the damping produced by eddy currents that develops in the ferromagnetic ring, b) the inner air damping that develops in the gap between the coil and the magnetic element.
As shown in Figure A.4, when the coil magnet transducer is used as an inertial transducer, the following equations holds for the moving mass m_m (the moving Yoke and coil assembly):

$$m_m \ddot{w}_m = -f_m, \tag{A.17}$$

$$f_{ext} - f_m = 0. \tag{A.18}$$

Similarly, for the base magnetic mass m_b the following equations holds:

$$m_b \ddot{w}_b = f_b, \tag{A.19}$$

$$f_b - f_{ext} = 0. \tag{A.20}$$

Solving Eqs.(A.17)- (A.20) gives:

$$f_{ext} = -m_m \ddot{w}_m, \tag{A.21}$$

$$f_{ext} = m_b \ddot{w}_b. \tag{A.22}$$

These expressions can be insert in Eq.(A.16), so that the following two equations of motion are obtained for the inertial and base masses:

$$m_m \ddot{w}_m = iBl - k_m w_r - c_m \dot{w}_r \quad \text{(A.23)}$$

$$m_b \ddot{w}_h = -iBl + k_m w_r + c_m \dot{w}_r + f_h \quad \text{(A.24)}$$

Here f_h is the external force applied to the base mass m_b. Eqs. (A.23), (A.24) are the two laws that characterise the mechanical response of the transducer.

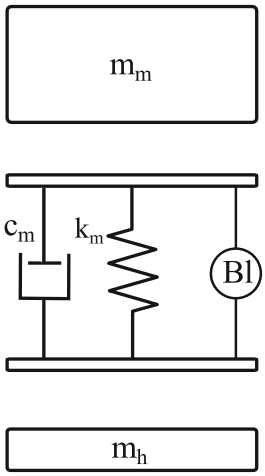

Figure A.4: Schematic representation of the equivalent mechanical transduction mechanism of a real transducer.

Moving to the electrical response of the transducer, at first let's consider the usual generic conductor, which for the sake of simplicity can be seen as a thread-like coil whose ends are placed very close, almost to coincide, so that the conductor can be modelled as a closed line. A concatenated flow $\phi_h(t) = \int_S \boldsymbol{B_h} \cdot \boldsymbol{n}\, ds$ can thus be associated to the surface of the close loop. The induced magnetic flux density field $\boldsymbol{B}_h$ and the concatenated flux ϕ_h are generated by the same current of the inductor i_h, which is assumed to be solenoidal (i.e. constant current density). If the vector lines of $\boldsymbol{B}_h$, which determine the flow ϕ_h concatenated with the wire, are due to the sole solenoidal current i_h of the inductor itself, the flow ϕ_h is called *autoconcatenated* or *self-inductioned*.

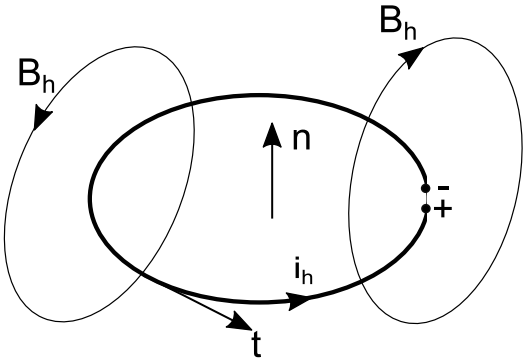

Figure A.5: Self induction flow of a loop wire.

In this situation the field $\boldsymbol{B}_h$ (and therefore the concatenated flux ϕ_h) must be a function only of the current i_h and the geometry of the conductor. Choosing the positive sign of the current in the direction of the tangent versor $\boldsymbol{t}$, which is linked to the versor **n** via the right-handed screw rule, the inductance can be defined as follows:

$$L(t) \triangleq \frac{\phi_h(\mathrm{t})}{i_h(t)}. \tag{A.25}$$

In the absence of hysteresis phenomena, the induction L is always defined as positive because ϕ_h and i_h have always the same sign. In the hypothesis of linearity and non deformability of the inductor, L is constant (i.e. $dL\ /\ dt = 0$) and for the given sign convection therefore the current related self-induced flow can be written as:

$$\frac{d\phi_h}{dt} = L\frac{di_h}{dt}. \tag{A.26}$$

Applying the Faraday-Neumann law in Eq.(A.26) follows:

$$e_h(t) = -\frac{d\phi_h}{dt} = -L\frac{di_h}{dt}. \tag{A.27}$$

Since the coil has a self-inductance, which opposes to the change in current, a sort of inertia effect is produced. Thus, the auto-induced f.e.m is opposed to the variation of current passing through it. If, as in the case of the coil magnet, the conducting wire is composed by N turns, the auto induced field ϕ_h becomes $N\phi_h$. Thus Eq.(A.27) should be simply modified multiplying the value of the inductance by N.

If the auto-induced voltage is generated by the motion of a loop wire with respect to the magnetic flux density B, Eq.(A.15) can be substituted into (A.27) giving:

$$\dot{w}_r Bl = -L\frac{di_h}{dt}. \tag{A.28}$$

Eq.(A.28) describes the fact that if the current i_h in the loop increases, a negative velocity is produced between the magnet and the coil elements (i.e. under positive currents the force generated by the transducer (i.e. -f_{ext}) tends to bring magnet and wire closer together).
Rewriting Eq.(A.28) in canonical form:

$$\dot{w}_r Bl + L\frac{di_h}{dt} = 0, \tag{A.29}$$

leads to the classical Kirchhoff law applied to a purely inductive circuit in series with a generator of f.e.m. In analogy to a mechanical oscillator, introducing the dissipative term R_e due to the internal resistance of the filiform conductor gives:

$$Bl\dot{w}_r + R_e i_h + L_e\frac{di_h}{dt} = 0. \tag{A.30}$$

Eq.(A.30) identifies the Kirchhoff law of the circuit depicted in Figure A.6. Assuming the circuit is connected to a generic electric network that produces a voltage drop e_h, applying the Kirchhoff's law gives:

$$e_h = Bl\dot{w}_r + R_e i_h + L_e\frac{di_h}{dt}. \tag{A.31}$$

Eqs.(A.23), (A.24), (A.31) represent the constitutive relations of the electromagnetic transducer shown in Figure 2.1 (c). It can be observed that Eq.(A.31) identifies the Kirchhoff's law applied to the mesh in Figure A.7 under the generator convention for the two-port bipole.

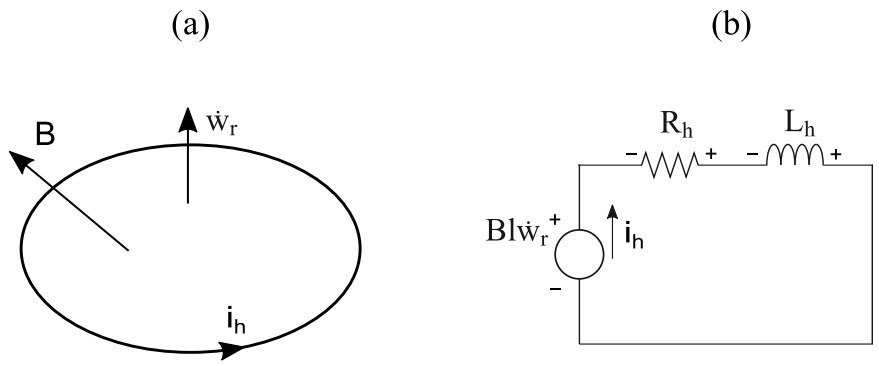

Figure A.6: Moving wire (a), equivalent circuit model (b).

In order to move back to a standardized representation (see Ref. [184]–[186]) and since the resistive and inductive dipoles are of the passive type, it is more appropriate to apply the user convention, thus reversing the signs of all voltages. Thus although Eq.(A.31) maintains the same form, it identifies the circuit shown in Figure 2.1 (c).

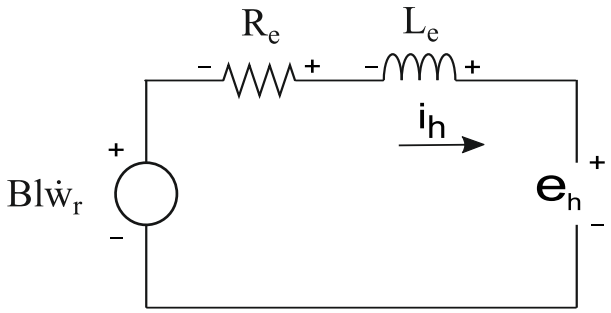

Figure A.7: Equivalent circuit schematic representation of the electrical transduction mechanism.

In summary, the constitutive equations of the electromechanical coil magnet transducer are given by:

$$m_m \ddot{w}_m = iBl - k_m w_r - c_m \dot{w}_r, \tag{A.32}$$

$$m_b \ddot{w}_h = -iBl + k_m w_r + c_m \dot{w}_r + f_h, \tag{A.33}$$

$$e_h = Bl\dot{w}_r + R_e i + L_e \frac{di}{dt}. \tag{A.34}$$

Assuming time harmonic functions, after some mathematical manipulations, the three Eqs.(A.32), (A.33), (A.34) can be reduced to the following two constitutive equations for the seismic coil–magnet transducer:

$$f_h = \left\{ \mathrm{j}\omega m_b + \frac{\left(\frac{k_m}{\mathrm{j}\omega} + c_m\right)\mathrm{j}\omega m_m}{\left(\frac{k_m}{\mathrm{j}\omega} + c_m + \mathrm{j}\omega m_m\right)} \right\} \dot{w}_h + \left\{ \psi_{CM} \frac{\mathrm{j}\omega m_m}{\left(\frac{k_m}{\mathrm{j}\omega} + c_m + \mathrm{j}\omega m_m\right)} \right\} i_h, \tag{A.35}$$

$$e_h = -\left\{ \psi_{CM} \frac{\mathrm{j}\omega m_m}{\left(\frac{k_m}{\mathrm{j}\omega} + c_m + \mathrm{j}\omega m_m\right)} \right\} \dot{w}_h + \left\{ R_e + \mathrm{j}\omega L_e + \frac{\psi_{CM}^2}{\left(\frac{k_m}{\mathrm{j}\omega} + c_m + \mathrm{j}\omega m_m\right)} \right\} i_h. \tag{A.36}$$

A.2 EDDY CURRENTS (SKIN EFFECT)

As discussed in the previous section, the electrodynamic behaviour of a linear coil magnet device shown in picture (a) of Figure 2.1 is typically modelled in terms of a resistor and inductor connected in series. Measurements taken on real coil-magnet devices show that eddy currents in the coil wire are responsible for a semi-inductive behaviour at high frequencies, which differs from the normal inductive behaviour usually assumed in the classical theory. This phenomenon, known as "Skin effect", causes the effective resistance of the conductor to increase at higher frequencies. The skin effect is due to opposing eddy currents induced by the changing magnetic field resulting from the alternating current in the wire. This section presents a model of lossy inductor that can be used to justify the experimental results shown in Figure 2.2 and Figure 2.3.

A.2.1 Principles

The starting point for the formulation of the current-field problem comes from the four Maxwell's equations under the condition of no-displacement currents (negligible in conductors) [210] :

$$\nabla \times \mathbf{E} = -\frac{\partial \mathbf{B}}{\partial \mathrm{t}}, \tag{A.37}$$

$$\nabla \times \mathbf{H} = \mathbf{J}, \tag{A.38}$$

$$\nabla \cdot \mathbf{B} = 0, \tag{A.39}$$

$$\nabla \cdot \mathbf{D} = \frac{\rho}{\varepsilon} = 0. \tag{A.40}$$

Here **B** and **H** are the magnetic field density and magnetic field intensity. Also ***E*** and **D** are the electric and displacement field . Finally **J** is the current density.
Assuming linear, isotropic and homogenous material, the constitutive relations between the fields are given by:

$$\mathbf{B} = \mu_e \mathbf{H}, \tag{A.41}$$

$$\mathbf{D} = \varepsilon_e \boldsymbol{E}, \tag{A.42}$$

$$\mathbf{J} = \sigma_e \mathbf{E}, \tag{A.43}$$

where μ_e, ε_e, σ_e are the (constant) electric permeability, permittivity and conductivity.
Using Eq.(A.41) into Eq.(A.37) gives:

$$\nabla \times \mathbf{E} = -\frac{\partial(\mu_e \mathbf{H})}{\partial t}. \tag{A.44}$$

Taking the rotor of Eq.(A.44):

$$\nabla\nabla \cdot \mathbf{E} - \nabla^2 \mathbf{E} = -\mu_e \frac{\partial(\nabla \times \mathbf{H})}{\partial t}, \tag{A.45}$$

and using Eqs.(A.40), (A.42) gives:

$$\nabla^2 \mathbf{E} = \mu_e \frac{\partial(\nabla \times \mathbf{H})}{\partial t}. \tag{A.46}$$

Finally using Eqs.(A.38), (A.43) it follows:

$$\nabla^2 \mathbf{J} = \mu_e \sigma_e \frac{\partial \mathbf{J}}{\partial t}, \tag{A.47}$$

which identifies a classical diffusion equation where $\mu_e \sigma_e$ is the inverse analogues of the thermal diffusivity. In the Cartesian coordinate system Eq.(A.47) is decoupled in three components of **J**:

$$\boldsymbol{\nabla^2} J_{\mathrm{i}} = \mu_{\mathrm{e}}\sigma_{\mathrm{e}}\frac{\partial J_{\mathrm{i}}}{\partial \mathrm{t}} \quad , \qquad \mathrm{i} = x, y, z \tag{A.48}$$

Assuming for simplicity that the current density $\boldsymbol{J}$ has only one component along the z direction it follows:

$$\frac{\partial^2 J_z}{\partial \mathrm{y}^2} = \mu_{\mathrm{e}}\sigma_{\mathrm{e}}\frac{\partial J_z}{\partial \mathrm{t}}. \tag{A.49}$$

Adopting separation of variables such that $J = f_1(y)f_2(t)$ and assuming harmonic time functions given in exponential form the current density can be written as follows:

$$J_z(y,t) = J_z(y)\mathrm{e}^{\mathrm{i}\omega \mathrm{t}}. \tag{A.50}$$

This expression can be used in Eq.(A.49) such that:

$$\frac{\mathrm{d}^2 \mathrm{J_z}}{\mathrm{dy}^2}\mathrm{e}^{\mathrm{i}\omega \mathrm{t}} = \mathrm{i}\omega\mu_{\mathrm{e}}\sigma_{\mathrm{e}}\mathrm{J_z}\mathrm{e}^{\mathrm{i}\omega \mathrm{t}}. \tag{A.51}$$

Since Eq.(A.51) applies to every t, eliminating the time dependence follows:

$$\frac{\mathrm{d}^2 \mathrm{J}_z}{\mathrm{dy}^2} = \alpha^2 \mathrm{H}_z, \tag{A.52}$$

where $\alpha \triangleq \sqrt{\mathrm{i}\omega\mu_{\mathrm{e}}\sigma_{\mathrm{e}}}$. The solution of Eq.(A.52) can take the general form:

$$\mathrm{J}_z = A_1\mathrm{e}^{\alpha y} + A_2\mathrm{e}^{-\alpha y}, \tag{A.53}$$

where A_1 and A_2 are the two constants that depend on the boundary condition. Setting the radius of the conductive wire to infinity (hypothesis of semi – infinite medium) and assuming an alternating current at the surface $y = 0$ of the wire, the two boundary conditions give:

$$J_z(0) = J_0\mathrm{e}^{\mathrm{i}\omega \mathrm{t}}, \tag{A.54}$$

$$J_z(y \to \infty) = 0, \tag{A.55}$$

which applied to Eq.(A.53) gives:

$$J_z = \mathrm{H}_0 \mathrm{e}^{\mathrm{i}\omega \mathrm{t}} \mathrm{e}^{-\alpha y}. \tag{A.56}$$

Introducing the definition of skin depth δ [211]:

$$\delta \triangleq \sqrt{\frac{2}{\omega \mu_\mathrm{e} \sigma_\mathrm{e}}}, \tag{A.57}$$

rearranging α as $\alpha = (1 + \mathrm{i})/\delta$ and substituting it in Eq.(A.56) gives:

$$J_z = J_0 \mathrm{e}^{-\frac{y}{\delta}} \mathrm{e}^{\mathrm{i}\left(\omega \mathrm{t} - \frac{y}{\delta}\right)}. \tag{A.58}$$

Finally taking only the real part:

$$J_z(y,t) = J_0 \mathrm{e}^{-\frac{y}{\delta}} \cos\left(\omega \mathrm{t} - \frac{y}{\delta}\right). \tag{A.59}$$

The current i_z may be shown to behave in a similar manner [211]:

$$i_z(y,t) = i_0 \mathrm{e}^{-\frac{y}{\delta}} \cos\left(\omega \mathrm{t} - \frac{y}{\delta}\right), \tag{A.60}$$

which describes the distribution of a steady state alternating current with a linearly phase shift proportional to y and whose magnitude decrease exponentially.

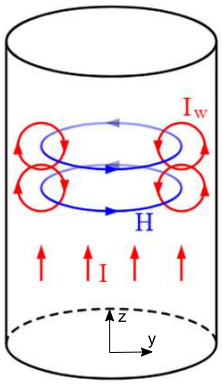

Figure A.8: Skin depth due to the circulating eddy currents I_w (arising from a changing H field) cancelling the current flow in the centre of a conductor and reinforcing it in the skin.

The alternating current in a conductor decreases exponentially from its value at the surface. For y much greater than δ the current is substantially negligible. Eq.(A.60) describes the Skin depth effect generated on the coil wire of the electromagnetic harvester when an AC current is present [212].

A.2.2 Lossy inductor (Model)

The theoretical impedance of a lossless voice coil is characterised by 90° phase. However, due to the skin effect generated on the surface of the wire, experiments show that the phase values are usually measured in the range of 60°-70° [179] (see also Figure 2.2 (d), Figure 2.3 (d)). For a lossy inductor, a general frequency dependent model can be expressed as a power series in ω [178]. An impedance model of a loss inductor that leads to excellent agreement with experimental data is proposed by [177] and can be written as:

$$\mathrm{Z}_L(j\omega) = \mathrm{K}\omega^n \left[\cos\left(\frac{n\pi}{2}\right) + \mathrm{j}\sin\left(\frac{n\pi}{2}\right)\right] = \mathrm{K}\omega^n e^{\frac{jn\pi}{2}}, \tag{A.61}$$

where n and K are constants. A method to determine such coefficients based on Ref. [177] is summarised below. Based on the expression defined in Eq.(2.5) and derived in Eq.(A.36) a general formula, which identifies the electrical impedance Z_{ei} of a coil magnet device, can be expressed as:

$$\mathrm{Z}_{ei}(j\omega) = R_e + \tilde{\mathrm{Z}}_L(j\omega) + \frac{R_M \frac{1}{Q_M}\frac{j\omega}{\omega_n}}{\left(\frac{j\omega}{\omega_n}\right)^2 + \frac{1}{Q_M}\frac{j\omega}{\omega_n} + 1}, \tag{A.62}$$

where R_e is the internal resistance of the voice coil, $\tilde{\mathrm{Z}}_L$ is the lossy impedance of the coil, Q_M is the mechanical quality loss factor and R_M is peak amplitude of the impedance at the fundamental mechanical resonance frequency ω_n of the device. Considering Eq.(A.62), the lossy impedance can thus be written as follows:

$$\tilde{\mathrm{Z}}_L(j\omega) = \mathrm{Z}_{ei} - R_e - \frac{R_M \frac{1}{Q_M}\frac{j\omega}{\omega_n}}{\left(\frac{j\omega}{\omega_n}\right)^2 + \frac{1}{Q_M}\frac{j\omega}{\omega_n} + 1}. \tag{A.63}$$

The natural logarithms of Eqs.(A.61), (A.63) are given by:

$$\ln(\mathrm{Z}_L) = \ln(\mathrm{K}) + \mathrm{n}\ln(\omega) + \frac{jn\pi}{2}, \tag{A.64}$$

$$\ln\left(\tilde{\mathrm{Z}}_L\right) = \ln\left|\tilde{\mathrm{Z}}_L\right| + j\,\arg\left(\tilde{\mathrm{Z}}_L\right). \tag{A.65}$$

Assuming that the electrical impedance Z_{ei} is measured at a set of N frequencies and Z_L is known in a defined range of frequencies, with reference to specific n and K parameters, if $\ln(\mathrm{Z}_L) - \ln\left(\tilde{\mathrm{Z}}_L\right) = 0$ over that frequency range, then Z_L is the exact impedance model of the lossy inductor. A method that minimizes the mean magnitude square difference can be obtained introducing an error function ϵ:

$$\epsilon = \sum_{r=1}^{N} \left| \ln[\mathrm{Z}_L(j\omega_r)] - \ln[\tilde{\mathrm{Z}}_L(j\omega_r)] \right|^2, \tag{A.66}$$

which can be minimized by setting $\frac{\partial \epsilon}{\partial n}$ and $\frac{\partial \epsilon}{\partial \ln(K)}$; so that:

$$n = \frac{1}{\Delta}\left[\sum_{r=1}^{N} \ln\left|\tilde{\mathrm{Z}}_L(j\omega_r)\right| \ln(\omega_r) - \frac{1}{N}\sum_{r=1}^{N} \ln\left|\tilde{\mathrm{Z}}_L(j\omega_r)\right| \sum_{r=1}^{N} \ln(\omega_r) + \frac{\pi}{2}\sum_{r=1}^{N} \arg[\tilde{\mathrm{Z}}_L(j\omega_r)]\right], \tag{A.67}$$

$$\ln(K) = \frac{1}{N}\left[\sum_{r=1}^{N} \ln|\mathrm{Z}_L(j\omega_r)| - \mathrm{n}\sum_{r=1}^{N} \ln(\omega_r)\right], \tag{A.68}$$

where Δ is defined as:

$$\Delta = \sum_{r=1}^{N} [\ln(\omega_r)]^2 - \frac{1}{N}\left[\sum_{r=1}^{N} \ln(\omega_r)\right]^2 + N\left(\frac{\pi}{2}\right)^2. \tag{A.69}$$

When Eqs.(A.67), (A.68) are satisfied the lossy impedance Z_L fit the measured $\tilde{\mathrm{Z}}_L$ with the minimum squared error.

A.3 EDDY CURRENTS (DAMPING)

Eddy currents produce a damping effect, which can be derived from the magnetic distribution of the field in the outer cylindrical Yoke that holds the coil. In this section the theoretical basis to understand the phenomenon is presented.

A.3.1 Fundamental -Equation

Let's consider a circular magnetic strip carrying a current loop of intensity I, considering the notation shown in Figure A.9, the magnetic flux density $\mathrm{d}\boldsymbol{B}$ at a generic point (x, y, z), can be expressed as follows [211], [213], [214]:

$$\mathrm{d}\boldsymbol{B} = \frac{\mu_0 I}{4\pi}\frac{d\boldsymbol{l} \times \boldsymbol{R}_l}{R_l^3}. \tag{A.70}$$

From Maxwell's equations, the magnetic field $\boldsymbol{B}$ field has zero divergence everywhere in space (i.e. $\nabla \cdot \boldsymbol{B} = 0, \ \forall \mathrm{x, y, z}$). Therefore such field can be associated to a vector field called *potential vector* $\boldsymbol{A}$:

$$\boldsymbol{B} = \nabla \times \mathbf{A}. \tag{A.71}$$

As shown in [211], [213], the derivation of **B** can also be obtained calculating the potential vector:

$$\mathrm{d}\boldsymbol{A} = \frac{\mu_0 I}{4\pi}\frac{d\boldsymbol{l}}{|\boldsymbol{R}_l|}, \tag{A.72}$$

and by taking the curl $\boldsymbol{A}$:

$$\mathrm{d}\boldsymbol{B} = \nabla \times \mathrm{d}\mathbf{A}. \tag{A.73}$$

The derivation of **B** from **A** is simpler with respect to the direct calculation of Eq.(A.70).
Considering Figure A.9, the following relations can be obtained:

$$\boldsymbol{R} = (R\cos\theta', 0, R\sin\theta'), \tag{A.74}$$

$$d\boldsymbol{l} = (-a\sin\phi, a\cos\phi, 0)\,\mathrm{d}\phi, \tag{A.75}$$

$$\boldsymbol{r} = (a\cos\phi, a\sin\phi, 0), \tag{A.76}$$

$$|\boldsymbol{R} - \boldsymbol{r}| = |\boldsymbol{R}_l| = \sqrt{a^2 + R^2 - 2Ra\cos\theta'\cos\phi}, \tag{A.77}$$

where $(\hat{\boldsymbol{x}}, \hat{\boldsymbol{y}}, \hat{\boldsymbol{z}})$ are the unit vectors of the Cartesian coordinate system for a loop of radius a located in the x-y plane.

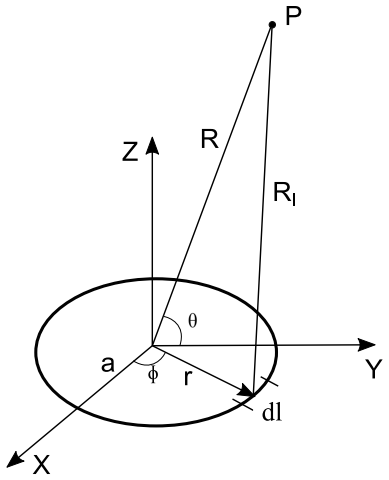

Figure A.9: Schematic of the circular magnetized strip

Substituting Eqs.(A.74)-(A.77) into Eq.(A.72) and integrating along the circular current distribution I follows:

$$\boldsymbol{A} = \frac{\mu_0 I}{4\pi}\oint \frac{d\boldsymbol{l}}{|\boldsymbol{R}_l|} = \frac{\mu_0 I}{4\pi}\left[\int_0^{2\pi} \frac{-a\sin\phi\,\mathrm{d}\phi}{\sqrt{a^2 + R^2 - 2Ra\cos\theta'\cos\phi}}\hat{\boldsymbol{x}} + \int_0^{2\pi} \frac{a\cos\phi\,\mathrm{d}\phi}{\sqrt{a^2 + R^2 - 2Ra\cos\theta'\cos\phi}}\hat{\boldsymbol{y}}\right]. \tag{A.78}$$

From the axial symmetry of the problem, the first integral can be removed (i.e. the contribution of $\boldsymbol{A}$ along the x direction is zero and the integration of the y component of $\boldsymbol{A}$ can be doubled by changing the limit of integration from $0 \div 2\pi$ to $0 \div \pi$):

$$\boldsymbol{A} = \frac{\mu_0 I}{4\pi}\oint \frac{d\boldsymbol{l}}{|\boldsymbol{R}_l|} = \frac{\mu_0 I}{4\pi} 2\left[\int_0^{\pi} \frac{a\cos\phi \,\mathrm{d}\phi}{\sqrt{a^2 + R^2 - 2Ra\cos\theta'\cos\phi}}\right]\hat{\boldsymbol{y}}. \tag{A.79}$$

Introducing cylindrical coordinates:

$$\rho^2 = x^2 + \mathrm{y}^2, \qquad \tan\phi = \frac{y}{x}, \qquad z = z, \tag{A.80}$$

Eq.(A.79) can be rewritten as follows:

$$\boldsymbol{A} = \frac{\mu_0 I}{4\pi}\oint \frac{d\boldsymbol{l}}{|\boldsymbol{R}_l|} = \frac{\mu_0 I}{2\pi}\int_0^{\pi} \frac{a\cos\phi \,\mathrm{d}\phi}{\sqrt{a^2 + \rho^2 + z^2 - 2\rho b\cos\phi}}\widehat{\boldsymbol{\phi}}, \tag{A.81}$$

where, switching to the cylindrical coordinate solution, the y component becomes ϕ component. Eq.(A.81) does not have a closed form solution but can be solved by converting the integral into the Elliptic integrals [213], [215], [216]:

$$K(k,\varphi) = \int_0^{\pi/2} \frac{d\varphi}{\sqrt{1 - k^2\sin^2(\varphi)}}, \tag{A.82}$$

$$E(k,\varphi) = \int_0^{\pi/2} \sqrt{1 - k^2\sin^2(\varphi)}\, d\varphi. \tag{A.83}$$

The solution of Elliptic integrals is provided in tabulated functions and their derivatives obey to the following relations:

$$\frac{dK}{dk} = \frac{E}{k(1-k^2)} - \frac{K}{k} \quad , \quad \frac{dE}{dk} = \frac{E}{k} - \frac{K}{k}. \tag{A.84}$$

So introducing the change of variable $\phi = \pi + 2\theta$ and rearranging the denominator, Eq.(A.81) written in scalar notation becomes:

$$A_\phi = \frac{\mu_0 I}{\pi}\frac{a}{\sqrt{a^2 + \rho^2 + z^2}}\int_0^{\pi/2} \frac{(2\sin^2(\theta) - 1)}{\sqrt{1 - k^2\sin^2(\theta)}} d\theta, \tag{A.85}$$

where:

$$\mathrm{d}\phi = 2\mathrm{d}\theta \quad , \quad k^2 = \frac{4a\rho}{(\rho+a)^2+z^2}. \tag{A.86}$$

The integrand in Eq.(A.85) can be decomposed as:

$$\frac{(2\sin^2(\theta)-1)}{\sqrt{1-k^2\sin^2(\theta)}} = \frac{2\sin^2(\theta)}{\sqrt{1-k^2\sin^2(\theta)}} - \frac{1}{\sqrt{1-k^2\sin^2(\theta)}}, \tag{A.87}$$

and noting that

$$\frac{k^2\sin^2(\theta)}{\sqrt{1-k^2\sin^2(\theta)}} = \frac{1}{\sqrt{1-k^2\sin^2(\theta)}} - \sqrt{1-k^2\sin^2(\theta)}, \tag{A.88}$$

Eq.(A.87) becomes:

$$\frac{(2\sin^2(\theta)-1)}{\sqrt{1-k^2\sin^2(\theta)}} = \frac{2}{k^2}\left(\frac{1}{\sqrt{1-k^2\sin^2(\theta)}} - \sqrt{1-k^2\sin^2(\theta)}\right) - \frac{1}{\sqrt{1-k^2\sin^2(\theta)}}. \tag{A.89}$$

Substituting Eq.(A.89) into Eq.(A.85) and using Eqs.(A.82), (A.83) follows:

$$A_\phi = \frac{\mu_0 I}{2\pi}\sqrt{\frac{a}{x}}k\left[\left(\frac{2}{k^2}-1\right)K(k) - \frac{2}{k^2}E(k)\right]. \tag{A.90}$$

The magnetic field $\boldsymbol{B}$ is performed from the vector potential $\boldsymbol{A}$ taking the curl of Eq.(A.90) in cylindrical coordinates:

$$\begin{aligned}\mathbf{B} = \nabla\times\mathbf{A} \triangleq \frac{1}{\rho}&\begin{vmatrix}\widehat{\boldsymbol{\rho}} & \rho\widehat{\boldsymbol{\phi}} & \widehat{\boldsymbol{k}}\\ \frac{\partial}{\partial\rho} & \frac{\partial}{\partial\phi} & \frac{\partial}{\partial z}\\ A_\rho & \rho A_\phi & A_z\end{vmatrix}\\ &= \left(\frac{1}{\rho}\frac{\partial A_z}{\partial\phi} - \frac{\partial A_\phi}{\partial z}\right)\widehat{\boldsymbol{\rho}} + \left(\frac{\partial A_\rho}{\partial z} - \frac{\partial A_z}{\partial x}\right)\widehat{\boldsymbol{\phi}}\\ &+ \frac{1}{\rho}\left(\frac{\partial(\rho A_\phi)}{\partial x} - \frac{\partial A_x}{\partial\phi}\right)\widehat{\boldsymbol{k}}\\ &= -\frac{\partial A_\phi}{\partial z}\widehat{\boldsymbol{\rho}} + \frac{1}{\rho}\frac{\partial(\rho A_\phi)}{\partial\rho}\widehat{\boldsymbol{k}} \triangleq B_\rho\widehat{\boldsymbol{\rho}} + B_z\widehat{\boldsymbol{k}}.\end{aligned} \tag{A.91}$$

Substituting Eq.(A.90) into Eq.(A.91) and using the relations between the Elliptic integrals

$$\frac{\partial E}{\partial \rho} = \frac{\partial E}{\partial k}\frac{\partial k}{\partial \rho} \quad , \quad \frac{\partial K}{\partial \rho} = \frac{\partial E}{\partial k}\frac{\partial k}{\partial \rho}, \tag{A.92}$$

$$\frac{\partial E}{\partial z} = \frac{\partial E}{\partial k}\frac{\partial k}{\partial z} \quad , \quad \frac{\partial K}{\partial z} = \frac{\partial K}{\partial k}\frac{\partial k}{\partial z}, \tag{A.93}$$

it follows that radial and axial magnetic flux density generated by a current loop I are given by:

$$B_\rho(\rho, z) = \frac{\mu_0 I}{2\pi}\frac{1}{\rho}\frac{z}{\sqrt{(a+\rho)^2 + z^2}}\left[E\frac{a^2+\rho^2+z^2}{(a-\rho)^2+z^2} - K(k)\right], \tag{A.94}$$

$$B_z(\rho, z) = \frac{\mu_0 I}{2\pi}\frac{1}{\sqrt{(a+\rho)^2 + z^2}}\left[E\frac{a^2-\rho^2-z^2}{(a-\rho)^2+z^2} + K(k)\right]. \tag{A.95}$$

One approach that can be used to study the physics of a permanent magnet is the current model (Ampere's Equivalence) [215], [216], which reduces the cylindrical permanent magnet as an equivalent cylinder where a surface $\boldsymbol{j_m}$ current density circulates around the external surface. Assuming a cylindrical magnet polarized along the $\boldsymbol{z}$ axis, the source current surface density can be defined as:

$$\boldsymbol{j_m} = M_z\widehat{\boldsymbol{\phi}}, \tag{A.96}$$

where $\widehat{\boldsymbol{\phi}}$ is the tangential unit vector around the cylinder and M_z is the magnetization intensity, property of the magnet material [215], [216].

Considering the circular magnetic strip carrying a current loop of density j_m, extending from $-l_m/2$ and $l_m/2$, the components of the magnetic filed **B** at a point in the plane (ρ, z) can be derived from Eqs.(A.94), (A.95) as follows :

$$B_\rho(\rho, z) = \frac{\mu_0 M_z}{2\pi}\int_{-l_m/2}^{l_m/2}\frac{z-z'}{x\sqrt{(a+\rho)^2+(z-z')^2}}\left[E\frac{a^2+\rho^2+(z-z')^2}{(a-\rho)^2+(z-z')^2} - K(k)\right]dz', \tag{A.97}$$

$$B_z(\rho, z) = \frac{\mu_0 M_z}{2\pi}\int_{-l_m/2}^{l_m/2}\frac{1}{\sqrt{(a+\rho)^2+(z-z')^2}}\left[E\frac{a^2-\rho^2-(z-z')^2}{(a-\rho)^2+(z-z')^2} + K(k)\right]dz', \tag{A.98}$$

where M_z and z' are respectively the magnetization intensity and the variable of integration. Also:

$$k^2 = \frac{4a\rho}{(\rho + a)^2 + (z - z')^2}. \tag{A.99}$$

Eqs.(A.97), (A.98) describe the spatial magnetic distribution $\boldsymbol{B}$ of a permanent magnet axially magnetized of radius a and length l_m characterised by an magnetization of intensity M_z. Considering now the configuration in Figure A.10, in which a permanent magnet moves freely inside the conductive housing cylinder of the electromagnetic transducer. Neglecting the surface charge on the outside, the current density j_{ed} induced in the conducting cylinder is related to the induced motional electric field $\boldsymbol{E}_{ed}$ by the ohm's law

$$\mathbf{j}_{ed} = \sigma_y \boldsymbol{E}_{ed} = \sigma_y \dot{\boldsymbol{w}}_r \times \boldsymbol{B}, \tag{A.100}$$

where σ_y is the electrical conductivity of the material and $\dot{\boldsymbol{w}}_r$ is the relative velocity between the material and the magnetic flux density of the moving magnet.

The Lorentz force produced by the magnetic field $\boldsymbol{B}$ acting in an induced current loop $\boldsymbol{i}_{ed}$ can be calculated from the second Laplace's law:

$$\boldsymbol{F} = \oint i_{ed} \mathrm{d}\boldsymbol{l} \times \boldsymbol{B}, \tag{A.101}$$

where the integral is performed along the medium circumference of the Yoke.

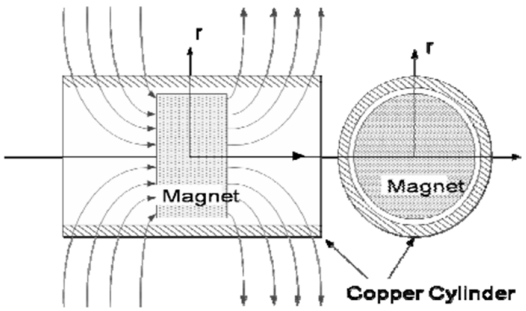

Figure A.10: Example of permanent magnet moving in a tube [175].

Since the circulating current i_{ed} can be obtained integrating the current density $\mathbf{j}_{ed}$ on the transverse area A of the cylinder; i.e:

$$i_{ed} = \int_A \mathbf{j}_{ed}\, \mathrm{d}\boldsymbol{A}, \tag{A.102}$$

substituting Eq.(A.100) and Eq.(A.102) into Eq.(A.101) it follows:

$$\boldsymbol{F} = \sigma_y \int_{V_y} (\dot{\boldsymbol{w}}_r \times \boldsymbol{B}) \times \boldsymbol{B}\, \mathrm{d}V, \tag{A.103}$$

where V_y identifies the conductor's Yoke volume.
Computing Eq. (A.103) in Cartesian coordinates results

$$\begin{aligned} \boldsymbol{F} &= \sigma_y \int \begin{vmatrix} \hat{\boldsymbol{x}} & \hat{\boldsymbol{y}} & \hat{\boldsymbol{z}} \\ (\dot{\boldsymbol{w}}_{\boldsymbol{r}} \times \boldsymbol{B})_x & (\dot{\boldsymbol{w}}_{\boldsymbol{r}} \times \boldsymbol{B})_y & (\dot{\boldsymbol{w}}_{\boldsymbol{r}} \times \boldsymbol{B})_z \\ B_x & B_y & B_z \end{vmatrix} \mathrm{d}V \\ &= \sigma_y \int_{V_y} \left[\dot{w}_r (B_x B_z)\hat{\boldsymbol{\imath}} + \dot{w}_r \left(B_y B_z v_z\right) \hat{\boldsymbol{\jmath}} - \dot{w}_r \left(B_x^2 + B_y^2\right)\hat{\boldsymbol{k}}\right] dV, \end{aligned} \tag{A.104}$$

where $\dot{\boldsymbol{w}}_{\boldsymbol{r}} = \dot{w}_r \hat{\boldsymbol{k}}$ and $\boldsymbol{B} = B_x \hat{\boldsymbol{\imath}} + B_y \hat{\boldsymbol{\jmath}} + B_z \hat{\boldsymbol{k}}$. The repulsion force on the moving magnet comes only from the z component:

$$\boldsymbol{F}_{ed} = -\sigma_y \dot{w}_r \left[\int_{V_y} B_\rho^2 dV\right] \hat{\boldsymbol{k}}, \tag{A.105}$$

where $B_\rho^2 = B_x^2 + B_y^2$. Eq.(A.105) represents a force-velocity relationship similar to that of an ideal mechanical viscous damper. In fact, the relative motion between the magnet and the conducting element generates eddy currents and produces repulsive force proportional to the relative velocity between the two components.

Assuming time harmonic motion, the eddy current force acting on the magnet varies along z direction because it depends on the interaction between the induced current i_{ed} in the housing cylinder and on the changing magnetic field gradient of the permanent magnet, whose distribution depends on the magnet position itself along the z axes.

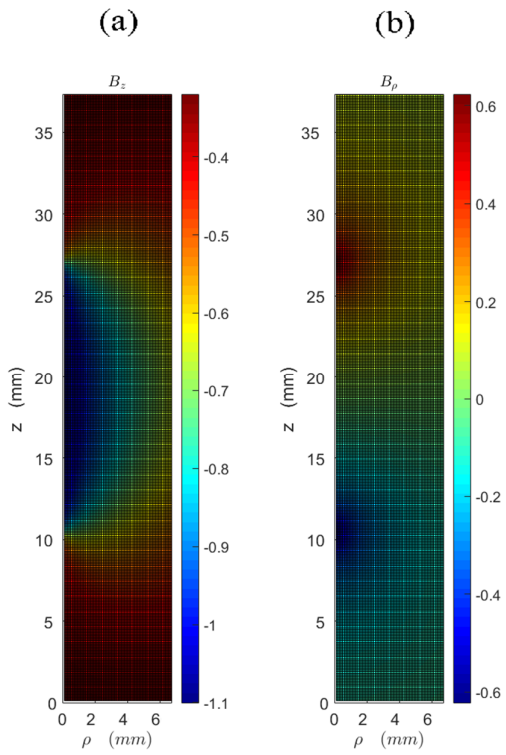

Figure A.11: Magnetic flux distribution a) axial B_z b) Radial B_ρ along the transverse section of the ferromagnetic Yoke.

Considering for simplicity the magnet in the instant of maximum relative velocity $\dot{w}_r$ and thus in the middle of the housing yoke, according to Eq.(A.105), the eddy current damping coefficient c_{ec} can be defined as follows:

$$c_{ec} = \sigma_y \int_{V_y} B_\rho^2(y,z) dV_y = 2\pi\sigma_y \int_{-\frac{L_y}{2}}^{\frac{L_y}{2}} \int_{R_{yi}}^{R_{ye}} \rho B_\rho^2(\rho,z)\, d\rho\, dz, \qquad \text{(A.106)}$$

where L_y, R_{ye}, R_{yi} are the length and the internal and external radius of the cylindrical conducting Yoke, while B_ρ is the radial distribution of the magnetic field density generated by the permanent magnet. Eqs.(A.97), (A.106) cannot be solved analytically and thus require a numerical approach. See [174]–[176], [217]–[219] for further details.

A.4 LOSSY COIL-MAGNET MODEL

As discussed in Refs. [177]–[179], coil-magnet transducers are characterised by eddy currents that develops in the coil wire of the transducer and produce inductance losses. Thus, as shown in Figure 2.1, the electrical response of the coil element in the seismic transducer has been modelled in terms of a resistor in series with a lossy inductor having complex inductance $\tilde{L}_e(\omega)$. As discussed in Refs. [177], [178] and shown in Figure A.12 (b,c) the lossy inductor can in turn be modelled as a frequency dependent resistor and a frequency dependent lossless inductor connected either in series (Figure A.12(b)) or in parallel (Figure A.12(c)). According to Ref. [177], the impedance for the series model is given by: $Z_L = R_s(\omega) + \mathrm{j}\omega L_s(\omega)$, where the frequency dependent resistance and inductance are respectively given by $R_s(\omega) = K_e\omega^n \cos(n\pi/2)$ and $L_s(\omega) = K_e\omega^{n-1}\sin(n\pi/2)$, with $0 \le n \le 1$. Alternatively, the impedance for the parallel model is given by: $\frac{1}{Z_L} = \frac{1}{R_p(\omega)} + \frac{1}{j\omega L_p(\omega)}$, where the frequency dependent resistance and inductance are respectively given by $R_p(\omega) = \left[\frac{K_e}{\cos(n\pi/2)}\right]\omega^n$ and $L_p(\omega) = \left[\frac{K_e}{\sin(n\pi/2)}\right]\omega^{n-1}$, with $0 \le n \le 1$. As one would expect, the two models give the same equivalent impedance, which can written in the following form:

$$Z_L = K_e\omega^n\left[\cos\left(\frac{n\pi}{2}\right) + \mathrm{j}\sin\left(\frac{n\pi}{2}\right)\right]. \tag{A.107}$$

This expression can be rewritten in terms of a complex lossy inductance $\tilde{L}_e$ as follows:

$$Z_L = \mathrm{j}\omega\tilde{L}_e(\omega), \tag{A.108}$$

where

$$\tilde{L}_e(\omega) = K'_e(\omega)(1 - \mathrm{j}\eta_L). \tag{A.109}$$

Here $K'_e(\omega) = \sin(n\pi/2)K_e\omega^{n-1}$ and the inductive loss factor is given by $\eta_L = \cos(n\pi/2)/\sin(n\pi/2)$. As proposed in Refs. [177], [178] , in this study the parameters K_e and n were identified from the log-log Plot of the magnitude of the measured transducer electrical impedance at higher frequencies such that the two constants

were found to be given by $K_e = 0.034$ and $n = 0.78$. As a result, the real and imaginary components of Z_L are given respectively by: $\mathrm{Re}\{Z_L\} = R_s(\omega) = 0.01\omega^{0.78}$ and $\mathrm{Im}\{Z_L\} = \omega L_s(\omega) = 0.03\omega^{0.78}$. The impedance of the lossy inductor is thus characterised by both real and imaginary parts that rise with frequency proportionally to $\omega^{0.78}$. For simplicity, in this study the complex lossy inductance given in Eq.(A.8) has been adopted in the constitutive Eqs. (A.6) such that:

$$f_h = \left\{ \mathrm{j}\omega m_b + \frac{\left(\frac{k_m}{\mathrm{j}\omega} + c_m\right)\mathrm{j}\omega m_m}{\left(\frac{k_m}{\mathrm{j}\omega} + c_m + \mathrm{j}\omega m_m\right)} \right\} \dot{w}_h + \left\{ \psi_{CM} \frac{\mathrm{j}\omega m_m}{\left(\frac{k_m}{\mathrm{j}\omega} + c_m + \mathrm{j}\omega m_m\right)} \right\} i_h, \tag{A.110}$$

$$e_h = -\left\{ \psi_{CM} \frac{\mathrm{j}\omega m_m}{\left(\frac{k_m}{\mathrm{j}\omega} + c_m + \mathrm{j}\omega m_m\right)} \right\} \dot{w}_h + \left\{ R_e + \mathrm{j}\omega \widetilde{L}_e + \frac{\psi_{CM}^2}{\left(\frac{k_m}{\mathrm{j}\omega} + c_m + \mathrm{j}\omega m_m\right)} \right\} i_h. \tag{A.111}$$

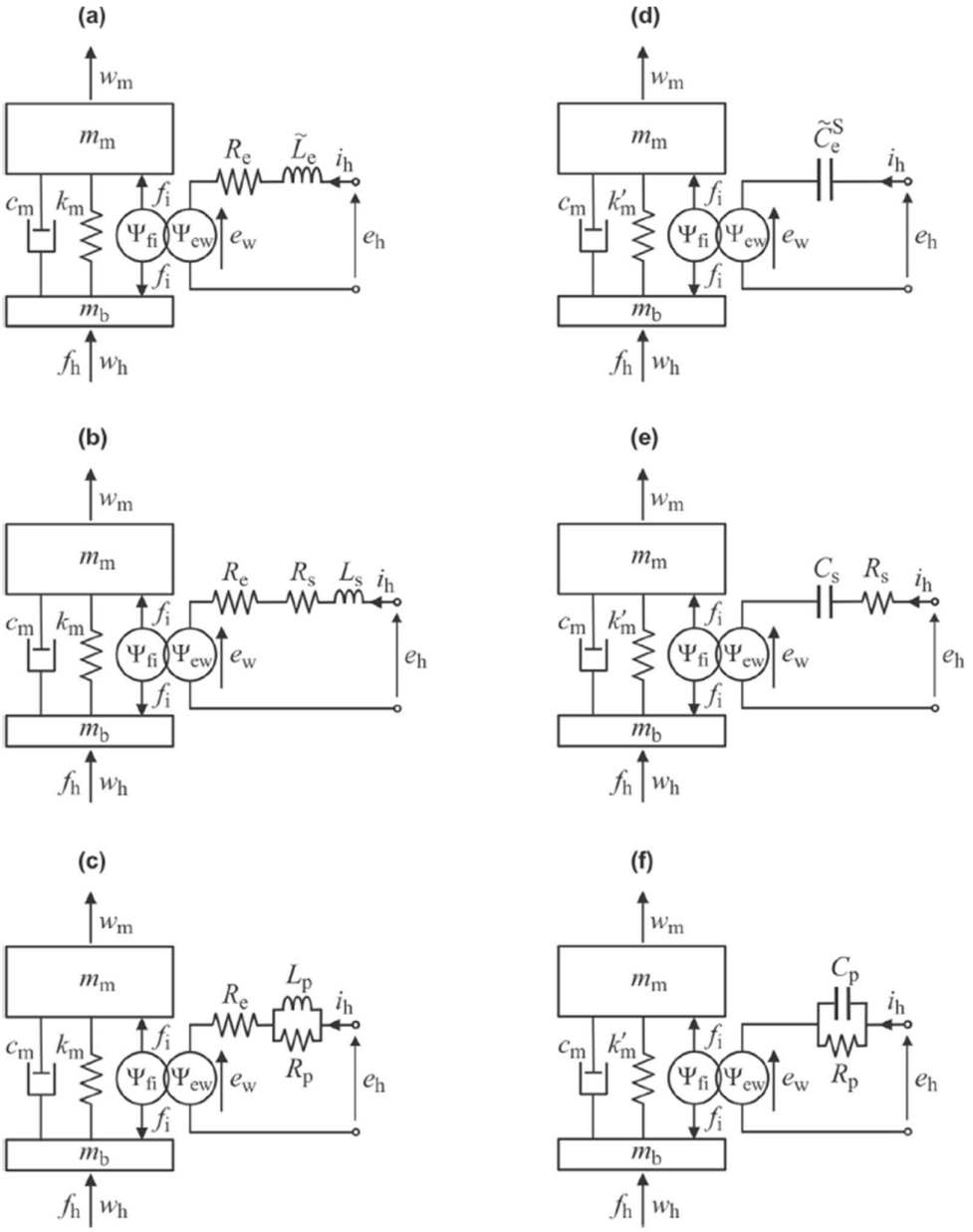

Figure A.12: Lumped parameter schematics for the electromagnetic (left hand side) and piezoelectric (right hand side) seismic transducers. (a) and (d) complex inductance/capacitance models. (b) and (e) series resistance-inductance/resistance-capacitance models. (c) and (f) parallel resistance-inductance/resistance capacitance models.

A.5 EDDY CURRENT EFFECTS ON THE TRANSDUCER

As discussed in Section A.3, the electromagnetic seismic transducer considered in this paper is characterised by eddy currents losses, which damp the mechanical response of the transducer at frequencies close to its fundamental resonance frequency so that the maximum energy that can be harvested in this frequency range is lowered. To evaluate the extent of this phenomenon, the maximum power that can be harvested at each frequency with a purely resistive harvesting load is here calculated assuming the transducer is ideally affected only by air damping or instead affected by both air and a strong eddy currents damping, which is the case for the prototype transducer considered in this study. This is done by setting respectively $c_m = c_a$ and $c_m = c_{ec} + c_a$ in the constitutive equations for the electromagnetic transducer given in Section 2.2.

Figure A.13, Figure A.14 and Figure A.15 show respectively the simulated spectra of the electric impedance $Z_{h,R}$, of the maximum harvested power $\bar{P}_{h,R}$ (Plot a) and input power $\bar{P}_{i,R}$ (Plot b) and of the stroke per unit base displacement $\frac{(w_m - w_h)}{w_h}$ considering the optimal real (resistive) harvesting impedance load given Eq.(2.34), i.e. $Z_{h,R} = |Z_{ei}|$, when the transducer constitutive equations do (solid blue line) and do not (dashed black line) take into account the effect of eddy currents losses. As discussed in Section 2.5, at the fundamental natural frequency of the transducer, the electrical impedance Z_{ei} is purely real and is characterised by the electrical resistive effect of the coil, R_e, and the transduced mechanical dissipative effect of the harvester, which is given by ψ_{CM}^2/c_m. Considering the data listed in Table 2-1, the damping factor for the air loss only, $c_a = 2.15$ Ns/m, is about 3.8 times smaller than the damping factor due to the aggregate eddy currents and air losses $c_m = c_{ec} + c_a = 9.52$ Ns/m.

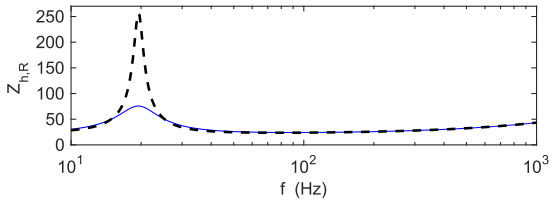

Figure A.13: Simulated spectra of the optimal real (resistive) harvesting impedance function $Z_{h,R} = |Z_{ei}|$ considering the electromagnetic seismic transducer is (solid blue line) and is not (dashed black line) characterised by eddy currents losses.

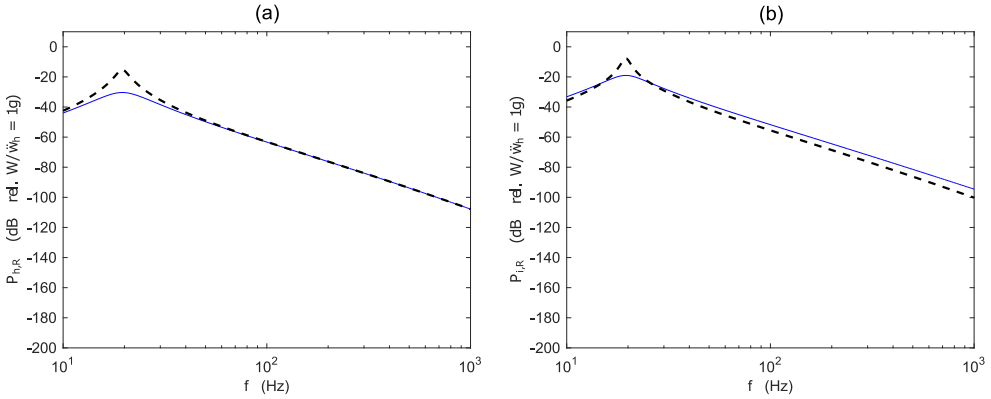

Figure A.14: Simulated spectra of the harvested power $\bar{P}_{h,R}$ (a) and input power $\bar{P}_{i,R}$ (b) assuming $Z_{h,R} = |Z_{ei}|$ and considering the electromagnetic seismic transducer is (solid blue line) and is not (dashed black line) characterised by eddy currents losses.

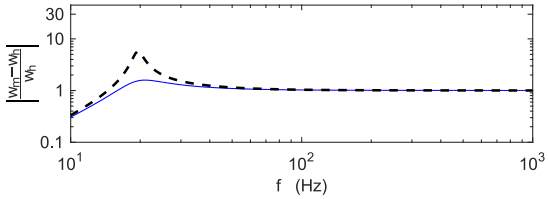

Figure A.15: Simulated strokes per unit base displacement of the electromagnetic seismic harvester assuming $Z_{h,R} = |Z_{ei}|$ and considering the electromagnetic seismic transducer is (solid blue line) and is not (dashed black line) characterised by eddy currents losses.

Thus as shown in Figure A.13, in correspondence to fundamental resonance frequency of the transducer, the optimal resistive harvesting impedance is characterised by a much higher peak when there are no eddy currents losses (dashed black line) than in presence of eddy currents losses (solid blue line). As shown in Figure A.14, this reflects into a higher capacity of peak power harvesting of 173 mW/1g in contrast to the 33 mW/1g that can be harvested in presence of eddy currents losses. Therefore, the peak energy harvesting with the electromagnetic seismic harvester strongly depends on the presence or absence of eddy currents damping. Finally, as shown in Figure A.15, the stroke per unit base displacement at the fundamental resonance frequency of the transducer rises by 3.8 times, that is from a value of 1.5 to 5.7.

In conclusion, the transducer considered in this study is indeed affected by rather strong electromagnetic damping due to the eddy currents that develops in the ferromagnetic outer ring. Vanderkooy [179] discussed this effect for voice coil loudspeakers, and showed that presence of eddy currents can be effectively lowered by cutting the outer ring along the longitudinal axis for example. Another solution that is normally used in electrical motors, consists in using an assembly of iron laminations rather than a single peace ring element. These are key design features that should be taken into account for the construction of effective electromagnetic seismic transducers for energy harvesting purposes.

B

PIEZOELECTRIC SEISMIC TRANSDUCER

This chapter presents a brief overview of piezoelectric transducers and in particular, of composite materials formed by a beam substrate with piezoelectric layers. The constitutive equations of the beam laminate are introduced together with the material constitutive equations to derive and identify the piezoelectric lumped seismic transducer model used in this thesis.

B.1 LUMPED MODEL CONSTITUTIVE EQUATIONS

B.1.1 Piezoelectric constitutive equations: Reduced Equations for a Thin Beam

In general, piezoelectric transducers are characterised by the so-called direct and inverse transduction effects. Piezoelectric materials are dielectric materials, which can be polarised in presence of an electric field, also by applications of a mechanical stress. In 1880 Pierre and Jacques Curie conducted experiments on single crystals, such as tourmaline, quartz, topaz, cane sugar and Rochelle Salt, that displayed surface charges when they were mechanically stressed. This effect was lately classified as direct piezoelectric effect. In 1881 Lippmann predicted from fundamental laws of thermodynamics the inverse effect, that is, an imposed electric field produced by mechanical deformation of the crystals, which was then experimentally confirmed by Pierre and Jacques Curie.
In simplified form, the basic relationships between the electrical and elastic properties (for a static or quasi static application at constant temperature) can be represented as follows [181], [220]–[222]:

$$\begin{bmatrix} \boldsymbol{S} \\ \boldsymbol{D} \end{bmatrix} = \begin{bmatrix} \boldsymbol{s}^E & \boldsymbol{d}^t \\ \boldsymbol{d} & \boldsymbol{\varepsilon}^T \end{bmatrix} \begin{bmatrix} \boldsymbol{T} \\ \boldsymbol{E} \end{bmatrix}, \tag{B.1}$$

where **S** is the mechanical strain vector, ***D*** is the electric flux density vector, ***T*** is the mechanical stress component and **E** is the electric field vector. The superscripts *T, E*, and *t* denote the constant stress, constant electric field and transposte respectively. Finally, the quantities **d**, **s** and ***ε*** represent the vectors with the permittivity, the charge or strain coefficient and the elastic compliance coefficients. These relationships apply only to small electrical and mechanical amplitudes.

The subscripts of the coefficients that characterise Eq.(B.1) are conventionally labelled according to the *Voigt notation* [72] and are designated by 1, 2 and 3 axes, corresponding to principal axes X, Y, Z, defined according to the classical right-hand rule, whereas the shear axes are designated with 4,5,6:

Table B-1: Contracted axes notation.

Axis	**Notation**
X	1
Y	2
Z	3
Shear around X	4
Shear around Y	5
Shear around Z	6

In most general form the matrix in Eq.(B.1) contains 21 elastic mechanical strain components $s_{i,j}^{E}$ (from 36 to 21 according to the elastic theory taken into account $s_{i,j}^{E} = s_{j,i}^{E}$), 6 permittivity coefficients $\varepsilon_{i,j}^{E}$ and 18 piezoelectric strain/charge constants $d_{i,j}$. The two piezoelectric patches considered in the study have comparatively small thickness, such that the stress components other than T_1 can be neglected [223]–[225], i.e. $T_i = 0, i = 2 \div 6$. Along with this simplification, if the thin electrodes are deposited on the piezoelectric patches perpendicular to the 3-direction, Eq.(B.1) reduces to:

$$\begin{bmatrix} S_1 \\ D_3 \end{bmatrix} = \begin{bmatrix} s_{11}^{E} & d_{31} \\ d_{31} & \varepsilon_{33}^{T} \end{bmatrix} \begin{bmatrix} T_1 \\ E_3 \end{bmatrix}, \tag{B.2}$$

where it is implicitly assumed that $E_1 = E_2 = 0$.

The permittivity coefficient ε_{33}^{T} indicates the charge density produced by an electric field applied along the same direction (i.e. 3). The piezoelectric strain/charge constant is represented by d_{31}, where the sub-index 31 means that the electric field is

applied or the charge is collected in the 3 direction for a displacement or a stress force produced in the 1 direction. Two interpretations of this constant coefficient can be derived: 1) it is the ratio between the produced strain and the applied electrical field when external stresses are constant $[V/m]$ 2) it is the ratio between the charge density flowing through the electrodes perpendicular to the 3 direction and the mechanical stress applied in the 1 direction $[C/N]$. Finally the elastic compliance coefficient s_{11}^{E} represents the ratio of the mechanical strain to the mechanical stress in direction 1.

From Eq.(B.2) the stress-electric displacement form of the reduced constitutive equations for a thin beam can be rewritten as follows:

$$\begin{bmatrix} T_1 \\ E_3 \end{bmatrix} = \begin{bmatrix} c_{11}^{E} & -e_{31} \\ e_{31} & \varepsilon_{33}^{S} \end{bmatrix} \begin{bmatrix} S_1 \\ D_3 \end{bmatrix}, \tag{B.3}$$

where:

$$c_{11}^{E} = \frac{1}{s_{11}^{E}}, \qquad e_{31} = \frac{d_{31}}{s_{11}^{E}}, \qquad \varepsilon_{33}^{S} = \varepsilon_{33}^{T} - \frac{d_{31}^{2}}{s_{11}^{E}}, \tag{B.4}$$

and the superscript S and E denotes that the respective constants are evaluated at constant strain and constant electric field.

B.1.2 Constitutive equations for the beam composite

Considering bending strain, the equilibrium with reference to the rotation and translation in directions x and z respectively (Figure B.1)) of a segment of beam under the hypothesis of the uniform *Euler–Bernoulli beam model* are given by [223]–[225]:

$$\frac{dT}{dx} = -f(x), \tag{B.5}$$

$$\frac{dM}{dx} = -T, \tag{B.6}$$

where M and T are the internal bending moment (caused by the stress components along the axial direction x) and shear force at any cross-section of the beam and $f(x)$

is the external transverse force (i.e. z axis) per unit of length of the beam. Combining Eqs.(B.5), (B.6) follows:

$$\frac{d^2M}{dx^2} = f(x). \tag{B.7}$$

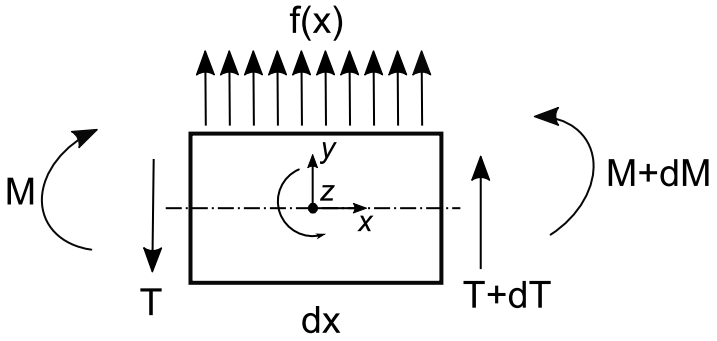

Figure B.1: Infinitesimal element of a beam.

The bending moment at any transverse section of the beam is thus related to the bending displacement as follows:

$$M = B\frac{d^2w}{dx^2}. \tag{B.8}$$

Here $B = E_sI_s$ is the *bending stiffness term* of the cross section of the beam, in which E_s is the Young's modulus of the material and I_s is the cross sectional moment of inertia about the second moment of area of cross-section of the beam about the *neutral axis*. Substituting Eq.(B.8) into Eq. (B.7) follows:

$$B\frac{d^4w}{dx^4} = f(x). \tag{B.9}$$

In order to identify the equation of motion the effect of transverse inertia should be taken into account, which gives $f(x,t) = -m\frac{\partial^2 w(x,t)}{\partial t^2}$, where m is the mass per unit of length of the beam. Thus equation (B.9) becomes:

$$m\frac{\partial^2 w(x,t)}{\partial t^2} + B\frac{\partial^4 w(x,t)}{\partial x^4} = f(x), \tag{B.10}$$

where in this case $f(x)$ is the externally applied transverse force per unit length of the beam. The equation of motion is characterised by a fourth-order term in space and a second order term in time. Thus to solve Eq.(B.10) four boundary conditions and two initial conditions are required. The boundary conditions of interest in this thesis are those for a beam clamped at the end $x = 0$ and with a free end at $x = L$. In addition, a mass M_t with rotational inertia I_M is attached at the end of the beam $x = L$:

$$w(x,t)|_{x=0} = 0, \tag{B.11}$$

$$\left.\frac{\partial w(x,t)}{\partial x}\right|_{x=0} = 0, \tag{B.12}$$

$$B\left.\frac{\partial^2 w(x,t)}{\partial x^2}\right|_{x=L} + I_M\left.\frac{\partial^3 w(x,t)}{\partial t^2 \partial x}\right|_{x=L} = 0, \tag{B.13}$$

$$B\left.\frac{\partial^3 w(x,t)}{\partial x^3}\right|_{x=L} - M_t\left.\frac{\partial^2 w(x,t)}{\partial t^2}\right|_{x=L} = 0. \tag{B.14}$$

The fixed end requires that the displacement and the slope of the displacement are both zero as indicated in Eqs.(B.11) and (B.12) respectively. The free end requires that the sum of the moments and the sum of the shear forces acting at $x = L$ must be zero, as indicated in Eqs.(B.13) and (B.14) respectively. The force F_M and the moment Γ_M caused by the tip mass M_t is expressed using the second law of dynamics and the principle of conservation of the angular momentum

$$\Gamma_M = I_M\ddot{\theta}_M = M_t\left.\frac{\partial^2 w(x,t)}{\partial x \partial t^2}\right|_{x=L}, \tag{B.15}$$

$$F_M = M_t\ddot{w}_M = M_t\left.\frac{\partial^2 w(x,t)}{\partial t^2}\right|_{x=L}. \tag{B.16}$$

The method of separation of variables can be used to solve the linear homogenous partial differential equation associated to Eq.(B.10). More specifically the transverse displacement can be written as follows:

$$w(x,t) = \phi(x)q(t), \tag{B.17}$$

where $\phi(x)$ is only a function of x and $q(t)$ is only a function of t. Substituting Eq.(B.17) into Eq. (B.10) follows:

$$m\frac{d^2q}{dt^2}\phi(x) + B\frac{d^4\phi}{dx^4}q(t) = 0. \tag{B.18}$$

The spatial and temporal terms can be separated considering that the above equation can be rewritten in the following form:

$$\frac{B}{m}\frac{1}{\phi}\frac{d^4\phi}{dx^4} = -\frac{1}{q}\frac{d^2q}{dt^2} \triangleq \gamma. \tag{B.19}$$

Since the left side of Eq.(B.19) depends only on the spatial coordinate while the right hand side depends on the temporal variable alone and these two variables are independent from each other, both sides of Eq.(B.19) must be equal to the same arbitrary constant γ, known as *separation constant* [226]. Thus, Eq.(B.19) yields two ordinary differential equations:

$$\frac{d^4\phi}{dx^4} + \gamma\frac{m}{B}\phi = 0, \tag{B.20}$$

$$\frac{d^2q}{dt^2} + \gamma q = 0. \tag{B.21}$$

Eqs.(B.20) and (B.21) are differential equations with constant coefficients whose solutions can be readily derived. It is important to note that γ is an arbitrary constant. Also, since the problem in exam is a vibration problem, the time-dependent solution of Eq.(B.21) is given by an harmonic function and thus γ should be a positive constant. Under this assumption, the solutions form of Eq.(B.20) and (B.21) can be written as follows:

$$\phi(x) = A\cos\left(\frac{\lambda}{L}x\right) + B\cosh\left(\frac{\lambda}{L}x\right) + C\sin\left(\frac{\lambda}{L}x\right) + D\sinh\left(\frac{\lambda}{L}x\right), \tag{B.22}$$

$$q(t) = E\cos(\omega t) + F\sin(\omega t), \tag{B.23}$$

where has been defined:

$$\omega^2 \triangleq \gamma, \;\; \lambda^2 = \gamma L^2\frac{m}{B}. \tag{B.24}$$

From the solution of Eq.(B.17) the product $\phi(x)q(t)$ must also satisfy the four boundary conditions (B.11)-(B.14), which are valid for every time t. Thus substituting Eq.(B.17) into Eqs.(B.11)-(B.14), for no trivial solution (i.e. $q(t) \neq 0$), considering that from Eq.(B.23) results that $\frac{d^2q}{dt^2} = -\omega^2 q(t)$, the following *boundary value problem* is derived:

$$\phi(x)|_{x=0} = 0, \tag{B.25}$$

$$\left.\frac{d\phi}{dx}\right|_{x=0} = 0, \tag{B.26}$$

$$B\left.\frac{d^2\phi}{dx^2}\right|_{x=L} - I_M\left.\frac{d\phi}{dx}\right|_{x=L}\omega^2 = 0, \tag{B.27}$$

$$B\left.\frac{d^3\phi}{dx^3}\right|_{x=L} + M_t\phi(L)\omega^2 = 0. \tag{B.28}$$

The values of γ (i.e. ω^2) for which there are no trivial solutions ϕ are the *eigenvalues* while a nontrivial solution ϕ which exist only for certain values of γ is called e*igenfunction* of the *eigenvalue* γ.

Because Eq.(B.20) is of fourth order, its solution in Eq.(B.22) contains four constants of integration, in addition to the parameter γ, for a total five unknowns coefficients. To evaluate these unknowns, the four boundary conditions (B.25)-(B.28) are invoked. Because there are only four boundary conditions, it is not possible to evaluate all the unknowns uniquely. In fact, since Eq. (B.20) is homogenous, only the general shape of ϕ can be determined uniquely, but not the amplitude. Thus applying Eqs.(B.25), (B.26) into Eq.(B.22), results:

$$\phi(x) = A\left[\cos\left(\frac{\lambda}{L}x\right) - \cosh\left(\frac{\lambda}{L}x\right)\right] + C\left[\sin\left(\frac{\lambda}{L}x\right) - \sinh\left(\frac{\lambda}{L}x\right)\right]. \tag{B.29}$$

Using the remaining two boundary conditions (B.27), (B.28) in (B.29) it follows:

$$\begin{pmatrix} \cos(\lambda) + \cosh(\lambda) - \frac{I_M\lambda^3}{mL^3}[\sin(\lambda) + \sinh(\lambda)] & \sin(\lambda) + \sinh(\lambda) + \frac{I_M\lambda^3}{mL^3}[\cos(\lambda) - \cosh(\lambda)] \\ \sin(\lambda) - \sinh(\lambda) + \frac{M_T\lambda}{mL}[\cos(\lambda) + \cosh(\lambda)] & -\cos(\lambda) - \cosh(\lambda) + \frac{M_T\lambda}{mL}[\sin(\lambda) - \sinh(\lambda)] \end{pmatrix}\begin{pmatrix} A \\ C \end{pmatrix} = \begin{pmatrix} 0 \\ 0 \end{pmatrix}. \tag{B.30}$$

In order to obtain no trivial solutions (i.e. A = C = 0), the eigenvalues γ must satisfy the following characteristic equation, obtained setting the determinant of the matrix in Eq.(B.30) to zero:

$$\begin{aligned} 1 + \cos(\lambda)\cosh(\lambda) + \frac{M_T}{m}\beta[\cos(\lambda)\sinh(\lambda) - \sin(\lambda)\cosh(\lambda)] \\ - \frac{I_M\lambda^3}{mL^3}[\cosh(\lambda)\sin(\lambda) + \sinh(\lambda)\cos(\lambda)] \\ + \frac{I_M\lambda^3 M_T}{mL^3}[1 - \cos(\lambda)\cosh(\lambda)] = 0. \end{aligned} \tag{B.31}$$

Since Eq.(B.31) is a nonlinear algebraic equation; the solution can be obtained with an iterative numeric procedure. Figure B.2 shows the graphical solutions.

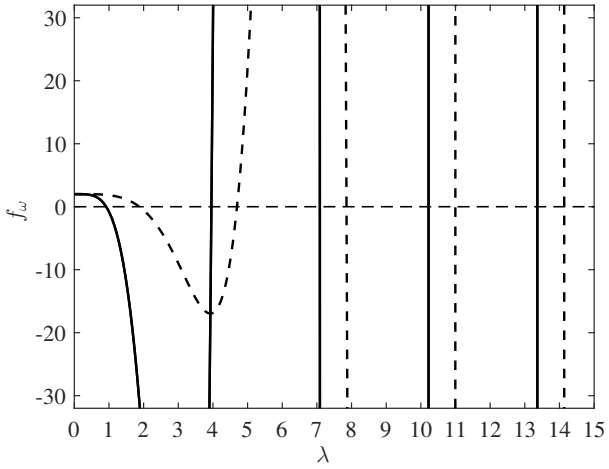

Figure B.2: Graphical solution of Eq.(B.31) considering the tip mass M_t (solid line) and with the only distributed inertial contribution of the beam (dotted line).

The zeros of Eq.(B.31), which identifies the no trivial solutions, gives the following eigenvalues:

$$\gamma_r = \omega_r^2 = \lambda_r^4 \frac{m}{BL^4}. \tag{B.32}$$

The square roots ω_r for the eigenvalues γ_r are recognized as the *natural frequencies* of the system and the eigenfunctions ϕ_r as the *natural modes*. In conclusion the natural mode ϕ_r corresponding to the natural frequency ω_r is given by:

$$\phi_r(x) = A_r\left[\cos\left(\frac{\lambda_r}{L}x\right) - \cosh\left(\frac{\lambda_r}{L}x\right) + \sigma_r\left(\sin\left(\frac{\lambda_r}{L}x\right) - \sinh\left(\frac{\lambda_r}{L}x\right)\right)\right], \qquad \text{(B.33)}$$

where $\sigma_r = \frac{A_r}{C_r} = \frac{\sin(\lambda_r)-\sinh(\lambda_r)+\frac{\lambda_r M_t}{mL}[\cos(\lambda_r)-\cosh(\lambda_r)]}{\cos(\lambda_r)+\cosh(\lambda_r)-\frac{\lambda_r M_t}{mL}[\sin(\lambda_r)-\sinh(\lambda_r)]}$ is obtained from the second row of Eq.(B.30). In order to uniquely obtain the amplitude of the mode, the constant A_r is determined through a normalization procedure. The corresponding unique natural modes are referred to as *normal modes.* For brevity the relations, which can be used to mass normalize the eigenfunctions, are here reported with no mathematical proof (for more details see [72],[226]) :

$$\int_0^L \phi_s(x) B\frac{d^4\phi_r(x)}{dx^4}dx - \left[\phi_s(x) B\frac{d^3\phi_r(x)}{dx^3}\right]_{x=L} + B\left[\frac{d\phi_s}{dx}\frac{d\phi_r}{dx}\right]_{x=L} = {\omega_r}^2\delta_{rs}, \qquad \text{(B.34)}$$

$$\int_0^L m\,\phi_s(x)\phi_r(x)dx + \phi_s(L)M_t\phi_r(L) + I_M\left[\frac{d\phi_s}{dx}\frac{d\phi_r}{dx}\right]_{x=L} = \delta_{rs}. \qquad \text{(B.35)}$$

In summary, the solutions of equation (B.17) satisfying the specific boundary conditions (B.25)-(B.28) can be defined for each corresponding natural frequency ω_r. The constants ϕ_r and ω_r represent *internal factors* and depend on the inherent nature of the differential equations and boundary conditions, whereas q_r represent *external factor*, defined from the initial conditions (displacement and velocity profile).

For the physical problem considered in this thesis, a unique solution to initial value problem exists for every rth solution. In analogy to the Fourier analysis (in which for one period T a function of arbitrary shape can be expanded in an infinite series of orthogonal harmonic functions), the *expansion theorem* [226] can be used to represent any possible displacement of the beam. As a result, any function, which represents a possible displacement of the beam $w(x)$ that satisfies boundary conditions and such that ${d^4w}/{dx^4}$, is a continue function, that can be expanded in the absolutely and uniformly convergent series of the eigenfunctions:

$$w(x) = \sum_{r=1}^{\infty} \phi_r(x), \tag{B.36}$$

where the relations between σ_r^2 and ω_r^2 are verified from the orthonormal properties of Eqs.(B.34), (B.35). As shown in Eq.(B.17), every natural motion $w(x,t)$ is obtained from the natural modes $\phi_r(x)$ (which are orthogonal and hence by definition independent) multiplied by time dependent harmonic functions $q_r(t)$ of frequencies equal to the natural frequency ω_r. Since every mode is independent, the consequence is that every one of the natural modes can be excited independently from the other. Hence, consistent with this, the solution $w(x,t)$ of equation (B.10) can be expressed in the form:

$$w(x,t) = \sum_{r=1}^{\infty} \phi_r(x) q_r(t). \tag{B.37}$$

B.1.3 Constitutive equations for the piezoelectric energy harvester

The cantilever configuration shown in Figure 2.1 is assumed thin (i.e. the length to thickness aspect ratio is greater than 20) such that, for small flexural deformations, Euler Bernoulli beam theory can be employed, which neglects the rotational inertia and shear deformation effects. The core substrate is made of a homogeneous, isotropic, linearly elastic steel material. The outer piezoelectric layers are given by two piezoelectric patches that cover the whole surface of the core layer. The piezoelectric layers are made of homogeneous, transversally isotropic, linearly elastic piezoelectric materials. The thin electrodes deposited on the piezoelectric patches are perfectly conductive such that a single potential difference can be assumed across the patches and thus a uniform electric field is generated along the length of the patches. Also, since the piezoelectric material is homogeneous and the patches have constant thickness, the electric fields in the patches is assumed constant.

It is assumed that the clamped base of the beam undergoes a transverse input motion w_h, which is persistent, so that continuous electrical outputs can be extracted from the electromechanical system. The instantaneous average bending strains in the top and the bottom layers at an arbitrary position x over the beam length have the opposite sign (one is in tension while the other is in compression). The piezoelectric

layers of the laminate shown in Figure 2.1 are poled in the thickness along the same direction (z or 3 direction) and are assumed electrically connected in parallel.

Using the Newtonian or the Hamiltonian approach, the governing equation for an undamped vibrations of a uniform Euler Bernoulli beam (with time dependence) can be derived in Eq.(B.7), i.e.:

$$\frac{\partial^2 M}{\partial x^2} = f(x,t), \tag{B.38}$$

where $M(x,t)$ is the internal bending moment (excluding the strain rate damping effect) and $f(x,t)$ is the transverse force per unit of length of the beam (in the z - direction). Considering Figure B.1, the convention chosen for the moment $M(x,t)$ is such that the positive bending moment creates positive curvature. The total bending moment for the three layers laminate is given by:

$$M(x,t) = -b\int_{-h_s/2-h_{pe}}^{-h_s/2} T_1^{pe}(x,z,t)zdz - b\int_{-h_s/2}^{+h_s/2} T_1^{s}(x,z,t)zdz - b\int_{h_s/2}^{h_s/2+h_{pe}} T_1^{pe}(x,z,t)zdz, \tag{B.39}$$

where b is the width, h_{pe} is the thickness of each piezo ceramic layer and h_s is the thickness of the substructure layer. T_1^s, T_1^{pe} are the normal stress components in direction 1 that develop in the substrate and piezoelectric layers respectively. Considering Euler-Bernoulli hypothesis, they are given by the following relations [72], [226], [225]:

$$T_1^s(x,z,t) = Y_s S_1^s(x,z,t), \tag{B.40}$$

$$T_1^{pe}(x,z,t) = Y_{pe}^E S_1^{pe}(x,z,t) - \bar{e}_{31}E_3(x,t), \tag{B.41}$$

where Y_s and Y_{pe}^E are the Young's modulus of elasticity respectively for the metallic substrate and for the piezoelectric layers under constant electric field, i.e. $E_3 = 0$. Also, as shown in Eq.(B.3), $\bar{e}_{31} = Y_{pe}^E d_{31}$ is the piezoelectric stress/charge constant for the uniaxial normal stress field in the beam, assuming the electric field in the transverse direction 3 is constant, i.e. $E_3 = 0$.

Finally $S_1^{pe}(x)$ and $S_1^s(x)$ are the normal strains in direction 1 of the metallic substrate and piezoelectric layers respectively, which according to Euler–Bernoulli hypothesis are given by the following linear strain–displacement relations:

$$S_1^s(x,z,t) = -z\frac{\partial^2 w(x,t)}{\partial x^2}, \tag{B.42}$$

$$S_1^{pe}(x,z,t) = -z\frac{\partial^2 w(x,t)}{\partial x^2}, \tag{B.43}$$

where w is the transverse displacement of the beam mid–plane. The transverse electric fields $E_3(t)$ in the two piezoelectric layers can be expressed in terms of the electric potential differences between the electrodes of the two layers, which, for the counter-phase parallel connection result equal with opposite sign (negative for the top layer and positive for the bottom layer). This opposite sign for the voltage is due to the fact that for positive bending the upper layer is compressed while the bottom layer is stressed. Thus from the definition of electric voltage the electric field can be defined as:

$$E_3(x,t) = \mp\frac{e_h(t)[H(x) - H(x-L)]}{h_{pe}}, \tag{B.44}$$

where $H(x)$ is the Heaviside function [72], [227] used in Eq.(B.44) to introduce the spatial dependence of the electric component E_3, which is function of the time only. It is important to keep in mind that the two piezoelectric layers are connected in parallel and thus the voltage across the electrodes of both is equal to $e_h(t)$.
Substituting Eqs.(B.40)-(B.43), (B.44) into Eq.(B.39) the internal bending term can be defined as:

$$M(x,t) = B\frac{\partial^2 w(x,t)}{\partial x^2} - \Theta_{pe}e_h(t)[H(x) - H(x-L)], \tag{B.45}$$

where the coupling term Θ_{pe} for the parallel connection is given by:

$$\Theta_{pe} = \bar{e}_{31}b\left(h_s + h_{pe}\right), \tag{B.46}$$

and the bending stiffness B of the composite cross – section for the short-circuited condition of the piezo beam is given by:

$$B = Y_s I_s + Y_{pe}^E I_{pe}, \tag{B.47}$$

where $I_s = b\frac{h_p^3}{12}$ and $I_p = \frac{2}{3}b\left[\left(h_p + \frac{h_s}{2}\right)^3 - \frac{h_s^3}{8}\right]$ are the second moment of the cross section (about the neutral axis) of the substructure and piezo layer respectively.

Substituting of Eq.(B.45) into Eq.(B.38) gives the following coupled (undamped) partial differential equation of motion for the flexural vibration of the uniform beam clamped:

$$B\frac{\partial^4 w(x,t)}{\partial x^4} + m\frac{\partial^2 w(x,t)}{\partial t^2} - \Theta_{pe}e_h(t)\left[\frac{\mathrm{d}\delta(x)}{\mathrm{d}x} - \frac{\mathrm{d}\delta(x-L)}{\mathrm{d}x}\right] = 0, \qquad \text{(B.48)}$$

where δ is the delta Dirac function [227] and $f(x,t) = -m\frac{\partial^2 w(x,t)}{\partial t^2}$ is the inertial force of the beam laminate, with m is the mass per unit length:

$$m = b\left(\rho_s h_s + 2\rho_{pe}h_{pe}\right), \qquad \text{(B.49)}$$

where ρ_s and ρ_{pe} are the mass density of the steel substructure and piezoelectric layers respectively, b is the width of the beam, h_s and h_{pe} are the thicknesses of the substrate and piezoelectric layers respectively.

Assuming that the left support of the beam is excited in vertical direction, the absolute displacement (relative to the fixed reference frame) of the beam mid–plane $w(x,t)$ can be written as a simple superposition of the displacement of the base w_h and beam displacement relative the base where the beam is clamped w_r:

$$w(x,t) = w_h(t) + w_r(x,t). \qquad \text{(B.50)}$$

Thus substituting Eq.(B.50) into (B.47), (B.48) the free coupled vibration equation for the absolute vibratory motion of the beam becomes a forced vibration equation for the vibratory motion of the beam:

$$B\frac{\partial^4 w_r(x,t)}{\partial x^4} + m\frac{\partial^2 w_r(x,t)}{\partial t^2} - \Theta_{pe}e_h(t)\left[\frac{\mathrm{d}\delta(x)}{\mathrm{d}x} - \frac{\mathrm{d}\delta(x-L)}{\mathrm{d}x}\right] = f_i(\mathrm{x},\mathrm{t}), \qquad \text{(B.51)}$$

where $f_i(\mathrm{x},\mathrm{t})$ is the external inertial term:

$$f_i(\mathrm{x},\mathrm{t}) = -[m + M_t\delta(x-L)]\frac{\mathrm{d}^2 w_h(t)}{\mathrm{d}t^2}. \tag{B.52}$$

In order to use the standard modal approach, a particular model of damping should be examined. Banks and Inman [228] demonstrate that the *strain rate damping* model for the internal damping mechanism and the *viscous air damping* model for the external damping mechanism are the analogue to proportional damping (i.e. a linear combination of mass and stiffness operators) and therefore are compatible with the modal approach of the corresponding *undamped free vibration problem.* For simplicity and as in common practise in structural dynamics the damping will be introduced in the modal equations. Based on the linear assumption, the transverse vibration response relative to the base of the beam can be represented as a convergent series of the eigenfunctions as derived in Eq.(B.37):

$$w_r(x,t) = \sum_{r=1}^{\infty} \phi_r(x) q_r(t), \tag{B.53}$$

where $\phi_r(x)$ is the r-th flexural natural mode of the beam and tip mass assumed clamped on the right hand side and $q_r(t)$ is the r-th generalised coordinate for the flexural vibration of the composite beam for the short circuited configuration ($e_h(t) = 0$). Substituting the solution (B.53) in Eq.(B.51), multiplying both side of the equation by the generic mass normalize eigenfunction $\phi_s(x)$, integrating over the length of the beam follows:

$$\begin{aligned}\sum_{=1}^{\infty}\left[\frac{d^2 q_r(t)}{dt^2}\int_0^L m\phi_s(x)\phi_r(x)\,dx\right] \\ + \sum_{r=1}^{\infty}\left[q_r(t)\int_0^L B\phi_s(x)\frac{d^4\phi_r(x)}{dx^4}dx\right] \\ - \Theta_{pe}e_h(t)\int_0^L \phi_s(x)\left[\frac{\mathrm{d}\delta(x)}{\mathrm{d}x} - \frac{\mathrm{d}\delta(x-L)}{\mathrm{d}x}\right]dx = \\ -\frac{\mathrm{d}^2 w_h(t)}{\mathrm{d}t^2}\int_0^L \phi_s(x)[m + M_t\delta(x-L)]\,dx\,.\end{aligned} \tag{B.54}$$

Substituting into Eq.(B.54) the conditions of orthogonality (B.34), (B.35):

$$\begin{aligned}\sum_{r=1}^{\infty}\left[\frac{d^2q_r(t)}{dt^2}\left(\delta_{rs}-\phi_s(L)M_t\phi_r(L)-I_M\left[\frac{d\phi_s(x)}{dx}\frac{d\phi_r(x)}{dx}\right]_{x=L}\right)\right]\\ +\sum_{r=1}^{\infty}\left[q_r(t)\left({\omega_r}^2\delta_{rs}+\left[\phi_s(x)B\frac{d^3\phi_r(x)}{dx^3}\right]_{x=L}\right.\right.\\ \left.\left.-B\left[\frac{d\phi_s(x)}{dx}\frac{d^2\phi_r(x)}{dx^2}\right]_{x=L}\right)\right]-\Theta_{pe}e_h(t)\left[-\frac{\mathrm{d}\phi_s}{\mathrm{d}x}\Big|_{x=0}+\frac{\mathrm{d}\phi_s}{\mathrm{d}x}\Big|_{x=L}\right]\\ =-\ddot{w}_h(t)\left[\int_0^L m\phi_r(x)dx+M_t\phi_r(L)\right],\end{aligned} \tag{B.55}$$

and rearranging the terms follows:

$$\begin{aligned}\sum_{r=1}^{\infty}\left\{\frac{d^2q_r(t)}{dt^2}\delta_{rs}+q_r(t){\omega_r}^2\delta_{rs}+\left[\phi_s(x)\left(-\frac{d^2q_r(t)}{dt^2}M_t\phi_r(x)+q_r(t)B\frac{d^3\phi_r(x)}{dx^3}\right)\right]_{x=L}\right.\\ \left.-\left[\frac{d\phi_s(x)}{dx}\left(\frac{d^2q_r(t)}{dt^2}I_M\frac{d\phi_r(x)}{dx}+q_r(t)B\frac{d^2\phi_r(x)}{dx^2}\right)\right]_{x=L}\right\}\\ -\Theta_{pe}\frac{\mathrm{d}\phi_s}{\mathrm{d}x}\Big|_{x=L}e_h(t)\quad=-\ddot{w}_h(t)\left[\int_0^L m\phi_r(x)dx+M_t\phi_r(L)\right].\end{aligned} \tag{B.56}$$

Applying the boundary conditions given in Eqs. (B.25)-(B.28) the last two terms on the left side of Eq.(B.56) are zero:

$$\begin{aligned}\sum_{r=1}^{\infty}\left(\frac{d^2q_r(t)}{dt^2}\delta_{rs}+q_r(t){\omega_r}^2\delta_{rs}\right)-\Theta_{pe}\frac{\mathrm{d}\phi_s}{\mathrm{d}x}\Big|_{x=L}e_h(t)\\ =-\ddot{w}_h(t)\left[\int_0^L m\phi_r(x)dx+M_t\phi_r(L)\right].\end{aligned} \tag{B.57}$$

Thus a set of Eqs. in the form:

$$\begin{aligned}\delta_{rr}\ddot{q}_r(t)+\delta_{rr}\omega_r^2q_r(t)++\delta_{rr}2\xi_r\omega_r\dot{q}_r(t)-\Pi_re_h(t)\\ =-\ddot{w}_h(t)\left[\int_0^L m\phi_r(x)dx+M_t\phi_r(L)\right],\end{aligned} \tag{B.58}$$

are obtained. The modal strain-rate damping ratio ξ_r has introduced in Eq.(B.58) in standard form where the electromechanical modal coupling term is given by $\Pi_r=\Theta_{pe}\frac{\mathrm{d}\phi_r}{\mathrm{d}x}\Big|_{x=L}$.The Kronecker delta operator $\delta_{rr}=1$ is retained in this and in the following equations to underline the presence of a mass term such that the units of all terms in the equations could be properly verified.

Considering now the electric part, in order to obtain the governing electrical circuit equations of the bimorph configurations for parallel connections of the two piezoelectric layers, the second constitutive equation of piezoelectric transducers, under Euler-Bernoulli hypothesis (Eq. (B.2)), should be considered:

$$D_3(x,z,t) = \bar{e}_{31} S_1^{pe}(x,z,t) + \bar{\varepsilon}_{33}^S E_3(x,t). \tag{B.59}$$

Using Eq.(B.43) and Eq.(B.44), Eq.(B.59) can be specified for the *upper* piezoelectric layer as:

$$D_3(x,z,t) = -\bar{e}_{31} z \frac{\partial^2 w(x,t)}{\partial x^2} - \bar{\varepsilon}_{33}^S \frac{e_{\mathrm{h}}(t)}{h_{pe}}. \tag{B.60}$$

From the Gauss's law [72] the separation of charge contained in the two piezoelectric layers can be written as $q_e = \int_A \boldsymbol{D} \cdot \boldsymbol{n}\, dA$, where A is a generic closed surface enclosing the free charge q_e contained in the electrode of the beam and $\boldsymbol{D}$ and $\boldsymbol{n}$ are respectively the electric displacement and the versor perpendicular to the surface A. In the present case, the only contribution to the inner product of the integrand in Eq. (B.60) comes from D_3 (since the electrodes are perpendicular to the 3-axis) and thus the surface A simply becomes the surface of the piezoelectric layer:

$$q_e = b \int_0^L D_3(x,z,t)\,\mathrm{dx}\Big|_{z=+h_{spe}} = -h_{spe} b \bar{e}_{31} \int_0^L \frac{\partial^2 w(x,t)}{\partial x^2}\,\mathrm{dx} - \bar{\varepsilon}_{33}^S \frac{bL}{h_{pe}} e_{\mathrm{h}}(t), \tag{B.61}$$

where $h_{spe} = \left(h_s + h_{pe}\right)/2$ is the distance between the neutral axis of the composite beam and the centre of each piezoelectric patch. The electrodes of the upper piezo layer are connected to a generic circuit, the electric current $i_1(t)$ produced by the upper piezoelectric patch can be derived from the *conservation of the charge* integral [72], which, written in scalar notation, gives:

$$i_1(t) = -\frac{dq_e}{dt} = h_{spe} b \bar{e}_{31} \int_0^L \frac{\partial^3 w(x,t)}{\partial t\, \partial x^2}\,\mathrm{dx} + \bar{\varepsilon}_{33}^S \frac{bL}{h_{pe}} \frac{de_{\mathrm{h}}}{dt}. \tag{B.62}$$

Here, in analogy to the coil magnet, the minus sign convention in Eq.(B.62) highlights the nature of generator of the piezoelectric transducer. That is, the electric charges leave the electrodes of the piezoelectric patch i.e. $dq_e/dt < 0$.

Substituting the modal expansion given in Eq.(B.53), Eq.(B.62) can be expressed with reference to the generalised coordinate for the flexural vibration of the composite beam as follows:

$$i_1(t) = h_{spe} b \bar{e}_{31} \left(\sum_{r=1}^{\infty} \int_0^L \frac{d^2 \phi_r}{dx^2} \mathrm{dx} \right) \frac{dq_r}{dt} + \bar{\varepsilon}_{33}^S \frac{bL}{h_{pe}} \frac{de_h}{dt}, \tag{B.63}$$

and, since $\frac{d\phi_r}{dx}\Big|_{x=0}$,

$$i_1(t) = h_{spe} b \bar{e}_{31} \left(\sum_{r=1}^{\infty} \frac{d\phi_r}{dx}\Big|_{x=L} \frac{dq_r}{dt} \right) + \bar{\varepsilon}_{33}^S \frac{bL}{h_{pe}} \frac{de_h}{dt}. \tag{B.64}$$

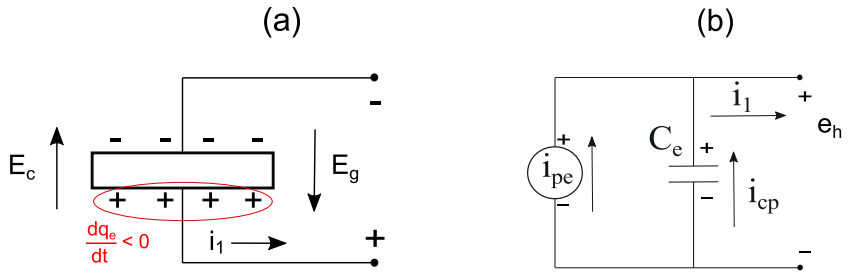

Figure B.3: (a) Piezoelectric layer, source of an electromotive force E_g and generator of a moving electric charge b) Equivalent electric circuit representation.

Considering the schemes shown in Figure B.3, Eq.(B.64) represents, for the upper piezo layer, the Kirchhoff's Current Law of a current source i_{pe} in parallel with a capacitance. At this point, assuming a parallel connection of the two piezoelectric patches bounded on the cantilever beam, the total electric inherent flowing from the two transducers results:

$$i_h(t) = 2h_{spe} b \bar{e}_{31} \left(\sum_{r=1}^{\infty} \frac{d\phi_r}{dx}\Big|_{x=L} \frac{dq_r}{dt} \right) + 2\bar{\varepsilon}_{33}^S \frac{bL}{h_{pe}} \frac{de_h}{dt}. \tag{B.65}$$

Thus rearranging the terms in Eq.(B.65):

$$i_h(t) = \sum_{r=1}^{\infty} \Pi_r \dot{q}_1(t) + C_e^S \dot{e}_h(t), \tag{B.66}$$

where $\Pi_r = \Theta_{pe} \frac{\mathrm{d}\phi_r}{\mathrm{d}x}\Big|_{x=L}$ and $C_e^S = 2\bar{\varepsilon}_{33}^S \frac{bL}{h_{pe}}$.

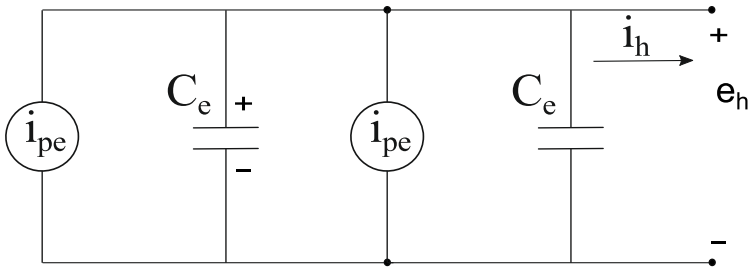

Figure B.4: Electric circuit representing the parallel connection of the two piezoelectric layers.

It can be observed that Eq.(B.66) identifies the Kirchhoff's law applied to Figure B.4, assuming the generators convention for the two piezoelectric patch transducers. In analogy to the electromagnetic harvester, as shown in Figure 2.1, the user convention is employed, thus reversing the orientation of all voltages. This choice only effects the graphical representation of the electric circuit, but doesn't change the form of the constitutive electric equation.

B.1.4 Lumped model for the piezoelectric energy harvester

As derived in the previous section, the closed form of the *r*th coupled beam equation and the electrical circuit equation in modal coordinates are obtained from Eqs.(B.58), (B.66):

$$\delta_{rr}\ddot{q}_r(t) + \delta_{rr}\omega_r^2 q_r(t) + +\delta_{ii}2\xi_i\omega_i\dot{q}(t) - \Pi_r e_h(t) = -\ddot{w}_h(t)\left[\int_0^L m\phi_r(x)dx + M_t\phi_r(L)\right], \tag{B.67}$$

$$i_h(t) = \sum_{r=1}^{\infty} \Pi_r \dot{q}_r(t) + C_e^S \dot{e}_h(t). \tag{B.68}$$

As discussed in Section 2.6, for tonal disturbances, the maximum energy harvesting occurs in correspondence of the fundamental resonance frequency of the seismic harvesting transducer. Thus, normally the harvester is operated at its fundamental

resonance frequency. In this case, the flexural response of the laminate composite beam with tip mass could be derived by taking into account the contribution of the first bending natural mode only i.e. $w_r(x,t) \cong \phi_1(x)q_1(t)$. Thus, Eqs.(B.67), (B.68) can be rewritten as follows:

$$\delta_{11}\ddot{q}_1(t) + \delta_{11}\omega_1^2 q_1(t) + +\delta_{11}2\xi_1\omega_1\dot{q}(t) - \Pi_1 e_h(t) = -\ddot{w}_h(t)\left[\int_0^L m\phi_r(x)dx + M_t\phi_r(L)\right], \tag{B.69}$$

$$i_h(t) = \Pi_1\dot{q}_1(t) + C_e^S\dot{e}_h(t). \tag{B.70}$$

At this point, since the generalised coordinate $q_1(t)$ is given by $q_1(t) \cong w_r(x,t)/\phi_1(x)$, Eqs. (B.69), (B.70) can be rewritten with respect to $w_r(x,t)$ as follows:

$$\begin{aligned}\frac{\delta_{ii}}{\phi_1^2(x)}\ddot{w}_r(x,t) + \frac{\delta_{ii}2\xi_1\omega_1}{\phi_1^2(x)}\dot{w}_r(x,t) + \frac{\delta_{ii}\omega_1^2}{\phi_1^2(x)}w_r(x,t) - \frac{\Pi_1}{\phi_1(x)}e_h(t) \\ = -\frac{1}{\phi_1(x)}\left[\int_0^L m\phi_1(x)dx + M_t\phi_1(L)\right]\ddot{w}_h(t),\end{aligned} \tag{B.71}$$

$$i_h(t) = \frac{\Pi_1}{\phi_1(x)}\dot{w}_r(x,t) + C_e^S\dot{e}_h(t), \tag{B.72}$$

where, in order to get the same electromechanical transduction term $\Pi_1/\phi_1(x)$ in Eq.(B.71) and (B.72), the right and left hand sides of Eq.(B.71) have been divided by $\phi_1(x)$. Eq.(B.71) is similar to the equation of motion that would be derived for the suspended mass when the equivalent lumped parameter model shown in Figure 2.1 is employed to derive the response of the seismic transducer. In detail, a close examination of Eq.(B.71) shows that, this is the case when the left hand side inertia term is equal to the right hand side inertia term, and so when

$$\frac{\delta_{11}}{\phi_1(x)} = \left[\int_0^L m\phi_1(x)dx + M_t\phi_1(L)\right]. \tag{B.73}$$

This implicit equation is verified by a coordinate $\bar{x}$, which, in this study, has been derived numerically to be given by $\bar{x} = 0.9L = 0.13$ m. Thus, from Eq.(B.50), the schematic picture shown in Figure 2.1 can be employed to model the electromechanical response of the piezoelectric seismic transducer assuming the displacement of the suspended equivalent mass is given by the following relation:

$$w_m(t) = w_h(t) + w_r(\bar{x}, t). \tag{B.74}$$

In this case, Eq.(B.71) becomes:

$$\begin{aligned} m_m\, \ddot{w}_r(\bar{x}, t) + c_m\, \dot{w}_r(\bar{x}, t) + k_m\, w_r(\bar{x}, t) - \psi_{PZT} e_h(t) \\ = -m_m\, \ddot{w}_h(t), \end{aligned} \tag{B.75}$$

such that, Eq.(B.71) and (B.72) can be re-written as follows:

$$m_m\, \ddot{w}_m(t) = -c_m\, \dot{w}_r(\bar{x}, t) - k_m\, w_r(\bar{x}, t) + \psi_{PZT} e_h(t). \tag{B.76}$$

$$i_h(t) = \psi_{PZT} \dot{w}_r(\bar{x}, t) + C_e^S \dot{e}_h(t), \tag{B.77}$$

where, m_m, c_m, k_m, ψ_{PZT} are respectively the equivalent seismic mass, the equivalent visco-elastic damping factor, the equivalent beam flexural stiffness (assuming the electrodes are short circuited) and the equivalent piezoelectric transduction factor, which are given by the following expressions:

$$m_m = \frac{\delta_{ii}}{\phi_1^2(\bar{x})}\ c_m = \frac{\delta_{rr} 2\xi_1 \omega_1}{\phi_1^2(\bar{x})}\ \ k_m = \frac{\delta_{rr} \omega_1^2}{\phi_1^2(\bar{x})}\ \ \psi_{PZT} = \bar{e}_{31} b\left(h_s + h_{pe}\right) \frac{\phi_1'(L)}{\phi_1(\bar{x})}. \tag{B.78}$$

At this point, a second equation of motion can be derived for the base mass, which, considering the elastic, damping and electromechanical bending actions exerted by the composite beam and tip mass clamped to it and the action produced by the external force f_h, results given by the following expression:

$$m_b \ddot{w}_h(t) = c_m\, \dot{w}_r(\bar{x}, t) + k_m\, w_r(\bar{x}, t) - \psi_{PZT} e_h(t) + f_h(t). \tag{B.79}$$

Assuming time harmonic functions and setting $w_r(\bar{x}, t) = w_m(t) - w_h(t)$, after some mathematical manipulations, the three Eqs. (B.76), (B.77) and (B.79) give the following two constitutive equations for the seismic piezoelectric transducer:

$$f_h = \left\{ \mathrm{j}\omega m_b + \frac{\left[\frac{k_m'}{\mathrm{j}\omega} + c_m\right] \mathrm{j}\omega m_m}{\left[\frac{k_m'}{\mathrm{j}\omega} + c_m + \mathrm{j}\omega m_m\right]} \right\} \dot{w}_h + \left\{ \frac{\psi_{PZT}}{\mathrm{j}\omega C_e^S} \frac{\mathrm{j}\omega m_m}{\left[\frac{k_m'}{\mathrm{j}\omega} + c_m + \mathrm{j}\omega m_m\right]} \right\} i_h, \tag{B.80}$$

$$e_h = \left\{ \frac{\psi_{PZT}}{\mathrm{j}\omega C_e^S} \frac{\mathrm{j}\omega m_m}{\left[\frac{k'_m}{\mathrm{j}\omega} + c_m + \mathrm{j}\omega m_m\right]} \right\} \dot{w}_h + \left\{ \frac{1}{\mathrm{j}\omega C_e^S} + \frac{\psi_{PZT}^2}{\omega^2 C_e^{S^2} \left[\frac{k'_m}{\mathrm{j}\omega} + c_m + \mathrm{j}\omega m_m\right]} \right\} i_h \qquad \text{(B.81)}$$

Here $k'_m = k_m + \Delta k$ is composed by two stiffness terms: the first, which is characterised by the constant k_m, represents the equivalent bending stiffness when the electrodes are in short circuit whereas the second, $\Delta k = K_{pe} \frac{k_{31}^2}{1-k_{31}^2}$, with $K_{pe} = \frac{Y_{pe}^E b h_{pe} \left(h_s + h_{pe}\right)^2 \phi'_1(L)^2}{2L\phi_1(\bar{x})^2}$, represents the additional equivalent bending stiffness effect produced in open circuit configuration of the electrodes.

As will be shown in the following paragraph, the piezoelectric materials are characterised by dielectric losses. These effects are normally modelled with a complex permittivity $\tilde{\varepsilon}_{33}^T = \bar{\varepsilon}_{33}^T(1 - \mathrm{j}\eta_C)$, where η_C represents the dielectric loss factor, which, at low frequencies can be approximated with the following expression [67]:

$$\eta_c(\omega) \cong \frac{\sigma_{pe}}{\bar{\varepsilon}_{33}^T \omega}, \qquad \text{(B.82)}$$

where σ_{pe} is the electrical conductivity of the piezoelectric material. Thus, the capacitance of the piezoelectric layers under constant stress, $C_e^T = 2\bar{\varepsilon}_{33}^T \frac{bL}{h_{pe}}$, results: $\tilde{C}_e^T = C_e^T(1 - \mathrm{j}\eta_C)$. Likewise the electromechanical coupling factor $k_{31}^2 = Y_{pe}^E \, d_{31}^2 / \bar{\varepsilon}_{33}^T$ is also complex and given by $\tilde{k}_{31}^2 = k_{31}^2/(1 - \mathrm{j}\eta_C)$. As a result, the capacitance of the piezoelectric layers under constant strain, $C_e^S = C_e^T(1 - k_{31}^2)$, is given by the following complex term $\tilde{C}_e^S = \tilde{C}_e^T\left(1 - \tilde{k}_{31}^2\right)$. Therefore Eqs.(B.80), (B.81) become:

$$f_h = \left\{ \mathrm{j}\omega m_b + \frac{\left[\frac{\tilde{k}'_m}{\mathrm{j}\omega} + c_m\right] \mathrm{j}\omega m_m}{\left[\frac{\tilde{k}'_m}{\mathrm{j}\omega} + c_m + \mathrm{j}\omega m_m\right]} \right\} \dot{w}_h + \left\{ \frac{\psi_{PZT}}{\mathrm{j}\omega \tilde{C}_e^S} \frac{\mathrm{j}\omega m_m}{\left[\frac{\tilde{k}'_m}{\mathrm{j}\omega} + c_m + \mathrm{j}\omega m_m\right]} \right\} i_h \qquad \text{(B.83)}$$

$$e_h = \left\{ \frac{\psi_{PZT}}{\mathrm{j}\omega \tilde{C}_e^S} \frac{\mathrm{j}\omega m_m}{\left[\frac{\tilde{k}'_m}{\mathrm{j}\omega} + c_m + \mathrm{j}\omega m_m\right]} \right\} \dot{w}_h + \left\{ \frac{1}{\mathrm{j}\omega \tilde{C}_e^S} + \frac{\psi_{PZT}^2}{\omega^2 \tilde{C}_e^{S^2} \left[\frac{\tilde{k}'_m}{\mathrm{j}\omega} + c_m + \mathrm{j}\omega m_m\right]} \right\} i_h \qquad \text{(B.84)}$$

where $\tilde{k}'_m = k_m + \Delta\tilde{k}$ with $\Delta\tilde{k} = K_{pe} \frac{\tilde{k}_{31}^2}{1-\tilde{k}_{31}^2}$. As will be derived in Appendix B and shown in Figure A.12, the complex impedance of the lossy piezoelectric layers $Z_C = 1/\left(\mathrm{j}\omega \tilde{C}_e^S\right)$ can be modelled with resistor and capacitor elements connected either in

series or in parallel. In fact, the complex impedance can be derived in the following form:

$$Z_C = \frac{\eta_C}{\omega C_e^T \gamma} + \mathrm{j}\frac{(k_{31}^2 - 1)}{\omega C_e^T \gamma}, \tag{B.85}$$

where $\gamma = \eta_C^2 + (1 - k_{31}^2)^2$. Thus, the resistance and capacitance for the series scheme are given by: $R_s(\omega) = \frac{\eta_C}{\omega C_e^T \gamma}$ and $C_s(\omega) = C_e^T \gamma/(1 - k_{31}^2)$, whereas for the parallel scheme they are given by: $R_p(\omega) = \frac{1}{\omega C_e^T \eta_C}$ and $C_p(\omega) = C_e^T(1 - k_{31}^2)$. As can be readily be noticed from Eq.(B.85), both the real and imaginary parts of the complex impedance of the piezoelectric lossy capacitor vary proportionally to ω^{-1} with frequency. In contrast to the real part, the imaginary part assumes negative values since the reactive component of the impedance is given by $(k_{31}^2 - 1)/(\omega C_e^T \gamma)$.

B.2 DIELECTRIC LOSS EFFECTS

As pointed by Krupka [229], there are two basic types of polarization mechanism in solids: *Electronic* and *Ionic*. Electronic polarization describes the separation of the canters of "gravity" of the electron charges in orbitals such that the dipoles formed with the positive charge in the nucleus is always present. Ionic polarization, which characterises the piezoelectric materials, is identified by a net effect of changing the distance between neighbouring ions in an ionic crystal. All polarization mechanisms respond to an electrical field by shifting masses around. Therefore masses are accelerated and decelerated. This phenomenon takes some time. When an external time – varying field is applied to the material, displacement of the bound charges occurs, giving rise to the polarization density P. For a sinusoidal steady state, the polarization P varies at the same frequency as the applied field E. For low frequencies, P is also in phase with E and both quantities reach the maximum and minima at the same point of the cycles. As the frequency increases, however, the inertia of the particles and also the elastic and frictional forces that keep them together tends to prevent the polarization. As a result, the polarization field will be progressively more and more out of phase with the electric field. If the frequency is very large the whole polarization mechanism will die out. The condition of out of phase polarization P that occurs at high frequencies can be characterised by a complex dielectric susceptibility

χ and hence by a complex permittivity coefficient $\varepsilon \triangleq \varepsilon_0(1+\chi)$. Thus considering Eq.(B.2), a complex permittivity ε_{33}^T for the piezoelectric layer material can be introduced as follows:

$$\bar{\varepsilon}_{33}^T(\omega) = \varepsilon_{33}^{T\prime}(\omega) - j\varepsilon_{33}^{T\prime\prime}(\omega). \tag{B.86}$$

In general the validity of a damping model for a linear time invariant system in the frequency domain is linked to the mathematical condition of causality, which is usually denoted in the so called Kramers – Kroning relation [230]:

$$\varepsilon_{33}^{T\prime}(\omega) = -\frac{2\omega}{\pi}\int_0^\infty \frac{\bar{\omega}\varepsilon_{33}^{T\prime\prime}(\bar{\omega})}{\bar{\omega}^2-\omega^2}\,d\bar{\omega}, \tag{B.87}$$

$$\varepsilon_{33}^{T\prime\prime}(\omega) = \frac{2\omega}{\pi}\int_0^\infty \frac{\varepsilon_{33}^{T\prime}(\bar{\omega})}{\bar{\omega}^2-\omega^2}\,d\bar{\omega}. \tag{B.88}$$

If an ideal dielectric material (i.e. perfect insulator) is considered, only displacement currents occurs for alternating electric field E_3. According to Eq.(B.2), the current density can be obtained as $j(t) = \frac{dD_3}{dt}$, thus assuming time-harmonic functions:

$$J(\omega) = j\omega D_3(\omega) = j\omega\bar{\varepsilon}_{33}^T(\omega)E_3(\omega), \tag{B.89}$$

where a constant stress i.e. $T_1 = 0$ is assumed for simplicity. Substituting Eq.(B.86) into Eq.(B.89) gives:

$$J(\omega) = \omega\varepsilon_{33}^{T\prime\prime}(\omega)E_3 + j\omega\varepsilon_{33}^{T\prime}(\omega)E_3. \tag{B.90}$$

The total power density S, defined as the product between current and electrical field can be defined as:

$$S = \omega\varepsilon_{33}^{T\prime\prime}(\omega)E_3^2 + j\omega\varepsilon_{33}^{T\prime}(\omega)E_3^2, \tag{B.91}$$

which identifies two components, the real active power, which is the power deposited in the system that heats in the material, and the reactive power which cycles back and forth. Since $\varepsilon_{33}^{T\prime\prime}(\omega)$ depends on the frequency, the maximum dissipation corresponds to the frequency which maximize the product $\omega\,\varepsilon_{33}^{T\prime\prime}(\omega)$. In analogy to the definition

of the mechanical loss factor η_m, the measure of the quality factor of a dielectric material can be identified as the quotient between the real and reactive power:

$$\eta_d(\omega) \triangleq tan(\delta_d) = \frac{\varepsilon_{33}^{T\prime\prime}(\omega)}{\varepsilon_{33}^{T\prime}(\omega)}. \tag{B.92}$$

Thus, using Eq.(B.92) into Eq.(B.90) the displacement current density can be rewritten as

$$J(\omega) = j\omega\varepsilon_{33}^{T\prime}(\omega)(1 - j\eta_d). \tag{B.93}$$

The relations of Eqs.(B.90), (B.93) can be modelled as the equivalent circuit diagram shown in Figure B.5, which consists of an ideal capacitor $C_e(\omega) = \varepsilon_{33}^{T\prime}$ and ideal resistor $R_e(\omega) = {}^{1}/_{\omega\varepsilon_{33}^{T\prime\prime}}$:

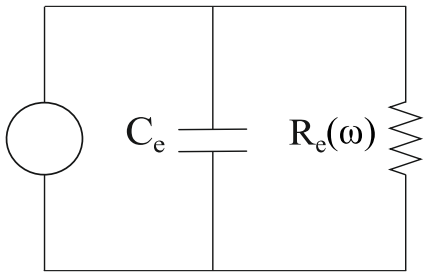

Figure B.5: Graphical representation of Eq.(B.93).

At low frequencies, $\omega\varepsilon_{33}^{T\prime\prime}$ is small due to ω being small and due to the fact that $\varepsilon_{33}^{T\prime\prime}$ is itself small so that the losses are largely negligible and no current flows to the resistance ($R_e \to \infty$). However, at higher frequencies, $\omega\varepsilon_{33}^{T\prime\prime}$ increases and produces a macroscopic effect as if the dielectric had effective conductivity $\sigma_{eff} = \omega\varepsilon_{33}^{T\prime\prime}$ (in a conducting material in response to a constant applied filed E, from Ampere's law a DC current density $j = \sigma E$ is always generated) and thus for a perfect dielectric piezoelectric material the losses are completely contained in the imaginary part $\varepsilon_{33}^{T\prime\prime}$ of $\bar{\varepsilon}_{33}^{T}$. Therefore, when the dielectric is excited at frequencies high enough for $\omega\varepsilon_{33}^{T\prime\prime}$ to be appreciable, an alternating current density of $\omega\varepsilon_{33}^{T\prime\prime}(\omega)E_3(\omega)$ and a displacement current density $\omega\varepsilon_{33}^{T\prime}(\omega)E_3(\omega)$ flows through the material. All this is only true for a perfect insulator where at low frequencies the permittivity tends to be zero; in reality

there is always a finite conductivity σ_{pe} also for DC current. In this case, it is sufficient considering an additional electrical conductivity σ_{pe} effect in Eq.(B.90); that is:

$$J(\omega) = \omega\varepsilon_{33}^{T\prime\prime}(\omega)E_3 + j\omega\varepsilon_{33}^{T\prime}(\omega)E_3 + \sigma_{pe}E_3. \tag{B.94}$$

From the definition of current density in Eq.(B.93), Eq.(B.94) can be rewritten in terms of a new permittivity $\eta_c(\omega)$ for non perfect piezoelectric insulators:

$$J(\omega) = j\omega\varepsilon_{33}^{T\prime}(\omega)(1 - j\eta_c), \tag{B.95}$$

where

$$\eta_c = \frac{\varepsilon_{33}^{T\prime\prime}(\omega)}{\varepsilon_{33}^{T\prime}(\omega)} + \frac{\sigma_{pe}}{\omega\varepsilon_{33}^{T\prime}(\omega)} = tan(\delta_d) + \frac{\sigma_{pe}}{\omega\varepsilon_{33}^{T\prime}(\omega)}. \tag{B.96}$$

Here $\tan(\delta_d)$ is the dielectric loss tangent associated with the pure dielectric loss mechanism (polarization) and $\frac{\sigma_{pe}}{\omega\varepsilon_{33}^{T\prime}(\omega)}$ is the loss component due to the conductivity of the dielectric, which can be modelled in terms of two resistors in parallel as shown in Figure B.6.

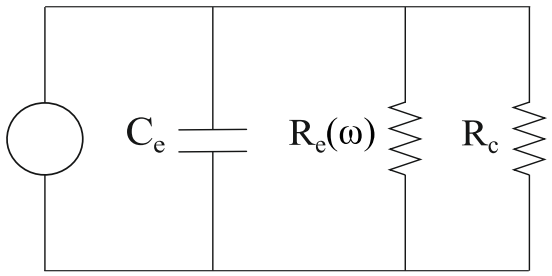

Figure B.6: Graphical representation of the dielectric losses identified by Eq.(B.96) in a piezoelectric material.

As shown in Figure B.7, for many piezoelectric materials, the conductivity is very low and the frequencies of interest are in the region of kilohertz and higher. Thus usually the contribution of the polarization lag is much larger than the DC conductivity effect. Despite that, the seismic (and reactive) piezoelectric harvesters operate at very low frequencies (i.e. < KHz), so the permittivity real part $\varepsilon_{33}^{T\prime}(\omega)$ is constant with frequency while the imaginary part $\varepsilon_{33}^{T\prime\prime}(\omega)$ is close to zero. No phase lag between the electric

field E_3 and the vector displacement D_3 is appreciable. Thus the conductivity term is dominant and imposes an inverse frequency dependence for the dissipation effect, which usually is not taken into account for the majority of the dielectric materials [229], [231], [232], [233]. Thus for such range of frequencies, the loss factor η_c can be approximated as follows:

$$\eta_c \cong \frac{\sigma_{pe}}{\omega \varepsilon_{33}^{T\prime}}. \tag{B.97}$$

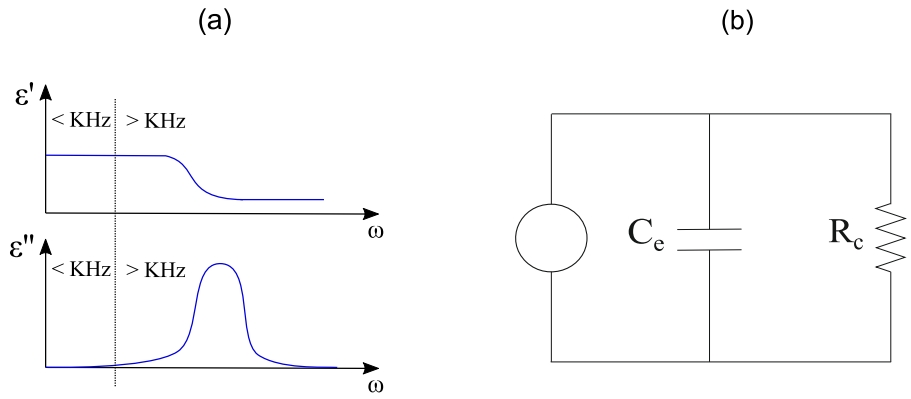

Figure B.7: (a) Approximation of the permittivity in the range of frequency of work for the seismic harvesters (b) Equivalent simplified circuit.

B.2.1 Dielectric loss effects on the piezoelectric harvester

The dielectric losses η_c play an important role in the response and energy harvesting with the piezoelectric seismic transducer studied in this thesis. According to Eq. (2.33), the maximum power that can be harvested at each frequency is given by

$$\bar{P}_h = \frac{1}{8}\frac{|T_{ew}|^2}{\mathrm{Re}\{Z_{ei}\}}|\dot{w}_h|^2. \tag{B.98}$$

Considering Eqs.(2.4), (2.5), (2.11), and (2.14), (2.15), and assuming there are no dielectric losses in the piezoelectric layers, i.e. $\eta_C = 0$,

$$T_{ew} = \Psi_{ew}\frac{Z_m}{Z_t} = \frac{\psi_{PZT}\dfrac{Z_m}{Z_t}}{\mathrm{j}\omega C_e^S}, \tag{B.99}$$

$$Z_{ei} = Z_e - \frac{\Psi_{fi}\Psi_{ew}}{Z_t} = \frac{1}{\mathrm{j}\omega \mathrm{C}_e^S} + \frac{\psi_{PZT}^2}{\omega^2 C_e^{S^2}} \frac{1}{Z_t}. \tag{B.100}$$

Thus, substituting Eqs.(B.99) and (B.100) into Eq.(B.98), and recalling Eqs.(2.6), (2.13), the maximum power that can be harvested at each frequency would result constant and equal to:

$$\overline{P}_h|_{\eta_C=0} = \frac{1}{8} \frac{\omega^2 m_m^2}{c_m} |\dot{w}_h|^2. \tag{B.101}$$

This phenomenon is confirmed in Figure B.8 and Figure B.9, which shows respectively the simulated spectra of the electric impedance Z_{ei} and of the maximum power that can be harvested at each frequency $\bar{P}_h$ with (solid blue line) and without (dashed black line) dielectric losses. If dielectric losses are not presented, the real part of the electric impedance Z_{ei} would be very small apart from a narrow frequency peak centred at the fundamental resonance frequency of the seismic transducer, i.e. 20 Hz, where the viscoelastic mechanical losses become relevant via the mechanical to electrical transduction effect. Instead, if dielectric losses are present, the real part assumes relatively large values in the whole frequency range. As predicted in Eq.(B.97), this is particularly visible at low frequencies below 50 Hz, where the effect of dielectric losses is particularly strong. These effects have a direct impact on the maximum power $\bar{P}_h$ that can be harvested at each frequency. In fact, as shown in Figure B.9, if the dielectric losses were not taken into consideration (dashed black line), the harvested power would be constant and equal to the value given by Eq.(B.101). Alternatively, in presence of dielectric losses, the spectrum of the harvested power assumes the typical feature for seismic transducers, with a resonance peak in correspondence to the fundamental resonance of the seismic transducer as was found in the experimental results shown in Figure 2.8. This peculiar phenomenon can be described by recovering the equivalent electrical components of the optimal harvesting impedance and then converting this components into equivalent mechanical lumped elements in the mechanical scheme of the transducer. According to Eq. (2.32) the optimal impedance of the harvester is given by $Z_h = Z_{ei}^*$, which, recalling Eqs. (2.5), (2.11), (2.13) and (2.14), (2.15) results:

$$Z_h = Z_{ei}^* = Z_e^* - \frac{\Psi_{fi}^* \Psi_{ew}^*}{Z_t^*} = -\frac{1}{\mathrm{j}\omega C_e^S} + \frac{\psi_{PZT}^2}{\omega^2 C_e^{S^2}} \frac{1}{-\frac{k_m'}{\mathrm{j}\omega} + c_m - \mathrm{j}\omega m_m}. \qquad \text{(B.102)}$$

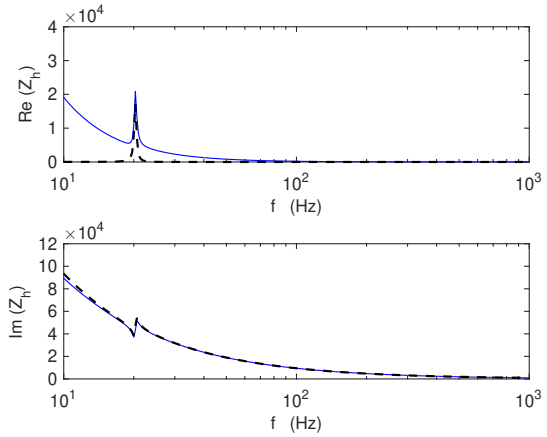

Figure B.8: Comparison between the simulated spectra of the complex impedance function $Z_h = Z_{ei}^*$ with (solid blue line) and without (dashed black line) dielectric losses.

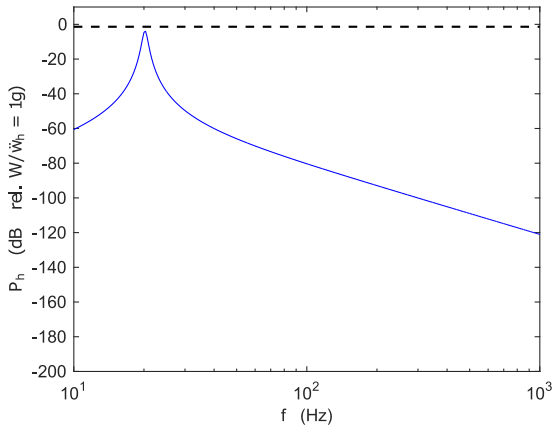

Figure B.9: Comparison between the simulated spectra of the maximum power that can be harvested at each frequency $\bar{P}_h$ assuming the piezoelectric patches are (solid blue line) and are not (dashed black line) characterised by dielectric losses.

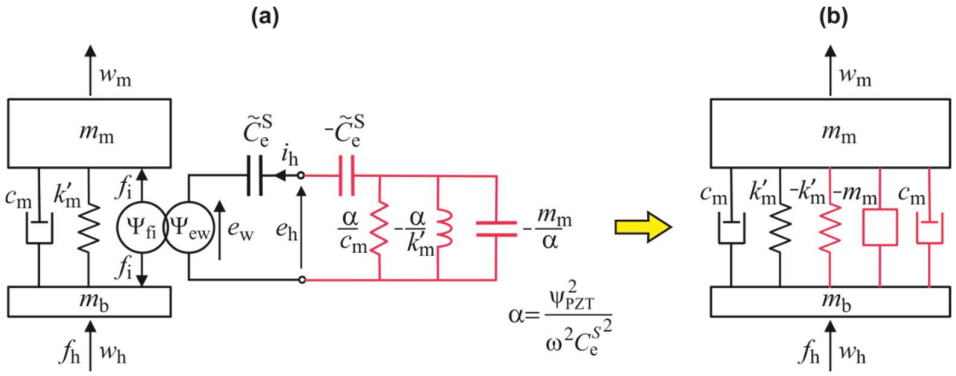

Figure B.10: a) Piezoelectric seismic harvester connected to the optimal complex harvesting load. b) Equivalent mechanical lumped parameter model. The electrical and mechanical lumped parameters of the harvesting load are highlighted in red.

As shown in Figure B.10 (a), this harvesting impedance is composed by a negative capacitance $-\mathrm{C}_e^S$ connected in series with a parallel RLC mesh formed by a resistance $R_h = \alpha/c_m$, by a negative inductance $L_h = -\alpha/k_m$ and by a negative capacitance $C_h = -m_m/\alpha$, where $\alpha = \psi_{PZT}^2/(\omega^2 C_e^{S^2})$. The negative capacitance $-\mathrm{C}_e^S$ eliminates the positive capacitance effect of the piezoelectric patches. The parallel RLC elements can then re-defined into equivalent mechanical elements noting that

$$\frac{f_i}{\dot{w}_m - \dot{w}_h} = -\frac{\Psi_{fi}\Psi_{ew}}{Z_{RLC}} = -\frac{k'_m}{\mathrm{j}\omega} + c_m - \mathrm{j}\omega m_m, \tag{B.103}$$

where $Z_{RLC} = -\frac{\Psi_{fi}^*\Psi_{ew}^*}{Z_t^*} = \frac{\psi_{PZT}^2}{\omega^2 C_e^{S^2}} \frac{1}{-\frac{k'_m}{\mathrm{j}\omega} + c_m - \mathrm{j}\omega m_m}$ and $-\Psi_{fi}^*\Psi_{ew}^* = \frac{\psi_{PZT}^2}{\omega^2 C_e^{S^2}}$. As shown in Figure B.10 (a), the three terms which characterise Eq. (B.102) correspond to a negative stiffness $-k'_m$, an "harvesting damper" c_m and a negative inerter $-m_m$ [234]. It is interesting to note that the negative harvesting inductance $L_h = -\alpha/k_m$ produces a relative inductive effect, which results into a relative negative inertia effect between the base and seismic elements of the transducer. As presented and discussed by Smith [234], this effect can be modelled with an inerter mechanical element, which is represented by the square box in Figure B.10 (a). At this point, assuming the harvester undergoes a base velocity $\dot{w}_h$, the following equation of motion can be derived for the seismic mass m_m:

$$\begin{aligned} m_m\ddot{w}_m = &-k'_m(w_m - w_h) + k'_m(w_m - w_h) + m_m(\ddot{w}_m - \ddot{w}_h) \\ &- 2c_m(\dot{w}_m - \dot{w}_h), \end{aligned} \tag{B.104}$$

such that

$$\dot{w}_m = \frac{j\omega m_m + 2c_m}{2c_m}\dot{w}_h. \tag{B.105}$$

The time averaged power harvested by the "harvesting damper" c_m at each frequency is given by:

$$\bar{P}_h|_{\eta_C=0} = \frac{1}{2}c_m|\dot{w}_m - \dot{w}_h|^2, \tag{B.106}$$

which, after substitution of Eq.(B.105), results in the same expression as in Eq.(B.101), derived for the maximum power that can be harvested at each frequency:

$$\bar{P}_h|_{\eta_C=0} = \frac{1}{8}\frac{\omega^2 m_m^2}{c_m}|\dot{w}_h|^2. \tag{B.107}$$

Thus in conclusion, to properly model the response and energy harvesting of a seismic (and reactive) piezoelectric harvester, it is necessary to account for the dielectric losses that occur in the piezoelectric patches of the harvester.

C

REACTIVE TRANSDUCER

In this chapter the fundamental constitutive equations for the reactive coil–magnet and symmetric piezoelectric energy harvester shown respectively in Plots (a, b) of Figure 3.1 are presented.

C.1 ELECTROMAGNETIC TRANSDUCER: CONSTITUTIVE EQUATIONS

Considering the schematic in Figure 3.1 (a), application of Newton's law of motion to the base mass gives:

$$m_b \ddot{w}_h = -iBl + k_m w_r + c_m \dot{w}_r + f_h, \tag{C.1}$$

where f_h is the external force applied at the base of the transducer and m_b is the mass of the base magnetic element, which is fixed on the vibrating source. Also, k_m is the equivalent axial stiffness of the top and bottom spiral springs that, as shown in Figure 3.1, connect the outer yoke and coil assembly to the inner magnetic element. Finally, c_m is the sum of two terms: 1) the coefficients for the inner viscous damping effect that develops in the air gap between the coil and the magnetic element and 2) the eddy current damping generated in the inner Yoke. The sky-hook viscous damping generated by the outer air loading on the moving yoke-coil assembly was found comparatively smaller and thus has been neglected in this model.

The electrical response of the coil can be straightforwardly derived by applying Kirchhoff's laws to the electric mesh depicted in the scheme of Figure 3.1 (a), which gives:

$$e_h = Bl\dot{w}_r + R_e i + L_e \frac{di}{dt}, \tag{C.2}$$

where R_e and L_e are respectively the electric resistance and the lossless inductance of the coil (the scheme considers the lossy inductance $\tilde{L}_e$, which has been investigated in Section 2 and Appendix A). Assuming time harmonic functions, after some mathematical manipulations, the two Eqs.(C.1), (C.2) give the following two constitutive equations for the reactive coil–magnet transducer:

$$f_h = \left\{ \mathrm{j}\omega m_b + \frac{k_m}{\mathrm{j}\omega} + c_m \right\} \dot{w}_h + \psi_{CM}\, i_h, \tag{C.3}$$

$$e_h = -\psi_{CM}\, \dot{w}_h + \{R_e + \mathrm{j}\omega L_e\} i_h. \tag{C.4}$$

As discussed in Appendix A, if the eddy currents that develop in the coil wire of the electromagnetic harvester are considered, the response of the coil element is modelled as a lossy inductor having complex inductance $\tilde{L}_e(\omega)$ (Eq.(A.109)), which, used in the constitutive Eqs.(C.3), (C.4) gives:

$$f_h = \left\{ \mathrm{j}\omega m_b + \frac{k_m}{\mathrm{j}\omega} + c_m \right\} \dot{w}_h + \psi_{CM}\, i_h, \tag{C.5}$$

$$e_h = -\psi_{CM}\, \dot{w}_h + \{R_e + \mathrm{j}\omega \tilde{L}_e\} i_h. \tag{C.6}$$

C.2 PIEZOELECTRIC TRANSDUCER: CONSTITUTIVE EQUATIONS

Following the procedure described in Eq.(A.1) and considering the schematic in Figure 3.1 (b), application of the Newton's law of motion to a generic infinitesimal segment of the beam results (see Eq.(B.48)):

$$B \frac{\partial^4 w(x,t)}{\partial x^4} + m \frac{\partial^2 w(x,t)}{\partial t^2} - \Theta_{pe} e_h(t) \left[\frac{\mathrm{d}\delta(x)}{\mathrm{d}x} - \frac{\mathrm{d}\delta(x-L)}{\mathrm{d}x} \right] = 0, \tag{C.7}$$

where m is the mass per unit length of the beam laminate, Θ_{pe} is the coupling term for the piezoelectric layers connected in parallel, B is the bending stiffness of the composite beam, e_h is the voltage drop across the electric terminals and $w(x,t)$ is the transverse displacement of the beam mid–plane relative to its fixed end.

If a point force of amplitude f_h is applied to the base mass of the bimorph cantilever beam shown in Figure 3.1 (b), the governing Eq.(C.7) becomes:

$$B\frac{\partial^4 w(x,t)}{\partial x^4}+m\frac{\partial^2 w(x,t)}{\partial t^2}-\Theta_{pe}e_h(t)\left[\frac{\mathrm{d}\delta(x)}{\mathrm{d}x}-\frac{\mathrm{d}\delta(x-L)}{\mathrm{d}x}\right]=f_h(t)\delta(x-L). \qquad \text{(C.8)}$$

Also, with reference to Eq.(B.62), the governing electrical circuit equation of the bimorph configurations for the parallel connection of the two piezoelectric layers can be expressed as:

$$i(t)=2h_{spe}b\bar{e}_{31}\int_0^L\frac{\partial^3 w(x,t)}{\partial t\,\partial x^2}\mathrm{dx}+2\bar{\varepsilon}_{33}^S\frac{bL}{h_{pe}}\frac{de_\mathrm{h}}{dt}, \qquad \text{(C.9)}$$

where $\bar{e}_{31}$ is the piezoelectric stress/charge constant , $\bar{\varepsilon}_{33}^S$ is the permittivity of the piezoelectric material in transverse direction under constant strain, b is the width of the beam. The transverse response relative to the fixed end of the bimorph cantilever is formulated in terms of convergent series of eigenfunctions:

$$w(x,t)=\sum_{r=1}^{\infty}\phi_r(x)q_r(t). \qquad \text{(C.10)}$$

Substituting this expression into Eqs.(C.8), (C.9), integrating along the length of the beam and applying the boundary conditions of Eqs. (B.11)-(B.14) for the undamped problem, the mechanical and electrical constitutive equations become:

$$\delta_{rr}\ddot{q}_1(t)+\delta_{rr}2\xi_r\omega_r\dot{q}_1(t)+\delta_{rr}\omega_r^2q_r(t)-\Pi_re_h(t)=f_{_h}(t)\phi(L), \qquad \text{(C.11)}$$

$$i_h(t)=\Pi_r\dot{\mathrm{q}}_r(t)+C_e^S\dot{e}_h(t). \qquad \text{(C.12)}$$

Here $\Pi_i=\bar{e}_{31}b\big(h_s+h_{pe}\big)\phi_i'(L)$ and $C_e^S=C_e^T(1-k_{31}^2)$, where $C_e^T=2\bar{\varepsilon}_{33}^T\frac{bL}{h_{pe}}$ is the capacitance of the two piezoelectric layers under constant stress, i.e. $T_1=0$ and k_{31}^2 is the electromechanical coupling factor.

In analogy to Appendix B, the flexural response of the laminate beam with tip mass can be derived by taking into account the contribution of the first bending natural mode only. Thus, setting $w(x,t)=\phi_1(x)q_1(t)$ and expressing the generalised coordinate $q_1(t)$ as $q_1(t)=w(x,t)/\phi_1(x)$, Eqs.(C.11), (C.12) can be rewritten as follows:

$$\frac{\delta_{11}}{\phi_1^2(x)}\ddot{w}(x,t)+\frac{\delta_{11}2\xi_1\omega_1}{\phi_1^2(x)}\dot{w}(x,t)+\frac{\delta_{11}\omega_1^2}{\phi_1^2(x)}w(x,t)-\frac{\Pi_1}{\phi_1(x)}e_h(t)=f_h\frac{\phi(L)}{\phi_1(x)}, \qquad \text{(C.13)}$$

$$i_h(t) = \frac{\Pi_1}{\phi_1(x)}\dot{w}(x,t) + C_e^S \dot{e}_h(t). \tag{C.14}$$

Considering the free end of the bimorph beam $x = L$, Eqs.(C.13), (C.14) can be rewritten in terms of a lumped parameter schematic model as shown in the schematic (d) of Figure 3.1:

$$m_b\, \ddot{w}_h(t) = -c_m\, \dot{w}_h(t) - k_m\, w_h(t) + \psi_{PZT} e_h(t) + f_h(t), \tag{C.15}$$

$$i_h(t) = \psi_{PZT}\, \dot{w}_h(t) + C_e^S \dot{e}_h(t). \tag{C.16}$$

Here $w_h(t) = w(L,t)$ and $f_h(t)$ are respectively the absolute displacement and the external point force in correspondence of the free end of the bimorph cantilever beam. Also, m_m, c_m, k_m, ψ_{PZT} are respectively the equivalent reactive mass, the equivalent viscous-elastic damping factor, the equivalent beam flexural stiffness (for the short circuit configuration) and the equivalent piezoelectric transduction factor, which are given by the following expressions:

$$m_b = \frac{\delta_{11}}{\phi_1^2(L)},\quad c_m = \frac{\delta_{11} 2\xi_1 \omega_1}{\phi_1^2(L)},\quad k_m = \frac{\delta_{11}\omega_1^2}{\phi_1^2(L)},\quad \psi_{PZT} = \bar{e}_{31} b\big(h_s + h_{pe}\big)\frac{\phi_1'(L)}{\phi_1(L)}. \tag{C.17a-d}$$

Now, assuming time harmonic functions, after some mathematical manipulations of Eqs.(C.15), (C.16), the following two constitutive equations for the reactive piezoelectric transducer are derived:

$$f_h = \left\{ \mathrm{j}\omega m_b + \frac{k_m + \Delta k}{\mathrm{j}\omega} + c_m \right\} \dot{w}_h - \frac{\psi_{PZT}}{\mathrm{j}\omega C_e^S}\, i_h, \tag{C.18}$$

$$e_h = -\frac{\psi_{PZT}}{\mathrm{j}\omega C_e^S}\, \dot{w}_h + \frac{1}{\mathrm{j}\omega C_e^S} i_h. \tag{C.19}$$

Here $\Delta k = K_{pe}\frac{k_{31}^2}{1-k_{31}^2}$, where $K_{pe} = \frac{Y_{pe}^E b h_{pe}\left(h_s + h_{pe}\right)^2 \phi_1'(L)^2}{2L\phi_1(\bar{x})^2}$ represents the additional equivalent bending stiffness effect produced when the electrodes are in open circuit. If the dielectric losses characterising the piezoelectric material are taken into account, thus the capacitance of the piezoelectric layers is rewritten as a complex term $\tilde{C}_e^S = \tilde{C}_e^T(1 - \tilde{k}_{31}^2)$ with $\tilde{C}_e^T = \mathrm{C}_e^T(1 - \mathrm{j}\eta_C)$ and $\tilde{k}_{31}^2 = k_{31}^2/(1 - \mathrm{j}\eta_C)$ where η_C the dielectric loss factor (see Appendix B.1), Eqs.(C.18), (C.19) become:

$$f_h = \left\{ \mathrm{j}\omega m_b + \frac{k_m + \Delta\tilde{k}}{\mathrm{j}\omega} + c_m \right\} \dot{w}_h - \frac{\psi_{PZT}}{\mathrm{j}\omega \tilde{C}_e^S}\, i_h, \tag{C.20}$$

$$e_h = -\frac{\psi_{PZT}}{\mathrm{j}\omega \tilde{C}_e^S}\, \dot{w}_h + \frac{1}{\mathrm{j}\omega \tilde{C}_e^S} i_h, \tag{C.21}$$

where $\Delta\tilde{k} = K_{pe} \frac{\tilde{k}_{31}^2}{1-\tilde{k}_{31}^2}$.

D

SCALING OF PHYSICAL PARAMETERS

D.1 FREQUENCY OF MAXIMUM POWER TRANSFER

This section shows that, assuming the optimal complex electrical load is implemented, for lightly damped transducers, the optimal frequency of operation of the two harvesters that maximises the power harvested coincides to their mechanical natural frequency, i.e. $\omega = \omega_n = \sqrt{k_m/m_m}$. To this end, a closed form analytical solution can be obtained only in the optimal complex electric load case. Thus a numerical approach should be implemented for the case where the optimal load is purely real. Nevertheless, such numerical study has confirmed the result obtained for the real complex load.

D.1.1 Electromagnetic transducer

Considering harmonic vibrations, as derived in Eq.(2.33), when the optimal reactive impedance $Z_s = Z_{ei}^*$ is implemented, the frequency dependent harvested power is equal to:

$$\bar{P}_h = \frac{1}{8}\frac{|T_{ew}|^2}{Re\{Z_{ei}\}}|\dot{w}_h|^2. \tag{D.1}$$

This expression can be rewritten with respect the transduction and electrical FRFs T_{ew} and Z_{ei}:

$$\bar{P}_h = \frac{1}{8}\frac{\omega^3 m_m \psi_{CM}}{R_e(\omega^2 m_m - k_m)^2 + \omega^2 c_m(\psi_{CM}^2 + R_e c_m)}|\dot{w}_h|^2. \tag{D.2}$$

The effects of the coil loss inductance is not considered since it is assumed that in the frequency range where the device operates this phenomenon is negligible.
Setting $\frac{\partial \bar{P}_h}{\partial \omega} = 0$ gives:

$$\frac{m_m \psi_{CM}}{8} \frac{3\omega^2[R_e(\omega^2 m_m - k_m)^2 + \omega^2 c_m(\psi_{PZT}^2 + R_e c_m)] - \omega^3[4R_e(\omega^2 m_m - k_m)\omega m_m + 2\omega c_m(\psi_{CM}^2 + R_e c_m)]}{R_e(\omega^2 m_m - k_m)^2 + \omega^2 c_m(\psi_{CM}^2 + R_e c_m)} = 0. \tag{D.3}$$

After some mathematical manipulations, this equation is verified setting:

$$[R_e c_m]\omega^4 + [2\omega_n^2(R_e c_m(1 - 2\xi^2) + 2\xi^2\psi_{CM}^2)]\omega^2 - 3R_e c_m \omega_n^4 = 0, \tag{D.4}$$

where $\omega_n = \sqrt{\frac{k_m}{m_m}}$ and $\xi = c_m/2\sqrt{k_m m_m}$ are the mechanical natural frequency and damping ratio of a classical mass spring damper model.

For damping ratio ξ lower than $1/2$ the terms containing the second order ξ^2 can be neglected and Eq.(D.4) becomes approximately equal to:

$$\omega^4 + (2\omega_n^2)\omega^2 - 3\omega_n^4 = 0. \tag{D.5}$$

Solving Eq.(D.5) with respect to frequency, the only physically meaningful solution is:

$$\omega|_{Ph=max} = \omega_n = \sqrt{\frac{k_m}{m_m}}. \tag{D.6}$$

D.1.2 Piezoelectric transducer

Considering now the piezoelectric harvester, the time-averaged power harvested with the optimal complex electric load is given by (Eq.(4.45)):

$$\bar{P}_h = \frac{1}{8}\frac{|T_{iw}|^2}{\mathrm{Re}\{Y_{ei}\}}|\dot{w}_h|^2. \tag{D.7}$$

Using the FRFs of T_{iw} and Y_{ei}, this equation can be rearranged as follows:

$$\bar{P}_h = \frac{1}{8}\frac{\omega^3(m_m\psi_{PZT})^2}{C_e^S\eta_c(\omega^2 m_m - k_m)^2 + \omega^2 c_m^2 C_e^S\eta_c + \omega c_m\psi_{PZT}^2}|\dot{w}_h|^2. \quad (D.8)$$

Setting $\frac{\partial \bar{P}_h}{\partial \omega} = 0$ gives:

$$\frac{4\omega^3[C_e^S\omega_0(\omega^2 m_m - k_m)^2 + \omega^2 c_m^2 C_e^S\omega_0 + \omega^2 c_m\psi_{PZT}^2] - \omega^4[4C_e^S\omega_0(\omega^2 m_m - k_m)\omega m_m + 2\omega c_m^2 C_e^S\omega_0 + 2\omega c_m\psi_{PZT}^2]}{[C_e^S\omega_0(\omega^2 m_m - k_m)^2 + \omega^2 c_m^2 C_e^S\omega_0 + \omega^2 c_m\psi_{PZT}^2]^2} = 0, \quad (D.9)$$

where $\omega_0 = 1/\tau$ is the inverse of the piezoelectric time constant, which depends from the dielectric loss $\eta_c = \frac{\sigma_{pe}}{\bar{\varepsilon}_{33}^T\omega} \triangleq \frac{1}{\tau\omega}$.

Dividing Eq.(D.9) by $4k_m m_m\omega^2$ (Ip. $\neq 0$) and rearranging the terms in the numerator, it follows:

$$\left(\frac{\xi\psi_{PZT}^2}{\omega_n m_m}\right)\omega^2 - C_e^S\omega_0(1-2\xi^2)\omega^2 + C_e^S\omega_0\omega_n^2 = 0, \quad (D.10)$$

where $\omega_n = \sqrt{\frac{k_m}{m_m}}$ and $\xi = c_m/2\sqrt{k_m m_m}$ for definition.

For damping ratio ξ lower than $1/2$, the terms containing the second order ξ^2 can be neglected and thus Eq.(D.10) becomes approximately equal to:

$$\left(\frac{\xi\psi_{PZT}^2}{\omega_n m_m}\right)\omega^2 - C_e\omega_0\omega^2 + C_e\omega_0\omega_n^2 = 0. \quad (D.11)$$

Since the term $\frac{\xi\psi_{PZT}^2}{\omega_n m_m}$ is two order of magnitude lower respect to $C_e^S\omega_0$ the equation can be reduced as:

$$-C_e\omega_0\omega^2 + C_e\omega_0\omega_n^2 = 0. \quad (D.12)$$

Thus solving Eq.(D.12), the only physically meaningful solution results:

$$\omega|_{Ph=max} = \omega_n = \sqrt{\frac{k_m}{m_m}}. \quad (D.13)$$

D.2 COUPLING COEFFICIENTS

For frequencies close to the fundamental natural frequency of the transducer, the three non-dimensional coupling coefficients C_{eml}, C_{emh} and C_{pz} give approximately a measure of how the mechanical impedances of the transducers are influenced by their electro-mechanical and piezoelectric additional transduction effects, when the devices are short circuited and open circuited respectively.

D.2.1 Electromagnetic harvester

Assuming harmonic vibration at the base of the transducer, two equations are necessary to characterise the behaviour of the device:

$$m_m \ddot{w}_m = -k_m w_r - c_m \dot{w}_r + \psi_{CM} i_h, \tag{D.14}$$

$$e_h = \psi_{CM} \dot{w}_r + R_e i_h + L_e \frac{di_h}{dt}. \tag{D.15}$$

Assuming external base force excitation $f_{ext} = -m_m \dot{w}_h$, the mechanical impedance of the harvester in open-circuit configuration ($i_h = 0$) results:

$$Z_{ho} = \frac{f_{ext}}{\dot{w}_m - \dot{w}_h} = j\omega m_m + \frac{k_m}{j\omega} + c_m, \tag{D.16}$$

which, in correspondence of the mechanical natural frequency ω_n, becomes:

$$Z_{ho}|_{\omega=\omega_n} = \left.\frac{f_{ext}}{\dot{w}_m - \dot{w}_h}\right|_{\omega=\omega_n} = c_m. \tag{D.17}$$

For the short-circuit configuration ($e_h = 0$), the mechanical impedance becomes:

$$Z_{hs} = \frac{f_{ext}}{\dot{w}_m - \dot{w}_h} = j\omega m_m + \frac{k_m}{j\omega} + c_m + \frac{\psi_{CM}^2}{R_e + J\omega L_e}, \tag{D.18}$$

which, in correspondence of the mechanical natural frequency, becomes:

$$Z_{hs}|_{\omega=\omega_n} = \left.\frac{f_{ext}}{\dot{w}_m - \dot{w}_h}\right|_{\omega=\omega_n} = c_m + \frac{\psi_{CM}^2}{R_e + J\omega_n L_e}. \tag{D.19}$$

The ratio of the short-circuit mechanical impedance to the open circuit mechanical impedance gives:

$$\left.\frac{Z_{hs}}{Z_{ho}}\right|_{\omega=\omega_n} = \frac{c_m + \frac{\psi_{CM}^2}{R_e + j\omega_n L_e}}{c_m} = 1 + \frac{\psi_{CM}^2}{c_m(R_e + j\omega_n L_e)} = 1 + \frac{\psi_{CM}^2}{c_m R_e(1 + j\,\omega_n/\omega_c)}. \tag{D.20}$$

If the mechanical natural frequency $\omega_n = \sqrt{k_m/m_m}$ of the transducer is lower compared to the cut off frequency $\omega_c \triangleq R_e/L_e$ of the transducer electric mesh, the effect of the inductance can be neglected and thus Eq.(D.20) can be approximated with the following expression:

$$\left.\frac{Z_{ho}}{Z_{hs}}\right|_{\omega=\omega_n} \cong 1 + \frac{\psi_{CM}^2}{c_m R_e} \triangleq 1 + C_{eml}. \tag{D.21}$$

In the opposite case, where only the effect of the inductance is relevant, Eq.(D.20) can be rearranged as follows:

$$\left.\frac{Z_{ho}}{Z_{hs}}\right|_{\omega=\omega_n} \cong 1 - \mathrm{j}\frac{\psi_{CM}^2}{c_m \omega_n L_e} \triangleq 1 - \mathrm{j}C_{emh}. \tag{D.22}$$

D.2.2 Piezoelectric harvester

Assuming harmonic base vibrations, the two equations that characterise the behaviour of an ideal piezoelectric seismic transducer are:

$$m_m \ddot{w}_m = -k_m w_r - c_m \dot{w}_r - c_{am}\dot{w}_m + \psi_{PZT} e_h, \tag{D.23}$$

$$i_h = \psi_{PZT}\dot{w}_r + j\omega C_e^S e_h. \tag{D.24}$$

The mechanical impedance under base force excitation $f_{ext} = -m_m \dot{w}_h$ and short-circuited terminals ($e_h = 0$) results:

$$Z_{hs} = \frac{f_{ext}}{\dot{w}_m - \dot{w}_h} = j\omega m_m + \frac{k_m}{j\omega} + c_m + c_{am}, \tag{D.25}$$

which, in correspondence of the mechanical natural frequency ω_n of the transducer becomes :

$$Z_{hs}|_{\omega=\omega_n} = \left.\frac{f_{ext}}{\dot{w}_m - \dot{w}_h}\right|_{\omega=\omega_n} = c_m + c_{am}. \tag{D.26}$$

The mechanical impedance in open-circuited configuration ($i_h = 0$) results:

$$Z_{ho} = \frac{f_{ext}}{\dot{w}_m - \dot{w}_h} = j\omega m_m + \frac{k_m}{j\omega} + c_m + c_{am} + \frac{\psi_{PZT}^2}{j\omega C_e^S}, \tag{D.27}$$

which, calculated for frequencies equal to the mechanical natural frequency becomes:

$$Z_{ho} = \left.\frac{f_{ext}}{\dot{w}_m - \dot{w}_h}\right|_{\omega=\omega_n} = c_m + c_{am} + \frac{\psi_{PZT}^2}{j\omega C_e^S}. \tag{D.28}$$

Thus the ratio of the open circuit mechanical impedance to short circuit mechanical impedance is given by:

$$\left.\frac{Z_{ho}}{Z_{hs}}\right|_{\omega=\omega_n} = \frac{c_m + c_{am} + \frac{\psi_{PZT}^2}{j\omega_n C_e^S}}{c_m + c_{am}} = 1 - j\frac{\psi_{PZT}^2}{\omega_n C_e^S (c_m + c_a)} \triangleq 1 - jC_{pz}. \tag{D.29}$$

D.3 SCALING PHYSICAL PARAMETERS

Considering Ref. [235], this chapter introduces and reviews the basic scaling laws for the mechanical and electric parameters that characterise the electromagnetic and piezoelectric harvesters considered in this study.

D.3.1 Mechanical parameters

Based on the theory of stress in solids, normally constant mechanical stress is assumed, which under linear theory and constant material properties implies constant deformation. From this, it follows that the force exerted on the material simply scales as:

$$force \propto \text{area} \propto [L^2]. \tag{D.30}$$

Based on the assumption of constant material density, the mass scales with the volume:

$$mass \propto volume \propto [L^3]. \tag{D.31}$$

Both shear and normal stiffness depend on area and length, thus scales as:

$$shear\ stifness \propto \frac{area}{length} \propto [L^1], \tag{D.32}$$

$$normal\ stifness \propto \frac{area}{length} \propto [L^1]. \tag{D.33}$$

Alternatively, the bending stiffness of a circular rod or a rectangular beam scales as:

$$bending\ \ stifness \propto \frac{radius^4}{length^3} \propto \frac{width * thickness^3}{length^3} \propto [L^1], \tag{D.34}$$

denoting the same linear behaviour.

Moving to the dynamic properties of mechanical systems, the scaling property of distributed flexible system, can be redirected to the scaling of wave propagation [226]. For simplicity, the wave propagation due to longitudinal or transverse vibrating

strings or rods is considered, which, are characterised by propagation velocity $c = \sqrt{\frac{E}{\rho}}$ and $c = \sqrt{\frac{G}{\rho}}$ respectively, where E and G are the axial and shear moduli of elasticity and ρ is the material density. For these wave-types, the vibrational frequencies scale with the following law:

$$frequency \propto \frac{wave\ speed}{length} \propto [L^{-1}]. \tag{D.35}$$

Normal vibrational modes can also be described in terms of mass and stiffness modal parameters such that the natural frequency scales:

$$frequency \propto \sqrt{\frac{stiffness}{mass}} \propto [L^{-1}], \tag{D.36}$$

thus, describing the same scaling relationship as for the wave propagation.

D.3.2 Electrical parameters

Moving to the scaling of the electric parameters, it is convenient to assume that the electrostatic field strength E is indipendent from the dimension. Under this assumption, the scaling results obtained above continue to hold also for electromechanical systems. Under this assumption, the electric voltage scales as:

$$voltage \propto electric\ field\ strength * length \propto [L^1]. \tag{D.37}$$

Assuming a constant electric resistivity, from the Ampere's law it follows:

$$resistance \propto \frac{length}{area} \propto [L^{-1}], \tag{D.38}$$

from which:

$$ohmic\ current \propto \frac{voltage}{resistance} \propto [L^2], \tag{D.39}$$

and thus constant current density. From the definition of electrostatic energy:

$$electrostatic\ energy \propto volume * electrostatic\ field \propto [L^3], \tag{D.40}$$

which yields an expression for the scaling of capacitance:

$$capacitance \propto \frac{electrostatic\ energy}{voltage^2} \propto [L^1]. \tag{D.41}$$

Under the assumption of constant current density, the magnetic field generated by the current flowing through a conductor is derived from the Biot – Savart law, such that:

$$magnetic\ field \propto \frac{current}{distance} \propto [L^1], \tag{D.42}$$

while the corresponding magnetic field energy is:

$$magnetic\ energy \propto volume * (magnetic\ field)^2 \propto [L^5]. \tag{D.43}$$

Finally, the scaling of a lumped inductance element can be found from its storage magnetic energy:

$$inductance \propto \frac{magnetic\ energy}{current^2} \propto [L^1]. \tag{D.44}$$

D.4 ELECTROMAGNETIC HARVESTER – SCALING LAWS

D.4.1 Couette film damping

The scaling laws for the moving mass m_m and the helical spring stiffness k_m of the electromagnetic harvester can be derived from [190] and scales respectively as $[L^3]$ and $[L^1]$. More complicated is the derivation of the scaling behaviour for the damping term c_m since the dissipation effect depends on several phenomena. For example [204]

suggests that the dissipative effect is produced by the squeeze film generated between the central hole of the housing ring and the stinger, concluding that c_m is directly proportional to their linear dimension $c_m \propto [L^1]$. In this case, it was assumed that the magnitude of the air damping exceed the structural damping of the suspension system.

A different approach is proposed by Elliott *et al*. [203], where comparing the non-dimensional coupling factor:

$$\mathrm{C}_{em} = \frac{\psi_{CM}^2}{c_m R_e}, \tag{D.45}$$

of a large number of electromagnetic transducers with respect their size concludes that the damping c_m scales as the square power of the dimension

$$c_m \propto L^2, \tag{D.46}$$

under the assumption that the transduction coefficient ψ_{CM} and the electrical resistance of the coil R_e scales respectively proportional and inversely proportional to the dimension .

In fact, as already described in Chapter 4 the electric resistance R_e of a cylindrical shaped conductor (i.e. wire) can be described by the following equation [203]:

$$R_e = \rho_e \frac{l}{A}, \tag{D.47}$$

where ρ_e is the resistivity of the material and is independent from the size, l is the length of the wire and A is the cross sectional area of the wire too . Thus R_e clearly scales as $[L^{-1}]$. In addition, the transduction coefficient $\psi_{CM} = Bl$, defined as the product between the magnetic flux density B (independent from the size of the device) and the length of the wire gives a proportional scaling law $\psi_{CM} \propto [L^1]$. Considering experimental data, Elliott and Zilletti [203] found that C_{em} scales approximately linearly with the dimension, so $\mathrm{C}_{em} \propto [L^1]$. The scaling behaviour of c_m is thus obtained indirectly from such measures. In this case a non well-defined damping phenomenon is studied but a generic damping effect which may include many dissipative aspects is considered.

In addition, two other important damping effects may play an important role in the dissipative mechanism of electromagnetic transducers: 1) the Couette film damping generated through the air gap between the magnet and the internal surface of the housing yoke and 2) the eddy currents generated in the cylindrical ring of the device, caused by the interaction between the moving magnet and the conductor material.

Let's consider at first the Couette film damping effect. As pointed in Ref. [202], a Newtonian viscous fluid (air) moving between two surfaces in relative motion is subject to a constant stress τ_F and undergoes a Couette *Flow* with a linear velocity profile.

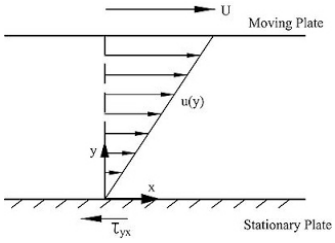

Figure D.1: Couette film damping.

Let's consider two rigid plates of surface area A, separated by an air gap h. Also, let's assume that one plate is free to move relatively to the other along the axial direction w. In this case the constant shear stress τ_F is proportional to the velocity gradient $d\dot{w}/dy$:

$$\tau_F = \mu_a \frac{d\dot{w}}{dy} \cong \mu_a \frac{\dot{w}}{y}, \tag{D.48}$$

where μ_a is a property of the fluid called *coefficient of viscosity* [202]. Thus, it follows that the friction force F_τ acting on the moving plate is:

$$F_\tau = \tau_F A. \tag{D.49}$$

So substituting Eq.(D.48) into Eq.(D.49) gives:

$$F_\tau = A \frac{\mu_a}{y} \dot{w}, \tag{D.50}$$

and rearranging the terms in compact form:

$$F_\tau = c_c \dot{w}. \tag{D.51}$$

Since the velocity gradient is inversely proportional to the size and the surface area is proportional to the square of the dimension it results:

$$c_c = \frac{F_\tau}{\dot{w}} \propto [L]. \tag{D.52}$$

A similar result can be obtained for the coil magnet transducer, where the magnet and external ring are separated by a small air gap and move relative to each other. This result shows that *Couette* and *Squeeze* film damping scales in the same manner (i.e. linear to the dimension size).

D.4.2 Eddy currents

Numerical simulations have been performed in order to evaluate how the damping coefficient c_{ec} scales with reference to the device characteristic dimension (i.e. $[L]$). The result shows that the radial magnetic field density B_ρ generated by the permanent magnet does not increase in value with the dimension of the device, provided the magnet maintains the same aspect ratio; i.e. the magnitude of the field remains constant while the field gradient ∇B_ρ increase if the dimension is reduced ([206], [207]). As a result, considering Eq.(A.106), it is straightforward to verify that c_{ec} scales with the volume of the transducer ant thus as the cube of the characteristic length (i.e. $[L^3]$).

However taking into account the results of Appendix A.2.1, the presence of a diffusion phenomenon, due to the interaction of the eddy currents with the magnetic field density of the permanent magnet, produces a reduction in the distribution of the current density along the radial direction of the conducting housing Yoke cylinder. In this case, Eq.(A.106) can be rearranged changing the limits of integration R_{ye} , R_{yi} as follows:

$$c_{ec} \;=\; 2\pi\sigma_e \int_{-\frac{L_y}{2}}^{\frac{L_y}{2}} \int_{R_{yi}}^{R_{yi}+\delta} \rho B_\rho^2(\rho, z)\, \mathrm{d}\rho\, \mathrm{dz}, \tag{D.53}$$

where δ is the skin depth defined in Eq.(A.57). If the electromagnetic harvester works close to its natural frequency the skin depth can be specified as $\delta \triangleq \sqrt{\frac{2}{\omega_n \mu_e \sigma_{pe}}}$. This implies that δ scales as $[L^{0.5}]$ (μ_e and σ_{pe} are properties of the material and ω_n scales proportional to $[L^{-1}]$) and thus the damping coefficient c_{ec} tends to vary as $[L^{2.5}]$ and not as the cube of the dimension.

D.4.3 Inductance

The only fundamental parameter that remains to be investigated to characterise the scaling behaviour of the electromagnetic power harvester studied in this thesis is the electrical inductance L_e of the coil:

$$L_e \triangleq \frac{\emptyset}{i}, \tag{D.54}$$

which is derived above as the quotient between the flux $\emptyset$ generated by the current i which flows through the wire of the coil and the current i. Recalling that the axial magnetic flux density generated by the current i of a generic voice coil of N turns, length l and radius R can be defined as $B_x = \mu_e \frac{N}{l} i$ and the auto-flux generated inside the coil is $\emptyset = N B_x \pi R^2$, Eq.(D.54) can be rewritten as:

$$L_e \triangleq \mu_e \frac{N^2 \pi R^2}{l}. \tag{D.55}$$

Since the magnetic permeability μ_e is a constant property of the material and assuming that the number N of the coil turns does not vary with the dimension, it follows that the inductance varies linearly with the dimension size of the transducer i.e. $L_e \propto [L]$.

D.5 PIEZOELECTRIC HARVESTER

D.5.1 Mass

Considering the piezoelectric harvester shown in Figure 4.2 , the scaling law of the equivalent moving mass m_m derived in Section B.1.4 can be obtained as follows.
The first flexural natural mode of the clamped composite beam with tip mass and the corresponding first natural frequency are given from Eqs.(B.32),(B.33):

$$\phi_1(x) = \mu_1 \left[cos\left(\lambda_1 \frac{x}{l}\right) - cosh\left(\lambda_1 \frac{x}{l}\right) + \sigma_1 \left(sin\left(\lambda_1 \frac{x}{l}\right) - sinh\left(\lambda_1 \frac{x}{l}\right)\right)\right], \tag{D.56}$$

$$\omega_1 = \frac{\lambda_1^2}{l^2}\sqrt{\frac{B}{m}}, \tag{D.57}$$

where $\sigma_1(x) = \frac{\sin\left(\lambda_1\frac{x}{l}\right)-\sinh\left(\lambda_1\frac{x}{l}\right)+\frac{\lambda_1 M_t}{lm}\left[\cos\left(\lambda_1\frac{x}{l}\right)-\cosh\left(\lambda_1\frac{x}{l}\right)\right]}{\cos\left(\lambda_1\frac{x}{l}\right)+\cosh\left(\lambda_1\frac{x}{l}\right)-\frac{\lambda_1 M_t}{lm}\left[\sin\left(\lambda_1\frac{x}{l}\right)-\sinh\left(\lambda_1\frac{x}{l}\right)\right]}$ and $B = Y_s I_s + Y_{pe}^E I_{pe}$ is the bending stiffness of the composite beam with Y the Young's module and I_{pe} the composite beam cross section second moment of inertia about the transverse axis y . Also m is the mass per unit of length l, M_t is the tip mass clamped at the end of the beam and ϕ is the 1-th eigenfunction. Finally μ_1 is the arbitrary constant of the first mode while λ_1 is the 1-th eigenvalue derived from the root of the characteristic equation of the eigenvalue problem:

$$1 + cos(\lambda_1)\,cosh(\lambda_1) + \frac{\lambda_i\, M_t}{ml}[cos(\lambda_1)\,sinh(\lambda_1) - sin(\lambda_1)\,cosh(\lambda_1)] = 0. \tag{D.58}$$

Since the product $\frac{M_t}{m\,l} \propto \frac{L^3}{L^2 L^1} = [L^0]$ doesn't scale with the size of the beam, Eq. (D.58) doesn't scale with the dimension an thus it is straightforward to verify that λ_1 is independent of the size of the harvester. Neglecting the rotational inertia of the tip mass clamped at the end, the orthonormality relation of the eigenfunctions gives:

$$\int_0^L m\phi_1\phi_1 dx + M_t\phi_1(L)\phi_1(L) = M_1, \tag{D.59}$$

where for simplicity, it is assumed that the arbitrary constant μ_1 for the 1-th mode is equal to $\mu_1 = 1$. In fact the term M_1 is the modal mass related to the first mode of the beam. It should be noted that in this study the mass normalization for the flexural natural mode is assumed i.e. $M_1 = 1$.

As shown in Appendix B.1, the equivalent physical seismic mass m_m in the lumped model can be derived as the quotient between the modal mass M_1 and the square of the first eigenfunction ϕ_1:

$$m_m = \frac{M_1}{\phi_1^2(\bar{x})}, \tag{D.60}$$

where $\bar{x}$ is a specific coordinate along the length l of the beam. Since the natural mode $\phi_1(x)$ is independent from the size and l, m, M_t scales respectively as L, L^2, L^3, it follows that the modal mass scales as $M_1 \propto [L^3]$ and thus:

$$m_m \propto \frac{L^3}{L^0} = [L^3]. \tag{D.61}$$

D.5.2 Natural frequency

From the eigenvalue problem, the relation between the fundamental natural frequency ω_1 of the 1-st eigenfunction and the first eigenvalue λ_1 is taken from Eq.(B.32):

$$\omega_1 = \frac{\lambda_1^2}{l^2}\sqrt{\frac{B}{m}}. \tag{D.62}$$

Since λ_1 is independent from the size and the bending stiffness B, the mass m and the length l of the composite beam scales respectively as L^4, L^2, L, it follows that the first natural frequency related to the first natural mode scales as:

$$\omega_1 \propto \frac{L^0}{L^2}\sqrt{\frac{L^4}{L^2}} = [L^{-1}], \tag{D.63}$$

D.5.3 Stiffness

As derived in Eq.(B.78), the equivalent beam flexural stiffness k_m calculated when the electrodes are short circuited is given by:

$$k_m = \frac{M_1\omega_1^2}{\phi_1^2(\bar{x})}. \tag{D.64}$$

Using the results obtained above, the flexural stiffness of the cantilever beam scales as:

$$k_m \propto \frac{L^3 L^{-2}}{L^0} = [L^1]. \tag{D.65}$$

The fundamental natural frequency ω_{n} of the equivalent piezoelectric lumped model shown in Figure 4.2 can be defined also in terms of its lumped parameters stiffness and mass so that $\omega_{\mathrm{n}} = \sqrt{k_m/m_m} = \omega_1$, which clearly identify the same scaling relationship in terms of the first modal frequency.

D.5.4 Transduction coefficient

As found in Eq.(B.78), the piezoelectric transduction coefficient of the composite beam can be defined as follows:

$$\psi_{PZT} = \bar{e}_{31} b\big(h_s + h_{pe}\big)\frac{\phi_1'(L)}{\phi_1(\bar{x})}, \tag{D.66}$$

where $\bar{e}_{31} \triangleq Y_{pe}^E d_{31}$ is the piezoelectric stress/charge constant for the uniaxial normal stress field in the beam under a constant electric filed E_3 , b is the width of the beam and h_s, h_{pe} are the thicknesses of the substrate and piezoelectric layers respectively. Finally $\phi_1'(L)$ is the first derivative of the 1-th mode calculated at the tip of the beam:

$$\phi_1'(L) = \frac{d\phi_1(x)}{dx}\Big|_{x=L} = \mu_1 \frac{\lambda_i}{l}\left[-sin(\lambda_1) - sinh(\lambda_1) + \sigma_1\left(cos(\lambda_1) - cosh(\lambda_1)\right)\right]. \quad \text{(D.67)}$$

Since μ_1 is a constant (set equal to 1), λ_1 is size independent and l varies linearly with the dimension, as a result $\phi_1'(L)$ scales as $[L^{-1}]$ and thus the transduction coefficient ψ_{PZT} scales as :

$$\psi_{PZT} \propto L^0 L^1 L^1 \frac{L^{-1}}{L^0} = [L^1]. \quad \text{(D.68)}$$

D.5.5 Material damping

The lumped constitutive equation of the harvester is obtained starting from the Euler Bernoulli beam Equation, which, as shown in Ref. [228], can be combined with two physical damping models, compatible with the modal model. The modal damping operators considered in this study are the *viscous air damping*:

$$\mathcal{L}_1 = \gamma \frac{\partial}{\partial t}, \quad \text{(D.69)}$$

and the *Kelvin Voigt damping* :

$$\mathcal{L}_2 = c_d I_s \frac{\partial^5}{\partial w^4 \partial t}. \quad \text{(D.70)}$$

In these expressions, γ, I_s, c_d are respectively the air damping factor, the cross section moment of area and the strain rate damping coefficient.

Recalling the Newton's law of motion for a generic infinitesimal segment of the beam under an imposed steady state base displacement w_h presented in Section B, which includes the two beam damping mechanisms:

$$\begin{aligned} \frac{\partial^2 M(x,t)}{\partial x^2} + c_s I \frac{\partial^5 w_r(x,t)}{\partial x^4\, \partial t} + \gamma \frac{\partial w_r(x,t)}{\partial \mathrm{t}} + m \frac{\partial^2 w_r(x,t)}{\partial t^2} \\ = -[m + M_t \delta(x-L)] \frac{\mathrm{d}^2 w_h(t)}{\mathrm{d}t^2} - \gamma \frac{\mathrm{d}w_h(t)}{\mathrm{dt}}, \end{aligned} \quad \text{(D.71)}$$

and applying the modal analysis:

$$M_{11}\ddot{q}_1(t) + M_{11}2\xi_1\omega_1\dot{q}_1(t) + M_{11}\omega_1^2 q_1(t) - \Pi_1 e_h(t) = -\ddot{w}_h(t)\left[\int_0^L m\phi_1(x)dx + M_t\phi_1(L)\right], \quad \text{(D.72)}$$

results the relation between the damping ration ξ_1 and the two damping operators is:

$$\gamma + c_d Y_s \frac{\lambda_1^4}{l^4} = 2M_{11}\xi_1\omega_1, \quad \text{(D.73)}$$

where λ_1 is the first *eigenvalue* and ω_1 is the first natural frequency. The first modal damping ratio can thus be expressed as:

$$\frac{\gamma}{2\omega_1 M_{11}} + c_d Y_s \frac{\omega_1 m}{2BM_{11}} = \xi_1, \quad \text{(D.74)}$$

indicating that the effect of air damping is inversely proportional to the natural frequency mode. This agrees with the physical intuition that higher order modes are less effective in displacing air. On the contrary, material damping increases for higher order modes.

The linear viscous external damping and KV internal damping models can be conveniently adopted in modal models for the beam response. However, since the origin of the coefficients γ and c_d cannot be well identified and different possible choices of the operators $\mathcal{L}_1$ and $\mathcal{L}_2$ can be selected for convenience, the nature of the scaling damping mechanism must be investigated separately in order to obtain results closer to the experiments. In order to identify the correct damping scale law, a review of the most used damping models is presented below.

One of the first attempts to generalize the equations of the classical elasticity theory was made by Kevin-Voigt, assuming that the tensile stress σ and strain ε are related to the equation:

$$\sigma = E\varepsilon + E^*\dot{\varepsilon}, \quad \text{(D.75)}$$

where E, E^* are viscous elastic material constants. In order to introduce the viscous damping parameter, the energy dissipation method is adopted in Ref. [236], so assuming a tonal a excitation $\varepsilon(t) = \varepsilon_0 \sin(\omega t)$, the energy loss per cycle is :

$$W_l = \int_0^{2\pi/\omega} (E\varepsilon + E^*\dot{\varepsilon})\dot{\varepsilon} dt = E^*\varepsilon_0^2\,\pi\omega. \tag{D.76}$$

As discussed in Ref. [237], a variety of expressions for the maximum energy stored for a dynamic steady state excitation could be chosen. In the case of maximum deformation per cyclic response, the following definition is used:

$$W = \int_0^{\varepsilon_0} E\varepsilon\, d\varepsilon = \frac{1}{2}E\varepsilon_0^2. \tag{D.77}$$

The loss factor η for a KV material is then defined as follows [237], [238]:

$$\eta \triangleq \frac{W_l}{2\pi W} = \frac{E^*\varepsilon_0^2\pi\omega}{\frac{1}{2}E\varepsilon_0^2 2\pi} = \frac{E^*\omega}{E}, \tag{D.78}$$

which can be interpreted as the energy loss per radiant $W_l/2\pi$ divided to the maximum energy available W. This parameter is one of the most commonly measure of damping used in dynamical analysis [236]. In the frequency domain, Eq.(D.75) can be rearranged as:

$$\sigma = E\varepsilon + j\omega E^*\varepsilon = E\varepsilon\left(1 + j\frac{\omega E^*}{E}\right) \triangleq E(1 + j\eta)\varepsilon. \tag{D.79}$$

This model is analogue to an ideal elastic spring k in parallel with an ideal dashpot c that acts as a linear viscous damper:

$$f_{ext} = kw + j\omega cw = k\left(1 + j\frac{\omega c}{k}\right) \triangleq k\big(1 + j\eta_{KV}(\omega)\big)w. \tag{D.80}$$

Actually, Eq.(D.80) does not match with real cases, since a solid subjected to an oscillating stress has not a linear frequency dependence $\eta(\omega)$ [236].
Another simple model, usually used in dynamic analysis, is the Kimball Lovell model, valid only in the frequency domain:

$$\sigma = E\varepsilon + jE^*\varepsilon = E\varepsilon\left(1 + j\frac{E^*}{E}\right) \triangleq E(1 + j\,tan\,\phi)\varepsilon. \tag{D.81}$$

This expression is composed by a complex Young module, which represent the fact that the equilibrium response of the material is not instantaneous. In this case the measure of damping is derived by the tangent of the loss angle $\tan\phi$, identified by the material properties alone. This model simply consists of a spring characterised by a complex term:

$$f_{ext} = kw + jk^*w = k\left(1 + j\frac{k^*}{k}\right) \triangleq k(1 + j\,tan\,\phi)w. \tag{D.82}$$

These two simple viscous loss models, which are usually adopted in reality are too simple to accurately replicate the behaviour of metals and other material solids. Boltzman [239] introduced the concept of memory mechanism defining that the effects of an applied stress on the material depends not only on the stress at a particular instant but also on the stresses applied at any prior instant of time. This mechanism is mathematically explained by a convolution expression between the first order derivative of the strain ε and a memory function C:

$$\sigma(t) = \int_{-\infty}^{+\infty} C(t-\tau)\frac{d\varepsilon}{d\tau}d\tau. \tag{D.83}$$

Since C is defined to be zero if $(t-\tau) > 0$, Eq.(D.83), can be integrated from minus infinity to the generic time t:

$$\sigma(t) = \int_{-\infty}^{t} C(t-\tau)\frac{d\varepsilon}{d\tau}d\tau. \tag{D.84}$$

A partial integration of Eq.(D.84) gives:

$$\sigma(t) = [C(t-\tau)\varepsilon(\tau)]_{-\infty}^{t} + \int_{-\infty}^{t} c(t-\tau)\varepsilon\,d\tau = C(0)\varepsilon(t) + \int_{-\infty}^{t} c(t-\tau)\varepsilon(\tau)\,d\tau, \tag{D.85}$$

where $\varepsilon(-\infty)$ tends to be zero, $c(t) \triangleq dC/dt$ and, as defined in Ref. [239], is found experimentally to be a negative and monotonically increasing function of time.

As first approximation, a generic memory function and its first derivative can be written as [239]:

$$C(t) = A_0 + A_1 e^{-\alpha_1 t}, \quad c(t) = -\alpha_1 A_1 e^{-\alpha_1 t}, \tag{D.86}$$

where A_0, A_1 and α_1 are real and positive. Substituting Eq.(D.86) into Eq.(D.85) gives:

$$\sigma(t) = C(0)\varepsilon(t) - \alpha_1 A_1 e^{-\alpha_1 t} \int_{-\infty}^{t} e^{\alpha_1 \tau} \varepsilon(\tau)\, d\tau. \tag{D.87}$$

Also, its derivative results:

$$\frac{d\sigma}{dt} = C(0)\frac{d\varepsilon}{dt} + \alpha_1^2 A_1 e^{-\alpha_1 t} \int_{-\infty}^{t} e^{\alpha_1 \tau} \varepsilon(\tau)\, d\tau - \alpha_1 A_1 \varepsilon(t), \tag{D.88}$$

where $C(0) = A_0 + A_1$. Multiplying Eq.(D.87) by α_1 and adding to Eq.(D.88) follows:

$$\alpha_1 \sigma(t) + \frac{d\sigma}{dt} = \left[\alpha_1 C(0) - \alpha_1 A_1\right]\varepsilon(t) + C(0)\frac{d\varepsilon}{dt}, \tag{D.89}$$

which can be rewritten as:

$$Y\sigma + Y^*\dot{\sigma} = E\varepsilon + E^*\dot{\varepsilon}, \tag{D.90}$$

where $E^* \triangleq (A_0 + A_1)/\alpha_1$ and $Y^* \triangleq 1/\alpha_1$ can be defined as material constants. Eq.(D.90) is known as *standard linear solid* model and was introduced by Zener and applied to estimate the damping for the fundamental mode of a uniform cantilever beam [240], [241]. Note that Eq.(D.90) includes the Voigt model as special case ($Y^* = 0$). The terms in Eq.(D.90) can be rearranged as:

$$\sigma + \tau_\varepsilon \dot{\sigma} = M_R(\varepsilon + \tau_\sigma \dot{\varepsilon}), \tag{D.91}$$

where $\tau_\varepsilon, \tau_\sigma$ are respectively the time of relaxation under condition of constant strain and stress while the *relaxed elastic moduly* $M_R = \sigma/\varepsilon$ is the final value of the ration of stress to strain when all relaxation has occurred ($\dot{\sigma}, \dot{\varepsilon} = 0$) [242].

Another important quantity can be introduced considering that in a very short time Δt the stress receives a finite increment $\Delta\sigma$. Integrating both sides of Eq. (D.91) in the time interval Δt, the quantities σ and ε tends to zero and thus:

$$\tau_\varepsilon \Delta\sigma = \tau_\sigma M_R \Delta\varepsilon. \tag{D.92}$$

It follows that:

$$\frac{\Delta\sigma}{\Delta\varepsilon} = \frac{\tau_\sigma}{\tau_\varepsilon} M_R \triangleq M_u. \tag{D.93}$$

The term M_u is called "*unrelaxed elastic moduly*" [242] and gives the relation between stress and strain when no relaxation has time to effect. The deviation between M_u and M_R from unity gives the effects of the relaxation phenomena. Solving Eq.(D.91) by using the complex response method gives:

$$\frac{\sigma(\omega)}{\varepsilon(\omega)} = \frac{1 + j\omega\tau_\sigma}{1 + j\omega\tau_\varepsilon} M_R. \tag{D.94}$$

Rearranging the formula in terms of the real and imaginary part:

$$\frac{\sigma(\omega)}{\varepsilon(\omega)} = M_R \frac{1 + \omega^2\tau_\sigma\tau_\varepsilon}{1 + (\omega\tau_\varepsilon)^2} + j\omega M_R \frac{\tau_\sigma - \tau_\varepsilon}{1 + (\omega\tau_\varepsilon)^2}, \tag{D.95}$$

and factoring by extracting the real factor it follows:

$$\frac{\sigma(\omega)}{\varepsilon(\omega)} = M_R \frac{1 + \omega^2\tau_\sigma\tau_\varepsilon}{1 + (\omega\tau_\varepsilon)^2} \left(1 + j \frac{\omega(\tau_\sigma - \tau_\varepsilon)}{1 + \omega^2\tau_\sigma\tau_\varepsilon}\right). \tag{D.96}$$

The complex term in the brackets identifies the loss factor for the Zener model:

$$\eta_z(\omega) = \frac{\omega(\tau_\sigma - \tau_\varepsilon)}{1 + \omega^2\tau_\sigma\tau_\varepsilon}. \tag{D.97}$$

Defining $\tau = \sqrt{\tau_\sigma\tau_\varepsilon}$ and $M = \sqrt{M_u M_R}$, Eq.(D.97) can be rearranged as follows:

$$\eta_z = \frac{M_u - M_r}{M} \frac{\omega\tau}{1 + (\omega\tau)^2}. \tag{D.98}$$

Eq.(D.98) can be specified for a cantilever beam [240], [241]:

$$\eta_z = \frac{\alpha^2 E\, T}{c} \frac{\omega\tau}{1+(\omega\tau)^2}, \tag{D.99}$$

where α, E, T, c are respectively the thermal coefficient, modulus of elasticity, absolute temperature, specific heat per unit of volume of the beam and:

$$\tau = \frac{h^2 c}{\pi^2 \kappa}, \tag{D.100}$$

where h, κ are the beam thickness and thermal conductivity respectively. Eq.(D.99) describes a loss mechanism due to heat, which flows from the warmed compressed fiber to the cooled tension fiber of the beam [240], [241]. It should be noted that in this model the damping loss factor η_z is maximum in correspondence of the relaxation frequency $f_0 = 1/\tau$ and decreases gradually at both higher and lower frequencies.

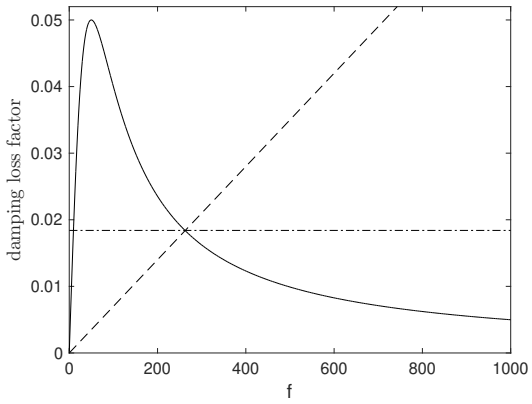

Figure D.2: Loss factor: Kelvin Voigt Model (dash line), Kimball and Lovell (dash-dotted line), Zener model (solid line).

Figure D.2 shows the frequency dependence of the loss factor for the three models proposed: Kelvin Voigt (KV), Kimball and Lovell (KL), Zener (Z).
Limiting the analysis to the 1-st natural frequency of the beam ω_n, Eq.(D.99) becomes:

$$\eta_z|_{\omega n} = \frac{\alpha^2 E\, T}{c} \frac{\omega_n\tau}{1+(\omega_n\tau)^2}, \tag{D.101}$$

From Eqs.(D.63), (D.100), ω_n and τ scales respectively as $[L^{-1}]$ and $[L^2]$ and thus from Eq. (D.101) the mechanical loss factor scales as:

$$\eta_z|_{\omega n} \propto \frac{\mathrm{L}}{1+\mathrm{L}^2}. \tag{D.102}$$

Therefore two asymptotic scaling relations can be derived:

$$\eta_z|_{\omega n} \propto L \quad \text{for } \mathrm{L} \to 0, \tag{D.103}$$

$$\eta_z|_{\omega n} \propto \frac{1}{\mathrm{L}} \quad \text{for } \mathrm{L} \to \infty, \tag{D.104}$$

indicating that the scaling loss should be characterised by a peak, centred at a specific dimension of the device. This result was experimentally investigated by Brantley [240], who studied how the damping factor of the first natural mode of four clamped cantilever beams of different scale varies with respect to their dimension. The experimental results, showed that the total damping given by the sum of two loss mechanisms, i.e. the structural material hysteresis and the joint damping, is essentially inversely proportional to the dimension of the beam:

$$\eta|_{exp} \propto [L^{-1}]. \tag{D.105}$$

Brantley [240] showed a good matching between the experimental results and the simulated results derived by Zener, but also clarified that these conclusion are valid only in the macro scale: "*the experimental results shown that caution should be used in extrapolating damping data obtained in tests of small models system since this estimation could lead gross over estimates of damping in the full-scale system*" [240].

The derivation of the scaling law for the material loss factor of a cantilever beam has required the introduction of a loss model (Zener), which is more complex to the KV and KL models. In order to reduce the mathematical complexity and tune these simple models to experimental results, the following consideration should be made. Recalling the loss factor for the KV and KL models, it follows:

$$\eta_{KV} = \frac{c_m \omega}{k}, \tag{D.106}$$

$$\eta_{KL} = \tan\phi = \text{const}, \tag{D.107}$$

which, specified in correspondence of the natural frequency ω_n of the piezoelectric harvester gives:

$$\eta_{KV}|_{\omega n} = \frac{c_m \omega_n}{k_m} = \frac{c}{\sqrt{k_m m_m}}, \tag{D.108}$$

$$\eta_{KL}|_{\omega n} = \tan\phi\,. \tag{D.109}$$

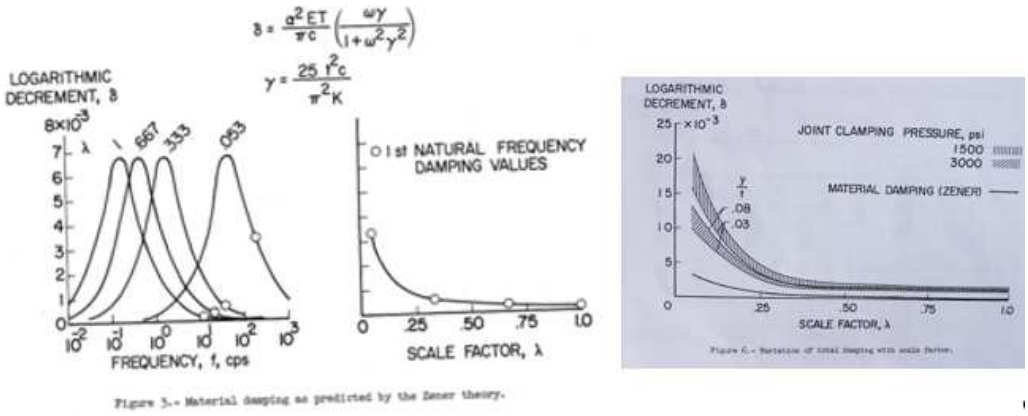

Figure D.3: Results predicted by Zener theory and experimental validation [240].

Considering KV and KL models, a dimensional dependent dashpot and loss tangent can be defined introducing the experimental loss factor $\eta|_{exp}$ obtained by Brantley:

$$\eta|_{exp} = \frac{c_m \omega_n}{k_m} = \frac{c_m}{\sqrt{k_m m_m}}, \tag{D.110}$$

$$\eta|_{exp} = \tan\phi\,. \tag{D.111}$$

As a result, the damping factor and loss tangent results:

$$c_m = \sqrt{k_m m_m}\,\eta|_{exp} \propto \sqrt{LL^3}L^{-1} = [\mathrm{L}], \tag{D.112}$$

$$\tan\phi = \eta|_{exp} \propto [L^{-1}]\,. \tag{D.113}$$

Eqs.(D.112), (D.113) represent the scaling laws of an ideal dashpot and loss tangent for KV and KL models respectively, applied to the first mode of a clamped cantilever beam. In terms of their scalability, the choice of the KV or KL damping model adopted for the lumped piezoelectric seismic harvester has no effect on the power

and efficiency results because their scaling behaviour are the same. In fact, recalling the Newton's law for both the models and assuming a steady state harmonic base excitation tuned to the natural frequency ω_n of the seismic transducer, it results:

$$f_{ext} = k_m \frac{\dot{w}}{j\omega_n} + jk_m^* \frac{\dot{w}}{j\omega_n} = k_m(1 + j\tan\phi)\frac{\dot{w}}{j\omega_n}, \tag{D.114}$$

$$f_{ext} = k_m \frac{\dot{w}}{j\omega_n} + c_m\,\dot{w}, \tag{D.115}$$

Taking into account the previous scaling results, it is straightforwardly verified that both models give the same scaling laws for the elastic and damping terms.

Table D-1: Scaling laws of the elastic and damping forces per unit of base velocity imposed

Model	Scaling law (stiffness effect)	Scaling law (damping effect)
KV	$k_m/\omega_n \propto L/L^{-1} = [L^2]$	$c_m \propto [L^1]$
KL	$k_m/\omega_n \propto L/L^{-1} = [L^2]$	$k_m \tan\phi/\omega_n \propto LL^{-1}/L^{-1} = [L^1]$

In conclusion, adopting the viscoelastic model damping of Figure 4.2 for the piezoelectric harvester and thus assuming the KV model for convenience, the damping material c_m scales proportional to the dimension i.e. $[L]$.

D.5.6 Air damping

The vibratory response of a mechanical system is dependent on many dissipative phenomena, due to internal hysteresis, joint frictions and external air damping. In particular as presented in Ref. [208], for a cantilever harvester, air damping may significantly exceed the structural damping. As discussed in Ref. [243], two simple theoretical equations can be used to describe the interaction between a vibrating cantilever beam and the surrounding fluid:

$$F_{D1} = c_a^* \dot{w}|\dot{w}|, \tag{D.116}$$

$$F_{D2} = c_a \dot{w}, \tag{D.117}$$

where F_{D1} and F_{D2} are the drug forces which acts along the beam, $\dot{w}$ is the instantaneous velocity at a certain point of the cantilever and c_a^* and c_a are parameters dependent on the beam dimension, frequency of excitation, mode shape, etc. Ref. [243] shows that in contrast to the coefficient c_a^*, that scales with the area of the beam normal to the flows, the dependency of the parameters c_a is not clearly identified.

An investigation of the free response decay time of a beam system was found by Stephens [208] and a mathematical damping relation in terms of the logarithmic decrement δ_a was proposed:

$$\delta_a = \frac{22\rho_a y A^{4/3}}{M_T}, \tag{D.118}$$

where M_T, A, are the tip mass and the surface area attached at the end of the beam and ρ_a, y are respectively the air density and the amplitude of displacement excitation. As described in Ref. [237], the log decrement for a viscous type force of the form Eq.(D.117) acting on a lumped mass spring system can be related to the loss factor η as follows:

$$\eta = \pi\delta. \tag{D.119}$$

This expression denotes the well-known relationship between the measured damping parameters under harmonic and transient response [244]. Eq.(D.119) has been identified under the hypothesis of low damping effect, i.e. $0 < \delta \leq 0.9$. Thus combining Eqs.(D.110), (D.118), (D.119) results:

$$c_a = \frac{22\pi k \rho_a y A^{4/3}}{\omega_n M_T}, \tag{D.120}$$

where k, ω_n are the flexural stiffness and the first natural frequency of cantilever beam respectively.

From Eqs.(D.63), (D.65), since the surface area A clearly scales as $[L^2]$, it follows that :

$$c_a \propto \frac{\mathrm{L}\mathrm{L}^{\frac{8}{3}}}{L^{-1}L^3} \cong [L^{1.7}], \tag{D.121}$$

suggesting that the air damping rise to the power of 1.7 .

D.5.7 Piezoelectric Capacitance

From Appendix B the capacitance of the piezoelectric harvester under constant stress and strain can be defined respectively as:

$$C_e^T = 2\bar{\varepsilon}_{33}^T \frac{bl}{h_{pe}}, \tag{D.122}$$

$$C_e^S = C_e^T(1 - k_{31}^2), \tag{D.123}$$

where $k_{31}^2 \triangleq \bar{e}_{31}^2/\left(\bar{\varepsilon}_{33}^T Y_{pe}^E\right)$ is the electromechanical coupling factor and b, l, h_{pe} are the width, length and thickness of the piezoelectric layer respectively. Since $\bar{e}_{31}$, $\bar{\varepsilon}_{33}^T$, Y_{pe}^E are constant properties of the composite layers, it follows that both capacitances scale linearly with dimension $[C_e^T] = [C_e^S] \propto [L^1]$. If the dielectric losses are taken into account a complex permittivity is introduced:

$$\varepsilon(\omega) = \varepsilon'(\omega)(1 - j\eta_e), \tag{D.124}$$

where from Appendix B.2:

$$\eta_e \triangleq tan(\delta_e) = \frac{\varepsilon''}{\varepsilon'} + \frac{\sigma_{\mathrm{pe}}}{\varepsilon'\omega} \triangleq tan(\delta_d) + \frac{\sigma_{\mathrm{pe}}}{\varepsilon'\omega} \cong \frac{\sigma_{\mathrm{pe}}}{\varepsilon'\omega}. \tag{D.125}$$

Since the scaling of the harvesters is specified for operational frequencies ω close to the natural frequency ω_n , Eq.(D.125) can be specified as :

$$\eta_e|_{\omega_n} = \frac{\sigma_{pe}}{\varepsilon'\omega_n}. \tag{D.126}$$

From Eq.(D.126) follows that the loss factor scales inversely to the natural frequency of the system and thus proportional to the scale factor L of the harvester:

$$\left[\eta_e|_{\omega_n}\right] = \left[\frac{\sigma_{\mathrm{pe}}}{\varepsilon'\omega_n}\right] \propto \frac{1}{L^0 L^{-1}} = [L^1]. \tag{D.127}$$

E

TWO PORT TRANSDUCER

E.1 ENERGY TRANSFORMER

In each system, the concepts of energy flow, storage and dissipation can be defined in terms of lumped parameter elements. These elements, usually known as *lumped one port elements* [245], form a set of blocks which are used to model and analyse the physical system under study. For an electrical or mechanical domain, three passive elements, two of which store energy (capacitance, inductance or spring and mass) and one dissipative (resistance or damper) can be defined. In addition, two active source elements (voltage and current or force and velocity) can be introduced to model the release of energy. These lumped elements are not sufficient to model every physical phenomena because the behaviour of many engineering systems are also characterised by the transfer and conversion of energy from one physical system to another (electrical motors, pumps, etc.). This process of conversion is known as transduction process and the elements that convert the energy are defined transducers. Some examples are shown in Figure E.1.

As shown in Figure E.2, the ideal transduction process that distinguish such systems, as for example those in Figure E.1, can be represented by a two-port losses element. Each port is identified by two variables. Power can flow in either side of the port.

Usually, regardless of the nature of the variables involved, the modelling of a real physical system requires the coupling of such two-port model with one or more one-port elements, necessary to account for the storage and dissipation phenomena that occurs in real transducers. Figure E.3 gives a schematic representation.

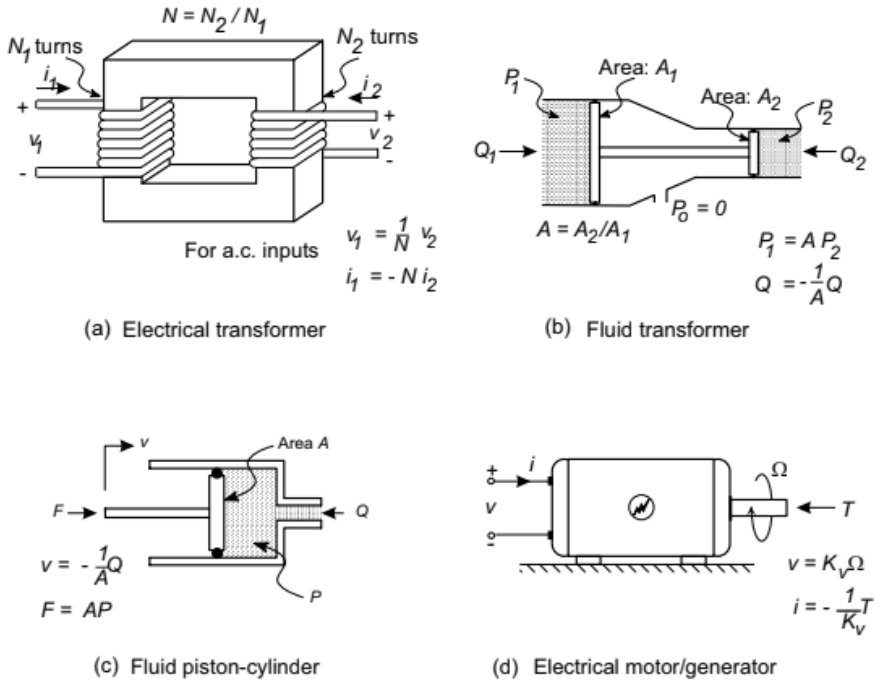

Figure E.1: Examples of two port transducers within a single energy domain (a, b) and between different energy domains (c, d) (from Ref. [245]).

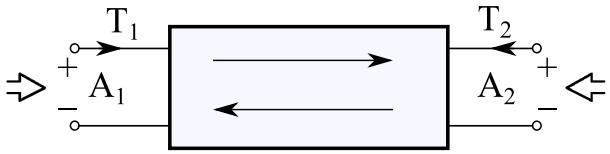

Figure E.2: Two port model representation of an ideal transformer.

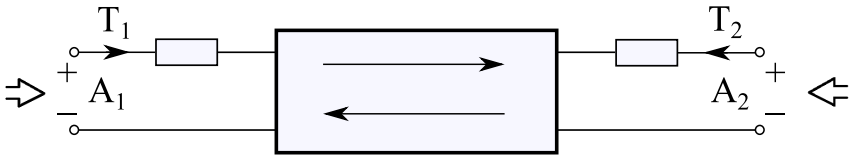

Figure E.3: Two port model representation of a real transformer.

E.1.1 Ideal Energy Transformer

The properties of an ideal transducer, which arise from a reversible linear two-port transformer shown in Figure E.2, can be summarised in the following three conditions:

1) *Linearity*: the functional operators F_A, F_B, which connect the power variables of the two-port element are linear and multiplicative in form. This is manifested by the following relation:

$$\begin{aligned} A_1 &= F_A(A_2, T_2) = c_{11}A_2 + c_{12}T_2, \\ T_1 &= F_B(A_2, T_2) = c_{21}A_2 + c_{22}T_2, \end{aligned} \tag{E.1}$$

which can be summarised in the following matrix form:

$$\begin{bmatrix} A_1 \\ T_1 \end{bmatrix} = \begin{bmatrix} c_{11}(t) & c_{12}(t) \\ c_{21}(t) & c_{22}(t) \end{bmatrix} \begin{bmatrix} A_2 \\ T_2 \end{bmatrix}. \tag{E.2}$$

Here, considering the scheme shown in Figure E.2, A_1, T_1 and A_2, T_2 are two pairs of generic trough and across variables at the ports.

2) *Losses*: no storage or dissipation phenomena take place in the transduction process.

Considering Figure E.2, the left hand side of the two port element identifies the instantaneous power which flows into the port 1, calculated as:

$$P_1(\mathrm{t}) = A_1 T_1. \tag{E.3}$$

Similarly, a net power into port 2 can be defined as follows:

$$P_2(\mathrm{t}) = A_2 T_2. \tag{E.4}$$

The losses power condition requires that the sum of the instantaneous power at the two ports must be zero:

$$P_1(\mathrm{t}) + P_2(\mathrm{t}) = 0, \tag{E.5}$$

where the power flow is defined to be *positive* in both ports.

3) *Static*: the relations between the power variables are constant and time independent.

The third condition combined with Eqs.(E.2), (E.4), (E.5) gives:

$$c_{11}c_{21}A_2^2 + c_{12}c_{22}T_2^2 + (1 + c_{11}c_{22} + c_{12}c_{21})A_2T_2 = 0. \tag{E.6}$$

Eq.(E.6) yields only two non-trivial solutions, which are respectively:

$$c_{12} = c_{21} = 0 \ \wedge \ c_{11} = -1/c_{22}, \tag{E.7}$$
$$c_{11} = c_{22} = 0 \ \wedge \ c_{12} = -1/c_{21}. \tag{E.8}$$

It should be noted that the minus sign in both Eqs.(E.7), (E.8) is related to the power convention, which is defined positive *into* both ports of the scheme in Figure E.2. Substituting Eq.(E.7) into Eq.(E.6) gives the ideal *transformer* relationship for the two port transducer:

$$\begin{bmatrix} A_1 \\ T_1 \end{bmatrix} = \begin{bmatrix} TF & 0 \\ 0 & -1/TF \end{bmatrix} \begin{bmatrix} A_2 \\ T_2 \end{bmatrix}. \tag{E.9}$$

Here $c_{11} = TF$ is defined as transformer ratio. In fact Eq.(E.9) relates the across and trough variables of both ports. Similarly, substituting Eq.(E.8) into Eq.(E.6) yields to the ideal *gyrator* relationship for the two port transducer:

$$\begin{bmatrix} A_1 \\ T_1 \end{bmatrix} = \begin{bmatrix} 0 & GY \\ -1/GY & 0 \end{bmatrix} \begin{bmatrix} A_2 \\ T_2 \end{bmatrix}. \tag{E.10}$$

Here $c_{12} = GY$ is defined as gyrator modulus. Eq.(E.10) relates the across variable of one port to the through variable of the other. Independent of the domain, Eq.(E.9) and (E.10) represent the most elementary form of power- continuous two port transducers [245]. It is easy to prove that Eqs.(E.9), (E.10) can be specified for the electromagnetic and piezoelectric transducer respectively:

$$\begin{bmatrix} f_{ext} \\ e_h \end{bmatrix} = \begin{bmatrix} 0 & -\psi_{CM} \\ \psi_{CM} & 0 \end{bmatrix} \begin{bmatrix} \dot{w} \\ i_h \end{bmatrix}, \tag{E.11}$$

$$\begin{bmatrix} f_{ext} \\ i_h \end{bmatrix} = \begin{bmatrix} 0 & -\psi_{pzt} \\ \psi_{pzt} & 0 \end{bmatrix} \begin{bmatrix} \dot{w} \\ e_h \end{bmatrix}. \tag{E.12}$$

The gyrating constant ψ_{CM} and the transformer constant ψ_{pzt} defined respectively in Eq.(E.11) and Eq.(E.12), represent the energy transduction for both actuator and generator applications. It is important to stress that the sign convention for the two transducers is consistent with the definition of positive power into both ports (Figure E.2). Thus adopting a sign convention with electrical power flowing out from the transducer as positive and mechanical power flowing into the transducer as positive, the non-trivial solutions found in Eqs.(E.7), (E.8) become:

$$c_{12} = c_{21} = 0 \ \wedge \ c_{11} = {}^{1}/_{c_{22}}, \tag{E.13}$$

$$c_{11} = c_{22} = 0 \ \wedge \ c_{12} = {}^{1}/_{c_{21}}. \tag{E.14}$$

Thus the relations in Eqs.(E.11), (E.12) turn into:

$$\begin{bmatrix} f_{ext} \\ e_h \end{bmatrix} = \begin{bmatrix} 0 & \psi_{CM} \\ \psi_{CM} & 0 \end{bmatrix} \begin{bmatrix} \dot{w} \\ i_h \end{bmatrix}, \tag{E.15}$$

$$\begin{bmatrix} f_{ext} \\ i_h \end{bmatrix} = \begin{bmatrix} 0 & \psi_{pzt} \\ \psi_{pzt} & 0 \end{bmatrix} \begin{bmatrix} \dot{w} \\ e_h \end{bmatrix}. \tag{E.16}$$

F

EQUIPMENT AND EXPERIMENTAL SETUP

This Appendix shows the experimental setups and lists the equipment used for the measurements of the electromagnetic and piezoelectric FRFs. The shaker and the transducers used in the tests were excited by a logarithmic sweep signal up to 1 KHz. The input voltage signal was fed by amplifiers and kept fixed during all measurements. All signals of interest (force, velocity, voltage, current) were acquired simultaneously (sampling frequency of 5 KHz) and then processed using the Data Physic analyser. The FRFs were obtained calculating the FFT (Fast Fourier Transform) of the input and output signals of interest. Also, the input and output channels of the Data Physic system were connected to anti-aliasing filters.

F.1 EQUIPMENT

The equipment used in the experimental tests is listed in Table F1.

Table F-1: List of the equipment used in the measurements.

No.	Equipment	Manufacturer	Model
1	ICP Impedance head	PCB	288D01
2	Shaker 1	PCB	2004E
3	Shaker 2	PCB	2075E
4	Shaker amplifier	PCB	2100E21-400
5	Quad amplifier	InterM	QD-4480
6	Signal analyser	DP Data Physics	Abacus
7	Current probe	Pico Technology	TA018

F.2 ELECTROMAGNETIC HARVESTER: EXPERIMENTAL SETUP

Figure F.1 shows the pictures of the experimental setups used to measure the base and electric impedances and the two transduction FRFs. For the base vibration tests, as shown in pictures (a b) of Figure F.1, the electromagnetic harvester was mounted on a shaker, which provided the base acceleration. The shaker was excited by a logarithmic sweep signal up to 1 KHz. This input voltage was generated by the Signal Analyser and fed through a power amplifier. For the base impedance FRF tests, the PCB impedance head mounted between the harvester and shaker was used to measure the base force and acceleration signals. When the voltage per unit velocity FRF was considered, the base acceleration and the voltage produced at the terminals of the device were measured and sent to the Data Analyser system (Abacus). The seismic harvester was kept in open circuit configuration during the two experiments.

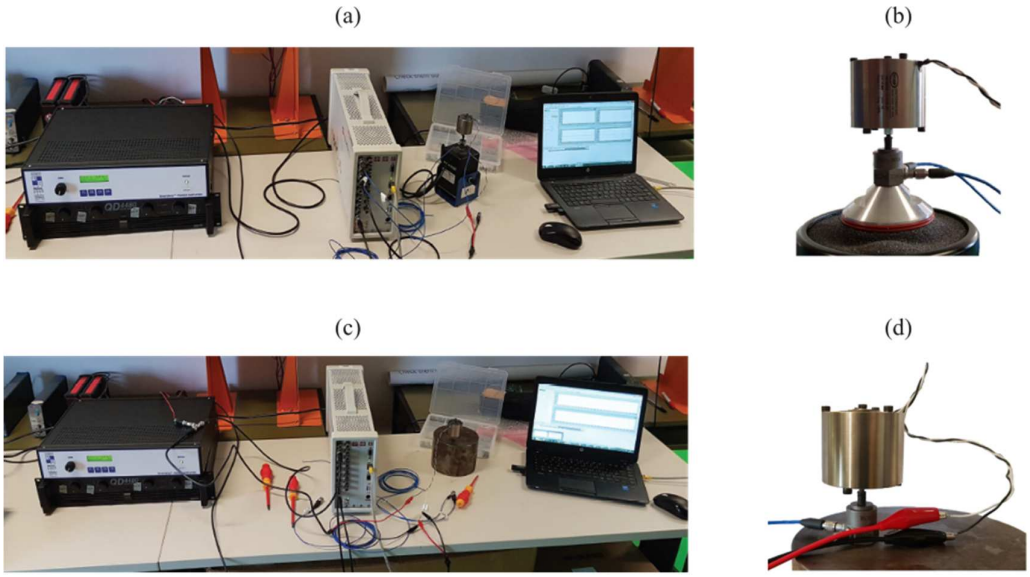

Figure F.1: Picture of the FRFs test setup: (a, b) Z_{mi}, T_{ew}, (c, d) Z_{ei}, T_{fi}

For the blocked base tests, Pictures (c, d) show that the electromagnetic harvester was attached to a rigid base and driven with an input voltage signal. The quad amplifier was used to drive the electromagnetic harvester with the logarithmic sweep signal generated by the Analyser system (Abacus). The PCB impedance head was placed between the harvester and the housing frame. For the electric impedance FRF measurement, the voltage across the terminals of the transducer and the current, which flows through the wire, were measured. For the current driven blocked force

FRF, the force exerted to the base and the current circulating in the device were aquired.

F.3 PIEZOELECTRIC HARVESTER: EXPERIMENTAL SETUP

Similarly to Figure F.1, Figure F.2 shows the pictures of the experimental setups used to measure the base and electric impedances and the two transduction FRFs of the piezoelectric transducer. The same equipment and experimental procedure than those used for the electromagnetic transducer were used and thus are not described in details.

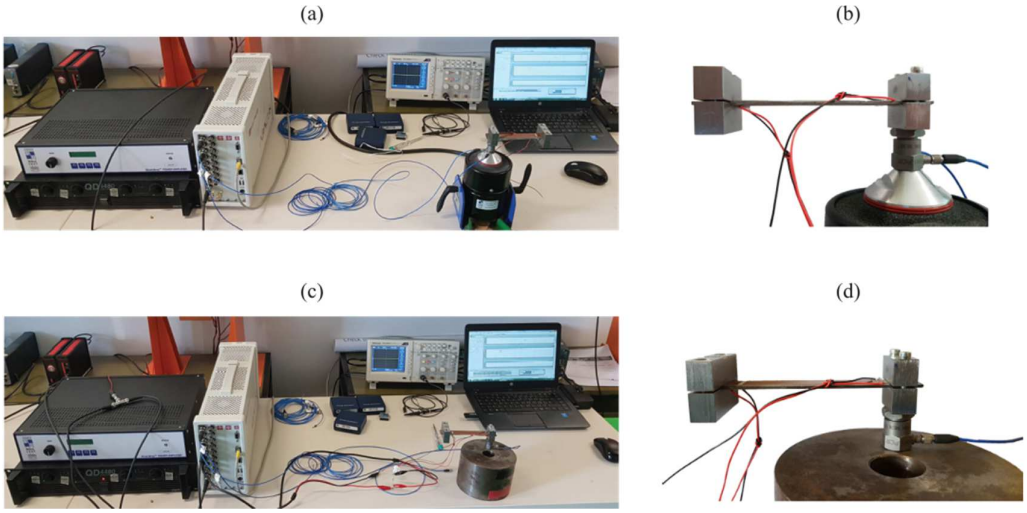

Figure F.2: Picture of the FRFs test setup: (a, b) Z_{mi}, T_{ew}, (c, d) Z_{ei}, T_{fi}

BIBLIOGRAPHY

[1] P. D. Mitcheson, E. M. Yeatman, G. K. Rao, A. S. Holmes, and T. C. Green, "Energy harvesting from human and machine motion for wireless electronic devices," *Proc. IEEE*, vol. 96, no. 9, pp. 1457–1486, 2008.

[2] P. Bauer, M. Sichitiu, R. Istepanian, and K. Premaratne, "The Mobile Patient: Wireless Distributed Sensor Networks for Patient Monitoring and Care," *2000 IEEE EMBS Int. Conf. Inf. Technol. Appl. Biomed.*, pp. 17–21, 2000.

[3] S. Leonhardt, "4th International Workshop on Wearable and Implantable Body Sensor Networks (BSN 2007)," vol. 13. Springer Berlin Heidelberg, Berlin, Heidelberg, 2007.

[4] B. Lo and G.-Z. Yang, "Key technical challenges and current implementations of body sensor networks," *Proc. 2nd Int. Work. Body Sens. Networks (BSN 2005)*, 2005.

[5] P. E. Ross, "Managing through the air," *Ieee Spectr.*, no. December, pp. 26–31, 2004.

[6] R. Fensli, E. Gunnarson, and T. Gundersen, "A Wearable ECG-recording System for Continuous Arrhythmia Monitoring in a Wireless Tele-Home-Care Situation," pp. 0–5, 2005.

[7] A. C. Voulkidis, "Energy Efficiency in Wireless Sensor Networks," vol. 5, no. 4, pp. 2795–2799, 2011.

[8] G. Asada, "Wireless Integrated Sensors Network: Low power systems on a chip," *Eur. Solid State Circuits Conf.*, 1998.

[9] P. Needham and L. Gamlyn, "Arrhythmia Analysis in the Community."

[10] K. Bult *et al.*, "Low power systems for wireless microsensors," *Proc. 1996 Int. Symp. Low Power Electron. Des.*, pp. 17–21, 1996.

[11] D. R. Tobergte and S. Curtis, "Energy Scavenging for Wireless Sensor Nodes with a Focus on Vibration to Electricity Conversion," *Clim. Chang. 2013 - Phys. Sci. Basis*, vol. 53, no. 9, pp. 1–30, 2010.

[12] J. Haase, J. Wenninger, C. Grimm, and J. Ou, "Energy Harvesting Systems," 2011, pp. 103–104.

[13] M. Niedermayer, S. Bennecke, R. Wirth, E. Armbruster, and K. Lang, "Wireless Condition Monitoring for Industrial Applications based on Radio Sensor Nodes with Energy Harvesting," *Int. J. Adv. Networks Serv.*, vol. 7, no. 3, pp. 130–137, 2014.

[14] V. C. Gungor and G. P. Hancke, "Industrial Wireless Sensor Networks: Challenges, Design Principles, and Technical Approaches," *IEEE Trans. Ind. Electron.*, vol. 56, no. 10, pp. 4258–4265, 2009.

[15] D. L. Churchill, M. J. Hamel, C. P. Townsend, and S. W. Arms, "Strain energy harvesting for wireless sensor networks," 2003, vol. 5055, p. 319.
[16] S. Kim *et al.*, "Health Monitoring of Civil Infrastructures Using Wireless Sensor Networks," in *2007 6th International Symposium on Information Processing in Sensor Networks*, 2007, pp. 254–263.
[17] J. P. Lynch, "A Summary Review of Wireless Sensors and Sensor Networks for Structural Health Monitoring," *Shock Vib. Dig.*, vol. 38, no. 2, pp. 91–128, 2006.
[18] F. Stajano, N. Hoult, I. Wassell, P. Bennett, C. Middleton, and K. Soga, "Smart bridges, smart tunnels: Transforming wireless sensor networks from research prototypes into robust engineering infrastructure," *Ad Hoc Networks*, vol. 8, no. 8, pp. 872–888, 2010.
[19] L. Doherty, B. A. Warneke, B. E. Boser, and K. S. J. Pister, "Energy and performance considerations for smart dust," *International Journal of Parallel and Distributed Systems and Networks*, vol. 4, no. 3. pp. 121–133, 2001.
[20] M. Atiquzzaman and D. Lilja, "Wireless sensor network for aircraft health monitoring," in *First International Conference on Broadband Networks*, 2004, pp. 748–750.
[21] T. Herndl, "Energy Harvesting Systems," 2011, pp. 141–142.
[22] M. Prauzek, J. Konecny, M. Borova, K. Janosova, J. Hlavica, and P. Musilek, "Energy Harvesting Sources, Storage Devices and System Topologies for Environmental Wireless Sensor Networks: A Review," *Sensors*, vol. 18, no. 8, p. 2446, 2018.
[23] V. J. Hodge, S. O. Keefe, M. Weeks, and A. Moulds, "Wireless Sensor Networks for Condition Monitoring in the Railway Industry: A Survey," *IEEE Trans. Intell. Transp. Syst.*, vol. 16, no. 3, pp. 1088–1106, 2015.
[24] P. Corke, T. Wark, R. Jurdak, W. Hu, P. Valencia, and D. Moore, "Environmental wireless sensor networks," in *Proceedings of the IEEE*, 2010, vol. 98, no. 11, pp. 1903–1917.
[25] K. H. Kwong *et al.*, "Practical considerations for wireless sensor networks in cattle monitoring applications," *Comput. Electron. Agric.*, vol. 81, pp. 33–44, 2012.
[26] M. reza Akhondi, A. Talevski, S. Carlsen, and S. Petersen, "Applications of Wireless Sensor Networks in the Oil, Gas and Resources Industries," in *2010 24th IEEE International Conference on Advanced Information Networking and Applications*, 2010, pp. 941–948.
[27] S. P. Beeby, M. J. Tudor, and N. M. White, "Energy harvesting vibration sources for microsystems applications," *Meas. Sci. Technol.*, vol. 17, no. 12, 2006.
[28] F. Karim and S. Zeadally, "Energy harvesting in wireless sensor networks : A comprehensive review," *Renew. Sustain. Energy Rev.*, vol. 55, pp. 1041–1054, 2016.
[29] M. reza Akhondi, A. Talevski, S. Carlsen, and S. Petersen, "Applications of Wireless Sensor Networks in the Oil, Gas and Resources Industries," in *2010 24th IEEE International Conference on Advanced Information Networking and*

Applications, 2010, pp. 941–948.

[30] H. A. Sodano, D. J. Inman, and G. Park, "A review of power harvesting from vibration using piezoelectric materials," *Shock Vib. Dig.*, vol. 36, no. 3, pp. 197–205, 2004.

[31] S. Roundy, D. Steingart, L. Frechette, P. Wright, and J. Rabaey, "Power Sources for Wireless Sensor Networks," pp. 1–17, 2004.

[32] M. Prauzek, J. Konecny, M. Borova, K. Janosova, J. Hlavica, and P. Musilek, "Energy Harvesting Sources, Storage Devices and System Topologies for Environmental Wireless Sensor Networks: A Review," *Sensors*, vol. 18, no. 8, p. 2446, 2018.

[33] K. A. Cook-Chennault, N. Thambi, and A. M. Sastry, "Powering MEMS portable devices - A review of non-regenerative and regenerative power supply systems with special emphasis on piezoelectric energy harvesting systems," *Smart Mater. Struct.*, vol. 17, no. 4, 2008.

[34] A. A. K. Arani, H. Karami, G. B. Gharehpetian, and M. S. A. Hejazi, "Review of Flywheel Energy Storage Systems structures and applications in power systems and microgrids," *Renew. Sustain. Energy Rev.*, vol. 69, no. September 2016, pp. 9–18, 2017.

[35] H. Louie and K. Strunz, "Superconducting Magnetic Energy Storage (SMES) for energy cache control in modular distributed hydrogen-electric energy systems," *IEEE Trans. Appl. Supercond.*, vol. 17, no. 2, pp. 2361–2364, 2007.

[36] C. Renner, "Lifetime Prediction for Supercapacitor-powered Wireless Sensor Nodes," pp. 55–58.

[37] S. R. Anton and H. A. Sodano, "A review of power harvesting using piezoelectric materials (2003-2006)," *Smart Mater. Struct.*, vol. 16, no. 3, 2007.

[38] A. Khaligh, P. Zeng, and C. Zheng, "Kinetic Energy Harvesting Using Piezoelectric and Electromagnetic Technologies ;State of the Art," *Ind. Electron. IEEE Trans.*, vol. 57, no. 3, pp. 850–860, 2010.

[39] X. Tan, Q. Li, and H. Wang, "Electrical Power and Energy Systems Advances and trends of energy storage technology in Microgrid," *Int. J. Electr. Power Energy Syst.*, vol. 44, no. 1, pp. 179–191, 2013.

[40] A. G. Olabi, "State of the art on renewable and sustainable energy," *Energy*, vol. 61, pp. 2–5, 2013.

[41] K. V. Selvan and M. S. Mohamed Ali, "Micro-scale energy harvesting devices: Review of methodological performances in the last decade," *Renew. Sustain. Energy Rev.*, vol. 54, pp. 1035–1047, 2016.

[42] P. D. Mitcheson, T. C. Green, and E. M. Yeatman, "Stresa, Italy, 26-28 April 2006 Power processing circuits for mems inertial energy scavengers," 2006, no. April, pp. 26–28.

[43] G. K. Ottman, H. F. Hofmann, A. C. Bhatt, and G. A. Lesieutre, "Adaptive piezoelectric energy harvesting circuit for wireless remote power supply," *IEEE Trans. Power Electron.*, vol. 17, no. 5, pp. 669–676, 2002.

[44] G. K. Ottman, H. F. Hofmann, and G. A. Lesieutre, "Optimized piezoelectric

energy harvesting circuit using step-down converter in discontinuous conduction mode," *IEEE Trans. Power Electron.*, vol. 18, no. 2, pp. 696–703, 2003.
[45] P. B. Koeneman, I. J. Busch-Vishniac, and K. L. Wood, "ref13 Feasibility of micro power supplies for MEMS," *J. Microelectromechanical Syst.*, vol. 6, no. 4, pp. 355–362, 1997.
[46] R. Amirtharajah and A. P. Chandrakasan, "Self-powered signal processing using vibration-based power generation," *IEEE J. Solid-State Circuits*, vol. 33, no. 5, pp. 687–695, 1998.
[47] H. a Sodano, D. J. Inman, and G. Park, "Journal of Intelligent Material Systems and Structures Comparison of Piezoelectric Energy Harvesting Devices for Recharging Batteries," vol. 16, no. 10, pp. 799–807, 2005.
[48] S. Roundy, P. K. Wright, and J. Rabaey, "A study of low level vibrations as a power source for wireless sensor nodes," *Comput. Commun.*, vol. 26, no. 11, pp. 1131–1144, 2003.
[49] J. Paradiso and T. Starner, "Human- Generated Power for Mobile Electronics," vol. 1990, pp. 45-1-45–35, 2004.
[50] T. Starner, "Human-powered-wearable-computing," *IBM Syst. J.*, vol. 35, no. 3.4, pp. 618–629, 1996.
[51] F. Akhtar and M. H. Rehmani, "Energy replenishment using renewable and traditional energy resources for sustainable wireless sensor networks: A review," *Renew. Sustain. Energy Rev.*, vol. 45, pp. 769–784, 2015.
[52] P. Kamalinejad, C. Mahapatra, Z. Sheng, S. Mirabbasi, V. C. M. Leung, and Y. L. Guan, "Wireless Energy Harvesting for Internet of Things," pp. 1–18.
[53] Jahangir Rastegar; Harbans S. Dhadwal, *Energy Harvesting for Low-Power Autonomous Devices and Systems*. 2017.
[54] J. Zhang, Z. Fang, C. Shu, J. Zhang, Q. Zhang, and C. Li, "A rotational piezoelectric energy harvester for efficient wind energy harvesting," *Sensors Actuators, A Phys.*, vol. 262, pp. 123–129, 2017.
[55] F. Mendonça, "Design and power production of small-scale wind turbines," 2017, pp. 3–8.
[56] D. Pimentel, P. Musilek, A. Knight, and J. Heckenbergerova, "Characterization of a Wind Flutter Generator."
[57] A. Baranov, D. Spirjakin, S. Akbari, A. Somov, and R. Passerone, "Sensors and Actuators A : Physical POCO : Perpetual ' operation of CO wireless sensor node with hybrid power supply," *Sensors Actuators A. Phys.*, vol. 238, pp. 112–121, 2016.
[58] J. D. Hobeck and D. J. Inman, "Artificial piezoelectric grass for energy harvesting from turbulence-induced vibration," *Smart Mater. Struct.*, vol. 21, no. 10, 2012.
[59] P. V. Amoli, "An Overview on Current Researches on Underwater Sensor Networks: Applications, Challenges and Future Trends," *Int. J. Electr. Comput. Eng.*, vol. 6, no. 3, p. 955, 2016.
[60] S. Ozeri and D. Shmilovitz, "Ultrasonic transcutaneous energy transfer for

powering implanted devices," *Ultrasonics*, vol. 50, no. 6, pp. 556–566, 2010.

[61] T. von Buren, P. Lukowicz, and G. Troster, "Kinetic Energy Powered Computing - An Experimental Feasibility Study," in *Seventh IEEE International Symposium on Wearable Computers, 2003.*, 2003, pp. 3–5.

[62] S. Roundy, "On the effectiveness of vibration-based energy harvesting," *J. Intell. Mater. Syst. Struct.*, vol. 16, no. 10, pp. 809–823, 2005.

[63] Y. Naruse, N. Matsubara, K. Mabuchi, M. Izumi, and S. Suzuki, "Electrostatic micro power generation from low-frequency vibration such as human motion," *J. Micromechanics Microengineering*, vol. 19, no. 9, 2009.

[64] A. T. Mineto, M. Pereira, D. S. Braun, and E. Harvesting, "Modeling of a cantilever beam for piezoelectric energy harvesting," *Dincon'10*, pp. 599–605, 2010.

[65] M. Rosa and C. D. M. Junior, "Modeling and Analysis of a Piezoelectric Energy Harvester with Varying Cross-Sectional Area," vol. 2014, 2014.

[66] P. D. Mitcheson, T. T. Toh, K. H. Wong, S. G. Burrow, and A. S. Holmes, "Tuning the Resonant Frequency and Damping of an Electromagnetic Energy Harvester Using Power Electronics," *Ieee Trans. Circuits Syst. Ii-Express Briefs*, vol. 58, no. 12, pp. 792–796, 2011.

[67] S. D. Moss, O. R. Payne, G. A. Hart, and C. Ung, "Scaling and power density metrics of electromagnetic vibration energy harvesting devices," *Smart Mater. Struct.*, vol. 24, no. 2, 2015.

[68] M. El-hami *et al.*, "Design and fabrication of a new vibration-based electromechanical power generator," *Sensors Actuators, A Phys.*, vol. 92, no. 1–3, pp. 335–342, 2001.

[69] Smart-Material, "Macro Fiber Composite (MFC)." p. 8, 2014.

[70] R. T. Aljadiri, L. Y. Taha, and P. Ivey, "Electrostatic Energy Harvesting Systems: A Better Understanding of Their Sustainability Electrostatic Energy Harvesting Systems: A Better Understanding of Their Sustainability," *J. Clean Energy Technol.*, vol. 5, no. 5, pp. 409–416, 2017.

[71] J. Siang, M. H. Lim, and M. Salman Leong, "Review of vibration-based energy harvesting technology: Mechanism and architectural approach," *Int. J. Energy Res.*, vol. 42, no. 5, pp. 1866–1893, 2018.

[72] A. Erturk and D. J. Inman, *Piezoelectric Energy Harvesting*. 2011.

[73] C. Gonsalez, V. Franco, M. Brennan, and S. Da Silva, "Energy Harvesting Using Piezoelectric and Electromagnetic Transducers," *Sbmac.Locaweb.Com.Br*, no. July 2015, pp. 1166–1171, 2007.

[74] D. P. Arnold, "Review of microscale magnetic power generation," *IEEE Trans. Magn.*, vol. 43, no. 11, pp. 3940–3951, 2007.

[75] G. Wang and Y. Lu, "An Improved Lumped Parameter Model for a Piezoelectric Energy Harvester in Transverse Vibration," *Shock Vib.*, vol. 2014, pp. 1–12, 2014.

[76] D. Spreemann and Y. Manoli, *Electromagnetic Vibration Energy Harvesting Devices*. 2012.

[77] S. Naifar, S. Bradai, C. Viehweger, and O. Kanoun, "Survey of electromagnetic and magnetoelectric vibration energy harvesters for low frequency excitation," *Meas. J. Int. Meas. Confed.*, vol. 106, pp. 251–263, 2017.
[78] H. A. Sodano, D. J. Inman, and G. Park, "Comparison of piezoelectric energy harvesting devices for recharging batteries," *J. Intell. Mater. Syst. Struct.*, vol. 16, no. 10, pp. 799–807, 2005.
[79] M. Friswell and S. Adhikari, "Sensor design for piezoelectric cantilever beam energy harvesters," *2010 Southampt. Conf.*, 2010.
[80] E. S. Leland and P. K. Wright, "Resonance tuning of piezoelectric vibration energy scavenging generators using compressive axial preload," *Smart Mater. Struct.*, vol. 15, no. 5, pp. 1413–1420, 2006.
[81] Z. Yang, S. Zhou, J. Zu, and D. Inman, "High-Performance Piezoelectric Energy Harvesters and Their Applications," *Joule*, vol. 2, no. 4, pp. 642–697, 2018.
[82] D. Spreemann, B. Folkmer, D. Mintenbeck, and Y. Manoli, "Novel non-resonant vibration transducer for energy harvesting," *Power MEMS*, pp. 144–146, 2005.
[83] R. Caliò *et al.*, "Piezoelectric Energy Harvesting Solutions," *Sensors*, vol. 14, no. 3, pp. 4755–4790, 2014.
[84] C. B. Williams and R. B. Yates, "Analysis of a micro-electric generator for microsystems, *Sensors and Actuators*, vol. 52, pp. 8–11, 1996.
[85] T. Sterken, K. Baert, C. Vanhoof, R. Puers, G. Borghs, and P. Fiorini, "Comparative modelling for vibration scavengers," *Proc. IEEE Sensors, 2004.*, pp. 1249–1252, 2004.
[86] N. G. Stephen, "On energy harvesting from ambient vibration," *J. Sound Vib.*, vol. 293, no. 1–2, pp. 409–425, May 2006.
[87] M. Hendijanizadeh, "Design and optimisation of constrained electromagnetic energy harvesting devices," University of Southampton, 2014.
[88] A. Erturk and D. J. Inman, "Issues in mathematical modeling of piezoelectric energy harvesters," *Smart Mater. Struct.*, vol. 17, no. 6, 2008.
[89] *L. Meirovitch, Fundamentals_of_Vibrations* .
[90] H. A. Sodano, D. J. Inman, and G. Park, "Estimation of Electric Charge output for Piezoelectric Energy Harvesting," vol. 40, no. 2, pp. 49–58, 2004.
[91] N. E. DuToit, B. L. Wardle, and S. G. Kim, "Design considerations for MEMS-scale piezoelectric mechanical vibration energy harvesters," *Integr. Ferroelectr.*, vol. 71, pp. 121–160, 2005.
[92] L. Dal Bo and P. Gardonio, "Comparison between electromagnetic and piezoelectric seismic vibration energy harvesters," *Proc. Int. Conf. Noise Vib. Eng. ISMA2016*, pp. 681–694, 2016.
[93] L. Dal Bo and P. Gardonio, "Energy harvesting with electromagnetic and piezoelectric seismic transducers: Unified theory and experimental validation," *J. Sound Vib.*, vol. 433, pp. 385–424, 2018.
[94] M. N. Fakhzan and A. G. A. Muthalif, "Harvesting vibration energy using piezoelectric material: Modeling, simulation and experimental verifications,"

Mechatronics, vol. 23, no. 1, pp. 61–66, 2013.

[95] H. A. Sodano, G. Park, D. J. Leo, and D. J. Inman, "Model of Piezoelectric Power Harvesting Beam," *Proc. IMECE'03*, pp. 345–354, 2003.

[96] K. Nakano, S. J. Elliott, and E. Rustighi, "A unified approach to optimal conditions of power harvesting using electromagnetic and piezoelectric transducers," *Smart Mater. Struct.*, vol. 16, no. 4, pp. 948–958, 2007.

[97] S. Shimose, K. Makihara, and J. Onoda, "Equivalent Circuit Modeling of Piezoelectric Energy Harvesters," vol. 2013, 2013.

[98] N. G. Elvin and A. A. Elvin, "A coupled finite element circuit simulation model for analyzing piezoelectric energy generators," *J. Intell. Mater. Syst. Struct.*, vol. 20, no. 5, pp. 587–595, 2009.

[99] S. Boisseau, G. Despesse, and B. a. Seddik, "Adjustable nonlinear springs to improve efficiency of vibration energy harvesters," *arXiv:1207.4559*, 2012.

[100] A. H. Nayfeh and D. T. Mook, "Nonlinear Oscillations," p. 720, 1985.

[101] M. Kulik and M. Jagieła, "Harvesting mechanical vibrations energy using nonlinear electromagnetic minigenerators – a survey of concepts," no. 90, 2017.

[102] S. P. Beeby *et al.*, "A comparison of power output from linear and nonlinear kinetic energy harvesters using real vibration data," *Smart Mater. Struct.*, vol. 22, no. 7, 2013.

[103] R. Masana and M. F. Daqaq, "Relative performance of a vibratory energy harvester in mono- and bi-stable potentials," *J. Sound Vib.*, vol. 330, no. 24, pp. 6036–6052, 2011.

[104] S. C. Stanton, B. A. M. Owens, and B. P. Mann, "Harmonic balance analysis of the bistable piezoelectric inertial generator," *J. Sound Vib.*, vol. 331, no. 15, pp. 3617–3627, 2012.

[105] L. Tang and Y. Yang, "A nonlinear piezoelectric energy harvester with magnetic oscillator," *Appl. Phys. Lett.*, vol. 101, no. 9, 2012.

[106] M. BOROWIEC *et al.*, "Energy Harvesting in Piezoelastic Systems Driven By Random Excitations," *Int. J. Struct. Stab. Dyn.*, vol. 13, no. 07, p. 1340006, 2013.

[107] M. Ghandchi Tehrani and S. J. Elliott, "Extending the dynamic range of an energy harvester using nonlinear damping," *J. Sound Vib.*, vol. 333, no. 3, pp. 623–629, 2014.

[108] B. P. Mann and B. A. Owens, "Investigations of a nonlinear energy harvester with a bistable potential well," *J. Sound Vib.*, vol. 329, no. 9, pp. 1215–1226, 2010.

[109] B. P. Mann and N. D. Sims, "Energy harvesting from the nonlinear oscillations of magnetic levitation," *J. Sound Vib.*, vol. 319, no. 1–2, pp. 515–530, 2009.

[110] G. Sebald, H. Kuwano, D. Guyomar, and B. Ducharne, "Experimental Duffing oscillator for broadband piezoelectric energy harvesting," *Smart Mater. Struct.*, vol. 20, no. 10, 2011.

[111] D. S. Ibrahim, A. G. A. Muthalif, and T. Saleh, "Piezoelectric based vibration energy harvester with tip attraction magnetic force : modeling and simulation," *Math. Comput. Sci. Ind.*, pp. 80–86, 2014.

[112] X. Dai, Y. Wen, P. Li, J. Yang, and G. Zhang, "Sensors and Actuators A :

Physical Modeling, characterization and fabrication of vibration energy harvester using Terfenol-D / PZT / Terfenol-D composite transducer," vol. 156, 2009, pp. 350–358.

[113] P. L. Green, K. Worden, and N. D. Sims, "On the identification and modelling of friction in a randomly excited energy harvester," in *Journal of Sound and Vibration*, 2013, vol. 332, no. 19, pp. 4696–4708.

[114] R. S. Langley, "A general mass law for broadband energy harvesting," *J. Sound Vib.*, vol. 333, no. 3, pp. 927–936, 2014.

[115] O. Of, T. Mass, and F. O. R. I. Excitation, "Feasibility study on energy harvesting using stochastic resonance," 2013, no. July, p. 2013.

[116] A. Erturk, J. Hoffmann, and D. J. Inman, "A piezomagnetoelastic structure for broadband vibration energy harvesting," *Appl. Phys. Lett.*, vol. 94, no. 25, pp. 128–130, 2009.

[117] A. Erturk and D. J. Inman, "Broadband piezoelectric power generation on high-energy orbits of the bistable Duffing oscillator with electromechanical coupling," *J. Sound Vib.*, vol. 330, no. 10, pp. 2339–2353, 2011.

[118] S. C. Stanton, C. C. McGehee, and B. P. Mann, "Nonlinear dynamics for broadband energy harvesting: Investigation of a bistable piezoelectric inertial generator," *Phys. D Nonlinear Phenom.*, vol. 239, no. 10, pp. 640–653, 2010.

[119] M. Ferrari, V. Ferrari, M. Guizzetti, B. Andò, S. Baglio, and C. Trigona, "Improved energy harvesting from wideband vibrations by nonlinear piezoelectric converters," *Sensors Actuators, A Phys.*, vol. 162, no. 2, pp. 425–431, 2010.

[120] S. Adhikari, M. I. Friswell, and D. J. Inman, "Piezoelectric energy harvesting from broadband random vibrations," *Smart Mater. Struct.*, vol. 18, no. 11, 2009.

[121] F. Cottone, L. Gammaitoni, H. Vocca, M. Ferrari, and V. Ferrari, "Piezoelectric buckled beams for random vibration energy harvesting," *Smart Mater. Struct.*, vol. 21, no. 3, 2012.

[122] M. J. Brennan, B. Tang, G. P. Melo, and V. Lopes, "An investigation into the simultaneous use of a resonator as an energy harvester and a vibration absorber," *J. Sound Vib.*, vol. 333, no. 5, pp. 1331–1343, 2014.

[123] N. Elvin and A. Erturk, "Broadband Vibration Energy Harvesting Techniques," in *Advances in Energy Harvesting Methods*, vol. 9781461457, 2013, pp. 1–455.

[124] D. Zhu, M. J. Tudor, and S. P. Beeby, "Strategies for increasing the operating frequency range of vibration energy harvesters: A review," *Meas. Sci. Technol.*, vol. 21, no. 2, 2010.

[125] T. Yildirim, M. H. Ghayesh, W. Li, and G. Alici, "A review on performance enhancement techniques for ambient vibration energy harvesters," *Renew. Sustain. Energy Rev.*, vol. 71, no. July 2015, pp. 435–449, 2017.

[126] V. R. Challa, M. G. Prasad, Y. Shi, and F. T. Fisher, "A vibration energy harvesting device with bidirectional resonance frequency tunability," *Smart Mater. Struct.*, vol. 17, no. 1, 2008.

[127] J. L. Kaplan, P. Bonello, and M. Alalwan, "A simulation of the performance of a self-tuning energy harvesting cantilever beam," *J. Phys. Conf. Ser.*, vol. 744, no. 1, 2016.

[128] H. Shen *et al.*, "A low-power circuit for piezoelectric vibration control by synchronized switching on voltage sources," *Sensors Actuators, A Phys.*, vol. 161, no. 1–2, pp. 245–255, 2010.

[129] Y. C. Shu, I. C. Lien, and W. J. Wu, "An improved analysis of the SSHI interface in piezoelectric energy harvesting," *Smart Mater. Struct.*, vol. 16, no. 6, pp. 2253–2264, 2007.

[130] Y. Wang and D. J. Inman, "A survey of control strategies for simultaneous vibration suppression and energy harvesting via piezoceramics," *J. Intell. Mater. Syst. Struct.*, vol. 23, no. 18, pp. 2021–2037, 2012.

[131] X. Cao, W. J. Chiang, Y. C. King, and Y. K. Lee, "Electromagnetic energy harvesting circuit with feedforward and feedback dc-dc PWM boost converter for vibration power generator system," *IEEE Trans. Power Electron.*, vol. 22, no. 2, pp. 679–685, 2007.

[132] P. By, "World ' s largest Science , Technology & Medicine Open Access book publisher Piezoelectric material-based energy harvesting devices : advances of SSH optimization."

[133] E. Lefeuvre, A. Badel, C. Richard, L. Petit, and D. Guyomar, "A comparison between several vibration-powered piezoelectric generators for standalone systems," *Sensors Actuators, A Phys.*, vol. 126, no. 2, pp. 405–416, 2006.

[134] D. Guyomar and M. Lallart, "Mechanical to electrical energy conversion enhancement and self- powered wireless applications," *Energy*, pp. 1–15, 2003.

[135] M. Lallart and D. Guyomar, "Self-Powered and Low-Power Piezoelectric Vibration Control Using Nonlinear Approaches," in *Vibration Control*, no. September, 2010.

[136] A. M. Wickenheiser and E. Garcia, "Power optimization of vibration energy harvesters utilizing passive and active circuits," *J. Intell. Mater. Syst. Struct.*, vol. 21, no. 13, pp. 1343–1361, 2010.

[137] S. Roundy and P. K. Wright, "A piezoelectric vibration based generator for wireless electronics," *Smart Mater. Struct.*, vol. 13, no. 5, pp. 1131–1142, 2004.

[138] D. Guyomar and M. Lallart, "Recent progress in piezoelectric conversion and energy harvesting using nonlinear electronic interfaces and issues in small scale implementation," *Micromachines*, vol. 2, no. 2, pp. 274–294, 2011.

[139] M. Anthony, B. Scott, and P. Shashank, "Multiple cell configuration electromagnetic vibration energy harvester," *J. Phys. D. Appl. Phys.*, vol. 44, no. 29, p. 295501, 2011.

[140] S. P. Beeby *et al.*, "A micro electromagnetic generator for vibration energy harvesting," *J. Micromechanics Microengineering*, vol. 17, no. 7, pp. 1257–1265, 2007.

[141] I. L. Cassidy, J. T. Scruggs, and S. Behrens, "Design of electromagnetic energy harvesters for large-scale structural vibration applications," vol. 7977, no. 919,

p. 79770P, 2011.
[142] R. R. Fabio Casciati, "A power harvester for wireless sensing applications," *Struct. Control Heal. Monit.*, vol. 19, no. 1, pp. 88–106, 2011.
[143] I. Sari, T. Balkan, and H. Kulah, "An electromagnetic micro power generator for wideband environmental vibrations," vol. 146, pp. 405–413, 2008.
[144] E. M. Yeatman, P. D. Mitcheson, and A. S. Holmes, "Micro-engineered devices for motion energy harvesting," *Tech. Dig. - Int. Electron Devices Meet. IEDM*, pp. 375–378, 2007.
[145] W. Shen, S. Zhu, H. Zhu, and Y. L. Xu, "Electromagnetic energy harvesting from structural vibrations during earthquakes," *Smart Struct. Syst.*, vol. 18, no. 3, pp. 449–470, 2016.
[146] L. Simeone, M. G. Tehrani, and S. Elliott, "Level-dependent load in a pendulum like energy harvester," *Mech. Syst. Signal Process.*, vol. 119, pp. 244–254, 2019.
[147] H. J. Jung, I. H. Kim, and S. J. Jang, "An energy harvesting system using the wind-induced vibration of a stay cable for powering a wireless sensor node," *Smart Mater. Struct.*, vol. 20, no. 7, 2011.
[148] P. D. Mitcheson, T. C. Green, E. M. Yeatman, and A. S. Holmes, "Architectures for vibration-driven micropower generators," *J. Microelectromechanical Syst.*, vol. 13, no. 3, pp. 429–440, 2004.
[149] P. D. Mitcheson, E. K. Reilly, T. Toh, P. K. Wright, and E. M. Yeatman, "Performance limits of the three MEMS inertial energy generator transduction types," in *Journal of Micromechanics and Microengineering*, 2007, vol. 17, no. 9.
[150] C. Serre *et al.*, "Design and implementation of mechanical resonators for optimized inertial electromagnetic microgenerators," *Microsyst. Technol.*, vol. 15, no. 8, pp. 1217–1223, 2009.
[151] A. Wickenheiser, "Analysis of Energy Harvesting Using Frequency Up-Conversion by Analytic Approximations," *Small-scale Energy Harvest.*, 2012.
[152] G. Poulin, E. Sarraute, and F. Costa, "Generation of electrical energy for portable devices: Comparative study of an electromagnetic and a piezoelectric system," *Sensors Actuators, A Phys.*, vol. 116, no. 3, pp. 461–471, 2004.
[153] F. Khameneifar, M. Moallem, and S. Arzanpour, "Modeling and Analysis of a Piezoelectric Energy Scavenger for Rotary Motion Applications," *J. Vib. Acoust.*, vol. 133, no. 1, p. 011005, 2011.
[154] J. D. Hobeck and D. J. Inman, "The dynamics of large arrays of flexible structures in fluid flow with applications to energy harvesting," in *International Conference on Noise and Vibration Engineering 2012, ISMA 2012, including USD 2012: International Conference on Uncertainty in Structure Dynamics*, 2012, vol. 2, pp. 1301–1308.
[155] X. D. Xie, Q. Wang, and N. Wu, "Potential of a piezoelectric energy harvester from sea waves," *J. Sound Vib.*, vol. 333, no. 5, pp. 1421–1429, 2014.
[156] P. Gardonio and M. Zilletti, "Vibration energy harvesting from an array of flexible stalks exposed to airflow: A theoretical study," *Smart Mater. Struct.*, vol. 25, no. 3, p. 0, 2016.

[157] N. G. Elvin, N. Lajnef, and A. A. Elvin, "Feasibility of structural monitoring with vibration powered sensors," *Smart Mater. Struct.*, vol. 15, no. 4, pp. 977–986, 2006.

[158] A. H. Alameh, M. Gratuze, M. Y. Elsayed, and F. Nabki, "Effects of proof mass geometry on piezoelectric vibration energy harvesters," *Sensors (Switzerland)*, vol. 18, no. 5, 2018.

[159] S. L. Kok, N. M. White, and N. R. Harris, "Fabrication and characterization of free-standing thick-film piezoelectric cantilevers for energy harvesting," *Proc. - IEEE Ultrason. Symp.*, vol. 20, 2009.

[160] R. J. Wood, E. Steltz, and R. S. Fearing, "Optimal energy density piezoelectric bending actuators," *Sensors Actuators A Phys.*, vol. 119, no. 2, pp. 476–488, 2005.

[161] R. Elfrink *et al.*, "Vibration energy harvesting with aluminium nitride-based piezoelectric devices," pp. 249–252, 2008.

[162] T. Note, "TECHNICAL NOTE A novel thick-film piezoelectric micro-generator," vol. 10, pp. 850–852, 2001.

[163] M. R. Sarker, A. Mohamed, and R. Mohamed, "Develop A Vibration Based MEMS Piezoelectric Energy Harvester Using Micro Cantilever Beam," *Int. J. Appl. Eng. Res. ISSN 0973-4562*, vol. 11, no. 5, pp. 3421–3426, 2016.

[164] J. Briscoe and S. Dunn, "Piezoelectric nanogenerators - a review of nanostructured piezoelectric energy harvesters," *Nano Energy*, vol. 14, pp. 15–29, 2014.

[165] Y. B. Jeon, R. Sood, J. H. Jeong, and S. G. Kim, "MEMS power generator with transverse mode thin film PZT," *Sensors Actuators, A Phys.*, vol. 122, no. 1 SPEC. ISS., pp. 16–22, 2005.

[166] S. Boisseau, G. Despesse, and B. Ahmed, "Electrostatic Conversion for Vibration Energy Harvesting," *Small-Scale Energy Harvest.*, pp. 1–39, 2012.

[167] R. Guillemet, P. Basset, D. Galayko, and T. Bourouina, "Combined optimization of electrical and mechanical parameters of in-plane and out-of-plane gap-closing electrostatic Vibration Energy Harvesters (VEHs)," *Procedia Eng.*, vol. 5, pp. 1172–1175, 2010.

[168] P. Miao, a S. Holmes, E. M. Yeatman, and T. C. Green, "Micro-Machined Variable Capacitors for Power Generation," in *Electrostatics*, 2003, no. 178, pp. 53–58.

[169] E. Halvorsen *et al.*, "An electrostatic energy harvester with electret bias," *TRANSDUCERS 2009 - 15th Int. Conf. Solid-State Sensors, Actuators Microsystems*, pp. 1381–1384, 2009.

[170] D. B. Hiemstra, G. Parmar, and S. Awtar, "Performance tradeoffs posed by moving magnet actuators in flexure-based nanopositioning," *IEEE/ASME Trans. Mechatronics*, vol. 19, no. 1, pp. 201–212, 2014.

[171] M. F. Daqaq, R. Masana, A. Erturk, and D. Dane Quinn, "On the Role of Nonlinearities in Vibratory Energy Harvesting: A Critical Review and Discussion," *Appl. Mech. Rev.*, vol. 66, no. 4, p. 040801, 2014.

[172] M. I. Friswell, S. F. Ali, O. Bilgen, S. Adhikari, A. W. Lees, and G. Litak, "Non-

linear piezoelectric vibration energy harvesting from a vertical cantilever beam with tip mass," *J. Intell. Mater. Syst. Struct.*, vol. 23, no. 13, pp. 1505–1521, 2012.
[173] C. R. McInnes, D. G. Gorman, and M. P. Cartmell, "Enhanced vibrational energy harvesting using nonlinear stochastic resonance," *J. Sound Vib.*, vol. 318, no. 4–5, pp. 655–662, 2008.
[174] H. A. Sodano, J. S. Bae, D. J. Inman, and W. Keith Belvin, "Concept and model of eddy current damper for vibration suppression of a beam," *J. Sound Vib.*, vol. 288, no. 4–5, pp. 1177–1196, 2005.
[175] J. S. Bae, J. H. Hwang, J. S. Park, and D. G. Kwag, "Modeling and experiments on eddy current damping caused by a permanent magnet in a conductive tube," *J. Mech. Sci. Technol.*, vol. 23, no. 11, pp. 3024–3035, 2010.
[176] P. Paul, C. Ingale, and B. Bhattacharya, "Design of a vibration isolation system using eddy current damper," *Proc. Inst. Mech. Eng. Part C J. Mech. Eng. Sci.*, vol. 228, no. 4, pp. 664–675, 2014.
[177] W. M. Leach Jr., "Loudspeaker Voice-Coil Inductance Losses: CircuitModels, Parameter Estimation, and Effect on Frequency Response," *J. Audio Eng. Soc.*, vol. 50, no. 6, pp. 442–449, 2002.
[178] W. M. Leach Jr., *Introduction to Electroacoustics and Audio Amplifiers Design*. 2010.
[179] J. Vanderkooy, "A Model of Loudspeaker Driver Impedance Incorporating Eddy Currents in the Pole Structure." Audio Engineering Society, 01-Mar-1988.
[180] S. Sherrit and B. K. B. K. Mukherjee, "Characterization of Piezoelectric Materials for Transducers," *arXiv*, vol. arXiv:0711, no. Nye, p. 45, 2007.
[181] T. L. Jordan and N. Langley, "Piezoelectric Ceramics Characterization," *ICASE*. p. 23, 2001.
[182] C. H. Park, "On the Circuit Model of Piezoceramics," *J. Intell. Mater. Syst. Struct.*, vol. 12, no. 7, pp. 515–522, Jul. 2001.
[183] M. Karpelson, G. Y. Wei, and R. J. Wood, "Driving high voltage piezoelectric actuators in microrobotic applications," *Sensors Actuators, A Phys.*, vol. 176, pp. 78–89, 2012.
[184] A. Preumont, *Mechatronics: Dynamics of electromechanical and piezoelectric systems*, vol. 136. 2006.
[185] F. V. Hunt, *Electroacoustics : the analysis of transduction, and its background*. American Institute of Physics, 1982.
[186] S. Crandall, "Dynamics of mechanical and electromechanical systems," 1968.
[187] A. Preumont, *Mechatronics*. 2006.
[188] L. Beranek and T. Mellow, *Acoustics: sound fields and transducers*. 2012.
[189] Charles B. Bright, "Sensors - June 2001 - Energy Coupling and Efficiency," 2018.
[190] C. González Díaz, C. Paulitsch, and P. Gardonio, "Active damping control unit using a small scale proof mass electrodynamic actuator," *J. Acoust. Soc. Am.*, vol. 124, no. 2, pp. 886–897, Aug. 2008.
[191] J. Rohlfing, P. Gardonio, and S. J. Elliott, "Base impedance of velocity feedback control units with proof-mass electrodynamic actuators," *J. Sound Vib.*, vol. 330, no. 20, pp. 4661–4675, Sep. 2011.

[192] P. Gardonio and D. Casagrande, "Shunted piezoelectric patch vibration absorber on two-dimensional thin structures: Tuning considerations," *J. Sound Vib.*, vol. 395, pp. 26–47, 2017.
[193] R. Ramlan, M. J. Brennan, B. R. MacE, and I. Kovacic, "Potential benefits of a non-linear stiffness in an energy harvesting device," *Nonlinear Dyn.*, vol. 59, no. 4, pp. 545–558, 2010.
[194] M. Hendijanizadeh, S. M. Sharkh, S. J. Elliott, and M. Moshrefi-Torbati, "Output power and efficiency of electromagnetic energy harvesting systems with constrained range of motion," *Smart Mater. Struct.*, vol. 22, no. 12, pp. 1–16, 2013.
[195] C. Desoer, "The maximum power transfer theorem for n-ports," *IEEE Trans. Circuit Theory*, vol. 20, no. 3, pp. 328–330, 1973.
[196] L. Dal Bo and P. Gardonio, "Vibration energy harvesting with electromagnetic and piezoelectric seismic transducers: Simulation and experimental results," in *8th Conference on Smart Structures and Materials, SMART 2017 and 6th International Conference on Smart Materials and Nanotechnology in Engineering, SMN 2017*, 2017, vol. 2017–Janua.
[197] M. I. Friswell and S. Adhikari, "Sensor shape design for piezoelectric cantilever beams to harvest vibration energy," *J. Appl. Phys.*, vol. 108, no. 1, 2010.
[198] M. O. E. H. S. Laugesen, "Bias errors in measurement of vibratory power and implication for active control of structural vibration," 1997.
[199] L. Zuo and X. Tang, "Large-scale vibration energy harvesting," vol. 24, no. 11, pp. 1405–1430, 2013.
[200] M. J. Madou, *Fundamentals of microfabrication : the science of miniaturization*. CRC Press, 2002.
[201] by William Trimmer, "Scaling Physical Laws, Behavior at Large and Small Scales," 1989.
[202] D. J. Acheson, *Elementary fluid dynamics*. Clarendon Press, 1990.
[203] S. J. Elliott and M. Zilletti, "Scaling of electromagnetic transducers for shunt damping and energy harvesting," *J. Sound Vib.*, vol. 333, no. 8, pp. 2185–2195, Apr. 2014.
[204] P. Gardonio and C. González Díaz, "Downscaling of proof mass electrodynamic actuators for decentralized velocity feedback control on a panel," *Smart Mater. Struct.*, vol. 19, no. 2, p. 025004, Feb. 2010.
[205] S. S. Rao, *Mechanical Vibrations*, vol. 67. 2010.
[206] T. O'Donnell, C. Saha, S. Beeby, and J. Tudor, "Scaling effects for electromagnetic vibrational power generators," *Microsyst. Technol.*, no. April, pp. 26–28, 2007.
[207] O. Cugat, J. Delamare, and G. Reyne, "Magnetic micro-actuators and systems (MAGMAS)," in *Magnetics, IEEE Transactions on*, 2003, vol. 39, no. 6, pp. 3607–3612.
[208] U. Ul, D. G. Stephens, and M. A. Scavullo, "Nasa technical note reproduced from best available copy investigation of air damping of circular and

rectangular plates, a cylinder, and a sphere," 2001.
[209] J. T. J. N. ROLAND H. GOOD, *Classical Theory of Electric and Magnetic Fields*. 1971.
[210] W. Lord and L. Upda, "Diffusion, Waves, Phase and Eddy Current imaging," *Rev. Prog. Quant. Nondestruct. Eval.*, vol. 4A, pp. 499–506, 1831.
[211] D. J. (Derek J. . Craik, *Magnetism : principles and applications*. Wiley, 1995.
[212] G. S. Smith, "A simple derivation for the skin effect in a round wire," *Eur. J. Phys.*, vol. 35, no. 2, 2014.
[213] K. Kuns, "Calculation of magnetic field inside plasma chamber," *UCLA Rep.*, vol. 2, no. 3, pp. 1–11, 2007.
[214] D. J. DeTroye and R. J. Chase, "The Calculation and Measurement of Helmholtz Coil Fields," *US Army Res. Lab.*, pp. 1–22, 1994.
[215] W. M. Saslow, *Electricity, magnetism, and light*. Academic Press, 2002.
[216] *Permanent Magnet and Electromechanical Devices*. Elsevier, 2001.
[217] J. Vrbancich, "Magnetic field distribution and design of Helmholtz coils," *Mater. Res. Lab.*, 1991.
[218] K. T. Mcdonald, "Pitching Pennies into a Magnet Acknowledgment," 1997.
[219] M. Definition, "Magnet Falling Through Copper Tube," 2012.
[220] B. Jaffe, W. R. Cook, and H. L. Jaffe, *Piezoelectric ceramics*. Academic Press, 1971.
[221] H. F. Tiersten, *Linear Piezoelectric Plate Vibrations*. Boston, MA: Springer US, 1969.
[222] H. Kragh, "The Beginnings of Piezoelectricity. A Study in Mundane Physics - by Shaul Katzir," *Centaurus*, vol. 49, no. 3, pp. 251–252, Dec. 2007.
[223] P. Hagedorn, A. DasGupta, and Wiley InterScience (Online service), *Vibrations and waves in continuous mechanical systems*. John Wiley, 2007.
[224] V. Engineers, *Fundamentals of Signal Processing*. .
[225] W. Weaver, S. Timoshenko, and D. H. (Donovan H. Young, *Vibration problems in engineering*. Wiley, 1990.
[226] L. Meirovitch, *Fundamentals of vibrations*. Waveland Press, 2010.
[227] F. G. (Friedrich G. Friedlander and M. S. (Mark S. Joshi, *Introduction to the theory of distributions.* Cambridge University Press, 1998.
[228] H. T. Banks and D. J. Inman, "On Damping Mechanisms in Beams," *J. Appl. Mech.*, vol. 58, no. 3, p. 716, Sep. 1991.
[229] J. Krupka, J. Breeze, A. Centeno, N. Alford, T. Claussen, and L. Jensen, "Measurements of permittivity, dielectric loss tangent, and resistivity of float-zone silicon at microwave frequencies," *IEEE Trans. Microw. Theory Tech.*, vol. 54, no. 11, pp. 3995–4000, 2006.
[230] I. Remarks, "Kramers-Kronig Relations and Sum Rules."
[231] "Dielectrics."[Online].Available:https://www.tf.unikiel.de/matwis/amat/elmat_en/kap_3/backbone/r3_1_1.html. [Accessed: 09-May-2017].
[232] S. O. R. Moheimani and A. J. Fleming, *Piezoelectric transducers for vibration control and damping*. Springer, 2006.
[233] N. W. Hagood, W. H. Chung, and A. Von Flotow, "Modelling of Piezoelectric

Actuator Dynamics for Active Structural Control," *J. Intell. Mater. Syst. Struct.*, vol. 1, no. 3, pp. 327–354, Jul. 1990.

[234] M. C. Smith, "Synthesis of mechanical networks: The inerter," *IEEE Trans. Automat. Contr.*, vol. 47, no. 10, pp. 1648–1662, 2002.

[235] K. E. Drexler, *Nanosystems : molecular machinery, manufacturing, and computation*.

[236] S. H. Crandall, "The role of damping in vibration theory," *J. Sound Vib.*, vol. 11, no. 1, pp. 3-IN1, Jan. 1970.

[237] E. Graesser and C. Wong, "The Relationship of Traditional Damping Measures for Materials with High Damping Capacity: A Review," *M.* pp. 316-316–28, 1991.

[238] M. Carfagni, E. Lenzi, and M. Pierini, "The loss factor as a measure of mechanical damping."

[239] A. Nilsson and B. Liu, "Frequency Domain," in *Vibro-Acoustics, Volume 1*, Berlin, Heidelberg: Springer Berlin Heidelberg, 2015, pp. 31–66.

[240] B. R. Hanks and D. G. Stephens, "The mechanisms and scaling of damping in a practical structural joint," Jan. 1966.

[241] Crandall and S. H., "On scaling laws for material damping," Dec. 1962.

[242] Clarence Zener, *Elasticity and Anelasticity of Metals - Clarence Zener - Google Books*. University of Chicago Press, 1948.

[243] W. E. Baker, W. E. Woolam, and D. Young, "Air and internal damping of thin cantilever beams," *Int. J. Mech. Sci.*, vol. 9, no. 11, pp. 743–766, Nov. 1967.

[244] A. D. Nashif, D. I. G. Jones, and J. P. (John P. Henderson, *Vibration damping*. Wiley, 1985.

[245] "Massachusetts Institute Of Technology Linear Graph Modeling : Two-Port Energy Transducing Elements 1.".